2D Infrared Spectroscopy for the Study of Membrane-bound Proteins and Peptides

By

Erin R. Birdsall

A dissertation submitted in partial fulfillment of

the requirements for the degree of

Doctor of Philosophy

(Chemistry)

at the

University of Wisconsin – Madison

2022

Date of final oral examination: 05/12/2022

The dissertation is approved by the following members of the Final Oral Committee:

Martin T. Zanni, Professor, Chemistry
Alessandro Senes, Professor, Biochemistry
Thomas Brunold, Professor, Chemistry
Tina Wang, Assistant Professor, Chemistry

Abstract

Proteins and peptides associated with cell membranes play a vital role in cell signaling and cell health. From ion channels that allow cells to transduce electrical signals to antibiotic peptides that break open cell membranes, membrane-associated and membrane-bound proteins are of interest due to their importance. However, due to the nature of lipid membranes, the ion channels and other membrane proteins have historically been more challenging to study since they cannot be simply in aqueous solution like soluble proteins. Increased knowledge of protein expression and purification in the last few decades has made membrane-associated and membrane-bound proteins and peptides more readily studied, however, there is still much to learn about the basic function of these macromolecules. For example, one of the most fundamental processes is ion channel conduction. In potassium channels, potassium ions flow at nearly the diffusion limit with exquisite selectivity when the channel is open. The previously established mechanism for ion transduction has been recently called into question. Two-dimensional infrared spectroscopy is an excellent method to study membrane-bound proteins and peptides because of its structural sensitivity, inherent time resolution, and ability to be modeled from structural and computational results.

In this dissertation, methods with which to study potassium channels, as well as other membrane-bound peptides are developed, along with strategies to study surfaces, including working with proteins bound in a single lipid bilayer. First, a voltage and pH-sensitive antimicrobial peptide is studied using surface-enhanced 2D IR spectroscopy and an applied voltage. Since the peptide is in a bilayer tethered to a surface, the sample is no longer isotropic and relative intensities of spectral peaks allowed for the extraction of insertion angles upon a change in pH and a change in voltage. Insertion angles were determined through modeling the

spectra based on the peptide structure and helical coupling values. Next, progress to studying the selectivity filter of two potassium channels is outlined, including experiment looking at an ester label in the selectivity filter. The ester label causes a water pocket in the ion channel to collapse and changes the binding sites for ions in the selectivity filter. Using waiting time analysis, the dynamics of the labeled residue can be measured. Finally advances to polarization controls to distinguish bulk and surface signals is theoretically developed to create a surface specific spectroscopy. Finally, a chapter is included to disseminate the work presented in this dissertation to the public.

Acknowledgements

Ph.Ds. don't happen in a vacuum. All of the work that I present here represents an enormous effort of the parts of many people both in tangible and intangible ways. I have been so lucky to have spent the last five years surrounded by brilliant scientists and wonderful friends who have helped me accomplish my research aims. Here, I want to start by thanking the many people who have made this work possible and for all of their support throughout my career.

First, I would like to thank Marty Zanni, who in being my research advisor, has been instrumental in my research and graduate career. I appreciate your insights and help in allowing me to dictate my own path in the group and create a project I loved. Also, thank you for always being a cheerleader for me and my ambitions as well as being supportive when times got tough, both experimentally and outside of grad school.

Next, I would like to thank my committee members for their support and insights into my work. John Wright, I really enjoyed your great questions about spectroscopy. Alessandro Senes, thank you for asking questions that made me think about the biology in context and challenged me to better explain spectroscopy to a broader audience. Thomas Brunold, thank you for stepping in for John and helping on my 4th year meeting. Tina Wang, thank you for joining me on this last step and for all of your chem-bio insights into my work.

I would also like to thank the many people in the department who have helped to make this work possible. Thank you to Jeff Nielson for keeping the building running and my laser lab the right temperature. Thank you to Steve Meyers for helping me find parts, unscrew too-tight nuts, and help in designing sample cells. Thank you to Bruce Goldade who helped me 3D print many sample cell prototypes and always had a smile. Thank you to Cheri Stephens and Mary Hansen for helping me navigate the university system and always being ready for a conversation.

My interest in chemistry began in high school with two really important science teachers: Mary Schifsky and Kathy Mielke. Thank you for teaching me so much about the fundamentals of chemistry and biology and for your support, encouragement, and sense of fun with science.

My journey with chemistry continued at Middlebury College where I worked with Professor Jim Larrabee. Thank you, Jim for teaching me the basics of research and allowing me to learn to be independent in lab. I also was hugely influenced by Professor Sunhee Choi, my academic advisor, who taught me gen chem, quantum, research methods, and super-duper lab. Thank you, Professor Choi, for teaching me a dedication to excellence and persistence in the face of a challenge.

I would also like to thank Dr. Greg Smith at the Indianapolis Museum of Art. I spent the summer of 2020 at the IMA learning about how to work as a conservation scientist. Thank you for taking me under your wing and mentoring me. Thank you so much for helping me find my place in the field.

When I was applying for graduate school, my brother (then, a 3rd year graduate student) told me that the most important thing to look for, was a group a graduate students and post-docs who will mentor you, since they are vital to success. I am lucky enough to have worked with a group of super smart and super kind people and I am so grateful for you all. I want to thank all previous Zanni group members, those who I have met and those who I haven't for your work in creating a lab culture that is generous with time and knowledge.

Of the Zanni group members I had the privilege to work with, I would first like to thank Michał Maj and Justin Lomont. Though we only overlapped for a short amount of time, I really appreciated how welcoming you both were with advice and were ready to pay for touch tunes at Plaza. Thank you for your advice and expertise in my early experiments.

Next, I would like to thank Jia-Jung Ho, Nick Kearns, and Kacie Rich. Jia-Jung, thank you so much for all of your help with COSMOSS and for rewriting parts of the code so that I could use it for my special case. Thank you for taking the time to meet with me from Taiwan. Nick, thank you for being able to answer questions about the fundamentals of 2D spectroscopy to me through book club and spending your time doing that even in your last year. Kacie, thank you for your expertise in working with proteins and for all the fun with the Buckyballs.

Andy Jones: thank you for always being ready to explain any concept and for your patience with me learning about 2D spectroscopy. I always loved your humor and observations. I really enjoyed sitting behind you in the office and hearing about your cross-country skiing.

Josh Ostrander: Thank you Josh for being such a patient mentor. You taught me so much about the fundamentals of spectroscopy, how to think about fixing the laser table, how to think about my data, and how to navigate graduate school. I always looked forward to seeing you in the office and hearing about your experiments and also your thoughts on seminar speakers or a journal article you read. Thank you for being a mentor and friend to me even after you graduated. Thank you for your generosity with your time. I quote you all of the time. Living the dream for sure.

Ariel Alperstein: Ariel, you have been so influential on my graduate career. You sold me on Madison and the Zanni group. Thank you for teaching me so much about spectroscopy and being a scientist. Thank you for all of your help in navigating graduate school and thinking about my data. Thank you for all of the walks and chats and GBBO nights. I also want to thank you for your emotional support during graduate school. You were always ready to help me when I was frustrated and always were ready to help me to find a solution. I am so incredibly proud of you

and your academic career and you are, to me, everything the new wave of academics should be. I am so excited that we will be living so close to each other starting this summer!

Jessi Flach: Jessi, thank you for being a such a leader in the Zanni group. Even though our research did not overlap at all, your influence in the Zanni group was so significant to me, in how you balanced fun and rigor and kept the group on the same page. I admired how you took the reins of your project and chose to focus on the parts you found interesting. I really liked being on the dodgeball team with you and seeing you outside of lab!

Megan Petti: Megan, I don't even think I can describe how much it meant to me that we got to work together. I could not have done this without you. Thank you so much for your support and guidance and friendship. Thank you for always being ready to drop what you were working on to help me. Thanks for your excellent questions about my data and your love of finding papers. Thank you for taking walks with me and for all of the mini therapy sessions in the laser lab. After you graduated, I played Taylor Swift in the laser lab so that it was like you were in there with me helping to realign the laser or solve whatever problem we were having. I missed aligning things with you and how we always knew what to do to help without having to say anything. Your intelligence and toughness and kindness were so inspiring to me and I cannot even begin to express how much I feel like my Ph.D. is half yours. Thank you <3

Miriam Bohlmann Kunz: Mirm, I feel so lucky that we got to do our Ph.Ds. together. I loved being able to ask you any silly spectroscopy question and really appreciated the time you took to help me. Thanks for being a friend inside and outside of lab. Thanks for all of your support during the hard times and always being ready to celebrate with me as well. You are so generous and so smart and it's such an admirable combination. You are always ready to listen and really engage with research that isn't your own. I just spent 5 minutes thinking of a good pun

to fit in and I literally cannot so I will say that your gift is that you can write one in the margins of the Zanni group copy. Thanks for every Stan pic as well.

Caitlyn Fields: Cat, again, I am so honored that we got to do our Ph.Ds. together. It was so fun to watch us grow together as scientists. You are so strong and hardworking and intelligent and the world is your oyster. I loved that we got to spend the last year hanging out on the 7th floor trying to get a single silver stain to show some oligomers. I really value and appreciate all the time you took to train me to make isotope labels and how you were generous with your time with so much of the group in terms of training. And thanks for all of your pep talks and words of encouragement when I got frustrated.

Kieran Farrell: Kieran, thanks for all of your help when I had a spectroscopy question or needed advice on troubleshooting the laser. I appreciate all the times you would drop what you were working on to help me. You are a good scientist and have an admirable work ethic. I am sure that wherever you end up will be lucky to have you.

Ryan Allen: Ryan, thanks for all of your help especially when we were in quantum together doing those problem sets. I admire your independence and your perseverance on your project. I admire your commitment to the pineapple and llama aesthetic and your skills on the dodgeball court.

Sidney Dicke: Sid, you are such a source of positive energy in the group. I really admire how to balance rigorous work in lab with a full-of-activity life outside. You are working on some really tough projects and I know you are going to go far with your work ethic and ability to balance.

Zachary Armstrong: Zach, thank you for your tough questions and generosity of attention and interest in projects across the group. I really admire how you are able to balance your work

and you love of life outside of lab as well. I have every confidence that with your scientific skills you will go far and find an amazing post doc that is just right for you in a place with elevation. I really enjoyed all of the time we got to spend together and all of the coffee breaks and chats about the nature of academia, and Strava goals, and just life in general. I am so glad we were office mates and that we got to spend so much of our graduate careers together.

Yulia Podorova; Yulia, you are such a bright light in the Zanni group. I really admire how despite all of the bumps in your research you maintain a positive energy and always bound into the office when you have had a success. I know you are going to have a great rest of your Ph.D. because of your persistence. Thank you for so many delicious treats made with love and for your infectious energy. Thanks also for your recommendations for music and podcasts, which are always wonderful.

Matt Ryan: Matt, I am so glad that you joined the Zanni group and joined the ion channel project. I think you bring so much to the team in terms of wanting to really get into the nanofabrication and having a very systematic approach to sample preparation and experimental design. Thank you for being patient with me as I taught you the fun quirks of the laser table and for not being scared away by the laser being down when you first joined. I have every confidence that you will have an amazing Ph.D. and will go far in whatever you want to pursue.

Yuzhe Zhang, Yuzhe, although we have not worked together much, I am impressed by your complete focus and dedication to your work. I really enjoyed journal club with you over the summer. Zac Faitz: Zac, it has been great to get to know you and hear about all of your progress on your project. Also thank you so much for all of your nut-containing LabSnacks. Harrison Esterly, Harrison, I enjoyed getting to know you and I wish you the best.

Nan Yang: Nan you have been such an asset to the Ion Channel project. Thank you so much for helping with so many coding projects that I had been putting off. Thanks also for your always-chill attitude and ability to face challenges with a can-fix attitude. I always like hearing about your flying progress. I wish you the best in finding an academic position.

Farzaneh Chalyavi: Farzaneh, I am so glad that you joined the Zanni group. You brought with you so much knowledge on sample prep and creative solutions for getting good spectra. I always appreciated your advice on how to improve my experiments. Furthermore, I am so grateful for your pep talks and positive attitude when experiments aren't working. You really helped me push through hard times and were always ready with a joke and advice for success.

Minjung Son: Mingjung, I have really enjoyed getting to know you and sitting next to you in the office. I really admire all of your hard work and persistence in getting data. Thanks for your advice in getting ready for presentations and for always offering to look over drafts and presentations for me. I wish you all the best on the job market next year! I am sure you will find a great position.

Beyond the Zanni group I want to thank my support network. I want to thank my parents for their love and support. I want to thank Adam and Rebekkah (and Nova) for advice and dog content. I want to thank all my extended family who have given me a ton of encouragement over the last five years over games of 500 and family gatherings. I also want to thank my partner Erik for always being there to support me, to give me advice, and to keep me interested in the world around me. <3

My time in Madison would not be complete without my friends here that I didn't list above. Logan, Sarah, Emily, Griffin, Kate, Veronica, Cole, and many more thank you for all of the fun memories in Madison and support. Madison has been such a wonderful place to spend

five years and I will miss the lakes and the Terrace and the coffee breaks. I am so grateful to be in a department with such wonderful, smart, and kind graduate students.

Table of Contents

List of Figures

List of Tables

1 Introduction, Background, and Motivation

1.1 Introduction

It has long been known that nerves and muscles are electrically excitable.[1–3] However, the root of this phenomenon, specifically the movement of ions across the membrane triggering the electrical excitation was not discovered until the early 1900s by Julius Bernstein and coworkers.[4,5] This discovery was expanded by the works of others leading to Nobel Prizes won by Hodgkin and Huxley for their work with the electrophysiology of squid axons, and MacKinnon and his first crystal structure of an ion channel.[1,6,7] Work in this field currently seeks to better understand the transport of ions and the response of ion channels to their environment.

We are working towards using 2D infrared (2D IR) spectroscopy to investigate the movement and ion transport in these channels. 2D IR spectroscopy allows for the characterization of secondary structure of proteins by looking at the frequency (or wavelength) of light absorbed by the protein.[8] In the case of infrared (IR) light, the energy of the light is equal to the energy of the vibrational motions of molecular bonds. To determine secondary structure of a protein, one can look at the amide I vibration, which has characteristic frequencies for β-sheets, α-helices, and other secondary strutures.[8–11] Furthermore, these vibrations are sensitive to the environment of the bond itself, so the technique is also sensitive, for example, to a protein in a lipid membrane versus in aqueous solution. Different labelling schemes can be used in order to isolated the vibration of a single amino acid out of the rest of the protein signal to get *site-specific* structural information.[12–14] This structural information can be verified and explained by straightforward computational models of proteins.[11,13] Finally, by using an ultra-fast laser

system, it is possible to create experiments that give time-dependent insights with extremely fine (picosecond) time resolution, allowing us to observe protein dynamics.[8] In this dissertation, I outline the methods developed to gain even deeper insights into membrane-bound proteins and peptides using 2D IR spectroscopy.

1.2 Background

1.2.1 Ion Channels

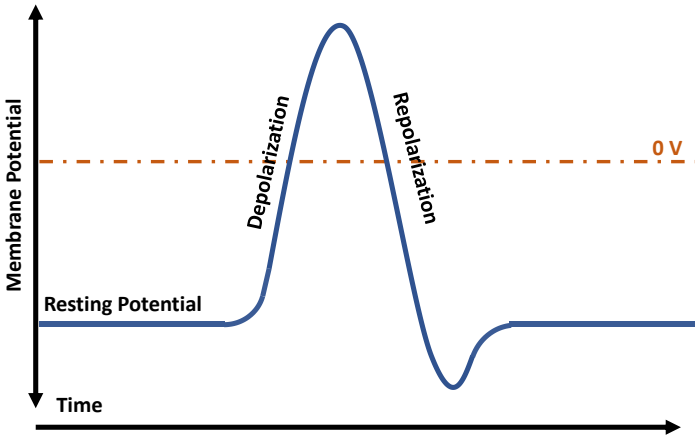

Figure 1.1 Cartoon depiction of an action potential. Potassium channels open, causing repolarization, and close to cause the membrane to reach resting potential.

Ions can move through channels passively or actively. This can be illustrated through the action potential of a nerve cell.[1,3] During the resting phase, the concentration of cations is such that there is a greater concentration of sodium outside the cell and a greater concentration of potassium inside the cell. When the action potential is triggered, sodium channels open and sodium ions stream passively along the concentration gradient into the cell, causing a change in the charge of the membrane called the depolarization phase. The change of the membrane potential in turn triggers the opening of potassium channels and potassium ions move out of the cell, also by passive diffusion, triggering the repolarization phase. The initial depolarization signal will then trigger then next set of sodium channels perpetuating the signal. Active transport ion pumps then use ATP to move the sodium and potassium to their original sides of the cell membrane.[15–17]

This requires energy because the ions are moved towards a more concentrated area. In this work, we are interested in passive transport ion channels.

Here, we are primarily concerned with studying K^+ channels. In humans, K^+ channels play a vital role in brain and heart function to due to their role in repolarization discussed above.[18–20] Mutations in K^+ channels have been shown to lead to disease such as cardiac arrhythmias and epilepsies.[21,22] K^+ channels are notable in that they have extremely high specificity to potassium. Despite this specificity, these channels maintain an ion flux at nearly the diffusion limit.[23–25] This is especially interesting in the case of K^+ channels, which are highly selective for K^+ over Na^+ despite the larger radius of K^+. Potassium channels open and close in response to stimuli, like changes in pH and voltage and such voltage gated channels are responsible for electrical signaling in cells.[26–29]

Generally, these ion channels are tetrameric and non-domain swapped proteins.[26,30,31] All potassium channels share a similar pore domain that consists of largely α-helices. The pore domain has a gate which opens and closes and allows the ions to pass through the selectivity filter.[7,32] In the selectivity filter, the ions and perhaps water are coordinated by the backbone carbonyls. In voltage-gated channels, there is an additional voltage sensing domain on each monomer. The voltage sensing domain is composed of four additional helices which likely allosterically control the gate in the pore domain.[30] Studies have begun looking at the mechanism of ion conduction of these channels. In K^+ channels, the sequence of amino acids in the selectivity filter is highly conserved.[33] Therefore, much research has been done on a very simple potassium channel, KcsA, which does not have a voltage sensing domain, to interrogate the mechanism. This is also the first ion channel to have its crystal structure solved.[7] Research then

progressed to other potassium channels of interest, which will be addressed individually in the following sections.

1.2.1.1 KcsA: A Simple Model Potassium Channel

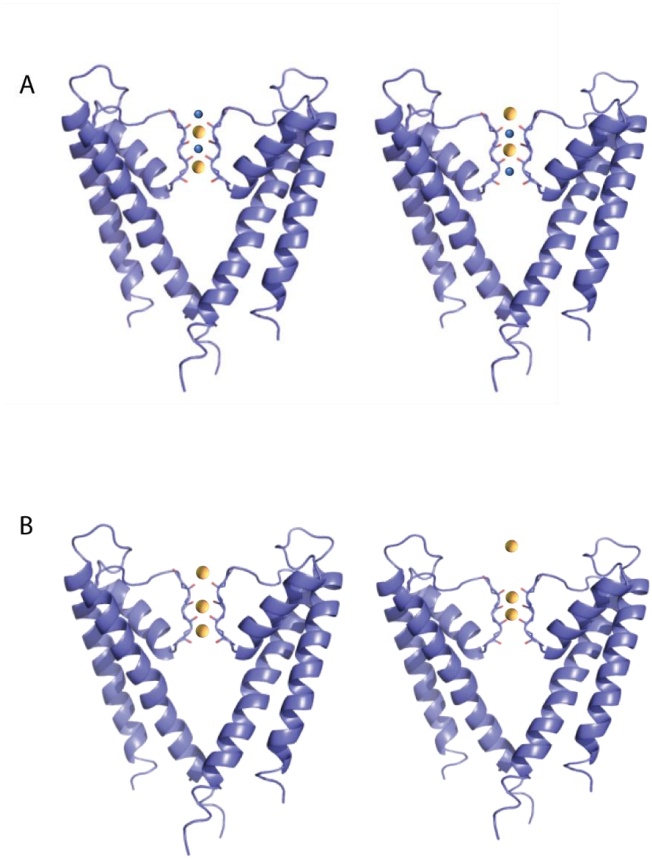

Figure 1.2 Structure of KcsA. Only two of four monomers are shown for clarity. Yellow balls in the selectivity filter represent potassium ions and blue balls represent water molecules. A) The canonical ion configurations. B) The new 'hard-knock' model PDB: 1BL8

KcsA has been highly characterized as a model for K^+ ion transduction. As stated above, KcsA is a homotetramer. Backbone carbonyls, along with the hydroxyl side chain of the threonine, in each monomer coordinate ions and waters in what is called the selectivity filter – where the K^+ is 'selected for' over other ions.[34] The sites formed by the carbonyls are labelled S1- S4. The selectivity filter has a highly conserved sequence (TVGYG). The structure of KcsA is show in figure 1.2. The selectivity filter has been highly characterized by x-ray crystallography, single channel electrophysiology experiments, NMR spectroscopy, radiotracer experiments, as well as molecular dynamics simulations.[6,35–39]

A considerable amount of evidence, including data generated previously in the Zanni group, has suggested that the ions permeate KcsA through the 'soft-knock' mechanism, which is also

sometimes referred to as the ‘canonical’ mechanism.[13,40] In the ‘soft-knock’ mechanism, there are always two potassium ions and two water molecules in the selectivity filter, and they alternate either being in S1 and S3 or S2 and S4, as shown in figure 1.2A. Recent work by de Groot and colleagues have suggested that a different permeation mechanism is happening.[41,42] The ‘hard-knock’ model has only potassium ions and no intervening water molecules, and the two configurations are potassium ions at S2 and S3 or S1, S2 and S4 as shown in figure 1.2B. Most evidence for the ‘hard-knock’ model has come from simulation, and previous 2D IR data from the Zanni group did not support this model.[41] However, the 2D IR data did not present a unique solution, so the question is still active as to mechanism of ion transduction, and with a larger array of experiments, we hope to eventually differentiate between the models experimentally.

Other experimental methods to determine the ion occupancy of the filter include using x-ray crystallography, including doping the channel with a heavier metal, like rubidium, which has a more easily observable density relative to water than potassium, making the configurations easier to observe.[25,38,43] Also, in order to probe the relative energies of different binding sites, ester mutations have been used to disrupt the channel. In the ester mutation experiments, it was found that an ester mutation at Y78 causes channel inactivation and the creating of a new binding site, S0.5.[44,45] These ester mutations and rubidium doping experiments cause similar ion occupancy, therefore are of interest as a way to compare inherently static x-ray crystallography experiments with the dynamics accessible with 2D IR spectroscopy that will be discussed in a later section.

1.2.1.1.1 NaK and NaK2K: A Non-selective Cation Channel and its selective mutant

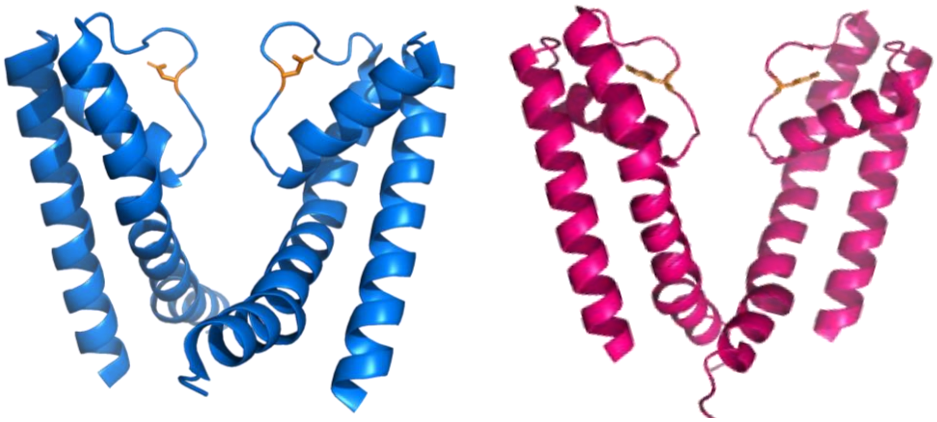

Figure 1.3 Structures of NaK (blue) PDB: 3E8H and NaK2K (red) PDB: 3OUF. Only two of the four units are shown for clarity the other two are orthogonal to the plane of the page. The D in the NaK selectivity filter and the Y in NaK2K selectivity filter is highlighted in orange.

Another channel that is of interest is the non-selective cation channel, NaK, originating from the bacteria *Bacillus cereus*. NaK allows both Na^+ and K^+ to passively flow through the channel. Like KcsA, it is a homotetramer with generally a similar structure as shown in figure 1.3. An important difference between the two channels is the amino acid sequence of the selectivity filter which is TVG**D**G rather than TVG**Y**G for NaK and KcsA respectively. The single substitution of Asp for Tyr causes NaK to have just two binding sites (S3 and S4) in the selectivity filter rather than four. The binding sites change because the backbone carbonyls of the G65 and D66 are now tangentially oriented to the axis of the pore and therefore no longer coordinate the ions as strongly.

Interestingly, the Jiang group at UT-Southwestern demonstrated that the selectivity filter sequence is changed to match that of KcsA, then K^+ selectivity is regained, and the selectivity filter again has four binding sites.[46] This mutant channel was named NaK2K to represent the function of the mutation. Crystallography experiments using anomalous diffraction on NaK2K have indicated that the 'hard-knock' model can be applied to NaK2K.[47] This supports the need to further study these channels to determine the method of ion transduction through the channels.

Furthermore, NaK and NaK2K are interesting in informing the method of selectivity generally. Similar studies can be carried out in NaK2K and KcsA to determine if mutants (such as an ester substitution) lead to similar impacts on structure and ion occupancy. Furthermore, studies on NaK2K in different ion buffers could also lead to better understanding of the root of ion selectivity.

1.2.1.2 KvAP: A Model Voltage-Gated Potassium Channel

Figure 1.4 Structure of KvAP. The pore domain is shown in light purple and the voltage sensing domain is shown in dark purple. Two of four monomers are shown for clarity. PDB: 6UWM

The last K^+ channel family of interest are the voltage-gated 'K_v' channels. The best studied of which is KvAP, a voltage-gated K^+ channel named after the archaebacterium from which it originates *Aerpyrum pernix*. KvAP is the first of the K_v channels to have a solved crystal structure and is therefore the best studied.[30,48–50] The channel is a non-domain-swapped tetramer.[51] The first four helical segments form the voltage-sensing domain. The last two helices form the pore domain. The pore domain is very similar to KcsA, and shares the same selectivity filter sequence, conferring its K^+ selectivity. In the voltage-sensing domain, the helix of greatest interest is the fourth transmembrane helix (TM4).[29,50,52–55] The TM4 helix is connected to the pore domain via a short unstructured linker. The TM4 helix contains charged amino acids (typically arginine) across the K_v family of channels.[50] In KvAP, there are five arginine residues spaced about one per turn along the helix.[50] It is thought that the charged residues are what sense and then mobilize in response to a change in membrane

polarization. It is yet unknown precisely how the TM4 helix moves in response to change in voltage. Different evidence from crystal structures as well as MD simulations suggest several options: a change in secondary structure between an α-helix and 3_{10}-helix, a change in insertion depth into the lipid membrane, a change in tilt of the TM4 helix, or a rotation of the TM4 helix.[29,52,54,56–59] Furthermore, it would be interesting to obtain well time resolved data on how long it takes for the different molecular motions to happen when a voltage is applied to the membrane. For reasons that I will outline below, 2D IR spectroscopy is a useful method to answer these questions.

1.2.2 Background of 2D IR spectroscopy

1.2.2.1 Theory of 2D IR spectroscopy

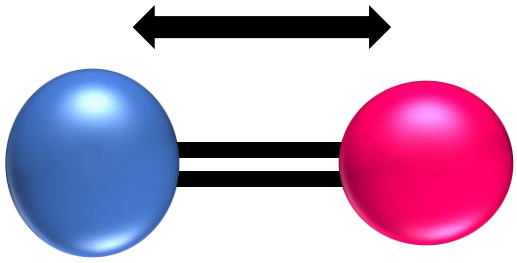

Figure 1.5 Simple oscillator representing a semi-classical simple oscillator where the bond between the atoms acts like a spring.

In this section the theory of 2D IR spectroscopy will be briefly described from basic principles. Standard vibrational spectroscopies probe the vibrational energy levels in the ground electronic state of the molecule. The vibrational energy levels can be probed either directly by observing the absorption of infrared light – the energy of which is equal to the energy difference between vibrational energy levels—or indirectly through Raman scattering, where higher energy light is used and the difference in energy between the light used to excite and the light emitted is measured.[8,60] In both cases, the frequencies of light measured correspond to vibrational motions of the molecular bonds. These frequencies are distinct and are often likened to the 'vibrational fingerprint' of the molecule. A vibrational spectrum can thus be used to characterize the

molecule. This dissertation makes use of the direct measurement of IR light absorbed by the sample.

Diatomic molecules are often used to describe simple vibrational motions as shown in figure 1.5. One can imagine this molecule as two atoms connected by a spring-like bond. In the ground vibrational state, the molecules vibrate at their lowest frequency. When light interacts with the molecule, the energy is dissipated through the molecule and the vibration is faster. The spring model is very intuitive: one can imagine this diatomic molecule being described by a simple harmonic oscillator classically:

$$V(x) = \frac{1}{2}kx^2$$

(1.1)

Where V(x) is the potential energy, k is the spring's (or bond's) force constant, and x is the distance between the atoms. However, this description does not take into account the quantized nature of vibration energy levels. The energy levels of a quantum harmonic oscillator are generated by using the Schrödinger equation with the classical potential energy as shown

$$E = \hbar\sqrt{\frac{k}{\mu}}(v + \frac{1}{2})$$

(1.2)

.

Where E is the allowed energy, $\hbar$ is Planck's constant, μ is the reduced mass of the system or molecule, and v is the vibrational energy level which must be an integer equal to or greater the 0. The energy, therefore, is dependent on the constituent atoms of the vibration being studied as

well as the strength of the bonds between them through reduced mass and the spring constant. The quantization of vibrational energy levels results in discrete values that fit within the harmonic oscillator potential energy curve. Each level is a different vibrational state that the molecule can be in, and each level is described by a different wavefunction. In harmonic oscillators, the difference in energy between the levels are equal. From the Boltzmann equation, we know that most molecules are in the ground vibrational state a room temperature. When light of a wavelength equal to the energy between the vibrational energy levels interacts with the sample, the molecule goes from the ground state ($v = 0$) to the first excited vibrational state ($v = 1$). These states are better described as representing probabilities of where the nuclei are. In the ground state they are more likely to be at the equilibrium internuclear distance, while at the first excited state, they are more likely to be at a larger distance.

However, molecules are not harmonic oscillators. A more accurate picture of vibrational spectroscopy of a diatomic is described by a Morse potential which is described classically as

$$V(x) = D_e(1 - e^{-a(x-x_e)})^2 .$$

(1.3)

Here, D_e is the bond dissociation energy, a is the potential energy function width, and x_e is the equilibrium position. As one can see, this equation takes into account the dissociation energy of the bond (since it cannot stretch infinitely far) and the anharmonicity of the potential energy well. When this equation is applied to the quantum harmonic oscillator, the anharmonicity causes each successive higher vibrational energy level to be slightly closer in energy. They are no longer evenly spaced.

Potential energy surfaces give an intuitive explanation of vibrational spectroscopy. Besides the potentials, one also needs to know how the molecules interact with the light. We now consider light as an electric field interacting with a dipole causing a perturbation. The change in the dipole is called the transition dipole (μ) and is related to the potential energy surfaces described above. The perturbation of the dipole is the macroscopic polarization (P) and it is related to the molecular susceptibility (χ) and the incident electric field (E) in the first order as

$$P^{(1)}(\omega) = \chi^{(1)}(\omega)E \tag{1.4}$$

in the frequency domain or

$$P^{(1)}(t) \propto \int_0^t dt\ R^{(1)}(t)E(t) \tag{1.5}$$

in the time domain where R is the molecular response. R is described as

$$R^{(1)}(t) \propto i\mu_{01}^2 e^{-i\omega_{01}t}e^{-t/T_2} \tag{1.6}$$

and contains the information desired about the vibration of interest. In this equation, $R^{(1)}(t)$ is the time-dependent first-order molecular response, μ_{01}^2 is the transition dipole strength squared of the 0→1 transition, ω_{01} is the frequency of the 0→1 transition, t is the time and T_2 is the homogeneous relaxation time. We consider generally the 0→1 transition here, as the ground state

is the most populated state at room temperature and vibrational selection rules are such that $\Delta v = \pm 1$. Further details of this derivation have been fully elucidated in previous papers and books.[8,60]

These equations describe a first-order response and first-order macroscopic polarizability which assumes a case of a single light-matter interaction. The change in polarizability produces a signal field, $E_{sig}^{(1)}$, which is phase shifted from the polarizability by 90°. This is the field that contains the desired information of the molecular response as shown:

$$E_{sig}^{(1)}(t) \propto iP^{(1)}(t) \tag{1.7}$$

What is measured then in vibrational experiments? The $E_{sig}^{(1)}$ is not the only electric field that reaches the detector. In many cases, such as in our spectrometer or in FTIR spectrometry, the incident electric field is also dispersed onto a square law detector in the frequency domain. Square law detectors, as the name suggests, measure the intensity of the light so the magnitude of the electric field is squared. The light in a monochromator is transformed from the time to frequency domain by a grating. We can do this mathematically by employing a Fourier transform. The signal in frequency ($S(\omega)$) is described as:

$$S(\omega) = \left| \int_0^t dt \left(E(t) + E_{sig}^{(1)}(t) \right) e^{i\omega t} \right|^2. \tag{1.8}$$

After squaring and simplifying we see that

$$S(\omega) \propto I_0(\omega) + 2Re\left(E(\omega) \cdot E_{sig}^{(1)}(\omega)\right) + I_{sig}(\omega).$$

(1.9)

Where I_0 is the intensity of the incident electric field, $Re\left(E(\omega) \cdot E_{sig}^{(1)}(\omega)\right)$ is the real part of the interference between the signal electric field and the incident electric field, and I_{sig} is the intensity of the signal electric field.

In these experiments we are interested in the absorbance which is conventionally defined as the logarithm of $S(\omega)$ divided by $I_0(\omega)$. The I_{sig} term is neglected because it is very small. Therefore, the absorbance is:

$$A(\omega) = \log\left(\frac{I_0(\omega) + 2Re\left(E(\omega) \cdot E_{sig}^{(1)}(\omega)\right)}{I_0(\omega)}\right) \approx 2Re\left(E(\omega) \cdot E_{sig}^{(1)}(\omega)\right)$$

(1.10)

Which makes intuitive sense as E and $E_{sig}^{(1)}$ destructively interfere. The interference decreases the light reaching the detector after the sample, which is how we think of absorbance.

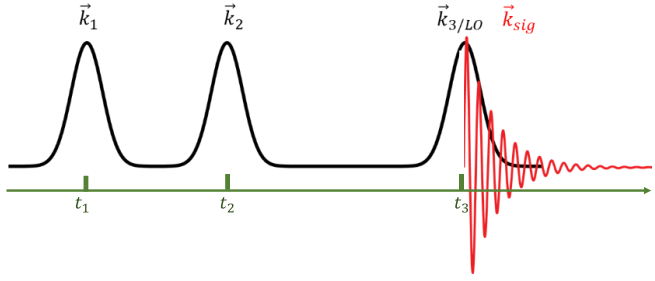

Figure 1.6 2D IR pulse sequence

Now that linear absorption vibrational spectroscopy has been explained, it can be extended to 2D IR spectroscopy. The difference in this case is the number of light-matter

interactions. In linear IR, a first-order spectroscopy, we consider a single photon entering the system and one photon exiting. 2D IR spectroscopy is a third-order spectroscopy and there are three incoming photons and one photon exiting. To create our three incoming light-matter interactions, we generate three laser pulses that pass through the sample. This pulse creation is described in detail in Chapter 2.3. We call the first two pulses 'pump pulses' and the third pulse the 'probe pulse'. The third-order polarizability, therefore considers the three electric fields and the three time-delays $t_1, t_2,$ and t_3 relative to *t* shown in the pulse sequence in Fig 1.6. It is similar in form to the first order as shown here.

$$P^{(3)}(t_3, t_2, t_1) \propto \int_0^\infty dt_3 \int_0^\infty dt_2 \int_0^\infty dt_1 \; E_3(t - t_3)E_2(t - t_3 - t_2)E_1(t - t_3 - t_2 - t_1)R^{(3)}(t_3, t_2, t_1) \tag{1.11}$$

Here, the subscripts designate which light field is interacting and $R^{(3)}$ is the third-order response. Response functions will be discussed in more detail later in this section. The third-order signal is proportional to the third-order polarizability, just as was the case in first-order spectroscopy. The emitted third-order signal field is also measured by using a square-law detector. However, a fourth pulse is used to interfere against the signal like the 'incident electric field' in the linear case described above. This pulse is called the local oscillator and the technique of using a local oscillator to interfere with the signal is called *heterodyning*. Incorporating these ideas into the mathematical description of the signal on a square law detector we get:

$$S(t_{LO};\, t_2, t_1) \propto \int_0^{\infty} \left| E_{LO}(t_3 - t_{LO}) + \, E_{sig}^{(3)}(t_3, t_2, t_1) \right|^2 dt_3$$

(1.12)

Which we can again simplify to

$$S(t_{LO};\, t_2, t_1) \approx \, I_{LO} + 2E_{LO}(t_3 - t_{LO}) \cdot E_{sig}^{(3)}(t_3, t_2, t_1) + \, I_{sig}^{(3)}$$

(1.13)

The absorptive signal is designated the ΔOD and is functionally measured on the set up used in this dissertation by cycling the pump pulses on and off to isolated our pump pulse which doubles as our local oscillator because of our experimental geometry. The ΔOD is therefore the logarithm of the signal with the pump on divided by the signal with the pump off. When the division is done, this results in

$$\Delta OD = \, log\left(\frac{I_{LO} + \, 2E_{LO}(t_3 - t_{LO}) E_{sig}^{(3)}(t_3, t_2, t_1)}{I_{LO}} \right) \approx \, \frac{2E_{LO}(t_3 - t_{LO}) E_{sig}^{(3)}(t_3, t_2, t_1)}{I_{LO}} \, .$$

(1.14)

At this point, one can perform a Fourier Transform over the difference between t_1 and t_2 as well as the difference between t_3 and t_{LO} to get a frequency-frequency spectrum of the pump and probe respectively. However, in our experiments we use a monochromator and grating to perform the Fourier transform of t_2, or the probe dimension. We do perform a Fourier transform of our t_1 axis during data processing.

But what is happening in these equations? What is the intuitive explanation as to how the laser pulse and the sample are interacting? This is what is illustrated in the third-order response function. There are many light-matter interactions that can occur, and because we are performing a bulk—rather than a single-molecule—experiment, the resulting spectrum contains all these (selection rule-allowed) combinations. An easy way to visualize these interactions is to use a double-sided Feynman diagram, six of which are shown in Figure 1.7. These show the evolution of the interactions over time The vertical lines, represent time increasing. Arrows represent light fields. The dotted arrow is the emitted electric field. An arrow pointing inward represents an excitation and an arrow pointing outward represents a deexcitation. The left and right side of the diagram interacts on represents the side of the matrix that is operated on or if it is a real or imaginary interaction respectively. The light must always be emitted in the real direction. The numbers represent the vibrational energy level of the oscillator.

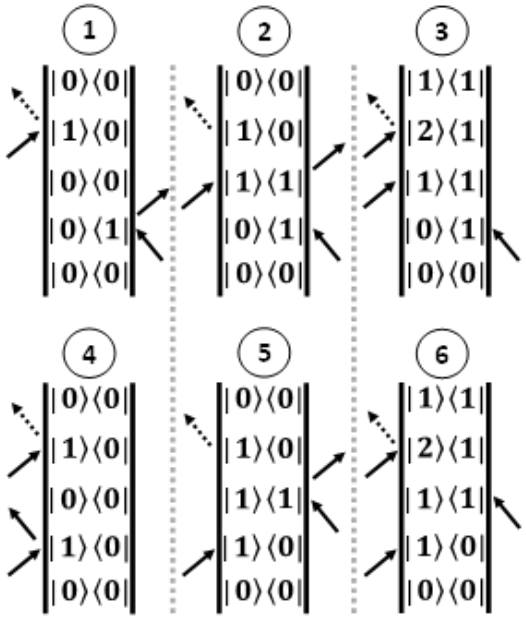

Figure 1.7 Six double-sided Feynman diagrams showing light matter interactions. 1-3 are all representative of rephasing pathways and 4-6 are representative of non-rephasing pathways.

The six diagrams can be divided into many categories. Firstly, 1, 2, and 3 are all rephasing pathways and 4, 5, and 6 are all non-rephasing pathways. These are designations that in some data collection geometries impact the direction of the emitted signal. However, this is not a factor in the pump-probe geometry utilized here. Sample geometries are discussed in the next section. The other set of categories is the kind of signal generated by the pathway. Diagrams

1 and 4 are called ‘ground state bleaches’ in which the response goes back through the ground vibrational state during t_2 or the population time. Diagrams 2 and 5 are called ‘stimulated emission’ in which the response is in the first vibrational state during the population time. In both ground state bleach and stimulated emission, the frequency measured is the 0→1 transition. The last two diagrams, 3 and 6, are called excited state absorption. This measures the 1→2 transition.

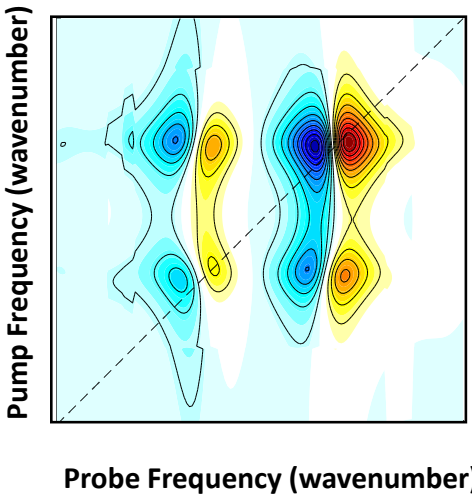

Figure 1.8 Model 2D IR spectrum. Positive peaks are shown in red and negative peaks are shown in blue. Cross peaks are seen between the coupled oscillators off of the diagonal.

The resulting spectrum from a model oscillator is shown in Fig 1.8. The pump frequencies are on the x-axis and probe frequencies are on the y-axis. For the single oscillator, there are two peaks. The peak where the pump and probe frequencies are equal is called the diagonal or fundamental peak and it is the transition between the ground and first vibrational states. Generally, we plot the diagonal peak as positive. The fundamental peak corresponds with the ground state bleach and stimulated emission pathways. The peak of opposite sign to the left of the fundamental is called the overtone and corresponds to the transition between the first and second excited vibrational stated. It is at a lower frequency due to the anharmonicity discussed earlier.

One major advantage of 2D IR spectroscopy is that it resolves peaks originating from interactions between coupled oscillators. A model spectrum of coupled oscillators is shown in Fig 1.8. There are two sets of the fundamental and overtone peaks, one for each oscillator.

Furthermore, there are additional ‘cross-peaks’ above and below the diagonal at the fundamental frequency of each. They occur because of the coupling of the oscillators where one is excited at t_1, and the other emits signal at t_3. The difference in frequency between the pair of cross peaks is called the ‘off diagonal anharmonicity’ and it corresponds to the coupling strength between the oscillators.[8]

Another benefit of 2D IR spectroscopy is the analysis of 2D line shapes. Monitoring these linewidths as a function of waiting time (or population time), defined here as the time between t_2 and t_3 when the system is in a population state rather than a coherence, can give insight into the dynamics of the system being measured and has been widely utilized. A common way of doing this measurement is called center line slope (CLS) analysis. In this analysis, the slope of the centerline is monitored over a variety of waiting times and plotted. This plot can then be used to extract the frequency-frequency correlation function which gives insights into the time scales of relaxation of the system. This will be explored in detail below.[8,61]

1.2.2.2 Experimental foundations

Though the bulk of the experimental details important to the work described here are found in their own chapter, there are some considerations in the design and implementation of the 2D IR spectrometer that are important to the foundations of the spectroscopy discussed here. There are several ways to collect 2D IR spectra. One such consideration is the geometry at the sample position. This is vital in determining the direction of the emitted signal field. The direction of the emitted signal is determined by direction of the wavevectors of the incident light fields as well as which signal that is being collected. In the third-order Feynman diagrams shown in figure 1.7, each diagram represents different possible sets of light-matter interactions. Sample

geometry can allow us to determine which of these sets of pathways we observe though 'phase-matching'. The third-order polarizations are convolutions of the response functions with the laser electric fields. These electric fields have wavevectors and phases as shown:

$$E_n(t) = E'_n(t)\cos(\vec{k}\cdot\vec{r} - \omega t + \varphi) \quad (1.15)$$

Where $\mathrm{E'_n}$ is the real-valued electrical field. In the third-order polarizabilities show in equation 1.11, one can see that there are three electric fields with wavevectors and phases, therefore, interacting with each other. The $\vec{k}$ values are additive, and lead to different signals emitting in different directions. A subscript on $\vec{k}$ denotes the ordering of the wavevectors. The Feynman diagrams can be used to determine which direction the signal field will be emitted. The first Feynman diagram would emit in the $-\vec{k}_1+\vec{k}_2+\vec{k}_3$ direction. Arrows pointing to the left denote a negative wavevector and arrows pointing to the right denote a positive wavevector. When looking at the Feynman diagrams in figure 1.7, therefore, one can determine that all of the rephasing diagrams emit in on direction $(-\vec{k}_1 + \vec{k}_2 + \vec{k}_3)$ and all of the non-rephasing diagrams emit in a different direction $(+\vec{k}_1 - \vec{k}_2 + \vec{k}_3)$. The difference in the direction of signal between pathways can be used to differentiate pathways. Further implications of 'phase-matching' as well as full derivations have been published.[8]

For example, in boxCARS geometry, which is a popular method, the three incoming laser pulses came from different angles and all three had to be separately spatially (and temporally) overlapped at the sample as seen in figure 1.9A.[8,62] Furthermore, in order to heterodyne, a fourth local oscillator is also passed through the sample. In this case, the rephasing and non-rephasing

signals were emitted in separated directions. To get purely absorptive data, then, the two sets of signals had to be collected separately then added together. A benefit to this method is being able to independently tune the local oscillator to maximize signal.[63] However, is it technically demanding and the post-processing of the data to ensure the correct phasing is not trivial.

The pump-probe geometry used here has been introduced more recently and is shown in figure 1.9B. The main benefit of the geometry is that the signal is collinear with the probe pulse. The probe then acts as the local oscillator and this circumstance is then called 'self-heterodyning'.[8,64] Furthermore, the phase-matching geometry makes it such that the rephasing and non-rephasing signal are also collinear, halving the collection time needed and eliminating the need to phase the data. Finally, it is less technically challenging because one only has to overlap two beams in space and time. Using a pulse shaper to create the two collinear pump pulses also allows for a high degree of phase control, even allowing for phase cycling which can eliminate scatter and increase data quality.[65] The lack of control of the intensity of the local

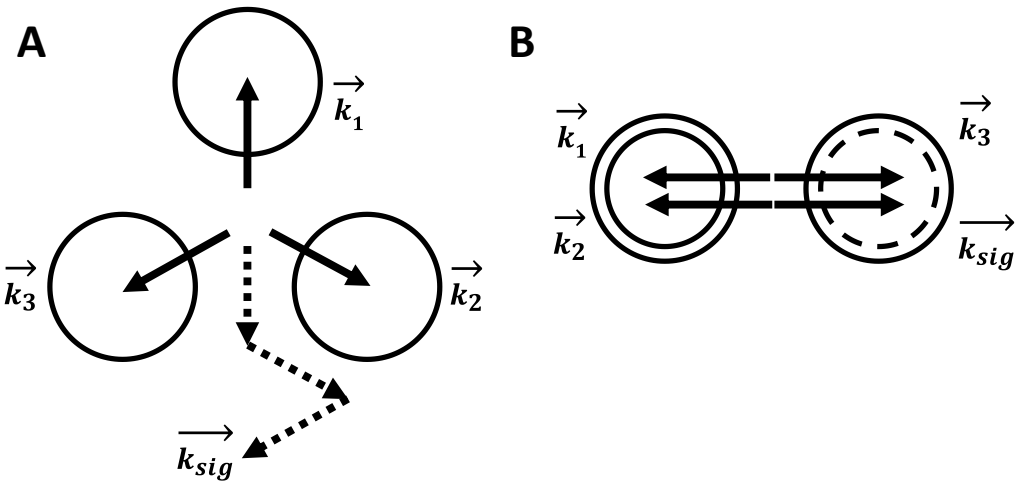

Figure 1.9 D Different sample collection geometries for 2D IR. A) boxCARS geometry B) Pump-probe geometry. Example wavevectors are shown to demonstrate the direction the signal is emitted for the rephasing pathways.

oscillator can be a drawback, but this is discussed further in the next section.

1.2.2.3 Signal-Enhanced 2D IR spectroscopy

A recent advancement in the 2D IR community has been incorporating signal enhancing techniques to 2D IR spectroscopy. This has been done in two ways: effectively reducing the power of the probe to lower the background and using plasmon enhancement to increase the electric fields interacting with the sample.[66–69] Both techniques will briefly be described here.

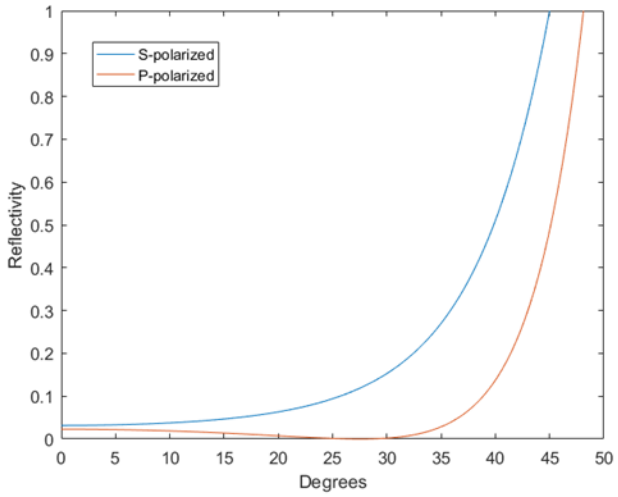

Figure 1.10 Graph depicting the angular dependence of light transmission for S and P polarized light for a CaF_2 – air interface.

First, the manipulation of the probe intensity in a pump-probe geometry was first introduced by Fayer and coworkers.[69] In the boxCARS geometry, the local oscillator is made as small as possible such that the denominator in equation 1.14 is very small as to make the measured signal higher. The pump-probe geometry is limited in the sense that since the probe is also the local oscillator, the local oscillator cannot be made less intense without also affecting the intensity of the signal. The goal of Fayer's work therefore was to take advantage of how different polarizations of light interact with interfaces of materials to decrease the local oscillator in a pump-probe geometry. When light hits an interface, some light is transmitted and some light is reflected.[70] The amount reflected and transmitted is different for S and P polarized light. This phenomenon is described by the Fresnel equations and the resulting angularly-dependent effects

for S and P polarized light are shown in figure 1.10. As indicated, at a certain angle (depending on the refractive indices of the two materials at the interface) no p-polarized light is reflected. This angle is called Brewster's angle. Fayer and coworkers demonstrated that if you collect your signal in a reflective as opposed to transmissive geometry with an angle close to Brewster's angle, that the attenuation of the local oscillator can result in up to 50 times signal enhancement.[69] Furthermore, this also can allow for the measurement of molecules in highly absorptive solvents. Analogous methods utilize polarization to reduce local oscillator intensity.[71]

The second technique that can be employed to enhance 2D IR signal is using plasmonic enhancement. In this case, rather than decreasing the amount of non-signal light hitting the detector, the signal itself is increased. There are several ways to use these plasmonic materials. Briefly, plasmons are the oscillations of electron density in metals relative to the positive metal ions. Typical metals used are silver, gold, platinum, and copper.[72,73] Nano-antennas of various shapes can be used to tune the frequency by choosing lengths of antenna that force the oscillations to be in the IR.[74] Or, a thin rough layer of metal can be deposited creating nano-islands which create localized surface plasmons that have resonant frequencies in the visible range.[75] There are benefits and drawbacks to each strategy. Stronger electric fields are generated by the antennas, but unless you are precisely at the resonant frequency, line shape distortions called Fano line shapes occur, which need to be corrected in order to interpret the spectra.[76] There is less enhancement in the localized surface plasmon case, but because the IR where we are interested is on the tail of the plasmon absorption, there are not noticeable line shape disruptions.

Polarization of the incident light is an important consideration in both of these cases. For the nano-antennas, the signal enhancement is highest when the light is polarized along the long

axis of the antenna.[77] When it is normal to this axis, very little enhancement is observed. In the case of the nano-islands, s-polarized light causes hot spots to form between the antennas while p-polarized light enhances electric fields on top of the islands.

These techniques have been implemented in the past five years by various members of the 2D IR community. Rubstov and coworkers have used various antenna geometries to enhance signal in inorganic molecules.[74,78] Hamm and colleagues have used rough, thin platinum to observed CO catalysis.[79] Some linear IR spectroscopies have used mixtures of nano-antennas tuned to the amide I and ester carbonyl regions to measure membrane-bound proteins as well as the ester carbonyl stretch of the lipid in the same experiment.[80] These applications demonstrate the utility of these techniques for measuring very small amounts of sample. In this dissertation, more applications for signal enhancement are described.

1.2.2.4 2D IR Lineshapes

The frequency of the vibrational transition changes over time due to the solvent molecules pushing and pulling on the molecule of interest. The pushing and pulling changes the potential energy surface and varies the frequency of the transition. The time-dependent variation of the frequency causes inhomogeneous dephasing (sampling many molecules in slightly different environment) and contributes to homogenous dephasing (intrinsic to the molecule of interest) due to the time dependence on pure dephasing (like damping).[8] Characterization of molecular dephasing allows for the study of the dynamics of the molecule and systems of interest.

Fundamentally dephasing can be understood by considering the impact of the solvent on a Morse potential. As the solvent pushes and pulls on the molecule, the potential stretches and compresses, slightly changing the frequency of the vibrational transition. As a function of time,

the instantaneous frequency fluctuates around the average frequency. When this happens to all of the molecules in a sample, over time, the different oscillating terms will begin to cancel each other out at longer times. This is what is considered, 'coming out of phase'. This is mathematically described by an equation called the frequency fluctuation correlation function (FFCF):

$$\langle \delta\omega_{01}(t)\delta\omega_{01}(0)\rangle = \frac{1}{T}\int_0^T \omega_{01}(\tau)\omega_{01}(\tau+t)\,d\tau$$

(1.16)

Where $\delta\omega_{01}$ is the instantaneous, fluctuating frequency, T is the total length of time, and t and τ represent arbitrary time points. This equation illustrates that the molecule's frequency becomes less correlated to its initial frequency as time increases. The FFCF describes the characteristic time scale over which this correlation decay occurs. This is related to both the vibration of interest, but also the solvent environment of the vibration.

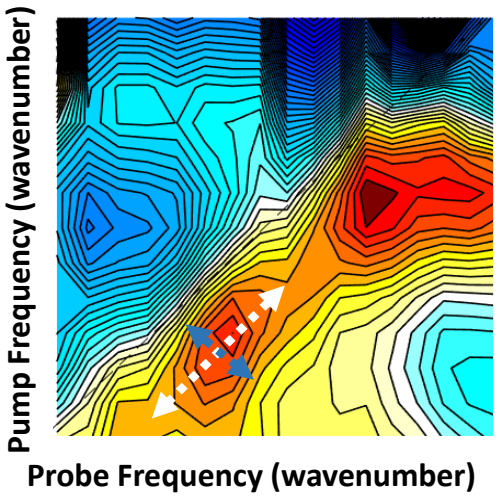

Figure 1.11 Example 2D IR spectrum. Diagonal Linewidth is shown with the white arrow and antidiagonal linewidth is shown with a blue arrow on the lower diagonal peak.

Qualitatively, this is seen in 2D IR spectra by measuring a sample with varying time between the second pump and probe pulses. Spectra often appear to be 'line-narrowed' that is to say that the observed peak is elongated along the diagonal and narrow along the antidiagonal. This occurs when the molecule or system remembers the pump frequency when it is probed. Probing

different delays between the pump and probe pulses allows spectral diffusion to be observed. If there is no change in lineshape as the time between the second pump pulse and the probe pulse increases, then there is no spectral diffusion and the homogenous linewidth is the antidiagonal linewidth and the total linewidth (including the inhomogeneous component) is the diagonal linewidth.[8,81] The linewidths are shown in an example spectrum in figure 1.11.

When spectral diffusion is exhibited, the 2D IR peak will appear to be more round over time. The spectra change as a function of t_2 as the memory of the pump frequency decays. Then the antidiagonal width increases as the correlation between the pump and probe diminishes. The broadening of the antidiagonal can also be conceptualized as a change in probability. At short t_2 times, the probability of finding the molecule at the probe frequency is a conditional probability assuming it was at the pump frequency at time 0. At long t_2 times, the probability shifts to a joint probability.

$$p(\omega_3, t_2|\omega_1, 0) \xrightarrow{t_2\to\infty} p(\omega_3)p(\omega_1) \tag{1.17}$$

Here ω_3 is the probe frequency and ω_1 is the pump frequency in a simple, two-level system. The relation here is a general and intuitive explanation to the lineshape changes.[8]

For the vibrational systems measured here, there are similar trends observed. The spectral diffusion times can be extracted from experimental spectra by finding an appropriate way to measure the change in linewidth as a function of t_2 time. A common method in recent literature is to measure the center line slope, or the slope generated from the probe frequency of the maximum of each pump frequency of the peak.[82,83] 2D IR spectra are taken for many t_2 times. The slopes for each spectrum can then be plotted as a function of t_2 and fit to a

(multi)exponential ansatz of the FFCF. The results of the fit and the number of exponentials needed give insights into the number and time of the vibrational lifetimes being studied. Lineshape analysis of ion channels can be used to study both the ion coordination in the selectivity filter and the dynamics of the voltage sensing domain.

1.2.3 Application of 2D IR spectroscopy to proteins

I am interested in applying the above 2D IR and surface enhancement techniques in order to study membrane-bound proteins and peptides. It is therefore important to describe how 2D IR is used to measure protein systems and what kind of data can be extracted from these experiments. IR spectroscopy has been used for a long time to look at the secondary structure of proteins and nucleic acids.[65,84,85] It is sensitive to different structures because coupling along the protein backbone causes the vibrational amide I modes to become delocalized over space, like along the axis of an α-helix or across a β-sheet. For example, every amino acid in a protein has a local mode that corresponds to its amide I vibration, but in infinitely long, linear chains, only one infrared transition in allowed[8] In finite chains, or chains with disorder other states will gain transition strength as they will no longer cancel, but the main transition will still dominate. 2D IR has typically narrower peaks than linear IR because of the fact that 2D IR intensities scale with $|\vec{\mu}|^4$ rather than $\overrightarrow{|\mu|}^2$ as in linear spectroscopy.[8] Another benefit of using 2D IR rather than linear is that the anharmonicity changes with increased delocalization. The anharmonic shift decreases when there is delocalization, which is resolvable in 2D IR spectra by measuring the distance between the diagonal and overtone peaks.[8,86]

Helices are the principal secondary structure observed here. Since the helices are not simply linear chains, there are more IR active states than in a simple linear chain. In helices there are three states—the *A* mode that goes along the helix (z) axis, and the double degenerate *E* modes

which are along the x- and y-axes.[8] The separation of these modes depends on the number of turns per helix. In α-helices there are 3.6 residues per turn and in 3_{10}-helices there are 3.2 residues per turn. They therefore have different energy splittings for their *A* and *E* modes.[8,11] The center frequency of the helix can change depending on the length of the helix as well as the disorder. These physical characteristics change the measured frequencies, since the center frequency is given by the sum of the coupling strengths, so additional long-range couplings will impact shift of the absorption band. Much work has been done to be able to calculate the impacts of structure and disorder on spectra, and this ability to use calculation to verify data is an asset in interpreting 2D IR spectra of proteins and peptides.[11,87–89]

1.3 Motivation

The main aim of the membrane-bound proteins and peptides project is the eventual voltage-gated transient experiment in which a voltage is applied across a single membrane, and the movements of the voltage-sensitive ion channel is monitored as it opens *in real time*. However, this experimental goal requires many technological and methodological steps for its success. Therefore, the main aims of my PhD have been focused on the study of membrane-bound proteins, surface enhancement, and voltage gated experiments to these ends.

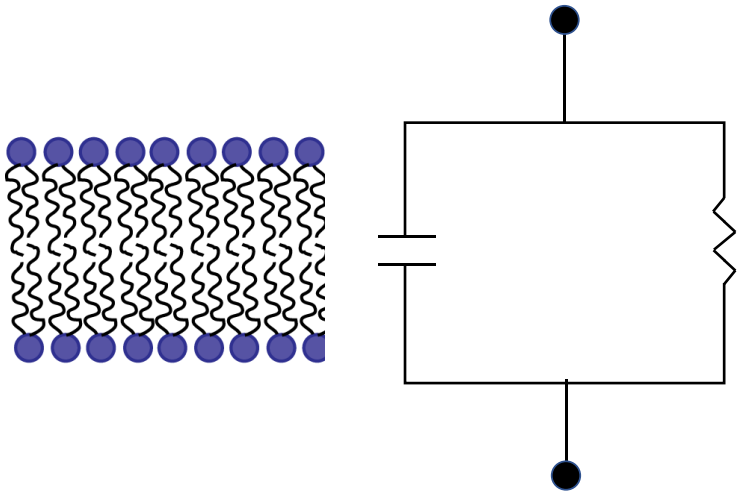

Figure 1.12 Cartoon of a voltage across a bilayer with the equivalent circuit of the bilayer.

1.3.1 Working in a single bilayer

When considering the eventual voltage-gated or voltage-jump experiment, the method of applying the potential is a central concern. Namely, how can an effective potential be applied across our sample such that it is easily reproducible to help with signal averaging and give sufficient signal. One way that has previously been used to trigger the opening of ion channels is using ionophores. In the case of studying a potassium channel with ionophores, vesicles with embedded potassium channels are created with a buffer differential with a higher K^+ ion concentration inside the vesicle, and with a sodium buffer outside of the vesicle. When the experiment begins, a sodium ionophore is introduced, acting like a sodium channel. The Na^+ ions flood into the vesicle, triggering the opening of the potassium channel, similarly to how action potentials are triggered in cells.[90] However, this type of experiment does not work in the contexts desired here. The opening of the channel can only be triggered once, which would correspond to a single spectrum. Typically to maximize signal to noise, about one thousand spectra are averaged together. The amount of sample and time required in this case to obtain a single spectrum eliminates this type of ionophore experiment as a possibility.

Membrane-bound proteins have been studied before in stacked bilayers.[81,91] This allows for sufficient concentration of protein in order to give enough 2D IR signal. One could imagine creating a circuit where the potential is applied over the bilayer as shown in figure 1.12. However, this would not work in the case of stacked bilayers due to the electrochemical nature of the lipid membrane. Stacked bilayers effectively act like stacking this equivalent circuit. The voltages required in order for all of the membrane bound proteins to feel the desired applied potential would require such high voltages that the samples will short circuit. However, a similar approach was used in a voltage-dependent solid-state crystallography experiment where

megavolts were applied across a crystal under vacuum in order to effectively apply an electric field.[92]

These constraints motivated the need to work with a single bilayer of lipid with embedded proteins. Using a single bilayer allows for the relatively straightforward application of a potential across a single membrane. The drawback of this approach is the very small amount of sample in the laser beam focal volume. Since the pathlength is effectively shortened, you only have the amount of sample that fits in the spot-size itself, which is only on the realm of 10^9 molecules when tightly packed on a surface—as opposed to 10^{12} molecules in a typical concentration in solution for a 'bulk' experiment. This led to the interest in using plasmonic enhancement. The enhancement from localized surface plasmons is at least 10^3, effectively making up for the difference between the bulk and surface experiment. Therefore, work in improving these surface techniques was central in the thrust of this work. Surface-specific and surface-sensitive spectroscopies are explained and developed in Chapter 3.

1.3.2 Voltage Dependent Experiments

A further development needed in order to progress in these experiments is to work on applying a voltage across the sample itself. Spectroelectricalchemical sample cells have previously been developed by several groups like the Hamm group and the Bredenbeck groups for several applications using 2D IR spectroscopies.[79,93] The Hamm group looked at catalysis of hydrogen at a platinum interface using an ATR geometry so they were able to use a large volume of solvent for the electrochemical cell since the collected light was reflected through the ATR window and then collected on the same side as the incident light.[79] The Pederson group applied a potential to their samples in order to measure the spectroscopic response to redox reactions.

These experiments were conducted in a transmission geometry.[93] These spectrochemical cells in particular were used as the basis of the designs used in this dissertation.

A benefit of using the plasmonic enhancement is the fact that a macroscopically conducting plasmonic gold layer can be used as the working electrode. The Hamm group showed that ideal conductance of a plasmonic layer is about 20 kΩ per centimeter.[89] Applying a voltage can cause a slight change in the plasmonic character of the material, potentially causing stronger enhancements. This can slightly complicate the interpretation of the spectra with direct comparisons of a no voltage applied spectrum and a voltage applied spectrum. Weighting these spectra can be used to slightly diminish this complication.

The impacts of an applied voltage have scientific importance in the realm of studying the structure and function of ion channels as well as other membrane-bound peptides. Since there is a small, negative resting potential on membranes, the 'native' structure of ion channels is one that is under an applied voltage. This applied voltage is often applied in MD simulations of ion channels.[42] Previous work in the Zanni group did not apply this voltage and this difference could explain discrepancies between our data and the MD simulations. Furthermore, applying voltages on some voltage-sensitive membrane-bound peptides can influence the insertion angle of the peptide. This work is further discussed in the methods section as well as chapter 3 of this dissertation.

1.3.3 Labelling schemes in large proteins

The bulk vibrations of the protein backbone in a large protein does not, inherently, give residue specific structural information. In a smaller peptide, general structure, like helical, β-sheet, and even amyloid fibril formation can be observed.[94] However, in large proteins, the bulk signal shows a large peal across the amide I region. For this reason, different labelling schemes

are often applied in order to gain a deeper understanding of what is happening in a single residue.[95] Isotope labels (^{13}C, ^{18}O, and both ^{13}C and ^{18}O together) are often used. Intuitively, one can explain the function of these labels classically. By increasing the reduced mass of the oscillator, it will vibrate more slowly. This can be seen spectrally as the combination ^{13}C and ^{18}O label red-shifts the peak of the labeled residue by 60 cm^{-1}. The frequency of the labeled residue follows the same trends as the normal amide I peak. These labels effectively uncouple the residue from the bulk. In previous work in the Zanni group, a triple label was used in the selectivity filter in order for the labeled carbonyls to couple together to increase signal.[13] However, due to the triple label, specific information about individual selectivity filter sites was lost.

Another useful label can be an ester carbonyl. Ester carbonyls are not found natively in peptides and vibrate in the 'clear window' in the 1700s. Gai and colleagues have investigated the use of this label when attached to an amino acid side chain.[96,97] It has a slightly smaller extinction coefficient compared to an amide I. They also looked into hydrogen bonding trends and found that more hydrogen bonds interacting with the carbonyl lead to a shift to lower energies compared to no hydrogen bonds interacting with the carbonyl. This follows the increased effective reduced mass argument, shifting the spectra as one of the atoms 'feels' heavier while retaining the same bond character since it is still an ester vibration. This argument does not hold across different functional groups due to different bond strengths (corresponding to the 'spring constant' in the classical model) across different vibrations.

There are also scientific implications to substituting the amide carbonyl with the ester carbonyl. Crystal structures and electrophysiological experiments have studied an ester carbonyl substitution in the amino acids in the selectivity filter of KcsA and NaK2K.[98] They have been

shown to cause much slower ion transduction rate and a different ion occupancy, largely due to the collapse of a pocket that holds a water molecule behind the selectivity filter. It is of interest to further explore the spectroscopic use of a backbone ester carbonyl label. Preliminary results for these experiments are discussed in chapter 4.

1.4 Summary

In this chapter I presented the background of the structure and dynamics of ion channels, as well as summarized the state of the field as we approached the projects discussed in later chapters. Furthermore, I motivated our use of 2D IR spectroscopy to study these channels by briefly describing the theory of multidimensional spectroscopy and explaining the utility of the data generated by these experiments to the questions we are interested in probing about the movement and ion transduction of potassium channels. Chapter 2 further details experimental methods—both in terms of 2D IR spectroscopy and also strategies for sample preparation for membrane-bound proteins and peptides. In chapter 3, the development of voltage-dependent, surface enhanced spectroscopy of a small membrane-bound peptide is discussed as well as insights gleaned about a voltage-sensitive peptides structure and orientation. Chapter 4 expands the sample from a small peptide to a full ion channel and preliminary results are discussed. Finally in Chapter 5, I include my contributions to thinking about surface-sensitive and surface-specific spectroscopic methods using polarization control and surface-enhanced spectroscopies. In sum, this dissertation combines method development to better study membrane-bound proteins and peptides as well as increasing understanding of the function of these macromolecules.

1.5 References

(1) Hodgkin, A. L.; Huxley, A. F.; Katz, B. Measurement of Current-voltage Relations in the

Membrane of the Giant Axon of Loligo. *J. Physiol.* **1952**, *116* (4), 424–448.

(2) Hille, B. Ionic Channels of Excitable Membranes 2nd Edition. *Journal of The Electrochemical Society*. 1987, p 343.

(3) Catterall, W. A.; Catterall, W. Voltage-Gated Sodium Channels at 60: Structure, Function and Pathophysiology. *J. Physiol.* **2012**, *590*, 2577–2589.

(4) Seyfarth, E.-A. Julius Bernstein (1839–1917): Pioneer Neurobiologist and Biophysicist. *Biol. Cybern.* **2006**, *94* (1), 2–8.

(5) Carmeliet, E. From Bernstein's Rheotome to Neher-Sakmann's Patch Electrode. The Action Potential. *Physiol. Rep.* **2019**, *7* (1), e13861.

(6) Zhou, Y.; Morais-Cabral, J. H.; Kaufman, A.; Mackinnon, R. Chemistry of Ion Coordination and Hydration Revealed by a K+channel-Fab Complex at 2.0 Å Resolution. *Nature* **2001**, *414* (6859), 43–48.

(7) Declan A. Doyle, João Morais Cabral, Richard A. Pfuetzner, Anling Kuo, Jacqueline M. Gulbis, Steven L. Cohen, Brian T. Chait, R. M. The Structure of the Potassium Channel: Molecular Basis of K+ Conduction and Selectivity. *Science (80-.).* **1998**, *280* (5360), 69–77.

(8) Hamm, P.; Zanni, M. *Concepts and Methods of 2D Infrared Spectroscopy*; 2011; Vol. 9781107000.

(9) Lomont, J. P.; Ostrander, J. S.; Ho, J. J.; Petti, M. K.; Zanni, M. T. Not All β-Sheets Are the Same: Amyloid Infrared Spectra, Transition Dipole Strengths, and Couplings Investigated by 2D IR Spectroscopy. *J. Phys. Chem. B* **2017**, *121* (38), 8935–8945.

(10) Marsh, D.; Müller, M.; Schmitt, F. J. Orientation of the Infrared Transition Moments for an Alpha-Helix. *Biophys. J.* **2000**, *78* (5), 2499–2510.

(11) La Cour Jansen, T.; Dijkstra, A. G.; Watson, T. M.; Hirst, J. D.; Knoester, J. Modeling the Amide I Bands of Small Peptides. *J. Chem. Phys.* **2006**, *125* (4).

(12) Ganim, Z.; Tokmakoff, A.; Vaziri, A. Vibrational Excitons in Ionophores: Experimental Probes for Quantum Coherence-Assisted Ion Transport and Selectivity in Ion Channels. *New J. Phys.* **2011**, *13*.

(13) Kratochvil, H. T.; Carr, J. K.; Matulef, K.; Annen, A. W.; Li, H.; Maj, M.; Ostmeyer, J.; Serrano, A. L.; Raghuraman, H.; Moran, S. D.; et al. Instantaneous Ion Configurations in the K+ Ion Channel Selectivity Filter Revealed by 2D IR Spectroscopy. *Science* **2016**, *353* (6303), 1040–1044.

(14) Moran, S. D.; Zanni, M. T. How to Get Insight into Amyloid Structure and Formation

from Infrared Spectroscopy. *J. Phys. Chem. Lett.* **2014**, *5* (11), 1984–1993.

(15) Garten, M.; Mosgaard, L. D.; Bornschlögl, T.; Dieudonné, S.; Bassereau, P.; Toombes, G. E. S. Whole-GUV Patch-Clamping. **2016**, *114* (2).

(16) Aimon, S.; Manzi, J.; Schmidt, D.; Larrosa, P.; Bassereau, J. A. Functional Reconstitution of a Voltage-Gated Potassium Channel in Giant Unilamellar Vesicles. *PLoS One* **2011**, *6* (10), 25529.

(17) Tombola, F.; Pathak, M. M.; Isacoff, E. Y. How Does Voltage Open an Ion Channel? *Annu. Rev. Cell Dev. Biol.* **2006**, *22* (1), 23–52.

(18) Jiang, D.; Gamal El-Din, T. M.; Ing, C.; Lu, P.; Pomès, R.; Zheng, N.; Catterall, W. A. Structural Basis for Gating Pore Current in Periodic Paralysis. *Nature* **2018**, *557* (7706), 590–594.

(19) Hodgkin, A. L.; Keynes, R. D. The Potassium Permeability of a Giant Nerve Fibre. *J. Physiol.* **1955**, *128* (1), 61–88.

(20) Abdelsayed, M.; Sokolov, S. Voltage-Gated Sodium Channels: Pharmaceutical Targets via Anticonvulsants to Treat Epileptic Syndromes. *Channels (Austin).* **2013**, *7* (3), 146–152.

(21) Loussouarn, G.; BarÃ^3, I.; Escande, D. KCNQ1 K+ Channel Mediated Cardiac Channelopathies. In *Ion Channels*; Humana Press: Totowa, NJ, 2006; pp 167–183.

(22) Villa, C.; Combi, R. Potassium Channels and Human Epileptic Phenotypes: An Updated Overview. *Front. Cell. Neurosci.* **2016**, *10*.

(23) Berneche, S.; Roux, B. A Microscopic View of Ion Conduction through the K+ Channel. *Proc. Natl. Acad. Sci.* **2003**, *100* (15), 8644–8648.

(24) LeMasurier, M.; Heginbotham, L.; Miller, C. KcsA: It's a Potassium Channel. *J. Gen. Physiol.* **2001**, *118* (3), 303–314.

(25) Morais-Cabral, J. H.; Zhou, Y.; MacKinnon, R. Energetic Optimization of Ion Conduction Rate by the K+ Selectivity Filter. *Nature* **2001**, *414* (6859), 37–42.

(26) Tilegenova, C.; Marien Cortes, D.; Jahovic, N.; Hardy, E.; Hariharan, P.; Guan, L.; Cuello, L. G. Structure, Function, and Ion-Binding Properties of a K+ Channel Stabilized in the 2,4-Ion–Bound Configuration. *Proc. Natl. Acad. Sci. U. S. A.* **2019**, *116* (34), 16829–16834.

(27) Xu, Y.; McDermott, A. E. Inactivation in the Potassium Channel KcsA. *J. Struct. Biol. X* **2019**, *3*.

(28) Kratochvil, H. T.; Maj, M.; Matulef, K.; Annen, A. W.; Ostmeyer, J.; Perozo, E.; Roux,

B.; Valiyaveetil, F. I.; Zanni, M. T. Probing the Effects of Gating on the Ion Occupancy of the K+ Channel Selectivity Filter Using Two-Dimensional Infrared Spectroscopy. *J. Am. Chem. Soc.* **2017**, *139* (26), 8837–8845.

(29) Sands, Z. A.; Sansom, M. S. P. How Does a Voltage Sensor Interact with a Lipid Bilayer? Simulations of a Potassium Channel Domain. *Structure* **2007**, *15* (2), 235–244.

(30) Lee, S.-Y.; Lee, A.; Chen, J.; MacKinnon, R. Structure of the KvAP Voltage-Dependent K+ Channel and Its Dependence on the Lipid Membrane. *Proc. Natl. Acad. Sci.* **2005**, *102* (43), 15441–15446.

(31) Bruhova, I.; Zhorov, B. S. KvAP-Based Model of the Pore Region of Shaker Potassium Channel Is Consistent with Cadmium- and Ligand-Binding Experiments. *Biophys. J.* **2005**, *89* (2), 1020–1029.

(32) Uysal, S.; Vásquez, V.; Tereshko, V.; Esaki, K.; Fellouse, F. A.; Sidhu, S. S.; Koide, S.; Perozo, E.; Kossiakoff, A. Crystal Structure of Full-Length KcsA in Its Closed Conformation. *Proc. Natl. Acad. Sci.* **2009**, *106*, 6644–6649.

(33) Jekhmane, S.; Medeiros-Silva, J.; Li, J.; Kümmerer, F.; Müller-Hermes, C.; Baldus, M.; Roux, B.; Weingarth, M. Shifts in the Selectivity Filter Dynamics Cause Modal Gating in K + Channels.

(34) Noskov, S. Y.; Bernéche, S.; Roux, B. Control of Ion Selectivity in Potassium Channels by Electrostatic and Dynamic Properties of Carbonyl Ligands. *Nature* **2004**, *431* (7010), 830–834.

(35) Xu, Y.; Zhang, D.; Rogawski, R.; Nimigean, C. M.; McDermott, A. E. Identifying Coupled Clusters of Allostery Participants through Chemical Shift Perturbations. *Proc. Natl. Acad. Sci. U. S. A.* **2019**, *116* (6), 2078–2085.

(36) Qasim, A.; Sher, I.; Hirschhorn, O.; Shaked, H.; Qasem, Z.; Ruthstein, S.; Chill, J. H. Investigation of a KcsA Cytoplasmic PH Gate in Lipoprotein Nanodiscs. *ChemBioChem* **2019**, *20* (6), 813–821.

(37) Poveda, J. A.; Giudici, A. M.; Renart, M. L.; Millet, O.; Morales, A.; González-Ros, J. M.; Oakes, V.; Furini, S.; Domene, C. Modulation of the Potassium Channel KcsA by Anionic Phospholipids: Role of Arginines at the Non-Annular Lipid Binding Sites. *Biochim. Biophys. Acta - Biomembr.* **2019**, *1861* (10).

(38) Zhou, Y.; MacKinnon, R. The Occupancy of Ions in the K+selectivity Filter: Charge Balance and Coupling of Ion Binding to a Protein Conformational Change Underlie High Conduction Rates. *J. Mol. Biol.* **2003**, *333* (5), 965–975.

(39) Thompson, A. N.; Kim, I.; Panosian, T. D.; Iverson, T. M.; Allen, T. W.; Nimigean, C. M.

Mechanism of Potassium-Channel Selectivity Revealed by Na+ and Li + Binding Sites within the KcsA Pore. *Nat. Struct. Mol. Biol.* **2009**, *16* (12), 1317–1324.

(40) Bernèche, S.; Roux, B. Energetics of Ion Conduction through the K+channel. *Nature* **2001**, *414* (6859), 73–77.

(41) Kopec, W.; Köpfer, D. A.; Vickery, O. N.; Bondarenko, A. S.; Jansen, T. L. C.; de Groot, B. L.; Zachariae, U. Direct Knock-on of Desolvated Ions Governs Strict Ion Selectivity in K+ Channels. *Nat. Chem.* **2018**, *10* (8), 813–820.

(42) Kopfer, D. A.; Song, C.; Gruene, T.; Sheldrick, G. M.; Zachariae, U.; de Groot, B. L.; Quigley, A.; Grieben, M.; Goubin, S.; Mukhopadhyay, S.; et al. Ion Permeation in K+ Channels Occurs by Direct Coulomb Knock-On. *Science (80-.).* **2014**, *346* (6207), 352–355.

(43) Komarov, A. G.; Linn, K. M.; Devereaux, J. J.; Valiyaveetil, F. I. Modular Strategy for the Semisynthesis of a K+ Channel: Investigating Interactions of the Pore Helix. *ACS Chem. Biol.* **2009**, *4* (12), 1029–1038.

(44) Infield, D. T.; Matulef, K.; Galpin, J. D.; Lam, K.; Tajkhorshid, E.; Ahern, C. A.; Valiyaveetil, F. I. Main-Chain Mutagenesis Reveals Intrahelical Coupling in an Ion Channel Voltage-Sensor. *Nat. Commun.* **2018**, *9* (1), 5055.

(45) Matulef, K.; Komarov, A. G.; Costantino, C. A.; Valiyaveetil, F. I. Using Protein Backbone Mutagenesis to Dissect the Link between Ion Occupancy and C-Type Inactivation in K + Channels. *Proc. Natl. Acad. Sci.* **2013**, *110* (44), 17886–17891.

(46) Sauer, D. B.; Zeng, W.; Raghunathan, S.; Jiang, Y. Protein Interactions Central to Stabilizing the K + Channel Selectivity Filter in a Four-Sited Configuration for Selective K + Permeation. *Proc. Natl. Acad. Sci.* **2011**, *108* (40), 16634–16639.

(47) Lam, Y. L.; Zeng, W.; Sauer, D. B.; Jiang, Y. The Conserved Potassium Channel Filter Can Have Distinct Ion Binding Profiles: Structural Analysis of Rubidium, Cesium, and Barium Binding in NaK2K. *J. Gen. Physiol.* **2014**, *144* (2), 181–192.

(48) Jiang, Y.; Lee, A.; Chen, J.; Ruta, V.; Cadene, M.; Chait, B. T.; MacKinnon, R. X-Ray Structure of a Voltage-Dependent K+ Channel. *Nature* **2003**, *423* (6935), 33–41.

(49) Broomand, A.; Männikkö, R.; Larsson, H. P.; Elinder, F. Molecular Movement of the Voltage Sensor in a K Channel. *J. Gen. Physiol.* **2003**, *122* (6), 741–748.

(50) Ruta, V.; Chen, J.; MacKinnon, R. Calibrated Measurement of Gating-Charge Arginine Displacement in the KvAP Voltage-Dependent K+ Channel. *Cell* **2005**, *123* (3), 463–475.

(51) Butterwick, J. A.; MacKinnon, R. Solution Structure and Phospholipid Interactions of the Isolated Voltage-Sensor Domain from KvAP. *J. Mol. Biol.* **2010**, *403* (4), 591–606.

(52) Mishima, E.; Sato, Y.; Nanatani, K.; Hoshi, N.; Lee, J.-K.; Schiller, N.; von Heijne, G.; Sakaguchi, M.; Uozumi, N. The Topogenic Function of S4 Promotes Membrane Insertion of the Voltage-Sensor Domain in the KvAP Channel. *Biochem. J.* **2016**, No. 2016, 4361–4372.

(53) Andersson, M.; Freites, J. A.; Tobias, D. J.; White, S. H. Structural Dynamics of the S4 Voltage-Sensor Helix in Lipid Bilayers Lacking Phosphate Groups. *J. Phys. Chem. B* **2011**, *115* (27), 8732–8738.

(54) Sands, Z. A.; Grottesi, A.; Sansom, M. S. P. The Intrinsic Flexibility of the Kv Voltage Sensor and Its Implications for Channel Gating. *Biophys. J.* **2006**, *90* (5), 1598–1606.

(55) Hessa, T.; White, S. H.; Von Heijne, G. Membrane Insertion of a Potassium-Channel Voltage Sensor. *Science (80-.).* **2005**, *307* (5714), 1427.

(56) Yao, H.; Bell, D. C.; Saenger, R. C.; Riley, J. H.; Siegelbaum, S. A. Changes in Local S4 Environment Provide a Voltage-Sensing Mechanism for Mammalian Hyperpolarization–Activated HCN Channels. *J. Gen. Physiol.* **2003**, *123* (1), 5–20.

(57) Andersson, M.; Freites, A. J.; White, S. H.; Tobias, D. J. Structural Dynamics of the S4 Voltage Sensor Helix in Bilayers Lacking Lipid Phosphates. *Biophys. J.* **2011**, *100* (3), 282a.

(58) Nishizawa, M.; Nishizawa, K. Molecular Dynamics Simulation of Kv Channel Voltage Sensor Helix in a Lipid Membrane with Applied Electric Field. *Biophys. J.* **2008**, *95* (4), 1729–1744.

(59) Kubota, T.; Lacroix, J. J.; Bezanilla, F.; Correa, A. M. Probing α -3 10 Transitions in a Voltage-Sensing S4 Helix. *Biophys. J.* **2014**, *107* (5), 1117–1128.

(60) Mukamel, S. *Principles of Nonlinear Optical Spectroscopy, Oxford University Press, New York*; 1995.

(61) Mukherjee, P.; Kass, I.; Arkin, I.; Zanni, M. T. Picosecond Dynamics of a Membrane Protein Revealed by 2D IR. *PNAS March* **2006**, *7* (10), 3528–3533.

(62) DeFlores, L. P.; Nicodemus, R. A.; Tokmakoff, A. Two-Dimensional Fourier Transform Spectroscopy in the Pump-Probe Geometry. *Opt. Lett.* **2007**, *32* (20), 2966.

(63) Rosenfeld, D. E.; Gengeliczki, Z.; Smith, B. J.; Stack, T. D. P.; Fayer, M. D. Structural Dynamics of a Catalytic Monolayer Probed by Ultrafast 2D IR Vibrational Echoes. *Science (80-.).* **2011**, *334* (6056), 634–639.

(64) Shim, S.-H.; Zanni, M. T. How to Turn Your Pump–Probe Instrument into a Multidimensional Spectrometer: 2D IR and Vis Spectroscopiesvia Pulse Shaping. *Phys. Chem. Chem. Phys.* **2009**, *11* (5), 748–761.

(65) Middleton, C. T.; Woys, A. M.; Mukherjee, S. S.; Zanni, M. T. Residue-Specific Structural Kinetics of Proteins through the Union of Isotope Labeling, Mid-IR Pulse Shaping, and Coherent 2D IR Spectroscopy. *Methods* **2010**, *52* (1), 12–22.

(66) Selig, O.; Siffels, R.; Rezus, Y. L. A. Ultrasensitive Ultrafast Vibrational Spectroscopy Employing the Near Field of Gold Nanoantennas. *Phys. Rev. Lett.* **2015**, *114* (23).

(67) Kraack, J. P.; Hamm, P. Vibrational Ladder-Climbing in Surface-Enhanced, Ultrafast Infrared Spectroscopy. *Phys. Chem. Chem. Phys.* **2016**, *18* (24), 16088–16093.

(68) Kraack, J. P.; Lotti, D.; Hamm, P. 2D Attenuated Total Reflectance Infrared Spectroscopy Reveals Ultrafast Vibrational Dynamics of Organic Monolayers at Metal-Liquid Interfaces. *J. Chem. Phys.* **2015**, *142* (21), 212413.

(69) Nishida, J.; Yan, C.; Fayer, M. D. Enhanced Nonlinear Spectroscopy for Monolayers and Thin Films in Near-Brewster's Angle Reflection Pump-Probe Geometry. *J. Chem. Phys.* **2017**, *146* (9).

(70) Osawa, M.; Kuramitsu, M.; Hatta, A.; Suëtaka, W.; Seki, H. Electromagnetic Effect in Enhanced Infrared Absorption of Adsorbed Molecules on Thin Metal Films. *Surface Science*. 1986.

(71) Xiong, W.; Zanni, M. T. Signal Enhancement and Background Cancellation in Collinear Two-Dimensional Spectroscopies. *Opt. Lett.* **2008**, *33* (12), 1371.

(72) Sarid, D.; Challener, W. Localized Surface Plasmons. In *Modern Introduction to Surface Plasmons*; 2013; pp 201–255.

(73) Quidant, R.; Enoch, S.; Kreuzer, M.; Badenes, G. Optical Sensing Based on Localized Surface Plasmons. In *Photonic Materials, Devices, and Applications*; 2005; Vol. 5840, p 272.

(74) Chuntonov, L.; Rubtsov, I. V. Surface-Enhanced Ultrafast Two-Dimensional Vibrational Spectroscopy with Engineered Plasmonic Nano-Antennas. *J. Chem. Phys.* **2020**, *153* (5), 050902.

(75) Kuklin, R. N.; Emets, V. V. Localized Plasmons on a Metal Surface. *Prot. Met. Phys. Chem. Surfaces* **2016**, *52* (1), 11–15.

(76) Tek, G.; Hamm, P. A Correction Scheme for Fano Line Shapes in Two-Dimensional Infrared Spectroscopy. *J. Phys. Chem. Lett.* **2020**, *11* (15), 6185–6190.

(77) Kraack, J. P.; Hamm, P. Surface-Sensitive and Surface-Specific Ultrafast Two-Dimensional Vibrational Spectroscopy. *Chem. Rev.* **2017**, *117* (16), 10623–10664.

(78) Mackin, R. T.; Cohn, B.; Gandman, A.; Leger, J. D.; Chuntonov, L.; Rubtsov, I. V.

Surface-Enhanced Dual-Frequency Two-Dimensional Vibrational Spectroscopy of Thin Layers at an Interface. *J. Phys. Chem. C* **2018**, *122* (20), 11015–11023.

(79) Lotti, D.; Hamm, P.; Kraack, J. P. Surface-Sensitive Spectro-Electrochemistry Using Ultrafast 2D ATR IR Spectroscopy. *J. Phys. Chem. C* **2016**, *120* (5), 2883–2892.

(80) Rodrigo, D.; Tittl, A.; Ait-Bouziad, N.; John-Herpin, A.; Limaj, O.; Kelly, C.; Yoo, D.; Wittenberg, N. J.; Oh, S.-H.; Lashuel, H. A.; et al. Resolving Molecule-Specific Information in Dynamic Lipid Membrane Processes with Multi-Resonant Infrared Metasurfaces. *Nat. Commun.* **2018**, *9* (1), 2160.

(81) Woys, A. M.; Lin, Y. S.; Reddy, A. S.; Xiong, W.; De Pablo, J. J.; Skinner, J. L.; Zanni, M. T. 2D IR Line Shapes Probe Ovispirin Peptide Conformation and Depth in Lipid Bilayers. *J. Am. Chem. Soc.* **2010**, *132* (8), 2832–2838.

(82) Yan, C.; Yuan, R.; Nishida, J.; Fayer, M. D. Structural Influences on the Fast Dynamics of Alkylsiloxane Monolayers on SiO2 Surfaces Measured with 2D IR Spectroscopy. *J. Phys. Chem. C* **2015**, *119* (29), 16811–16823.

(83) Fenn, E. E.; Fayer, M. D. Extracting 2D IR Frequency-Frequency Correlation Functions from Two Component Systems. *J. Chem. Phys.* **2011**, *135* (7), 074502.

(84) Wang, L.; Middleton, C. T.; Singh, S.; Reddy, A. S.; Woys, A. M.; Strasfeld, D. B.; Marek, P.; Raleigh, D. P.; De Pablo, J. J.; Zanni, M. T.; et al. 2DIR Spectroscopy of Human Amylin Fibrils Reflects Stable β-Sheet Structure. *J. Am. Chem. Soc.* **2011**, *133* (40), 16062–16071.

(85) Ghosh, A.; Ostrander, J. S.; Zanni, M. T. Watching Proteins Wiggle: Mapping Structures with Two-Dimensional Infrared Spectroscopy. *Chem. Rev.* **2017**, *117* (16), 10726–10759.

(86) Schneider, S. H.; Kratochvil, H. T.; Zanni, M. T.; Boxer, S. G. Solvent-Independent Anharmonicity for Carbonyl Oscillators. *J. Phys. Chem. B* **2017**, *121* (10), 2331–2338.

(87) Edington, S. C.; Flanagan, J. C.; Baiz, C. R. An Empirical IR Frequency Map for Ester C═O Stretching Vibrations. *J. Phys. Chem. A* **2016**, *120* (22), 3888–3896.

(88) Wang, L.; Middleton, C. T.; Zanni, M. T.; Skinner, J. L. Development and Validation of Transferable Amide I Vibrational Frequency Maps for Peptides. *J. Phys. Chem. B* **2011**, *115* (13), 3713–3724.

(89) Ho, J.-J.; Zanni, M. T. COSMOSS https://zanni.chem.wisc.edu/software/.

(90) te Winkel, J. D.; Gray, D. A.; Seistrup, K. H.; Hamoen, L. W.; Strahl, H. Analysis of Antimicrobial-Triggered Membrane Depolarization Using Voltage Sensitive Dyes. *Front. Cell Dev. Biol.* **2016**, *4*.

(91) Yano, Y.; Kondo, K.; Watanabe, Y.; Zhang, T. O.; Ho, J. J.; Oishi, S.; Fujii, N.; Zanni, M. T.; Matsuzaki, K. GXXXG-Mediated Parallel and Antiparallel Dimerization of Transmembrane Helices and Its Inhibition by Cholesterol: Single-Pair FRET and 2D IR Studies. *Angew. Chemie - Int. Ed.* **2017**, *56* (7), 1756–1759.

(92) Hekstra, D. R.; White, K. I.; Socolich, M. A.; Henning, R. W.; Šrajer, V.; Ranganathan, R. Electric-Field-Stimulated Protein Mechanics. *Nature* **2016**, *540* (7633), 400–405.

(93) El Khoury, Y.; Van Wilderen, L. J. G. W.; Vogt, T.; Winter, E.; Bredenbeck, J. A Spectroelectrochemical Cell for Ultrafast Two-Dimensional Infrared Spectroscopy. *Rev. Sci. Instrum.* **2015**, *86* (8), 083102.

(94) Buchanan, L. E.; Dunkelberger, E. B.; Tran, H. Q.; Cheng, P.-N. N.; Chiu, C.-C. C.; Cao, P.; Raleigh, D. P.; de Pablo, J. J.; Nowick, J. S.; Zanni, M. T. Mechanism of IAPP Amyloid Fibril Formation Involves an Intermediate with a Transient -Sheet. *Proc. Natl. Acad. Sci.* **2013**, *110* (48), 19285–19290.

(95) Torres, J.; Kukol, A.; Goodman, J. M.; Arkin, I. T. Site-Specific Examination of Secondary Structure and Orientation Determination in Membrane Proteins: The Peptidic 13C=18O Group as a Novel Infrared Probe. *Biopolymers* **2001**, *59* (6), 396–401.

(96) Pazos, I. M.; Ghosh, A.; Tucker, M. J.; Gai, F. Ester Carbonyl Vibration as a Sensitive Probe of Protein Local Electric Field. *Angew. Chemie Int. Ed.* **2014**, *53* (24), 6080–6084.

(97) Ahmed, I. A.; Gai, F. Simple Method to Introduce an Ester Infrared Probe into Proteins. *Protein Sci.* **2017**, *26* (2), 375–381.

(98) Valiyaveetil, F. I.; Sekedat, M.; MacKinnon, R.; Muir, T. W. Structural and Functional Consequences of an Amide-to-Ester Substitution in the Selectivity Filter of a Potassium Channel. *J. Am. Chem. Soc.* **2006**, *128* (35), 11591–11599.

2 Experimental Methods

This chapter outlines the main technical aspects of both the 2D IR collection set up as well as sample preparation methods. First the technical aspects of 2D IR spectroscopy in the form performed to collect the data in this thesis is described, including the light source and Mid-IR generation, the phase matching geometry and phase control, and the multidimensional spectrometer. A variety of plasmonic techniques as well as conductive substrates tried are then discussed. Finally different methods of sample preparation are described and discussed.

2.1 Light Source and Mid-IR generation

2.1.1 The Titanium Sapphire Regenerative Amplifier as Laser Source

The foundation of the work in this dissertation is the use of ultrafast lasers, which are have femtosecond (or faster) pulse lengths and high peak power. Mode-locking and chirped pulse amplification are used to generate ultrafast laser pulses.

Mode-locking is vital in making ultra-fast pulses. This happens due to the nonlinear optical Kerr effect where the refractive index of a medium is dependent on the intensity of the incident light. The laser beam is most intense at its center, so the medium changes refractive index more at the center of the beam profile than the edges. This change in refractive index of the material causes said material to act like a lens. For this reason, the effect is sometimes called ‘Kerr Lensing’. The laser system used for these experiments relies on a ‘self-mode-locking’ titanium sapphire (Ti:Sapph) laser where the Ti:Sapph material in the laser cavity is pumped by a continuous laser and the Kerr effect generated by the continuous laser beam on the Ti:Sapph creates a lens that self-focuses the light. In the cavity, the light performs many round-trips

through the Ti:Sapph crystal. Destructive interference from the cavity due to the Kerr lens causes phase-locked, short pulses to be generated.

High peak power in these ultrafast laser pulses is created by using chirped pulse amplification in a regenerative amplifier. This technology is so vital in the field that the regenerative amplifier won the Nobel Prize in 2018. Briefly, an ultrafast pulse is first 'stretched' by two gratings and two lenses in what is called a grating stretcher. This will elongate the pulse in time to about 100 ps and also disperse the frequencies such that the redder light leads and the bluer light is behind. Next, the stretched pulse is routed into the laser cavity which is pumped by the doubled output of a Neodunium:YLF laser. The cavity also contains Pockel cells which change polarization to allow the pulse in and out of the cavity. The power is amplified as the stretched pulse makes round trips through the cavity due to constructive interference with the pump light. In the laser system used for this work (Libra, Coherent), the power increases from about 3 nJ to 4 mJ. After being dumped out of the cavity, the light is then 'compressed' in the reverse of how it was stretched and the output pulse is 50 fs. The laser system described here has a repetition rate of 1 kHz with a center wavelength of 800 nm. The general power reading for the Libra is 3.2-3.4 W when pumping the cavity with the evolution set to 21 A.

2.1.2 Mid-IR generation

As discussed in the introduction, we are chiefly interested in the amide I and ester carbonyl regions of the infrared (~6000 nm), but the light from the regenerative amplifier is centered at 800 nm. Two non-linear processes are then used to generate the light necessary for these experiments: optical parametric amplification (OPA) and difference frequency generation (DFG).

2.1.2.1 Optical Parametric Amplification

The first step in this process is optical parametric amplification. This takes advantage of nonlinear qualities in some optical crystals which lack inversion symmetry, which can generate different wavelengths. In brief, two pulses, a strong pump pulse and a weak seed pulse (which have shorter and longer wavelengths, respectively) are overlapped temporally and spatially in the nonlinear crystal. The frequency of the pump is ω_{pump} and the frequency of the seed is ω_{signal}. When they are appropriately phase-matched, most pump photons are converted to what is called the idler field with frequency ω_{idler} where $\omega_{pump} = \omega_{idler} + \omega_{signal}$. Some pump photons are converted to the signal field, which increases the intensity of the signal.

The work presented here uses a commercial OPA platform (TOPAS, Light Conversion) installed after the regenerative amplifier. In this particular case, the first step in the process involves creating the signal and idler fields. The 800 nm light from the regenerative amplifier is directed into the Topas and split. Part (~3%) is focused into a sapphire crystal forming the seed: a white light continuum. Some (~10%) stays at 800 nm and is the pump. The signal and idler are then generated by overlapping the pump and seed in a β barium borate crystal, creating the signal (1400 nm) and idler (1800 nm) fields. A cube polarizer is used to separate the fields before the second step. In the second step of near IR generation in the OPA, the power of the signal is amplified by mixing the remaining pump not used above with the signal. The amplified signal and the idler are then collinearized and the pump is filtered. In the TOPAS, the wavelength can be set by computer. The desired signal is input, and the angle of the nonlinear crystal changes accordingly. Power can be optimized by adjusting the timing through a set of Brewster mirrors.

2.1.2.2 Difference Frequency Generation

After the signal and idler are generated, the next step is difference frequency generation (DFG). Again, this process takes advantage of nonlinear qualities of optical crystals. It is very similar to OPA, but the signal and idler have similar intensities. Although it is possible to have a commercial DFG set up connected to a TOPAS, in the spectrometer used in this work, the DFG set-up is homebuilt. After leaving the TOPAS, the signal and idler are separated with a dichroic beam splitter. This allows for the separate spatial control of the signal and idler as well as a manual stage to control the temporal overlap. The signal and idler then pass back through the dichroic and overlapped on a silver gallium sulfide crystal. Our crystal is cut at 42°. As the name suggests, the output frequency of the DFG is $\omega_{ouput} = \omega_{idler} - \omega_{signal}$. On this set-up modulation of the signal and idler frequencies along with rotation of the DFG crystal (to maintain the phase-matching conditions) can yield wavelengths in the mid-IR from ~6100 to ~5000 nm. After the DFG, the light is filtered with a germanium crystal to remove residual signal and idler from the final 100 fs-long mid IR laser pulse.

2.2 Multidimensional Spectrometer

After Mid IR generation, the IR light is overlapped with a red diode laser and directed into the home-built 2D IR spectrometer. Shortly after the overlap, the light passes through a 90/10 beam splitter that divides the light into the pump/probe lines respectively. In the pump line, the light passes through a periscope and then is directed into the mid-IR pulse shaper. The shaper uses lenses and flat mirrors rather than parabolic or spherical mirrors to achieve the 4F geometry. In the pulse shaper, the double pump-pulse is created, as further explained in chapter 2.3.2 below. The polarization of the pump pulse is controlled by a λ/2 waveplate. The λ/2 waveplate

rotates the incident field. For the purposes of the experiments of interest in this dissertation, the light is either perpendicular or parallel to the plane of the laser table. A polarizer is sometimes used after the λ/2 waveplate to filter out any light that is not properly polarized. After the shaper and the polarization control elements, the light is then directed towards the sample stage. A set of flip mirrors is also used to bypass the pulse shaper. The red diode light is absorbed by the germanium crystal of the pulse shaper and the bypass line allows for an easier alignment of the pump line at the sample.

The probe line was created to account for the additional time needed for the pump line to pass through the germanium crystal in the pulse shaper, as the pump and probe must also be overlapped in time at the sample. A notable feature of the probe line in a mechanical chopper that is used to decrease background due to highly scattering samples. In these cases, an 8-frame phase cycling scheme is used when the chopper is run at half the repetition rate of the laser, effectively giving a probe-on and probe-off pair for each of the normal 4-frames used, allowing us to subtract off any pump scatter present without the probe interacting with the sample. Also on the probe line is the motorized delay stage that allows for the control of the timing between the pump and probe pulses or t_2. Modulating t_2 allows for finding signal after a major realignment as well as spectral diffusion experiments. Finally, there is also a λ/2 waveplate and polarizer to accomplish the sample polarization control as on the pump line. The light is then directed to the sample stage.

Directly before the sample stage, both the pump and probe lines are aligned to be flat and straight, hitting a parabolic mirror in its center laterally, about half an inch apart vertically. Before the sample, the pump is higher than the probe. The parabolic mirror then causes the pump and probe (if properly aligned into the parabolic) at the focus of the parabolic. The parabolic

mirror before the sample has a focus of 7 cm. The focal volume is about 50 x 50 x 50 μm. Spatial overlap is tweaked (total alignment notes are in section 2.7.6) using only the last pump mirror before the parabolic. The sample is held in a three-dimensional manual translation stage. The Z-axis controls the focus and the X and Y axes are used to move the sample cell around to find the best spot to measure. After the sample a parabolic mirror with a focus of 5 cm is used to recollimated the light. Now the probe light (now acting as the local oscillator) and signal are collinear (due to the pump-prob geometry) and are the higher spot. An index card after the parabolic blocks the pump light, which is now lower, from being directed into the monochromator.

The spatially higher signal and local oscillator are then directed into a monochromator that uses both a 75 groove/mm and 150 groove/mm to disperse the light across a 64-pixel mercury cadmium telluride (MCT) array detector. A parabolic mirror is used to focus the light to the slit of the monochromator. The 75 groove/mm grating allows the entire width of the probe pulse to be measure. The 150 groove/mm grating shows approximately half the width of the probe light, but affords twice the resolution. A mirror can be placed after the parabolic mirror after the sample in order to best direct the pump light into the monochromator. This is useful in troubleshooting (see below) as well as when changing the center wavelength of the light to study different samples.

2.3 Phase Matching and Phase Control

2.3.1 Phase Matching Geometries

A principal component of the creation of a 2D IR spectrometer is determining the phase-matching geometry at the sample. This decision will dictate what signal you collect, the direction of the signal, impact how the signal is heterodyned, and how the data will need to be processed.

Two common phase matching geometries were briefly discussed in Chapter 1: boxCARS and pump-probe. Pump-probe geometry will be elaborated upon here, as it was the geometry utilized in the experiments presented in this thesis. The pump-probe geometry has a few advantages as compared to using the more traditional BOXCARS geometry. One, the signal is self-heterodyned and two, the method allows for the measurement of a purely absorptive spectrum. In all, this makes the experimental set up and data processing a bit easier, though it does forfeit some control over the individual pulses.

Understanding the pump-probe geometry begins by looking more closely at the impact of the geometry on the direction of the emitted signal. The signal of the rephasing (S_N) and non-rephasing (S_{NR}) pathways are convoluted with the incident electric fields and are described by

$$S_R \propto -k_1 + k_2 + k_3 + k_{LO} \tag{2.1}$$

and

$$S_{NR} \propto +k_1 - k_2 + k_3 + k_{LO}. \tag{2.2}$$

These equations describe the direction of signal field for their respective pathways. The sum of the rephasing and non-rephasing signals gives a purely absorptive spectrum. As shown in figure 1.9, in the pump-probe geometry, the signal from the rephasing and the non-rephasing pathways are collinear as well as the probe. The collinearity of the probe is what allows the signal to be *self-heterodyned*. This phenomenon is shown graphically with arrows. Figure 1.9 also compares

the BOXCARS geometry where the rephasing signal, the non-rephasing signal, and the probe pulse is not collinear. In this case, the rephasing and non-rephasing signals must be collected separately, and summed together along with some phase corrections. This difference allows for pump-probe spectra to be collected in much less time.

Finally, the pump-probe geometry is easier to set up technically, as only two beams have to be aligned and overlapped in space and time, as opposed to up to four beams in the BOXCARs geometry. This combined with the direct measurement of a purely absorptive spectrum decreases time dedicated to alignment and data collection, as well as difficulty in first implementing this type of experiment to a project.

2.3.2 Pulse Control through a Mid-IR Pulse Shaper

Phase control is a key component in 2D spectroscopy as alluded to above. In the experiments reported here, the probe axis is collected in the frequency domain, by using a monochromator to disperse light across an MCT array. Furthermore, we have inherent phase control because the probe is self-heterodyned – it is always going to be in phase with itself. The pump axis is collected in the time domain as described here. When data is collected in the time domain, what the detector is sensing is the intensity of light which oscillates as a function of the time between the two pump pulses (t_1). This oscillation is often called a free induction decay (FID) which is causes by coherences during t_1 and is then Fourier transformed to create the pump axis of the spectrum. In order for this measurement to be successful, there needs to be phase control between the two pump pulses so that t_1 is accurate. This means that the two pump pulses must have the same phase or the spectrum will have asymmetric peaks in the frequency domain.

The Zanni group often employs a pulse shaper in order to control the phases of the collinear pump pulses needed in the pump-probe geometry. Other methods that are used to create

two collinear pump pulses include a wedge pair or an interferometer, but those lack the ability to best control t_1. In a pulse shaper, light is first dispersed into the frequency domain with a grating, passes through a germanium acousto-optic modulator (AOM) where the pulse is 'shaped', then brought back into the time domains by hitting a second grating. The AOM shapes the light as follows. An RF amplifier applies a specific acoustic wave (referred to as a mask) to the germanium crystal, creating a diffraction grating. This system allows for shot-to-shot modulation of the pump, the ability to phase cycle to eliminate scatter, and collect data in the rotating frame. All together, these aspects of the pulse shaper and a pump-probe geometry allows for rapid collection of high-quality data.

2.4 Mid IR Plasmonics

There are many materials and methods that can be used to enhance signal in the mid-IR. This section details all methods tried over the course of my Ph.D. work, as well as comments as to their relative success and use for studying membrane-bound proteins and peptides.

2.4.1 Different Plasmonic Geometries

In this work, we tried largely two different tactics or geometries to generate our plasmonic enhancement: nano-islands and nano-antennas. Generally, plasmons are created by incident light causing electrons to oscillate across a (typically) noble metal nanostructure. The oscillations lead to highly localized electric fields. Higher electric fields lead to higher signals measured by our spectrometer. In a nano-islands, or rough films, the metal is thermally evaporated, to create randomly sized islands that have the desired average thickness. The size and spread of the nano islands can be optimized by changing the deposition rate. The average thickness can also yield macroscopic conductivity, dependent of thermal evaporation conditions.

Batch to batch variability in thermal evaporation led to differences in conductivity across the samples. Conductivity was determined by measuring the resistance across 1 cm of the gold-coated CaF_2 window. Values below 20 kΩ were considered sufficiently conductive. Since these islands are relatively small, the plasmon resonance is in the visible (Figure 3.9). As the thickness increases, the plasmon resonance shifts toward the red and near-IR.

The other geometry that was tried for the work presented here are nano-antennas. Nano-antennas are more engineered, rather than the more random thermal evaporation. Antennas can come in a variety of shapes, but here rectangles were used. Briefly, a polymer film (in this case polymethyl methacrylate or PMMA) is deposited onto the CaF_2 window. Then, an electron beam etches away where the antennas will go. Then, a layer of the noble metal is deposited, filling in the gaps and then creating another layer on top of the PMMA. Then, the PMMA is lifted off with acetone, removing the residual metal not attached directly to the CaF_2 window. A draw back of the antenna is that they are not inherently conductive, since they are spaced out in an array across the window. This can be addressed by adding a conductive layer, like indium tin oxide (ITO) under the windows, although this does create some background signal. However, the antenna length can be tuned to the exact frequency of preference. Being on resonance with the antenna leads to higher enhancements compared to the rough films. However, signals that are slightly-off resonance can have lineshape distortions that require post-collection processing. Ultimately, I found the rough film to work better for my particular applications, and that is what I used after trying many nano-antenna options. The PMMA absorbs in the ester carbonyl region and even plasma etching the antennas to try and remove any residual was not sufficient for the small amount of signal from the ester label to be clear. However, perhaps in the case of the isotope label, the nano-antenna will be a good option.

2.4.2 Different Materials and Combinations of Materials for best enhancement and conductivity

Several different materials were tried to create the plasmonic surfaces that both gave good signal enhancement, low background, and also had the possibility to be macroscopically conductive. Previous work I contributed to in the group used 3-nm average thickness rough gold to create signal enhancement through localized surface plasmons. We used gold as the noble metal of choice in most experiments because it is easy to functionalize it by using the strength and ease of gold-thiol chemistry. 3-nm rough gold gave good signal enhancement and no background. However, most 3-nm rough gold-coated CaF_2 windows were not macroscopically conductive. A series of windows with different thicknesses of gold were created with help from Vivek Saraswat in the Arnold group in the Materials Science and Engineering Department at UW-Madison. It was found that easily replicable macroscopic conductivity was found when the average thickness of gold was 8-nm or thicker. Windows with 2-4-nm thick gold gave comparably good enhancement. Once macroscopic conductivity was reached, however, a background streak along the diagonal was seen in most spectra, with some batch-to-batch variability. The background streak did not appear to be specific to location on the sample, applied voltage, or waiting time. It did not decrease with chopping on the probe line. In my published data with the thicker rough gold layer, subtraction was used in order to see the peaks under the background.

We also tried to use a relatively transparent conductive layer under a thinner layer of gold. In these cases, we used indium tin oxide (ITO) of 5-nm thick with 3-nm rough gold on top in order to have the conductivity without the diagonal background. However, we saw a different, non-diagonal, seemingly random background due to the ITO. We also tried 5-nm ITO with 0.5

nm gold to similar effect. Single layers of graphene were also used under the gold, due to the conductivity of graphene. The graphene also did not yield promising results in this case, but could be helpful in the future. One other method attempted was to use 10 nm palladium under 3 nm of gold. The system was conductive but we still had the conductive background stripe. Also, palladium is very expensive.

2.5 Sample preparation techniques

There are two main types of samples that were prepared over the course of this work. They mainly are dependent on the type of experiment of interest. Tethered bilayers are for the applied voltage experiments or when you want to orient a sample. These use gold-thiol chemistry to tether the sample to a gold substrate. For bulk experiments without voltage needed, then we simply layer a sample and perform an H/D exchange to remove any waters stuck in the lipid or detergent structures. General strategies are detailed for each below.

2.5.1 Tethered Bilayer Creation

For experiments published in this report, this method specifically was used to tether thio-lipids to a rough gold substrate. However, this strategy could also be used to tether any thiol to gold, whether it be a small molecule or a terminal cysteine on a protein. Furthermore, this chemistry can be used to tether to gold nano-antennas. Similar strategies could also be employed with silver as the plasmonic metal of choice.

The approach begins by creating the bottom layer of the lipids. 1,2-Dipalmitoyl-sn-Glycero-3-Phosphothioethanol (DPTE) from Avanti is measured out in chloroform solution and dried down under nitrogen. After drying down, the lipids are lyophilized overnight. The amount of lipids used can be modulated to change the fluidity of the membrane. This can be estimated by

determining the surface coverage of a mole of lipid and relating it to the surface area you are trying to cover. Full coverage will lead to a very stiff membrane, and may impact the insertion dynamics of the proteins of interest, so this may be of interest in future to further optimize sample preparation. After drying the DPTE on the lyophilizer overnight, then resuspend the DPTE in spectrophotometric-grade ethanol. Let the CaF_2/gold window sit in the solution overnight in a dedicated glass jar. It is best to lightly flush the headspace with nitrogen to minimize the risk of lipid oxidation.

The next step is to create the lipid vesicles. For the experiments outlined here, 1-palmitoyl-2-oleoyl-glycero-3-phosphocholine (POPC), also from Avanti, was used. POPC is a zwitterionic lipid that is present in eukaryotic membranes, and is typical in many biophysical experiments. POPC vesicles were typically prepared in large batches and flash frozen in aliquots for future use. Therefore, it was mostly important to maintain a concentration above the critical micelle concentration, which for POPC is about 0.5 nM. Vesicles were typically created at 200 μg/mL concentrations, well above the limit. Then later diluted as needed. POPC was dried under nitrogen then lyophilized overnight, concurrent with the DPTE. Then, the lipids were resuspended in 100 mM NaCl or 100 mM KCl (as needed). After suspension, vesicles were formed by five freeze-thaw cycles in dry-ice/isopropanol as the cold bath and lukewarm water (30-40 °C) as the warm bath. The vesicles were then sonicated in a bath sonicator for 30 minutes, to create 50 nm-100 nm unilamellar vesicles. Vesicles were then aliquoted into 5 mL aliquots and flash frozen in liquid nitrogen and stored at -20 °C, or used immediately.

After the overnight soak in DPTE, the window should be thoroughly washed with spectrophotometric grade ethanol. Then the window should be allowed to soak in a solution of the vesicles (5-10 mL needed, sometimes the window tries to float because of the

hydrophobicity, so slightly more solution will be needed) overnight, again flushing with nitrogen. The vesicles should also have their own dedicated jar for soaking. After the soak, wash with 18 MΩ water and let dry under nitrogen. An FTIR can be taken at this point to see if there are lipids, but this step is not necessary.

If the sample is something like alamethicin, which is purchased as a purified sample in methanol, then it can be directly dropped onto the sample at this point as described in chapter 3. If you are working with a sample that is in lipids already, then prepare just the DPTE layer of the bilayer and then allow the vesicles containing the sample to fuse with the bottom layer. This approach does not work for voltage-gated samples very well since, a full bilayer will not be formed, but will be sufficient to deposit the lipid-bound sample onto the plasmonic substrate.

2.5.2 Ion Channel sample preparation

For samples without the need for plasmonic enhancement, then it is best to work in the bulk, especially for a number of the equilibrium ion channel experiments. In these cases, ion channels in detergent (generally decyl maltoside) are pipetted in a small drop (2 μL) onto a bare, clean CaF_2 window, and allowed to dry under nitrogen. For the drying under a nitrogen environment, we create a small box made out of an old pipette holder that is connected to a lab nitrogen line, to keep our samples in a nitrogen environment. Samples are then H/D exchanged in order to remove any residual waters that are trapped, that previous members of the group have reported (unpublished) to create strange background in the spectra. The H/D exchange is performed by pipetting 0.2 μL of D_2O onto the small spot on the CaF_2 window in the nitrogen box. The spot is allowed to dry under the nitrogen, keeping the box closed between pipetting. Pipetting is repeated for a total of 50 times. Fewer repetitions have been tried with seeing a strange background, so 50 seems like the minimum number. In pipetting, it is important to try

and not touch the plastic of the pipette tip to the surface. This can cause abrasions in the sample that leads to increased scatter when it is measured. One should try to just touch the D_2O to the sample. It is helpful to support your pipetting hand with the edge of the box, or the counter. Finally, it is also important to move as quickly as possible (while being careful) to make sure that any water vapor in the air does not get reintroduced to the sample. The 50 repetitions should take about 2 hours total, though it is faster the dryer it is in lab. Samples should be rehydrated with 0.2 μL of D_2O before assembling the sample cell and measuring, using a greased, 12-μM spacer. The resulting spot should be about 0.5-0.75 cm in diameter and last for up to a week.

For samples that have either an ester or isotope label, it may be necessary to create layered bilayers. In these cases, it is better to get as high of a concentration of protein as possible. The maximum concentration hovers around 10 mg/mL with 0.25% detergent and 100 mM buffer/100 mM KCl. To create the layers, 2 μL of sample is pipetted onto the clean CaF_2 window and allowed to dry. This is then repeated for a total of 10 layers, allowing for drying underneath. In totally the layering should take 2-3 hours. Then it should be left to really dry under nitrogen overnight. Then, the H/D exchange is performed as described above, the sample is rehydrated with 0.2 μL D_2O, and assembled. It is best to batch the preparation of these samples in groups to save time in lab. Samples after H/D exchange can last about a week under nitrogen before rehydrating. The number of layers needed can be verified with FTIR. The label peak should be visible in order to have good signal to noise on the laser. Example FTIR spectra with sufficient signal are shown in Chapter 4 for comparison.

2.6 Silver Stain and Crosslinking Gel

This project is related to the amylin work in the Zanni group, but is included here as reference in conjunction with Cat Fields' crosslinking work as reference for future students. Silver stain is a gel imaging technique that is more sensitive than Coomassie for when working with small amounts of sample. It was being used to image SDS-PAGE gels run to identify oligomers trapped by crosslinking to show how mutants of amylin create a longer lag phase. More of the background of this work is found, again, in Cat Fields and Kacie Rich's dissertations.

My main contribution to this work was in terms of troubleshooting the running of the SDS-PAGE gel as well as the silver stain developing process. The gels used with gradient tris-tricine gels with a gradient of 10% to 20% acrylamide from Invitrogen. The gels are best for small proteins, which is good for amylin as the monomer is about 3 kDa. Gels were loaded to have 50-200 ng of protein in each well. Tris-Tricine SDS buffer was used (BioRad). The gels were run for 30 min at 30 V, then at 90 V until the dye front was about 75% down the length of the gel. The gel was then removed from the cassette using the palette knife to crack the plastic cassette and then gently in 18 MΩ water, allowing the gel to float off the plastic. You may need to loosen the gel by running a fingernail or the palette knife along the slot at the back of the gel cassette that is located where the tape is removed before the gel is run. The gel should be disassembled directly into the dedicated silver stain dish. We used a ~7-inch crystallization dish washed thoroughly with 18 MΩ water before each use. The gel was rinsed lightly in 18 MΩ water, then drained.

While the gel is running (starting from about 50% down the gel), start preparing the silver stain solutions as detailed in the silver stain kit (Invitrogen). For each solution, use dedicated

glassware that has never been used for anything but the solution. Label with tape and only use for developing solution, fixing solution etc. While making solutions, use fresh, sterilized, single use pipettes. ONLY USE THOSE THAT ARE INDIVIDUALLY PACKAGED. Always use 18 MΩ water, and have a dedicated container for the water as well.

Follow directions in the silver stain kit to stain the gel. When handling the gel itself, use new gloves every time and only touch the gel below the gel front. The silver stain is so sensitive that if you touch skin, hair, etc. with the glove then touch the gel, a fingerprint can be seen on the gel. Silver stain waste should all be disposed of in a carboy. Note which carboy it is since the silver nitrate should be on the disposal form, which is unique compared to the HPLC carboys which do have acetic acid and methanol in them as well. For the stopping solution, make sure you add it just when you think that it is getting dark, as it does darken a little more after it is added. If you see a large brownish background, it is likely that you have some contamination either in one of the staining solutions or did not use clean pipettes or glassware. Wash everything thoroughly and buy new glass containers for the solutions. Over time, the staining becomes less strong as the package reaches its expiration date. At this point it is better to reorder a fresh kit.

2.7 Troubleshooting the Kickapoo Laser Table

2.7.1 Cleaning Chiller Lines to Increase Power

If power of the light coming out of the chiller is decreasing and other methods to increase power are not working, it is worth considering cleaning out the chiller lines. Build-up of algae and other things can lead to a decrease in power of the pump laser. This method is a brief summary of a method supplied by Coherent representatives. The procedure can be done over two days, I will indicate when to take the overnight break. Day one is kind of long, but has a big 8-

hour break in the middle, so plan to get in early. The supplies required are: Alconox, at least 30 gallons of distilled water, buckets to move the water with, 2 filters and Optishield. Make a 1% w/v solution of alconox/distilled water. Make sure that the alconox is completely dissolved before adding the solution to the chiller, you might need to use warm water. If more liquid is needed, (there is about 1.5-2 gallons in the chiller including the volume of the chiller lines) just add additional water. Drain the chiller of the current water and the lines as best as possible. Then flush 2 times with just distilled water, by adding distilled water to the chiller and letting run for about 10 minutes each time, then draining the chiller and the lines. After the second flush, replace the filter with a fresh filter. Then, add the alconox mixture. Increase the chiller temperature to 26 degrees Celsius and let run for 8 hours. Stop the chiller and drain the fluid. Flush with distilled water by filling the chiller, letting the chiller run for 5 minutes (still at 26 °C to keep any alconox in solution), stopping the chiller and draining. After 2 rounds, you can call it a day. Refill with water and let it continue to run overnight. On day two, repeat the flushing process to a total of 10-20 times until you don't see any bubbles when you drain the chiller. When it is done being cleaned, drain the distilled water one last time, replace the filter, then add in the normal optishield/distilled water mixture. Set the chiller temperature back to normal (16 C) and let equilibrate for 1-2 hours before turning the laser back on. This will probably be overnight anyway.

2.7.2 Replacing pump laser diodes

The diodes that pump the Nd:YAG rod in the Evolution pump laser need to be replaced over time. This is another way to increase pump laser power. Replacement of these parts is relatively straightforward. First, measure the power out of the evolution with a power meter for reference. Power off and deenergize the laser following the posted instructions. Then, turn off

the chiller. The chiller lines going through the laser should also be drained as much as possible. The evolution lid is then carefully removed and the laser rod and diode assembly can be unplugged and unscrewed from the base. There may be a little residual water from the cooling lines, so be prepared with a Kim wipe to prevent too much dripping. Then, the assembly can be disassembled with Allen keys. Be careful to keep track of which beige wall goes where and to keep track of the O-rings. Extra O-rings (labelled for the diodes) are in the lab if needed, they are a very specific size and are not carried in the machine shop. Take out the diodes and replace with new diodes. Take care to inspect the laser rod for any cracks or other issues, as that can also cause a decrease in pump power. Carefully assemble, making sure that everything is tight. When reassembled, place back in Evolution, but don't plug back in yet. Then, reattach the chiller. Have one person turn on the chiller while another keeps an eye on the evolution to verify that there is no leaking. You may want to keep it open for a half hour or so to make sure that it is watertight. Then plug in the diodes and replace the lid of the evolution. Reenergize and turn back on the laser. Measure power out of the Evolution to check.

2.7.3 Realigning the laser cavity (Libra)

This is a brief overview of things to try to increase the power out of the Libra by tweaking the alignment of the laser cavity. This is best done with two people. One person is often needed because it is easy to trip the sensor on the seed laser, which means that no light will come out of the Libra, so the power meter will not be able to be read out. It is possible to align on low pump power, but it is easiest to have enough pump power that you can get a reading out of the regenerative amplifier. To do this make sure that you are wearing adequate laser safety glasses and post a sign outside of the laser lab saying that you are realigning the laser cavity.

There are small knobs with Allen key heads that can be used, but often times it is easier just to use the Allen key.

The tweaking is done by successively tweaking the mirrors in the cavity while the laser is on, looking for increases in power. Optical labels are found in figure 2-3 in the Libra manual supplied by Coherent. The most effective mirrors are PM2, RM1, RM4, and PM4. Successive tweaking of these mirrors should increase power. RM3 and RM2 can also be tweaked. Both RM1 and RM4 are HIGHLY SENSITIVE to change in angle due to their proximity to the Pockel cells, and should be tweaked very carefully. SM10 can also be optimized for overlap with the pump on the Ti:Sapph crystal. RM6 may need to be adjusted as well.

It may also be helpful to carefully clean the optics in the cavity with lens paper and high-quality methanol, folding the paper as described in the laser manual. However, wipe gently as to not bump the mirrors and change the alignment of the cavity. It is also possible to change the delay on the Pockel cells to add or subtract a round trip, though this is likely not necessary. Finally, the pattern of diffraction from the stretcher can be checked to make sure that the seed is properly aligned. This should also not need to be fixed, but it is worth verifying. At the end of all tweaking the compression motor should be used to maximize power output. The goal should be 3-3.5 W of 800 nm light.

2.7.4 Realigning and calibrating the OPA (Topas)

If there is sufficient light out of the Libra, then the next thing to check is light out of the TOPAS OPA. When working around 6 μm light after the DFG, the output of the OPA should be turquoise-green. This can quickly be checked by quickly looking at an index card right before the light enters the main purge box of the spectrometer. If there is no light, open the TOPAS and follow the alignment instructions in the manual until light is coming out of the OPA. After that, I

have found the manual lacking. Place the mid-IR probe (‘pyro’) after the DFG set up. It is best to tweak the OPA to the light you want, or otherwise you can end up with 800 nm leak through that you have aligned out of the OPA.

Carefully adjust the alignment into the OPA using the two silver mirrors between the Libra output and the input of the OPA. If this does not drastically increase power, then try walking by moving the mirror further from the OPA until the light decreases by 25-50% and trying to recover with the other mirror. Try going both ways to maximize. Adjust compression of the Libra, and tweak the crystal angles and delays in the TOPAS software. Iterate these steps until sufficient light. The bare minimum to run an experiment is about 70 mV as measured with the pyro detector. It should be possible to get 80-90 mV however, which is ideal.

2.7.5 Shaper realignment and calibration

This section discusses strategies to try to increase shaper efficiency through alignment. First, use the two irises and two mirrors after the pump/probe beam splitter to make sure that the light is coming in flat. Place the pyro on the pump line after the shaper. First, make sure that the light is being deflected and that there is no leak through. On the 2-frame mask, you should be able to see a flat line and a negative curve on the oscilloscope. If the line is not flat you have some zeroth order leaking thought. This can be rectified by either physically blocking it after the second grating or adjusting the alignment of the shaper. Next, the goal is to maximize the amplitude of the deflected signal. This can be done by walking the flat mirrors right before and after the AOM. The angle of the AOM can also be changed slightly to maximize light after the sample. The goal should be at least 25% efficiency (measured by using the bypass and then putting the light through the shaper to account for any water vapor in the pathlength). 30% should be readily attainable at 6 μm.

Shaper calibration is relatively straightforward. The main goal is to make sure that the pump axis is linear after calibration and that the AOM is applying the correct waveform to the corresponding pixel. Align the pump to the detector using the pump mirror after the sample. This is easiest to do if you put up the shaper bypass mirrors and align into the monochromator. Put down the bypass mirrors and then tweak alignment of the shaped pump light. Apply the 'multi mask', noting the center pixel, spacing, and width in the LabVIEW Mask VI. Take a scan of the pump spectrum. Then apply the 'single mask' with the same parameters and monochromator slit width as the 'multi mask'. Take a pump spectrum with the 'single mask' applied. These masks essentially let the light through the AOM for certain pixel widths. The light let through is then corresponded to the monochromator frequency. This is done with the shaper calibration code. The two spectra are uploaded when prompted and the width, spacing, and frequency are applied. Make sure to look at where the cut offs are to make sure that all of the peaks in the center of the pump spectrum are being marked by MATLAB. Not having these peaks will make a poor calibration. In the MATLAB code, you can scale the cut off value to make all relevant peaks be included. When the cutoffs are reasonable, the code will fit the peak frequency to pixel with a trinomial. The parameters can then be applied to the LabView Shaper Mask VI. An offset may be necessary. The offset can be found by taking a 2D IR spectrum of a sample with a known frequency from FTIR and adjusting the pump offset in the data processing code so that the standard has the correct pump frequency. After calibration, such a shift should be linear.

2.7.6 Finding Overlap at Sample

When you have sufficient Mid-IR power, but are still having trouble finding signal, it is likely that you are not well-overlapped either in time or space. Here, I discuss a straightforward approach to finding signal using a pinhole for overlap. Rather than trying to find oscillations

blindly, by carefully aligning the pump and probe lines to begin with, finding interference through the pinhole should be easy and the resulting high intensity of the oscillations will allow for the appropriate T_2 time to be identified.

First it is important to make sure that the pump and probe lines are going in straight and flat into the parabolic mirrors. If this is the case, then they should naturally cross at the focus. The first step is to check and optimize the overlap of the red diode laser and the IR using the irises and the two mirrors of each before they are overlapped after the DFG. Alignment of the probe line is done by checking all of the irises on the probe line first, and aligning through them all. Then, use a beam block and the two mirrors before the sample parabolic to make sure the probe beam is straight and flat relative to the table before the parabolic mirror. For the pump line, it is easiest to use the shaper bypass line. Again, it is important to make sure that after the last two flat mirrors before the sample, that the light is flat and straight.

Use the X and Y axes of the three-dimensional manual stage to align the center of the pinhole to make sure that the probe is going through the pinhole. Flip up the shaper bypass line so that the diode of the pump is visible after the shaper. Use the last pump mirror before the sample to align the pump through the pinhole as well. DO NOT TOUCH THE PROBE OR THE PINHOLE POSITION. Then, place the mirror labelled ‘pump’ after the sample and align the pump light into the monochromator. Undo the bypass and tweak alignment of the pump into the monochromator. The mask should be made to be 2 frame and 4 frame should be turned off on the pump-probe read out. Remove the pump mirror. There should be large oscillations on the pump-probe signal read out. If not, scan the length of the t_2 delay stage. Tweak overlap with the last pump mirror before the sample. The intensity of the oscillations should be about 0.1 ΔOD. Once you have maximized oscillations, then put n-methyl acetamide (NMA) or n-acetylproline (NAP)

–or any other standard sample—and look for pump probe signal by switching the mask and the pump-probe read out to 4-frame. Any additional tweaking can be done with signal on NMA. This can include small changes in focus (due to difference in sample cell), spatial overlap, or timing to maximize signal. Changes in dispersion correction can be applied here as well, though it should be noted that changing the group velocity dispersion and third order dispersion (GVD and TOD in the mask VI) will change the waiting time and that should be optimized again after the new values are applied.

3 Monitoring structure and insertion angle of alamethicin after applied voltage[1]

The structures of many membrane-bound proteins and polypeptides depend on the membrane potential. However, spectroscopically studying their structures under an applied field is challenging because a potential is difficult to generate across more than a few bilayers. We study the voltage dependent structures of the membrane bound polypeptide, alamethicin, using a spectroelectrochemical cell coated with a rough, gold film to create surface plasmons. The plasmons sufficiently enhance the 2D IR signal to measure a single bilayer. The film is also thick enough to conduct current and thereby apply a potential. The 2D IR spectra resolve features from both 3_{10}- and α-helical structures and cross peaks connecting the two. We observe changes in the peak intensity, not their frequencies, upon applying a voltage. A similar change occurs with pH, which is known to alter the angle of alamethicin relative to the surface normal. The spectra are modeled using a vibrational exciton Hamiltonian and the voltage-dependent spectra are consistent with a change in angle of the 3_{10}- and α-helices in the membrane from 55° to 44°and from 31° to 60° respectively. The 3_{10}- and α-helices are coupled by approximately 10 cm^{-1}. These experiments provide new structural information about alamethicin under a potential difference and demonstrate a technique that might be applied to voltage gated membrane proteins and compared to molecular dynamics structures.

[1] Reprinted with permission from **Erin R. Birdsall**, Megan K. Petti, Vivek Saraswat, Joshua S. Ostrander, Michael S. Arnold, and Martin T. Zanni. *Structure Changes of a Membrane Polypeptide under an Applied Voltage Observed with Surface-Enhanced 2D IR Spectroscopy* J. Phys. Chem. Lett. 2021, 12, 7, 1786–1792.

3.1 Introduction

Studying the structures of membrane proteins under an applied voltage is experimentally difficult. The crux of the problem is one of sensitivity. Most spectroscopies and scattering experiments require thick samples composed of many layers of proteins to produce enough signal. When a field is applied across a thick sample, the field strength is strongest at the surface and rapidly diminishes in the interior. As a result, extremely high voltages are required to elicit a structural response for those proteins near the interior of a thick sample. Indeed, there is only one example of an x-ray scattering experiment performed on a protein crystal under an applied voltage.[1] Techniques with high sensitivity that do not need thick samples but can be applied to monolayers, single bilayers, or single molecules, can be used to study voltage dependent proteins. For example, fluorescence spectroscopy has been used in conjunction with a patch clamp to study membrane proteins under an applied voltage[2,3] and surface enhanced infrared absorption spectroscopy (SEIRA) has been used to measure the IR spectra of a protein monolayer with an applied voltage.[4,5]

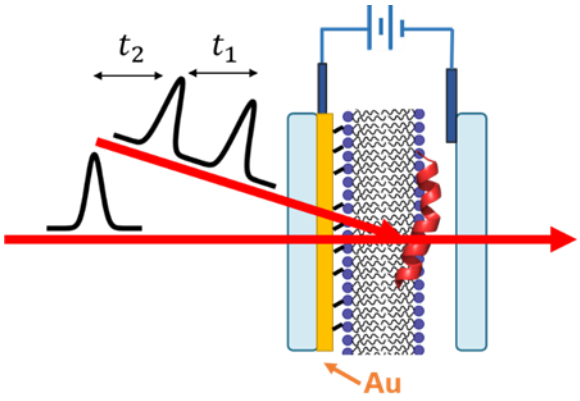

Figure 3.1 Schematic of the voltage-dependent experiment. Two colinear pump pulses and a probe pulse are directed into the sample cell. The working electrode consists of a rough, 10-nm thick layer of gold while the counter electrode is made of conductive aluminum.

Using mid-IR plasmonics, analogous to SEIRA, the sensitivity of 2D IR spectroscopy has recently been improved to the point where a single monolayer of molecules can be measured.[6–13]. Rezus and coworkers in 2015 used gold nanoantennas to create plasmons to measure thin organic films with 2D IR spectroscopy.[10] Hamm and coworkers used rough

metallic thin films to create localized surface plasmons to enhance the electric field strengths of the laser pulses sufficiently for measuring 2D IR spectra of carbon monoxide adsorbed on a surface.[14] They also applied a voltage to the thin metal film and observed and quantified the Stark shift of the immobilized carbon monoxide.[7] In a similar approach, Rubtsov and coworkers have used nanoantennas to study monolayers of ester containing molecules with 2D IR spectroscopy.[8] In this report, we use thin metallic films to both measure 2D IR signals of alamethicin bound to a single membrane bilayer while also utilizing the film to apply a voltage. Using 6-μm light in the mid-IR allows the amide I mode, which is the vibrational mode created by the carbonyl stretches of the backbone and is well-known to be sensitive to polypeptide secondary structure, to be measured.[15]

Alamethicin is a 20-residue antimicrobial peptaibol from the fungus Trichoderma viridae.[16] The monomer itself is comprised of α-helical region and 3_{10}-helical segments, on the N- and C-termini respectively.[17–19] The α-helix spans about 13 residues while the 3_{10}- helix is 4 to 5 residues. The two helical segments are separated by a kink formed from the proline at position 14. The structure of alamethicin has been characterized many times, both in organic solutions and in membranes by experimental techniques as well as molecular dynamics simulations.[20–24] The aforementioned 3_{10}-helix was identified by solid-state NMR, sum-frequency generation, and a variety of molecular dynamics simulations.[18,25–27] Using molecular dynamics simulations and sum frequency generation, it has also been established that a potential difference or a basic pH causes the alamethicin monomer to form bundles that create pores, though the number of monomers that contribute to the pore is yet to be determined.[20,28–31] Most evidence points to pores of 4-8 monomers, though pores of up to 12 monomers have been observed in simulations.[17,24,32,33] Another reason alamethicin was chosen in this study is because

of the previous work using Surface-Enhanced Infrared Absorption Spectroscopy (SEIRA) and polarization modulation-infrared reflection-adsorption spectroscopy to study the tilt angle of alamethicin.[34,35] Knowing that similar structural changes occur upon a potential difference as basic pH provides a good structural control to develop our technique.

3.2 Methods

Our approach is schematically shown in Fig. 3.1 and can be found in detail in the Supplementary Information. Briefly, a sample cell is constructed with two CaF_2 windows. For the first window, gold is thermally evaporated onto a CaF_2 surface to form a rough surface that is plasmonically active. For the pH studies, the gold thickness is 3 nm. For the voltage studies, the thickness is 10 nm so that the gold is conductive and can thereby act as the working electrode. For the voltage experiment, the counter electrode is made of conductive aluminum tape on the second CaF_2 window. The bilayer is created by soaking the gold coated window with 1,2-Dipalmitoyl-sn-Glycero-3-phosphothioethanol lipids which have a headgroup modified with a thiol group. The sulfur bonds to the gold, making a sparse lipid monolayer. The bilayer is created by adding vesicles of POPC (1-palmitoyl-2-oleoyl-sn-glycero-3-phosphocholine) lipids that fuse to the monolayer. The substrate is then washed to make sure that only the tethered bilayer remains and the alamethicin is deposited in potassium buffer solution on the POPC side of the bilayer at a peptide to lipid ratio of 1:20. 2D IR spectra are collected using a pump-probe beam geometry with the two, colinear pump pulses separated by t1, and a probe pulse delayed by t2 (see Fig. 3.1). In the two experiments the same sample was modulated either by changing the pH of the buffer between pH 6.8 and pH 12, or changing the potential across the sample from 0 V applied to -900 mV relative to the gold electrode. Since our setup has no reference electrode, the

absolute potential is not defined. Nonetheless, the structure of the alamethicin will be determined by the potential difference across the membrane.

3.3 Results

Fig. 3.2A shows the spectrum of membrane bound alamethicin at pH 6.8. There are three principal peaks along the diagonal at ~1630, 1640, and 1660 cm^{-1} as measured by their frequency along the pump axis (labeled i, ii, and iii, respectively). The most intense peak is at 1630 cm^{-1}. They have relative intensities of 1:0.5:0.2, for the 1630, 1640,1660 cm^{-1} features, respectively. Fig. 3.2B shows the spectrum of alamethicin at pH 12. The same three peak frequencies are observed, albeit with different relative intensities, which are 1:1.1:1.7 respectively. To verify that the peaks shown are indeed from the peptide and not from the membrane bilayer, spectra were also collected of the membrane itself (Figure 3.7). The membrane-only spectra contained features near 1750 cm^{-1} from the ester carbonyl stretches of the lipid headgroups, but no peaks in the amide I region were observed. Thus, the spectra in Fig. 3.2 are solely created by alamethicin. To further verify that the signal arises from the lipid-bound peptide, we also considered that the

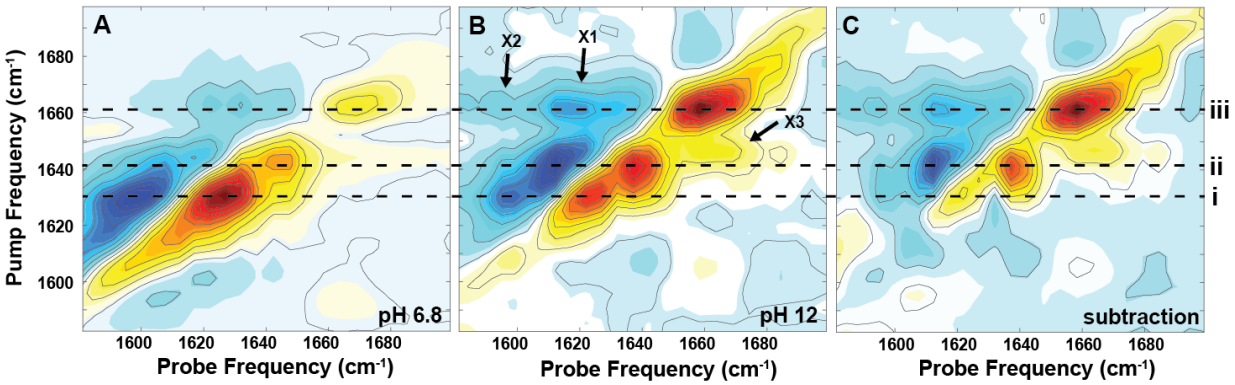

Figure 3.2 Spectra of the pH dependence of alamethicin. Alamethicin at (A) 6.8 and (B) at pH 12 in buffer. (C) Difference spectrum generated by subtraction of the pH 6.8 from the pH 12 spectrum. The spectra were normalized to their maxima and the subtraction was weighted 1:2 respectively. Cross peaks appear in all of the spectra and are labeled X1 – X3 in (B).

solvation free energy of alamethicin to POPC is about -115 kcal/mol (compared to -20 kcal/mol in water), and so most of the polypeptide is bound to the bilayer.[36] Nonetheless, free-floating

alamethicin would not contribute to the signal because the plasmonic enhancement of the signals only occurs within 50 nm of the gold surface.[37] Cross peaks also appear that correlate the 1660 cm^{-1} peak with the 1630 and 1640 cm^{-1} peaks. We label them X1-X3 in Fig. 3.2B, but they appear in all three spectra of Fig. 3.2.

Based on prior work, peaks i and ii are assigned to the 3_{10}-helical segment of the peptide, which has two peaks due to the splitting of the *A* and the *E* mode of the helix at approximately 1640 cm^{-1} and 1630 cm^{-1} respectively. The *A* and *E* modes are the modes along the axis of the helix and perpendicular to the axis of the helix, respectively. We use the terms *A* and *E* modes qualitatively. *A* and *E* modes are only rigorously correct in a perfectly ordered and infinitely long helix. In a finite helix and one with structural and environmental disorder, additional eigenstates gain oscillator strength. The frequency difference between the *A* and *E* modes depends on the number of residues per turn in the helix.[15] There are 3.6 residues per turn in an α-helix but only 3.2 residues per turn in a 3_{10}-helix. In α-helices, the *A* and *E* modes are separated by less than 5 cm^{-1} and so are not usually resolved from one another, but in 3_{10}-helices, the peaks are separated by about 10 cm^{-1}.[38] Peak iii at 1660 cm^{-1} is assigned to the α-helical section of alamethicin. This value is higher than an α-helix in buffer, but typical for membrane associated helices who have better defined structures and are protected from solvent, both of which result in a higher frequency.[39] Based on that assignment, cross peaks X1 and X3 correlate the *A* mode of the α-helix with the *A* mode of the 3_{10}-helix, above and below the diagonal while cross peak X2 correlates the α-helix and the *E* mode of the 3_{10}-helix. The *A* mode of the α-helix is largely responsible for this peak due to the fact that the E modes are much weaker than the *A* modes in the α-helix because the local mode transition dipoles lie nearly parallel to the helix axis. *E* modes for α-helices are rarely observed in 2D IR experiments, so we assume that the *A* mode

contributes mostly to this cross peak. Supporting that conclusion, our calculations predict that that the *E* mode intensity in our modeled spectra is 8.5% of the *A* mode in the α-helix. Cross peaks in Fig. 3.2B appear either entirely positive (blue) or negative (red). However, they are theoretically a pair of positive and negative peaks, separated by the off-diagonal anharmonicity.[15] Due to overlaps in the experimental spectra, they are partially obscured. This anharmonicity leads to positively signed cross peaks that do not appear directly above or below the transition as in the case of X2, as illustrated in the calculated spectrum in Fig. 3.6.

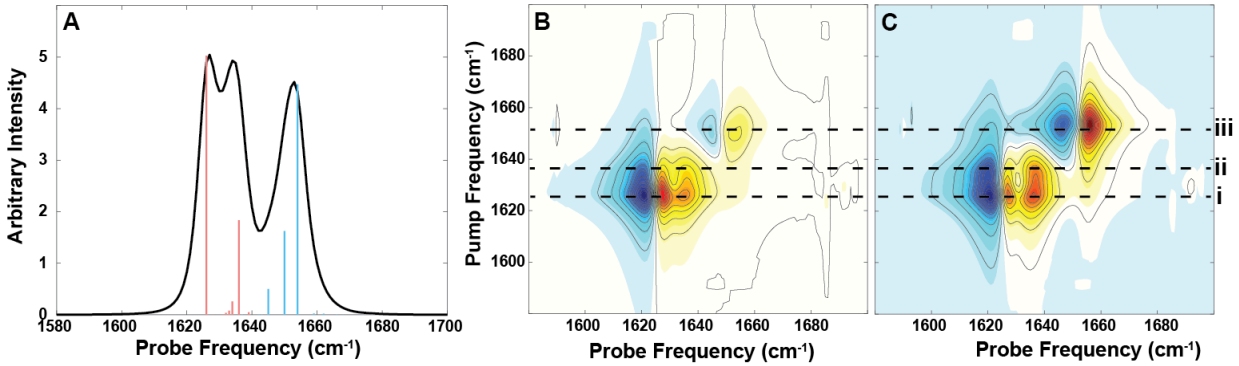

Figure 3.3 Calculated 2D IR spectra by summing simulations for the α- and 3_{10}-helices. (A) Diagonal slices of the 2DIR spectra with stick spectra (blue) for the α-helix and (red) for the 3_{10}-helix. (B) modeled 2D IR spectra with angles of 31° and 55° for the α- an and 3_{10}-helices that reproduce the relative diagonal peak intensities in the neutral pH experiment (Fig. 3.2A). (C) modeled 2D IR spectra with angles of 60° and 44° for the α- and 3_{10}-helices that reproduce the relative diagonal peak intensities in the basic pH experiment (Fig. 3.2B).

The 2D IR spectra were also simulated using COSMOSS, a program for modeling infrared spectra using vibrational excitons that is available on our website.[40] The transition dipole directions of the amide I modes were generated using the PDB file of alamethicin (1AMT).[16] Published values for the 3_{10} and α-helices coupling constants were used. The nearest neighbor couplings were held constant regardless of the precise dihedral angles from the PDB file. The coupling values for the 3_{10}-helix were: 0.9 cm^{-1} for nearest neighbor βi,i+1, -2.5 cm^{-1} for βi,i+2, -2.8 cm^{-1} for βi,i+3, -0.8 cm^{-1} for βi,i+4, and neglected for more distant residues. The coupling values for the α-helix were: 8 cm^{-1} for βi,i+1, -2 cm^{-1} for βi,i+2, -6 cm^{-1} for βi,i+3, -1 cm^{-1} for βi,i+4, -0.5 cm^{-1} for βi,i+5and neglected for further residues.[15,41] Local mode frequencies are set

at 1635 cm^{-1} for 3_{10}-helix and 1655 cm^{-1} for α-helix portions based on previously published experimental data.[28,39,42] Each transition in the 2D IR stick spectrum is scaled with respect to its orientation in the bilayer where the electric fields of the laser are normal to the bilayer, followed by convolution with a 10 cm^{-1} FWHM 2D Lorentzian. The spectra were calculated separately for the α- and 3_{10}-helices and the couplings between the helices were neglected (see Fig. 3.4 below for simulations that include couplings) so that the tilt of the α- and 3_{10}-helices in the membrane could be independently adjusted and their respective 2D IR spectra summed to best match the experiment.

Diagonal slices of simulated of 2D IR spectra are shown in Fig. 3.3A for comparison to Fig. 4.2. The calculated 3_{10}-helix peaks at 1627 and 1635 cm^{-1} correspond with peaks i and ii in Fig. 3.2. The calculated α-helical peak at 1655 cm^{-1} corresponds to peak iii. To match the peak intensities in the pH 6.8 spectrum (Fig. 3.2A), the 3_{10}-helix was set to 55° and the α-helix to 33° (relative to the membrane normal). Since the *A* and *E* modes are perpendicular to each other, their peak intensities depend inversely with one another as a function of the tilt angle of the peptide relative to the plane of the membrane. Thus, these two peaks give the tilt angle of the 3_{10}-helix. With those fixed, the relative ratio to the peak at 1655 cm^{-1}, gives the tilt of the α-helix. The error in these angles is tied to approximations in the model, such as the lack of disorder, but by systematically varying the model parameters we estimate the accuracy of these angles within our approximations to be ±10°. Amide I frequencies will also depend on helix length.[15] Since the frequencies are unchanged, the lengths of the helices most likely do not appreciably differ when inserted. We also note that the convoluted peaks represent the traditional *A* and *E* modes of helices, but the stick spectra contain additional transitions. *A* and *E* modes are based on symmetry in the approximation of infinitely long helices. The vibrational exciton simulations

presented here take into account the finite nature of the helices, which puts oscillator strength into eigenstate modes that are IR-forbidden in the symmetry approximation and, thus, are better for simulating the experimental peak intensities and extracting helix angles.

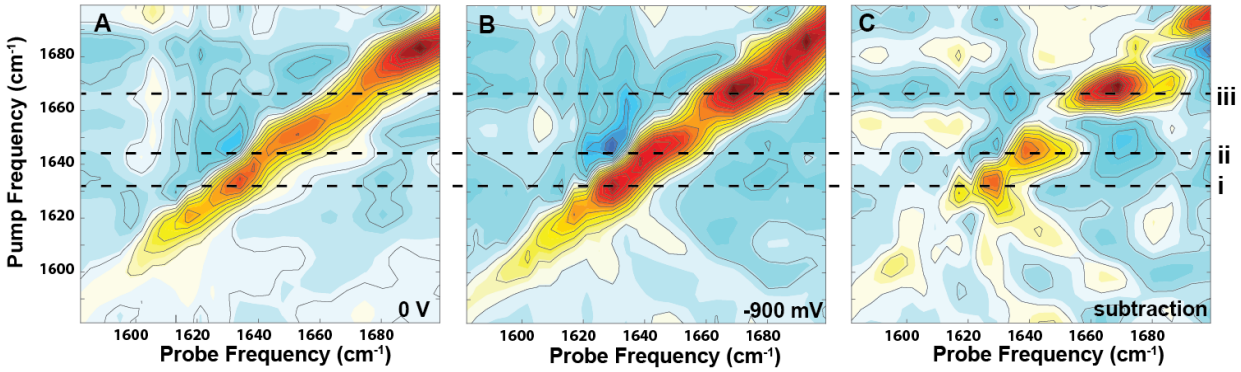

Figure 3.4 Spectra of the voltage-dependence of alamethicin. A) Alamethicin in a bilayer on 10 nm Au surface with 0 V applied B) alamethicin in a bilayer on 10 nm Au with -900 mV applied C) Difference spectrum of alamethicin at -900 mV and 0 mV. Real peaks corresponding to pH spectral peaks indicated with dashed lines i-iii, corresponding to those peaks in Fig. 3.2.

Shown in Fig. 3.4 are spectra of alamethicin on 10-nm gold with (A) no potential, (B) -900 mV potential difference, and (C) a difference spectrum of A subtracted from B. In (A) and (B), a background signal is observed along the diagonal that was not present in the samples prepared for the pH studies. “Potential difference” refers to the voltage set on the power meter. In addition to changing the conductivity, the gold thickness also shifts the resonant plasmon frequency to longer wavelengths (Fig. 3.9), which we attribute to the presence of the background. The background signal partially obscures the expected molecular features, but is reduced by approximately 90% in the difference spectrum of Fig. 3.4C as determined by the subtraction of the control sample seen in Fig. 3.8. Though the distance between the electrodes is 50 μM, the double layer thickness should be sufficient to create a potential across the bilayer because the bilayer is tethered to the gold. Previous Stark shift and SEIRA experiments have been able to generate a potential in this manner.[34,43–45] In Fig. 3.4C three diagonal peaks are observed at 1630, 1640, and 1660 cm^{-1} that correspond to the same peaks i, ii, and iii in the pH

spectra of Fig. 4.2. The relative intensities in the difference spectrum are 0.5:0.5:1, for i:ii:iii, respectively.

3.4 Discussion

As outlined above, previous work has found that the alamethicin membrane-bound structure is similar at pH 12 as it is under a potential difference.[27] Thus, we subtracted the pH 6.8 (Fig. 3.2A) from the pH 12 spectrum (Fig. 3.2B), to create a difference spectrum (Fig. 3.2C) for comparison to the difference voltage spectrum (Fig. 3.4C). Relative intensities of the pH spectra were adjusted for best agreement to Fig. 3.4C. The pH difference spectrum contains the same three peaks as the voltage difference spectrum with similar relative intensities. We note that in both the pH and the voltage subtraction spectra (Fig. 3.2C and Fig. 3.4C respectively, the overtone intensities are diminished due to destructive cancellation upon subtraction further validating the subtraction. Thus, we conclude that the structure adopted by alamethicin under a potential difference is similar to that at pH 12, in agreement with prior studies.[27,28]

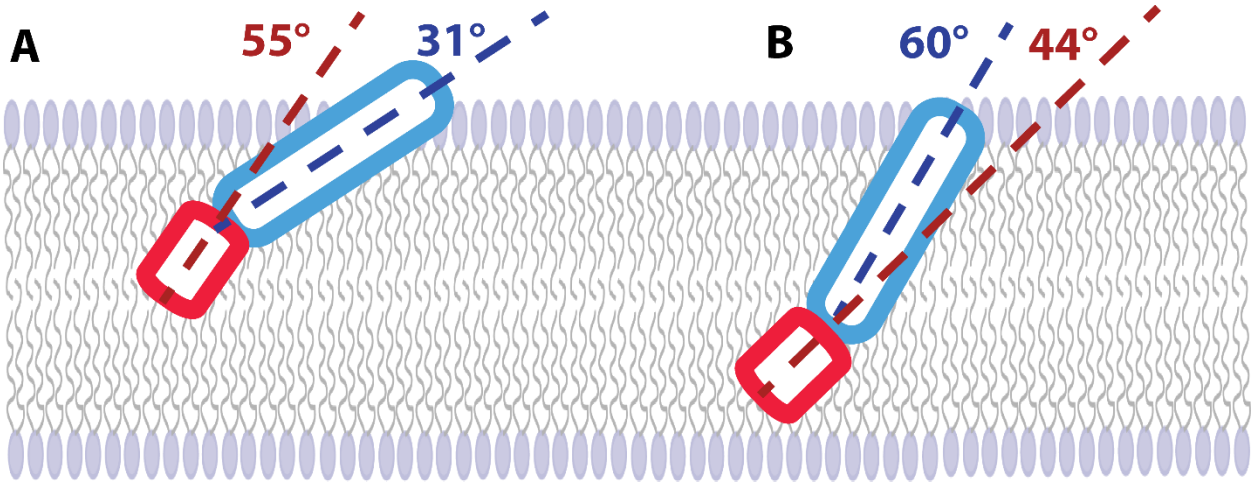

Figure 3.5 Graphical depiction of alamethicin corresponding to the tilt angles at A) 0 volts, and B) -900 mV applied. Red represents the 310-helix segment and blue represents the α-helical segment. Angles are defined in relation to the plane of the membrane.

Shown in Fig. 3.5 is an illustration of the change in structure that is consistent with the data presented here. We see no evidence in the spectra that there is a significant change in secondary structure because the peak frequencies and linewidths are unchanged when the potential is modulated (and at pH 12). A reduction in α-helix length, for example, would shift its frequency higher.[15] Instead, the data is consistent with a change in the tilt of the helices that alter the peak intensities, as the simulations in Fig. 3.3 show.[24,46,47] We estimate that tilt of the 3_{10}- helix decreases by 10° and the α-helix tilt increases by 29°.

The relative angle of 16° and 24° between the α- and 3_{10}- helices before and during insertion is consistent with previous molecular dynamics simulations,[46,47] which found the kink angle to be 24° ± 8°.[46] Indeed, those simulations found little change in the kink angle before and after insertion, also in agreement with our work. However, the simulations put the insertion angle, which is defined as the angle between the membrane plane and the line joining the centers of the first and last seven α-carbons of a helix[47] for alamethicin at 70° to 90°, which is much larger than the steepest angle (60°) in our experiments. Those simulations may not have converged to the equilibrated molecular structure because the angle of alamethicin in the membrane was still decreasing at the end of the 100 ns trajectories. The insertion angles do not appear consistent with the barrel stave model proposed previously for alamethicin, although these experiments do not explicitly test the bundle structure. To investigate the structure of the bundle, isotope labeling experiments looking at residue-specific couplings and 2D line shapes would be necessary.[42,48,49]

We also simulated spectra that included couplings between the 3_{10}- and α-helices in order to explore the origins of the cross peaks. To do so, 10 cm^{-1} couplings were added between the top 4 residues of the 3_{10}-helix and the bottom 4 residues of the α-helix. 10 cm^{-1} is consistent with

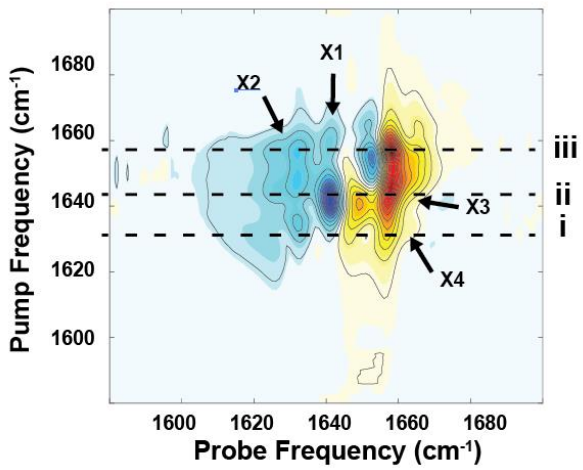

Figure 3.6 Calculated 2D IR spectrum of Alamethicin including 10 cm^{-1} coupling between the α- and 3_{10}-helices. Cross peaks are labeled X1-X4 as in Fig. 2B. Peak centers are labelled as i-iii and are consistent with the peak frequencies in experiment.

couplings between helix turns in helices. The Hamiltonian is found in section 4.7. The resulting spectrum (Fig. 4.6) contain cross peaks between the *A* mode of the α-helix and the *A* and *E* modes of the 3_{10}-helix, generating the experimental peaks X1-X3. The simulations also resolve a peak that we label X4, which correlates the *E* mode of the 3_{10}-helix to the *A* mode of the α-helix, analogous to peak X2 on the opposite side of the diagonal. Presumably, the structure of the polypeptide as it transitions from the 3_{10}- to the α-helix is complicated, with a kink and structural flexibility,[47] which would give rise to a distribution of couplings as well as disorder in the Hamiltonian. Thus, these simulations confirm our spectral assignment based on the frequencies of the cross peaks, but should be considered illustrative. 2D IR spectra can now be calculated from molecular dynamics simulations quite accurately and used to test atomic structures.[15,50,51] It is now also established that vibrational energy transfers over large distances, which might also contribute to the cross-peak intensities. Future studies might simulate 2D IR spectra from voltage-applied molecular dynamics simulations.

3.5 Conclusions

The experiments reported here demonstrate 2D IR spectroscopy applied to a membrane bound polypeptide under a potential difference. They build upon previous work using SEIRA to study voltage dependence of membrane proteins,[5,34,52–54] while providing additional information through couplings, 2D line shapes, and other observables intrinsic to multidimensional

spectroscopy. The signal enhancement that results from mid-IR plasmonics makes it possible to measure 2D IR spectra of a single bilayer, which in turn enables the application of an external voltage. It should be possible to generate fields with other plasmonic surfaces, such as islands, that might reduce the background.[55] Further work is also needed to characterize the magnitude of the potential difference; -900 mV is most certainly not the potential at the bilayer because the bilayers we created have imperfections that conduct and thereby decrease the local potential. Nonetheless, for alamethicin, we find that the potential difference causes the polypeptide tilt to increase in the bilayer but does not measurably change the relative populations or lengths of the 3_{10}- and α-helices. We suspect that the potential difference induces structural changes which occur at the transition between the 3_{10}- and α-helix that are not detected in our experiments, but they do create cross peaks in the spectra, as confirmed by simulations. More detailed structural information might be obtained with isotope labeled peptides to spectroscopically identify those residues.[56] As mentioned above, it is now relatively straightforward to accurately compute 2D IR spectra from molecular dynamics trajectories and thereby test atomic structures against experiment. That approach has been applied to membrane proteins.[50,51,57–59] Molecular dynamics simulations can also be used to study structures of membrane proteins under an applied potential. The methodology and 2D IR experiments detailed in this publication are early steps towards structural and dynamical studies of voltage gated membrane proteins.

3.6 References

(1) Hekstra, D. R.; White, K. I.; Socolich, M. A.; Henning, R. W.; Šrajer, V.; Ranganathan, R. Electric-Field-Stimulated Protein Mechanics. Nature 2016, 540 (7633), 400–405.

(2) Sonnleitner, A.; Mannuzzu, L. M.; Terakawa, S.; Isacoff, E. Y. Structural Rearrangements in Single Ion Channels Detected Optically in Living Cells. Proc. Natl. Acad. Sci. 2002, 99 (20), 12759–12764.

(3) Harms, G. S.; Orr, G.; Montal, M.; Thrall, B. D.; Colson, S. D.; Lu, H. P. Probing Conformational Changes of Gramicidin Ion Channels by Single-Molecule Patch-Clamp Fluorescence Microscopy. Biophys. J. 2003, 85 (3), 1826–1838.

(4) Enders, D.; Nagao, T.; Pucci, A.; Nakayama, T.; Aono, M. Surface-Enhanced ATR-IR Spectroscopy with Interface-Grown Plasmonic Gold-Island Films near the Percolation Threshold. Phys. Chem. Chem. Phys. 2011, 13 (11), 4935–4941.

(5) Kozuch, J.; Weichbrodt, C.; Millo, D.; Giller, K.; Becker, S.; Hildebrandt, P.; Steinem, C. Voltage-Dependent Structural Changes of the Membrane-Bound Anion Channel HVDAC1 Probed by SEIRA and Electrochemical Impedance Spectroscopy. Phys. Chem. Chem. Phys. 2014, 16 (20), 9546–9555.

(6) Kraack, J. P.; Kaech, A.; Hamm, P. Surface Enhancement in Ultrafast 2D ATR IR Spectroscopy at the Metal-Liquid Interface. J. Phys. Chem. C 2016, 120 (6), 3350–3359.

(7) Lotti, D.; Hamm, P.; Kraack, J. P. Surface-Sensitive Spectro-Electrochemistry Using Ultrafast 2D ATR IR Spectroscopy. J. Phys. Chem. C 2016, 120 (5), 2883–2892.

(8) Mackin, R. T.; Cohn, B.; Gandman, A.; Leger, J. D.; Chuntonov, L.; Rubtsov, I. V. Surface-Enhanced Dual-Frequency Two-Dimensional Vibrational Spectroscopy of Thin Layers at an Interface. J. Phys. Chem. C 2018, 122 (20), 11015–11023.

(9) Rodrigo, D.; Tittl, A.; Ait-Bouziad, N.; John-Herpin, A.; Limaj, O.; Kelly, C.; Yoo, D.; Wittenberg, N. J.; Oh, S.-H.; Lashuel, H. A.; et al. Resolving Molecule-Specific Information in Dynamic Lipid Membrane Processes with Multi-Resonant Infrared Metasurfaces. Nat. Commun. 2018, 9 (1), 2160.

(10) Selig, O.; Siffels, R.; Rezus, Y. L. A. Ultrasensitive Ultrafast Vibrational Spectroscopy Employing the Near Field of Gold Nanoantennas. Phys. Rev. Lett. 2015, 114 (23), 233004.

(11) Rezus, Y. L. A.; Selig, O. Impact of Local-Field Effects on the Plasmonic Enhancement of Vibrational Signals by Infrared Nanoantennas. Opt. Express 2016, 24 (11), 12202.

(12) Petti, M. K.; Ostrander, J. S.; Saraswat, V.; Birdsall, E. R.; Rich, K. L.; Lomont, J. P.; Arnold, M. S.; Zanni, M. T. Enhancing the Signal Strength of Surface Sensitive 2D IR Spectroscopy. J. Chem. Phys. 2019, 150 (2).

(13) Ostrander, J. S.; Lomont, J. P.; Rich, K. L.; Saraswat, V.; Feingold, B. R.; Petti, M. K.; Birdsall, E. R.; Arnold, M. S.; Zanni, M. T. Monolayer Sensitivity Enables a 2D IR Spectroscopic Immuno-Biosensor for Studying Protein Structures: Application to Amyloid Polymorphs. J. Phys. Chem. Lett. 2019, 10 (14).

(14) Lotti, D.; Hamm, P.; Kraack, J. P. Surface-Sensitive Spectro-Electrochemistry Using Ultrafast 2D ATR IR Spectroscopy. J. Phys. Chem. C 2016, 120 (5), 2883–2892.

(15) Hamm, P.; Zanni, M. Concepts and Methods of 2D Infrared Spectroscopy; 2011; Vol. 9781107000.

(16) Fox, R. O.; Richards, F. M. A Voltage-Gated Ion Channel Model Inferred from the Crystal Structure of Alamethicin at 1.5-Å Resolution. Nature 1982, 300 (5890), 325–330.

(17) Bechinger, B. Structure and Functions of Channel-Forming Peptides: Magainins, Cecropins, Melittin and Alamethicin. Journal of Membrane Biology. 1997, pp 197–211.

(18) Gibbs, N.; Sessions, R. B.; Williams, P. B.; Dempsey, C. E. Helix Bending in Alamethicin: Molecular Dynamics Simulations and Amide Hydrogen Exchange in Methanol. Biophys. J. 1997.

(19) Perrin, B. S.; Pastor, R. W. Simulations of Membrane-Disrupting Peptides I: Alamethicin Pore Stability and Spontaneous Insertion. 2016.

(20) Perrin, B. S.; Pastor, R. W. Simulations of Membrane-Disrupting Peptides I: Alamethicin Pore Stability and Spontaneous Insertion. Biophys. J. 2016.

(21) Sharma, V. K.; Mamontov, E.; Tyagi, M.; Qian, S.; Rai, D. K.; Urban, V. S. Dynamical and Phase Behavior of a Phospholipid Membrane Altered by an Antimicrobial Peptide at Low Concentration. J. Phys. Chem. Lett. 2016, 7 (13), 2394–2401.

(22) Leitgeb, B.; Szekeres, A.; Manczinger, L.; Vágvölgyi, C.; Kredics, L. The History of Alamethicin: A Review of the Most Extensively Studied Peptaibol. Chem. Biodivers. 2007, 4 (6), 1027–1051.

(23) North, C. L.; Franklin, J. C.; Bryant, R. G.; Cafiso, D. S. Molecular Flexibility Demonstrated by Paramagnetic Enhancements of Nuclear Relaxation. Application to Alamethicin: A Voltage-Gated Peptide Channel. Biophys. J. 1994.

(24) Tieleman, D. P.; Sansom, M. S.; Berendsen, H. J. Alamethicin Helices in a Bilayer and in Solution: Molecular Dynamics Simulations. Biophys. J. 1999, 76 (1 Pt 1), 40–49.

(25) North, C. L.; Barranger-Mathys, M.; Cafiso, D. S. Membrane Orientation of the N-Terminal Segment of Alamethicin Determined by Solid-State 15N NMR. Biophys. J. 1995.

(26) Nagao, T.; Mishima, D.; Javkhlantugs, N.; Wang, J.; Ishioka, D.; Yokota, K.; Norisada, K.; Kawamura, I.; Ueda, K.; Naito, A. Structure and Orientation of Antibiotic Peptide Alamethicin in Phospholipid Bilayers as Revealed by Chemical Shift Oscillation Analysis of Solid State Nuclear Magnetic Resonance and Molecular Dynamics Simulation. Biochim. Biophys. Acta - Biomembr. 2015, 1848 (11), 2789–2798.

(27) Yang, P.; Wu, F.-G.; Chen, Z. Dependence of Alamethicin Membrane Orientation on the Solution Concentration. J. Phys. Chem. C 2013, 117 (7), 3358–3365.

(28) Ye, S.; Li, H.; Wei, F.; Jasensky, J.; Boughton, A. P.; Yang, P.; Chen, Z. Observing a Model Ion Channel Gating Action in Model Cell Membranes in Real Time in Situ: Membrane Potential Change Induced Alamethicin Orientation Change. J. Am. Chem. Soc. 2012, 134 (14), 6237–6243.

(29) Yang, P.; Wu, F.-G.; Chen, Z. Lipid Fluid–Gel Phase Transition Induced Alamethicin Orientational Change Probed by Sum Frequency Generation Vibrational Spectroscopy. J. Phys. Chem. C 2013, 117 (33), 17039–17049.

(30) Su, Z.; Shodiev, M.; Leitch, J. J.; Abbasi, F.; Lipkowski, J. Role of Transmembrane Potential and Defects on the Permeabilization of Lipid Bilayers by Alamethicin, an Ion-Channel-Forming Peptide. Langmuir 2018, 34 (21), 6249–6260.

(31) Su, Z. F.; Shodiev, M.; Jay Leitch, J.; Abbasi, F.; Lipkowski, J. In Situ Electrochemical and PM-IRRAS Studies of Alamethicin Ion Channel Formation in Model Phospholipid Bilayers. J. Electroanal. Chem. 2018, 819, 251–259.

(32) Peter Tieleman, D.; Hess, B.; Sansom, M. S. P. Analysis and Evaluation of Channel Models: Simulations of Alamethicin. Biophys. J. 2002, 83 (5), 2393–2407.

(33) Zeilinger, S. Peptaibiotics and Peptaibols from Fungi. In Fungal Biomolecules; John Wiley & Sons, Ltd: Chichester, UK, 2015; pp 101–113.

(34) Forbrig, E.; Staffa, J. K.; Salewski, J.; Mroginski, M. A.; Hildebrandt, P.; Kozuch, J. Monitoring the Orientational Changes of Alamethicin during Incorporation into Bilayer Lipid Membranes. Langmuir 2018, 34 (6), 2373–2385.

(35) Su, Z. F.; Shodiev, M.; Jay Leitch, J.; Abbasi, F.; Lipkowski, J. In Situ Electrochemical and PM-IRRAS Studies of Alamethicin Ion Channel Formation in Model Phospholipid Bilayers. J. Electroanal. Chem. 2017, No. July.

(36) Mizuguchi, T.; Matubayasi, N. Free-Energy Analysis of Peptide Binding in Lipid Membrane Using All-Atom Molecular Dynamics Simulation Combined with Theory of Solutions. J. Phys. Chem. B 2018, 122 (13), 3219–3229.

(37) Adato, R.; Altug, H. In-Situ Ultra-Sensitive Infrared Absorption Spectroscopy of Biomolecule Interactions in Real Time with Plasmonic Nanoantennas. Nat. Commun. 2013, 4 (1), 2154.

(38) Londergan, C. H.; Wang, J.; Axelsen, P. H.; Hochstrasser, R. M. Two-Dimensional Infrared Spectroscopy Displays Signatures of Structural Ordering in Peptide Aggregates. Biophys. J. 2006, 90 (12), 4672–4685.

(39) Mukherjee, P.; Kass, I.; Arkin, I. T.; Zanni, M. T. Structural Disorder of the CD3ζ Transmembrane Domain Studied with 2D IR Spectroscopy and Molecular Dynamics Simulations. J. Phys. Chem. B 2006, 110 (48), 24740–24749.

(40) Ho, J.-J.; Zanni, M. T. COSMOSS https://zanni.chem.wisc.edu/software/.

(41) Wang, J.; Hochstrasser, R. M. Characteristics of the Two-Dimensional Infrared Spectroscopy of Helices from Approximate Simulations and Analytic Models. Chem. Phys. 2004, 297 (1–3), 195–219.

(42) Mukherjee, P.; Kass, I.; Arkin, I.; Zanni, M. T. Picosecond Dynamics of a Membrane Protein Revealed by 2D IR. PNAS March 2006, 7 (10), 3528–3533.

(43) Sorenson, S. A.; Patrow, J. G.; Dawlaty, J. M. Solvation Reaction Field at the Interface Measured by Vibrational Sum Frequency Generation Spectroscopy. J. Am. Chem. Soc. 2017, 139 (6), 2369–2378.

(44) Patrow, J. G.; Sorenson, S. A.; Dawlaty, J. M. Direct Spectroscopic Measurement of Interfacial Electric Fields near an Electrode under Polarizing or Current-Carrying Conditions. J. Phys. Chem. C 2017, 121 (21), 11585–11592.

(45) Oklejas, V.; Sjostrom, C.; Harris, J. M. SERS Detection of the Vibrational Stark Effect from Nitrile-Terminated SAMs to Probe Electric Fields in the Diffuse Double-Layer. J. Am. Chem. Soc. 2002, 124 (11), 2408–2409.

(46) Biggin, P. C.; Breed, J.; Son, H. S.; Sansom, M. S. P. Simulation Studies of Alamethicin-Bilayer Interactions. Biophys. J. 1997, 72 (2), 627–636.

(47) Tieleman, D. P.; Berendsen, H. J. C.; Sansom, M. S. P. Voltage-Dependent Insertion of Alamethicin at Phospholipid/Water and Octane/Water Interfaces. Biophys. J. 2001, 80 (1), 331–346.

(48) Manor, J.; Mukherjee, P.; Lin, Y.-S.; Leonov, H.; Skinner, J. L.; Zanni, M. T.; Arkin, I. T. Gating Mechanism of the Influenza A M2 Channel Revealed by 1D and 2D IR Spectroscopies. Structure 2009, 17 (2), 247–254.

(49) Remorino, A.; Korendovych, I. V.; Wu, Y.; DeGrado, W. F.; Hochstrasser, R. M. Residue-Specific Vibrational Echoes Yield 3D Structures of a Transmembrane Helix Dimer. Science (80-.). 2011, 332 (6034), 1206–1209.

(50) Reppert, M.; Tokmakoff, A. Computational Amide I 2D IR Spectroscopy as a Probe of Protein Structure and Dynamics. Annu. Rev. Phys. Chem. 2016, 67 (1), 359–386.

(51) Kratochvil, H. T.; Carr, J. K.; Matulef, K.; Annen, A. W.; Li, H.; Maj, M.; Ostmeyer, J.; Serrano, A. L.; Raghuraman, H.; Moran, S. D.; et al. Instantaneous Ion Configurations in the K+ Ion Channel Selectivity Filter Revealed by 2D IR Spectroscopy. Science 2016, 353 (6303), 1040–1044.

(52) Jiang, X.; Zaitseva, E.; Schmidt, M.; Siebert, F.; Engelhard, M.; Schlesinger, R.; Ataka, K.; Vogel, R.; Heberle, J. Resolving Voltage-Dependent Structural Changes of a Membrane Photoreceptor by Surface-Enhanced IR Difference Spectroscopy; 2008.

(53) Kycia, A. H.; Su, Z.; Brosseau, C. L.; Lipkowski, J. In Situ PM-IRRAS Studies of Biomimetic Membranes Supported at Gold Electrode Surfaces. In Vibrational Spectroscopy at Electrified Interfaces; John Wiley & Sons, Inc.: Hoboken, NJ, USA, 2013; pp 345–417.

(54) Brand, I. Application of Polarization Modulation Infrared Reflection Absorption Spectroscopy in Electrochemistry; Monographs in Electrochemistry; Springer International Publishing: Cham, 2020.

(55) Chuntonov, L.; Rubtsov, I. V. Surface-Enhanced Ultrafast Two-Dimensional Vibrational Spectroscopy with Engineered Plasmonic Nano-Antennas. J. Chem. Phys. 2020, 153 (5), 050902.

(56) Middleton, C. T.; Woys, A. M.; Mukherjee, S. S.; Zanni, M. T. Residue-Specific Structural Kinetics of Proteins through the Union of Isotope Labeling, Mid-IR Pulse Shaping, and Coherent 2D IR Spectroscopy. Methods 2010, 52 (1), 12–22.

(57) Baiz, C. R.; Lin, Y.-S.; Peng, C. S.; Beauchamp, K. A.; Voelz, V. A.; Pande, V. S.; Tokmakoff, A. A Molecular Interpretation of 2D IR Protein Folding Experiments with Markov State Models. Biophys. J. 2014, 106 (6), 1359–1370.

(58) Smith, A. W.; Lessing, J.; Ganim, Z.; Peng, C. S.; Tokmakoff, A.; Roy, S.; Jansen, T. L. C.; Knoester, J. Melting of a β-Hairpin Peptide Using Isotope-Edited 2D IR Spectroscopy and Simulations. J. Phys. Chem. B 2010, 114 (34), 10913–10924.

(59) Wang, L.; Middleton, C. T.; Zanni, M. T.; Skinner, J. L. Development and Validation of Transferable Amide i Vibrational Frequency Maps for Peptides. J. Phys. Chem. B 2011, 115 (13), 3713–3724.

3.7 Supplemental Information

3.7.1 Supplemental Figures

Shown in Figure 3.7 are control spectra of the lipids on 3-nm Au on a CaF_2 window. The leftmost spectrum shows the just thiolipid, 1,2-Dipalmitoyl-sn-Glycero-3-Phosphothioethanol, while the center is the completed bilayer with both thiolipid and 1-palmitoyl-2-oleoyl-glycero-3-phosphocholine. The absorptions are consistent with the ester carbonyl stretch in the lipid.[1] The rightmost spectrum zooms out on the spectrum to show the lipid absorption as well as the amide

I region (1620 cm^{-1}-1660 cm^{-1}) where no peaks are seen, ensuring there is no lipid background in the region of interest.

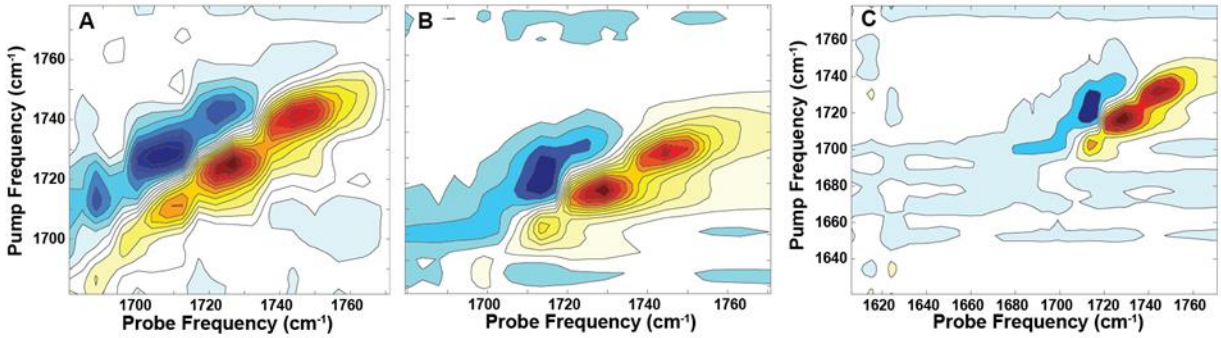

Figure 3.7 2D IR spectra of A) thiolipid tethered monolayer on 3-nm Au, B) thiolipid and POPC tethered bilayer on 3-nm Au, and C) thiolipid and POPC tethered bilayer with larger range showing lack of signal in the Amide I region.

Figure 3.8 shows control spectra for 10-nm Au. In 3.8A there is no applied voltage. In 3.8B there are -900 mV applied. In both, the diagonal 'stripe' is evident. When subtracted in Figure 3.8C, there are no obvious molecular signals, and the peak maximum on the diagonal of 3.8C is less than 10% of the maximum of 3.8A and 3.8B.

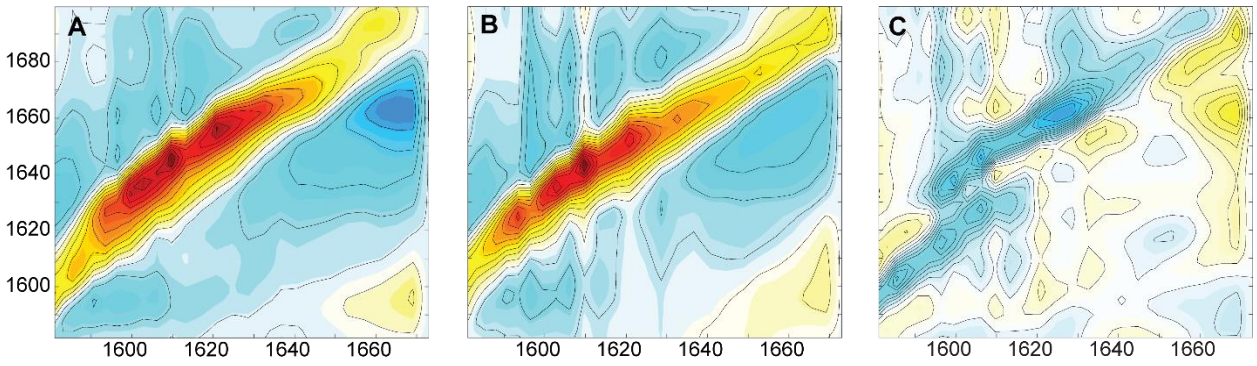

Figure 3.8 2D IR spectra of 10-nm Au on CaF2 in KCl/D2O buffer with A) 0 V applied, B) -900 mV applied, and C) a difference spectrum of B minus A. All are plotted on the same scale and the differences on the diagonal account for less than 10% of the maximum intensity

Figure 3.9 shows the visible/near IR absorbance spectra of 3-nm Au (blue) and 10-nm (red) on CaF_2 windows. Here there is an evident red shift of the thicker gold.

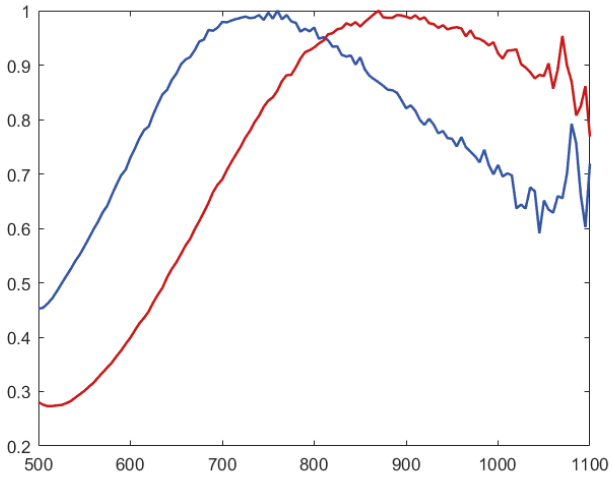

Figure 3.9 UV-vis spectra of 3-nm Au (blue) and 10-nm Au (red) thermally evaporated on 10-mm CaF2 windows.

3.7.2 Methods

Alamethicin derived from *Trichoderma viride* purchased from Sigma-Aldrich was diluted to a concentration of 2 mg/mL in methanol for storage purposes. Lipids, 1-palmitoyl-2-oleoyl-glycero-3-phosphocholine (POPC) and 1,2-Dipalmitoyl-sn-Glycero-3-Phosphothioethanol (DPTE) both at a concentration of 10 mg/mL in chloroform were purchased from Avanti Polar Lipids Inc. Calcium fluoride (CaF_2) windows (25 mm x 2 mm) were purchased from Crystran.

Gold films (Au% > 99.99%) were deposited via thermal evaporation to a thickness of 3 nm at the rate of 0.1 Å/s at a pressure of 8 x 10^{-7} torr onto the CaF_2 window. Conductivity was quantified by measuring the resistance across 1 cm of the gold-coated window. The 3-nm gold window had a resistance that was too high to measure while the 10-nm gold window had a resistance of 35 Ω.

Bilayer formation was adapted from Lipkowski and colleagues.[94] A 100-μL aliquot of DPTE in chloroform (10 mg/mL) and 250-μL aliquot of POPC in chloroform (10 mg/mL) were dried down under N_2 and lyophilized overnight to remove remaining solvent. DPTE was rehydrated in 10 mL of spectroscopic-grade ethanol. The coated window was then submerged in the DPTE/ethanol solution overnight. The window was then rinsed with ethanol and allowed to dry. POPC vesicles were prepared by rehydrating the POPC in 100 mM NaCl buffer and applying five freeze-thaw cycles in an isopropanol and dry ice bath and lukewarm water bath (40-50 °C) respectively. The solution was then placed in a bath sonicator for 10 minutes to create approximately 50-nm diameter vesicles. Window was then submerged in the POPC vesicle solution overnight to allow for vesicle rupture and bilayer creation. The window was then washed three times with deionized water. Alamethicin was prepared by diluting 5.2 μL of the 2 mg/mL alamethicin/methanol stock solution in 50 μL of deionized water. This was then distributed over half of the lipid-coated CaF_2 window. Assuming total surface coverage of lipid, this yields a 20:1 lipid:peptide ratio. The window was dried under N_2 and then rehydrated with D_2O or phosphate buffer (pH 6.8, 12) in D_2O and a second window was added separated with a 56-μm spacer.

The sample was held in a custom, 3D-printed plastic sample cell. Each CaF_2 window (one gold-coated and one bare) was connected to the circuit using conductive aluminum tape (Electron Microscopy Science Inc.) and was used as previously described by Hamm and coworkers.[95] Briefly, the tape was applied directly to the gold substrate, and the resistance was measured again and found to be equal as to the 35 Ω as before the tape was applied. The tape was applied such that it was on the edge of the window and not in contact with the buffer. The gold coated

window was attached to the positive lead and the bare window was attached to the negative lead of a potentiometer. The voltage was then applied (0V or -900 mV).

2D IR data acquisition: A Coherent Libra regenerative amplifier centered at 800 nm (3.4 W, 50 fs) pump an optical parametric amplifier (OPA) (Light Conversion TOPAS). The output signal and idler pulses are then mixed in a $AgGaS_2$ difference frequency generation (DFG) crystal to generate the mid-IR light centered at 6 μm with pulses of <100 fs with energies around 18 μJ. The mid-IR is then split with a 90/10 CaF_2 beam splitter into the pump and probe lines. The pump line is directed through an acousto-optical modulator (AOM) which shapes the pulses as previously described. The polarization (s- or p-) of both the pump and probe lines are modulated by successive half-wave plates and polarizers. A 7.5-cm focal length parabolic mirror is used to focus the spatially and temporally overlapped pulses at the sample. Due to the pump-probe geometry used, the probe/signal beam is then directed into a monochromator to be dispersed onto a 32-pixel MCT array.

2D IR simulation:

2D IR spectra were simulated using the COSMOSS app in MatLAB.[84] For this use, the PDB file of alamethicin (1AMT)[96] was uploaded to the app. coupling values for the 3_{10}-helix were: 0.9 cm^{-1} for nearest neighbor $\beta_{i,i+1}$, -2.5 cm^{-1} for $\beta_{i,i+2}$, -2.8 cm^{-1} for $\beta_{i,i+3}$, -0.8 cm^{-1} for $\beta_{i,i+4}$, and neglected for more distant residues. The coupling values for the α-helix were: 8 cm^{-1} for $\beta_{i,i+1}$, -2 cm^{-1} for $\beta_{i,i+2}$, -6 cm^{-1} for $\beta_{i,i+3}$, -1 cm^{-1} for $\beta_{i,i+4}$, -0.5 cm^{-1} for $\beta_{i,i+5}$and neglected for further residues.[8] These are the ideal values calculated for these helices.[97] The resulting FTIR and 2D IR spectra were generated as previously described.

The coupling matrix was created in a similar way, but adding in 10 cm^{-1} coupling values between the two halves of the helix. The one-exiton Hamiltonian is shown in Eq. 1 to show the $\beta_{i,i+n}$ couplings:

$$H = \begin{pmatrix}
0 & 0 & 0 & 0 & 0 & 0 & 0 & 0 & 0 & 0 & 0 & 0 & 0 & 0 & 0 & 0 & 0 & 0 & 0 & 0 \\
0 & 1650 & 8 & -2 & -6 & -1 & -0.5 & 0 & 0 & 0 & 0 & 0 & 0 & 0 & 0 & 0 & 0 & 0 & 0 & 0 \\
0 & 8 & 1650 & 8 & -2 & -6 & -1 & -0.5 & 0 & 0 & 0 & 0 & 0 & 0 & 0 & 0 & 0 & 0 & 0 & 0 \\
0 & -2 & 8 & 1650 & 8 & -2 & -6 & -1 & -0.5 & 0 & 0 & 0 & 0 & 0 & 0 & 0 & 0 & 0 & 0 & 0 \\
0 & -6 & -2 & 8 & 1650 & 8 & -2 & -6 & -1 & -0.5 & 0 & 0 & 0 & 0 & 0 & 0 & 0 & 0 & 0 & 0 \\
0 & -1 & -6 & -2 & 8 & 1650 & 8 & -2 & -6 & -1 & -0.5 & 0 & 0 & 0 & 0 & 0 & 0 & 0 & 10 & 0 \\
0 & -0.5 & -1 & -6 & -2 & 8 & 1650 & 8 & -2 & -6 & -1 & -0.5 & 0 & 0 & 0 & 0 & 0 & 10 & 0 & 0 \\
0 & 0 & -0.5 & -1 & -6 & -2 & 8 & 1650 & 8 & -2 & -6 & -1 & -0.5 & 0 & 0 & 0 & 10 & 0 & 0 & 0 \\
0 & 0 & 0 & -0.5 & -1 & -6 & -2 & 8 & 1650 & 8 & -2 & -6 & -1 & -0.5 & 0 & 10 & 0 & 0 & 0 & 0 \\
0 & 0 & 0 & 0 & -0.5 & -1 & -6 & -2 & 8 & 1650 & 8 & -2 & -6 & -1 & 10 & 0 & 0 & 0 & 0 & 0 \\
0 & 0 & 0 & 0 & 0 & -0.5 & -1 & -6 & -2 & 8 & 1650 & 8 & -2 & -6 & 0 & 0 & 0 & 0 & 0 & 0 \\
0 & 0 & 0 & 0 & 0 & 0 & -0.5 & -1 & -6 & -2 & 8 & 1650 & 8 & -2 & 0 & 0 & 0 & 0 & 0 & 0 \\
0 & 0 & 0 & 0 & 0 & 0 & 0 & -0.5 & -1 & -6 & -2 & 8 & 1650 & 8 & 0 & 0 & 0 & 0 & 0 & 0 \\
0 & 0 & 0 & 0 & 0 & 0 & 0 & 0 & -0.5 & -1 & -6 & -2 & 8 & 1650 & 0 & 0 & 0 & 0 & 0 & 0 \\
0 & 0 & 0 & 0 & 0 & 0 & 0 & 0 & 0 & 10 & 0 & 0 & 0 & 0 & 1650 & 0 & 0 & 0 & 0 & 0 \\
0 & 0 & 0 & 0 & 0 & 0 & 0 & 0 & 10 & 0 & 0 & 0 & 0 & 0 & 0 & 1650 & 0.9 & -2.5 & -2.8 & -0.8 \\
0 & 0 & 0 & 0 & 0 & 0 & 0 & 10 & 0 & 0 & 0 & 0 & 0 & 0 & 0 & 0.9 & 1650 & 0.9 & -2.5 & -2.8 \\
0 & 0 & 0 & 0 & 0 & 0 & 10 & 0 & 0 & 0 & 0 & 0 & 0 & 0 & 0 & -2.5 & 0.9 & 1650 & 0.9 & -2.5 \\
0 & 0 & 0 & 0 & 0 & 10 & 0 & 0 & 0 & 0 & 0 & 0 & 0 & 0 & 0 & -2.8 & -2.5 & 0.9 & 1650 & 0.9 \\
0 & 0 & 0 & 0 & 0 & 0 & 0 & 0 & 0 & 0 & 0 & 0 & 0 & 0 & 0 & -0.8 & -2.8 & -2.5 & 0.9 & 1650
\end{pmatrix} \quad (3.1)$$

For the angular dependence spectra, the 3_{10}-helix and α-helix were modeled separately and the resulting spectra were summed together. For the coupling spectrum, a single spectrum was generated from 1AMT and residues 1-13 were given the α-helical coupling values and 15-19 were given the 3_{10}-helical coupling values, within the respective segments of the helix. Coupling between the two segments were generated by assigning a value of 10 cm^{-1} between the first 4 residues of the α-helical segment and the last 4 residues of the 3_{10}-helical segment.

3.7.3 References

(1) Rodrigo, D.; Tittl, A.; Ait-Bouziad, N.; John-Herpin, A.; Limaj, O.; Kelly, C.; Yoo, D.; Wittenberg, N. J.; Oh, S.-H.; Lashuel, H. A.; et al. Resolving Molecule-Specific Information in Dynamic Lipid Membrane Processes with Multi-Resonant Infrared Metasurfaces. *Nat. Commun.* **2018**, *9* (1), 2160.

(2) Su, Z. F.; Shodiev, M.; Jay Leitch, J.; Abbasi, F.; Lipkowski, J. In Situ Electrochemical and PM-IRRAS Studies of Alamethicin Ion Channel Formation in Model Phospholipid Bilayers. *J. Electroanal. Chem.* **2018**, *819*, 251–259.

(3) Lotti, D.; Hamm, P.; Kraack, J. P. Surface-Sensitive Spectro-Electrochemistry Using Ultrafast 2D ATR IR Spectroscopy. *J. Phys. Chem. C* **2016**, *120* (5), 2883–2892.

(4) Ho, J.-J.; Zanni, M. T. COSMOSS https://zanni.chem.wisc.edu/software/.

(5) Fox, R. O.; Richards, F. M. A Voltage-Gated Ion Channel Model Inferred from the Crystal Structure of Alamethicin at 1.5-Å Resolution. *Nature* **1982**, *300* (5890), 325–330.

(6) Hamm, P.; Zanni, M. *Concepts and Methods of 2D Infrared Spectroscopy*; 2011; Vol. 9781107000.

(7) Wang, J.; Hochstrasser, R. M. Characteristics of the Two-Dimensional Infrared Spectroscopy of Helices from Approximate Simulations and Analytic Models. *Chem. Phys.* **2004**, *297* (1–3), 195–219.

4 Ester labels in Potassium Channels

In this chapter, I present work in progress towards measuring a backbone ester in the selectivity filter of two different potassium channels, KcsA and NaK2K. The experimental precedents developed for esters are reported, first developed for an ester-labeled side chain of an amino acid and then applied to the non-natural ester backbone in KcsA and NaK2K. I will also discuss anticipated results and the structural implications of an ester substitution in the protein backbone. Method developments towards measuring a single ester label are outlined as well as preliminary data supporting the ability to take these measurements. Current obstacles are described, as well as future directions and possible interpretations of the data so far acquired.

4.1 Introduction

Potassium channels have long been of interest due to the important roles that they play in cells generally and especially in human health.[2] Potassium channels, as the name suggests, are responsible for the selective translocation of potassium ions across biological membranes via passive diffusion.[24,98] In organisms they play a vital role in cell signaling and homeostasis.[99] They are of particular interest in humans because of their importance in cardiac and nervous system function. Mutations in potassium channels can lead to epilepsies, channelopathies, and cardiac arrythmias.[20,21,100] Despite the importance that these ion channels play in human health, there is still yet much to be understood about the mechanism of ion transduction and selectivity in the selectivity filter of the channel. Though the proteins studied here originate from bacteria, they have long been used as model systems to understand potassium channels. Bacterial expression allows the proteins to be readily expressed and studied. The selectivity filters between bacterial and human potassium channels are highly conserved and therefore results can translate to understanding these types of human channels. To this aim, it is important to build up a

fundamental understanding of potassium channels that can later be applied to human ion channels.

In this work, we focus on two ion channels: KcsA, a highly studied potassium channel,[23,26,28,40] and NaK2K, a mutant of a non-selective ion channel that has regained selectivity for potassium.[101] Both KcsA and NaK2K are well characterized structurally and share many structural traits.[24,101,102] The channels are homotetramers largely composed of α-helices.[101,103] They have a domain that acts as a gate that opens and closes the channel, and a selectivity filter which is the narrow point at which the ions pass through. The selectivity filter in both KcsA and NaK2K have identical amino acid sequences TVGYG.[99,102,104] The backbone carbonyls of this sequence of amino acids face inwards, creating the four binding sites labelled S1-S4 along with the side-chain of Thr as shown in figure 4.1.[6,103] The ions move from S4 to S1. Ion movement between the states happens at near the diffusion limit.[34,40] It has been posited, therefore, that ions moving between the conducting positions are kinetically coupled and that maximum ion flux occurs when the different ion configurations are energetically equivalent.[93] The energy equivalency is necessary since during the throughput cycle between different ion configurations, the energy barrier between the configurations must allow for quick interconversion.

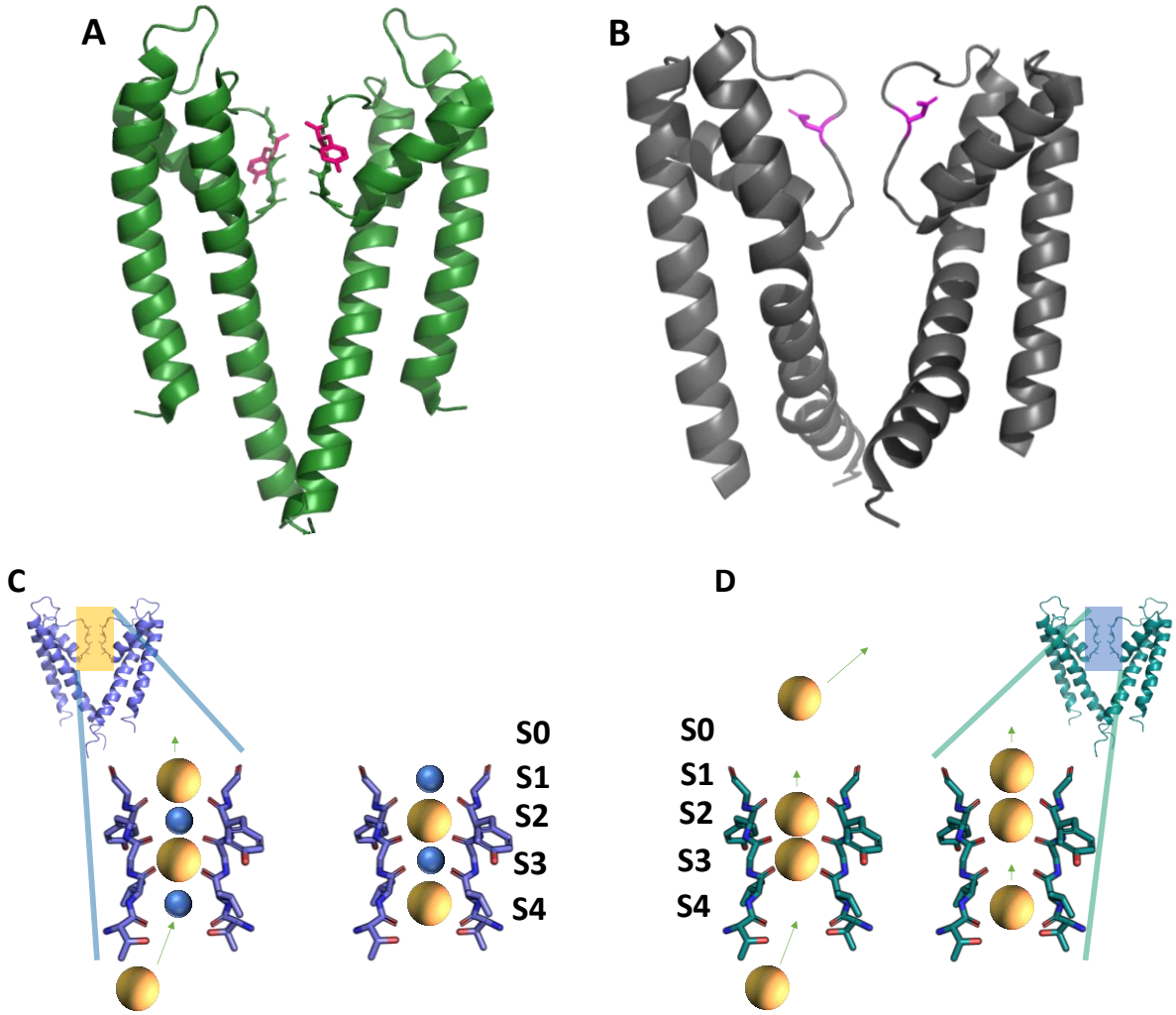

Figure 4.1 A) Structure of KcsA (green) B) Structure of NaK2K (gray) selectivity filters. Location of ester labels is shown in pink. C) Canonical mechanism of ion permeation. D) Hard-knock model of ion conduction.

The mechanism of the transduction is currently debated. Originally, most evidence seemed to support the canonical model of ion transduction, in which water molecules alternate with potassium ions.[13,38,93] However, later models from molecular dynamics simulations have suggested a new model in which no water passes through the channel and potassium ions are in adjoining positions.[41,42] Previous work in the Zanni group which compared experimental 2D IR data of isotope labels in the selectivity filter with complementary molecular dynamics simulations supported the canonical model, although work by de Groot and colleagues asserted

that it was not a unique solution.[13,41] Clearly, there is still much to understand about the mechanism of ion permeation in the selectivity filter.

Valiyaveetil and colleagues have previously studied the presence of an ester mutation in the selectivity filter of KcsA as a means with which to probe the relative energies of the ion binding sites, assuming the canonical model of ion binding.[93] To probe S1, a KcsA construct was created where the peptide bond between Tyr78 and Gly79 in the selectivity filter was replaced with an ester bond. The KcsA construct was generated initially in two parts. The C-terminus was created using solid-phase peptide synthesis and contained the ester bond. The N-terminus was expressed recombinantly. Native chemical ligation to join them creating a native peptide bond in a coupling reaction between an N-terminal cysteine and a peptide thioester. The protein was then folded. The ester construct ($KcsA_{ester}$) was less stable than the native channel ($KcsA_{WT}$). It was found that $KcsA_{ester}$ had lower ion conductance by about 50% as measured by current in single channel traces. This

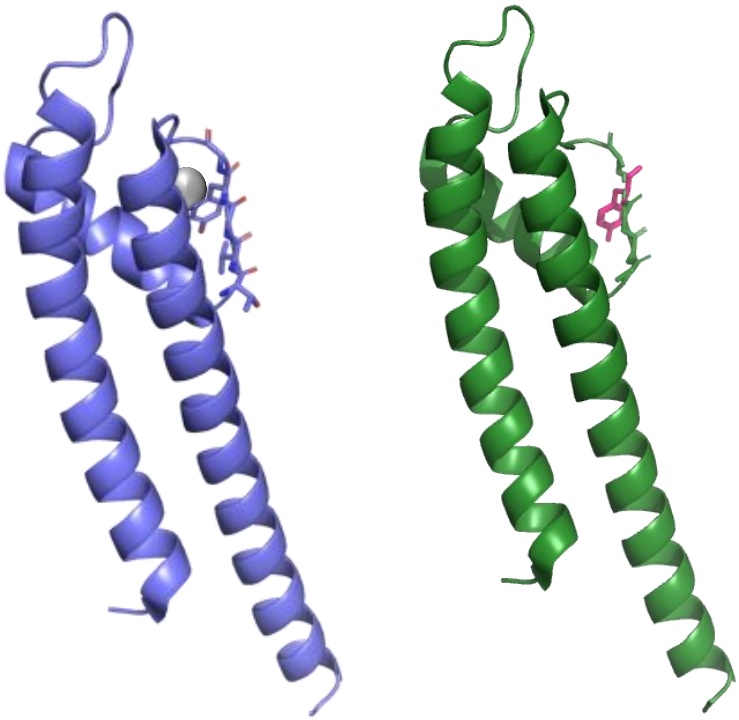

Figure 4.2 Structure of $KcsA_{WT}$ (blue) and $KcsA_{ester}$ (green) monomers. The ester label is shown in pink. The grey sphere represents the water molecule. Despite few visible differences, there is no water is $KcsA_{ester}$.

decrease in conductance was attributed to a loss in energetically equivalency between the S1/S3 and S2/S4 states due to the ester bond.

Structurally, $KcsA_{ester}$ was found to have generally the same structure as $KcsA_{WT}$ (RMSD< 0.7Å) when the structure was solved with x-ray crystallography.[93] A significant change, however, was the loss of a highly structured water found behind the selectivity filter in $KcsA_{WT}$ as seen in figure 4.2. This was attributed to the loss of a hydrogen bond donor when switching from an amide to ester. This loss of water could account for the lower stability of the $KcsA_{ester}$ tetramer. The crystal structures also showed a significant change in the ion distribution in the selectivity filter. As anticipated, it was largely S1 which was affected. There was a smaller electron density at S1 in $KcsA_{ester}$. Furthermore, just after the selectivity filter, there was also a change in electron density. In $KcsA_{WT}$ there are typically two sites with ion named S-1 and S0. In $KcsA_{ester}$ the density after the selectivity filter is different. The densities are split between S-1 and a new site which was then named S0.5 as it was between where S-1 and S0 typically are. It was posited that in the ester mutation, there are then three configurations of the potassium ions: S0.5/S3, S1/S3, S2/S4, rather than the two listed earlier. This work was supported by work in an inward rectifying potassium channel (Kir2.1) which saw decreased ion conductance after an ester mutation between S2 and S3.[105] The Valiyaveetil group has been able to generate similar ester mutations in the selectivity filter backbone as KcsA and have recently solved the crystal structure of ester-labelled NaK2K (unpublished). Therefore, it is of interest to see how the ester mutant changes ion occupancy and permeation in NaK2K and it there are any similarities and differences to the impacts of the ester mutant in KcsA.

Further studies were performed, systematically mutating backbone amide bonds to esters in the selectivity filter to further examine C-type inactivation: a channel inactivation that occurs

in the selectivity filter rather than the gate.[45,106,107] Ion occupancy is thought to drive inactivation, and certain sites are thought to act as a 'foot in the door' to prevent inactivation.[108–113] Since the ester mutation is thought to change ion binding due to a difference in electronegativity of the ester carbonyl compared to the amide carbonyl, the mutations were thought to be useful in finding important binding sites. Ester mutations at Tyr78 and G77 were found to decrease inactivation, while an ester mutation at G79 had very little effect.[45] Interestingly, though there was less inactivation with Tyr78 and G77, they did have lower overall conductance.

By solving the crystal structures of these mutants, a difference between the low-conductance, low-inactivation Tyr78 ester construct and the high-conductance, high-inactivation Gly79 ester construct was the ion density at S2.[45] Tyr79 had no density at S2, which is consistent with rubidium occupancy in $KcsA_{WT.}$ Rubidium-doped experiments have also shown little inactivation, suggesting that a lack of occupancy at S2 decreases the likelihood of C-type inactivation. From these studies it is evident that ester mutations allow for the study of both ion occupancy and also channel activation. However, much of this work can either study dynamics (through single channel experiments) or structure (through x-ray crystallography).[24,45,93,103,107,114] Two-dimensional infrared (2D IR) spectroscopy can be used to probe both structure and dynamics, and it therefore highly suited to measure answer lingering questions as to ion occupancy and dynamics in potassium channels.

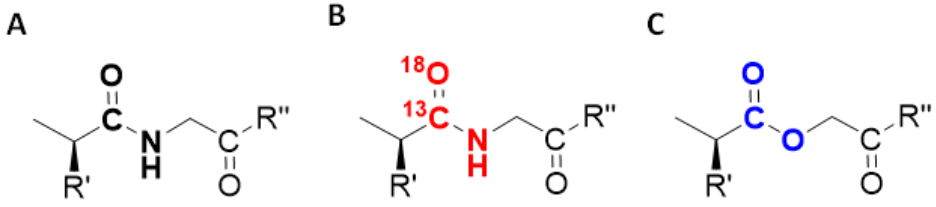

Figure 4.3 Dipeptides showing possible labelling schemes A) is an unlabeled dipeptide B) is an isotope labeled dipeptide, and C) is an ester label.

Past work in the Zanni group, has used $^{13}C^{18}O$ isotope labels on

backbone carbonyls to measure the vibration of individual amino acids via the amide I stretch.[13,14,58] These labels function by increasing the mass of the oscillator, and shift the signal about 60 cm^{-1} to lower energy. This strategy is beneficial in that it does not disrupt the structure of the protein, but creating the labelled peptides is time and resource intensive. However, there is a large zone with few vibrational features slightly higher than the amide I between 1700-1760 cm^{-1}. This is where the ester carbonyl stretch is located. Ester carbonyls are not common in protein samples, though lipids with ester linkers absorb between 1720 cm^{-1} and 1760 cm^{-1}.[75] Carboxylic acid side chains also absorb above 1700 cm^{-1}, but are slightly lower than the expected backbone ester frequency.[115] Therefore, using backbone ester carbonyls as a 'label' or probe into the selectivity filter could be a useful strategy to directly probe the ion occupancy of ion channel ester constructs, provided that they are in detergent rather than lipid. Differences in the labelling schemes are shown in figure 4.3.

Gai and colleagues have previously investigated using an ester label in a side chain.[91,92] The methyl ester was conjugated to a cysteine side chain via cysteine alkylation. Data were generated using linear FTIR spectroscopy, and trends with hydrogen bonding were determined. Simply, the more polar the environment, the more hydrogen bonding at work, the lower energy the transition. Having two hydrogen bonds, the frequency of the ester carbonyl was found to be between 1700 and 1710 cm^{-1}, one hydrogen bond caused the ester frequency to be between about 1720 and 1730 cm^{-1}, and the frequency of the ester with no hydrogen bonds was found to be between about 1740 and 1760 cm^{-1}. Spectra of the labels incorporated into the proteins demonstrated the ability to see a single label in FTIR with one label in about 600 residues.

Therefore, the aim of this project is to use the ester backbone mutation itself to probe the dynamics of the selectivity filter. The project is different to previous ester labels because it uses

various IR spectroscopies to probe a backbone mutation, rather than a labelled sidechain. In the case of the selectivity filter, the established trends of the impact of hydrogen bonding on ester carbonyl frequency will be useful. The backbone carbonyl will be able to probe the presence of a water, ion, or nothing in the selectivity filter. Here we measure potassium channels with a label at the Tyr78 position in KcsA as well as the Tyr66 ester construct of NaK2K, which is the equivalent position in the selectivity filter as KcsA. Analysis of the spectral diffusion of the labelled peaks will also give insight into the vibration lifetimes and if there are multiple timescales.

Another benefit of 2D IR spectroscopy is the relative ease of calculating model 2D IR spectra from trajectories generated by molecular dynamics simulations.[8] The method of which has been previously described. By adding in ester couplings into the calculations which have previously been generated, the creation of the spectra should be straightforward, though even comparison to molecular dynamics simulations of the ester ion channel constructs should also give qualitative explanations to dynamics trends seen in experimental 2D IR spectra. In sum, the work here seeks to gain insights into the impacts of the ester label in the selectivity filter of potassium channels to better characterize the ion occupancy and permeation through the channels.

4.2 Methods

4.2.1 Protein Synthesis and Recombinant Expression

Ion channel ester label constructs were prepared by Valiyaveetil group at the Oregon Health and Science University using recombinant expression, creating the ester with unnatural amino acid mutagenesis.[116] Wild type ion channels were expressed in *Escherichia coli* XL10 cells and purified with a cobalt affinity column. Ester-labelled channels were expressed stop genes at the

ester-labelled residue and were cloned into pBAD vectors, transformed with HPLAR tRNA synthetase. L-phenyl lactic acid (the unnatural amino acid) was introduced into the expression media to was incorporated at the amber stop codon and incorporated with the added tRNA synthetase. The ester-labelled ion channels were purified in the same manner as the wild type channels. The ion channels were delivered at various concentrations (as noted later) in 0.25% decyl β-D-maltoside (DM), 50 mM Tris, pH 7.5, and 150 mM KCl for KcsA and 0.25% DM, 20 mM Tris, pH 8.0, and 100 mM KCl for NaK2K.

4.2.2 Determining Necessary Protein Quantity

The inherent challenge of this set of experiments is that we have a single ester label in a large protein. KcsA is a homotetramer with 122 residues in each monomer and NaK2K is a homotetramer with 97 residues in each monomer. One of these residues is mutated to substitute the nitrogen in the backbone for an oxygen. Therefore, we are looking for a signal that is roughly on hundredth of the bulk amide I spectrum. Furthermore, the ester carbonyl stretch is slightly weaker than that of the amide I. Meaning that we will have to find a way to get as much absorption as possible in order to see signal of the ester.

In order to determine how much will be needed in terms of OD, made samples with a simple amide (n-methyl acetamide (NMA)) and a simple ester (ethyl acetate (EA)). A series of concentrations were made in ethanol in order to determine the minimum concentration that was visible with good signal-to-noise (above 3) on FTIR and 2D IR. The signal-to-noise threshold was determined by 2D IR spectra and then the resulting FTIR absorbance was noted as an easy way to monitor signal strength of a sample. Once the EA minimum concentration was established, a 100:1 mix of NMA:EA was created in ethanol and the FTIR was taken to get a

benchmark of amide I absorption in an ion channel with approximately 100 backbone amides and 1 backbone ester.

Originally, the ion channels were sent at approximately 1 mg/mL concentration in the buffers listed above. Samples were prepared by dropping 2 μL of sample on a bare CaF_2 window and were H/D exchanged 50 times with 0.2 μL D_2O. Samples were rehydrated with 0.2 μL D_2O and were assembled into a sample cell with another bare CaF_2 window and a 12 μm Teflon spacer. However, after taking FTIR and 2D IR of these samples, there was not enough signal strength to see the ester. Subsequently, stacked layers of sample were created to increase the pathlength of the sample by creating a thicker sample. 2-, 4-, 12-, 20-, and 60-layer samples were created with the 1 mg/mL NaK2K sample. Layers were created by pipetting 2 μL of sample and letting dry under nitrogen. Then another 2 μL were pipetted on top and repeated until the total number of layers was created. A pipetting robot was created with a computer-controlled translation stage and syringe pump to create more controlled layers to reduce scatter.

After trying the layered samples with 1 mg/mL ion channel concentration, the Valiyaveetil group prepared ion channels at about 10 mg/mL concentration, with the same buffer conditions. 1- and 10-layer samples were created as above. The samples were then H/D exchanged, rehydrated, and assembled as described above. Samples were measured first with FTIR spectroscopy and then measured with 2D IR spectroscopy.

4.2.3 Surface enhancement of ester-labelled ion channel samples

Using signal enhancement from surface plasmons was also attempted in conjunction with increasing the pathlength of the sample. First, one 2 μL layer of 1 mg/mL $NaK2K_{ester}$ and $NaK2K_{WT}$ were applied to a CaF_2 window with a rough layer of 3-nm gold. Only one layer was used since the enhancement of the localized surface plasmon does not extend more that 10-50

nm from the surface.[68] Further stacking of layers would not multiply, therefore, with the surface enhancement, and even interfere with data interpretation. The samples were then H/D exchanged and rehydrated as outlined above. 2D IR spectra were then taken of these samples.

Nanoantennas were also used as a possible signal enhancement strategy. Various combinations of nanoantennas were used. Methods to create these nanoantennas have been previously described.[117–120] Briefly, a layer of polymer (in this case polymethyl methacrylate, PMMA) is deposited on a CaF_2 window. The PMMA is then etched to the desired nanoantenna dimensions by electron beam lithography. Gold is evaporated to fill the holes in the PMMA. Anything not attached to the window is then lifted off with acetone, nominally removing all PMMA and leaving just the gold nanoantennas.

A broader, low intensity plasmon absorption was created with the following dimensions: 2208 nm x 260 nm for the antenna size with a spacing of 3792 nm in the longer antenna dimension and 740 nm in the shorter antenna dimension. This was deemed the ‘broad’ plasmon. A narrower, higher intensity plasmon absorption was created with the following dimensions: 2243 nm x 260 nm for the antenna size with a spacing of 757 nm in the longer antenna dimension and 1740 nm in the shorter antenna dimension. This was deemed the ‘narrow’ plasmon. $NaK2K_{WT}$ was applied in a single, 2-μL layer to these antennas and H/D exchanged and rehydrated as above. 2D IR spectra were taken of these samples. A sample of the narrow plasmon on top of a conductive layer of indium tin oxide (ITO) was also prepared similarly. A 2D IR spectrum was taken of this sample as well.

Further refinement of the center frequency of the plasmon absorption was optimized. Three different arrays were created with the following dimensions. For array 1, the dimensions were the same as the above ‘narrow’ plasmon. For array 2 the dimensions were: 2334 nm x 260

nm for the antenna size with a spacing of 666 nm in the longer antenna dimension and 1740 nm in the shorter antenna dimension. For array 3 the dimensions were: 2152 nm x 260 nm for the antenna size with a spacing of 848 nm in the longer antenna dimension and 1740 nm in the shorter antenna dimension. 2D IR spectra were obtained from each sample to determine which was best suited to these experiments.

After working with samples with residual PMMA, which contains esters and was creating ester features in samples without ester labels, more samples were made with the 'narrow' plasmon nanoantenna array, with the difference that plasma etching was used after electron-beam lithography and also after lift-off in order to eliminate any PMMA. Spectra of NaK2K$_{WT}$ were taken with 2D IR spectroscopy.

4.2.4 Angular Dependence: intensity vs background

Spectra were collected of the single layer of 1 mg/mLNaK2K$_{WT}$ sample on the 'narrow' plasmon nanoantennas as a variety of angles. The enhancement generated from the plasmons are strongest with the light is polarized along the long axis of the antenna. In an attempt to truncate background signal from the plasmon, a series of 2D IR spectra were taken at 0°, 10°, 20°, 30° and 45° degrees of rotation in the plane perpendicular to the direction of light propagation as shown in figure 4.4A. Furthermore, spectra were taken

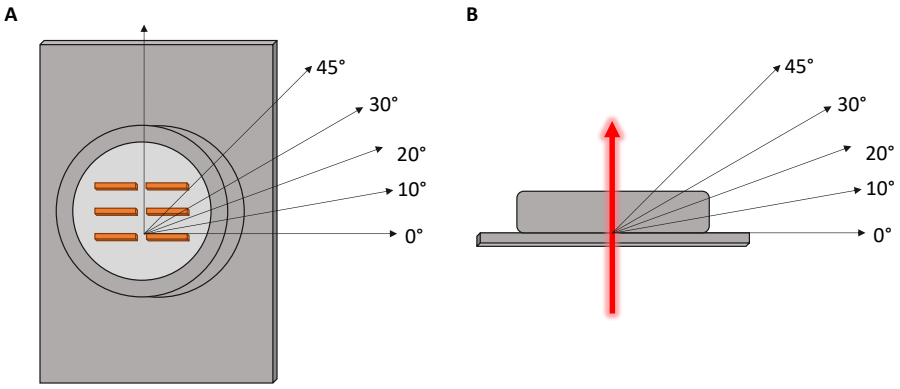

Figure 4.4 A) Rotation dependence experiment showing rotation perpendicular to the direction of light propagation. B) Angular dependence set up for rotation in the plane of the direction of light propagation.

at 0°, 10°, 20°, 30°, and 45° of rotation in the plane created by the light propagation and the short axis of the antennas as shown in figure 4.4B.

4.2.5 2D IR spectroscopy methods

2D IR spectroscopy was used to probe protein structure as well as dynamics. Creation of a 2D IR spectrometer using mid-IR pulse shaping and a pump-probe geometry has been previously described.[8,61] Spectra were taken at different delays between the pump and probe pulses. Changing the delay between these pulses allow for the spectral diffusion times to be extracted from the data. Center-line slope (CLS) analysis was then performed on the sets of spectra from different delay times. CLS has been described previously.[8,78] Another use of the delay times was in the case of the surface-enhanced samples, the plasmonic background delays quickly, and spectra are easier to interpret at longer (500 fs) waiting times. For proof of concept and method development experiments, longer waiting times were therefore used.

4.3 Results

4.3.1 Determining minimum ester concentration

Samples of varying concentrations of NMA and EA in ethanol were created and measured

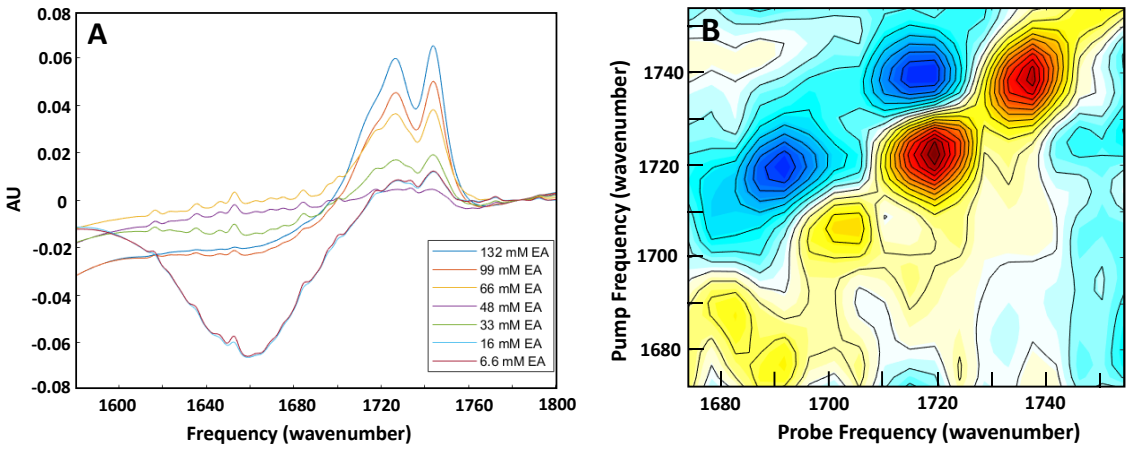

Figure 4.5 A) FTIR spectra of different concentrations of ethyl acetate B) Representative 2D IR spectrum of 16 mM ethyl acetate.

with FTIR and 2D IR spectroscopy in order to determine the minimum concentration of ester required for adequate signal to noise. Resulting FTIR spectra for EA absorbance are shown in figure 4.5A. The intensity of the absorption has a linear dependence on concentration until the lowest concentration of 6.6 mM. Figure 4.5B shows a representative 2D IR spectrum of 16 mM EA with a signal to noise ratio of above 3. This was taken to be a baseline necessary ester concentration in a sample. Spectra of 1 mg/mL NaK2K$_{WT}$ and NaK2K$_{ester}$ with different numbers of layers were created and measured to replicate the linear absorbance found with EA. Representative FTIR spectra of 4 layers, 20 layers, and 60 layers are shown in figure 4.6A-C. Spectra are stacked with both samples to show the small difference in intensity at about 1720 cm^{-}

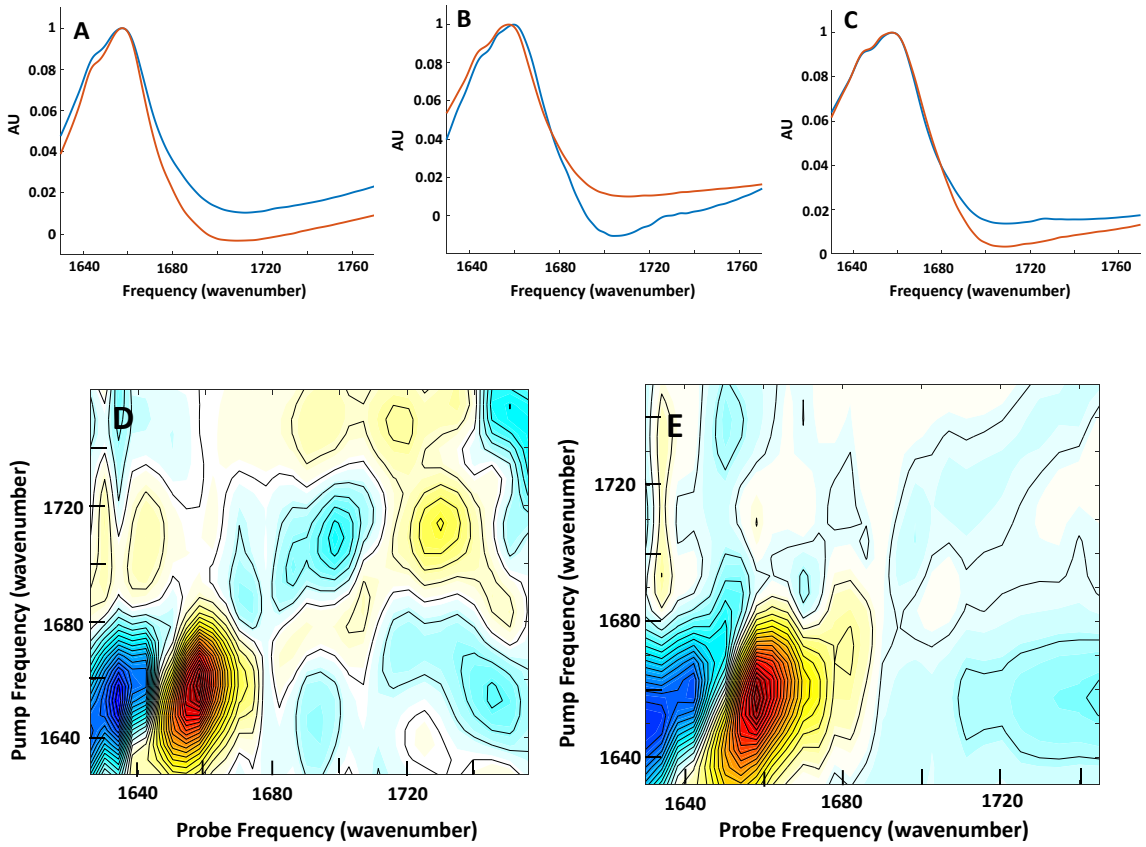

Figure 4.6 Spectra of layered NaK2K samples. A) FTIR of 4 layers of NaK2K samples with NaK2K$_{ester}$ in blue and NaK2K$_{WT}$ in red. B) FTIR of 20 layers of NaK2K samples with NaK2K$_{ester}$ in blue and NaK2K$_{WT}$ in red. C) FTIR of 60 layers of NaK2K samples with NaK2K$_{ester}$ in blue and NaK2K$_{WT}$ in red. D) 2D IR of 60 layers of NaK2K$_{ester}$ E) 2D IR of 60 layers of NaK2K$_{WT}$

[1]. This absorbance is consistent with an ester carbonyl stretch. 2D IR spectra were then acquired for these samples. The 60-layer NaK2K$_{ester}$ and NaK2K$_{wt}$ spectra are shown in figure 4.6D-E. A peak is observed in the NaK2K$_{ester}$ spectrum that is not present in the NaK2K$_{WT}$ spectrum. The peak is at 1720 cm^{-1} similar to the corresponding FTIR spectrum. However, it was difficult to replicate this result.

4.3.2 Surface-enhanced 2D IR spectroscopy of ester-labelled NaK2K

Surface-enhanced 2D IR spectra were taken of NaK2K ion channel samples. First, samples of NaK2K$_{WT}$ and NaK2K$_{ester}$ were prepared on a CaF_2 window coated in a 3-nm thick layer of rough gold. 2D IR spectra of NaK2K$_{WT}$ and NaK2K$_{ester}$ on 3-nm rough gold were then acquired.

Then, samples of NaK2K$_{WT}$ were made on two different nanoantenna arrays, one which has a narrow but strong plasmon absorbance around 1750 cm^{-1} (designated the 'narrow' array) and the other which had a broad, but weaker plasmon absorbance around 1750 cm^{-1} (designated the broad array). This center frequency was selected to be close to the ester carbonyl stretch. The absorbance spectra of the two arrays are seen in figure 4.18. 2D IR spectra were acquired for the NaK2K$_{WT}$ sample for both arrays as shown in figure 4.7. The spectra are shown at a 500-fs delay between the pump and

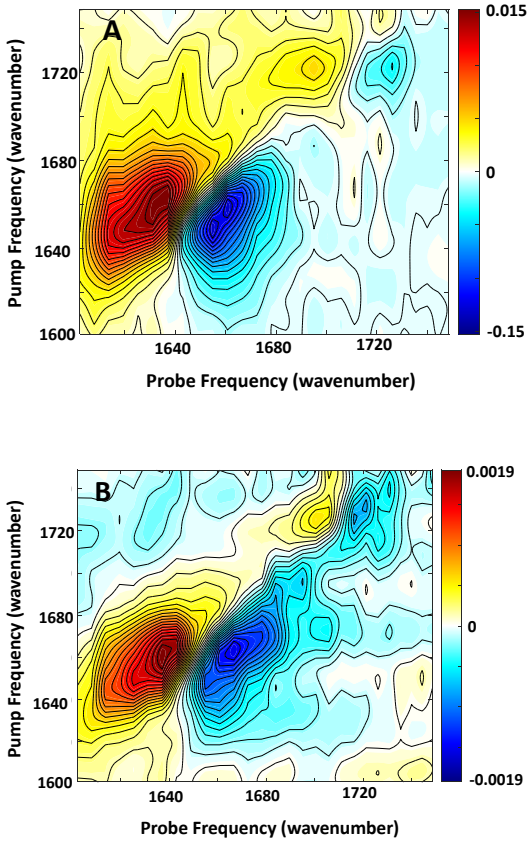

Figure 4.7 Surface-enhanced 2D IR spectra of NaK2K$_{WT}$ using A) a narrow, intense plasmon, B) a broad, weaker plasmon.

probe pulses for clarity. The impact of delay time on plasmonic background is seen in figure 4.17. There is a signal in the ester carbonyl region. However, this absorbance is also present in 2D IR spectra where no signal is present. Therefore, it is not from the sample, but rather likely from residual PMMA on the window, which also contains an ester carbonyl. A spectrum of the narrow array with ITO under the array as a conductive layer was acquired for $NaK2K_{WT}$. However, there was a high amount of background, so this method was abandoned.

The angular dependence of enhancement and plasmonic background of $NaK2K_{WT}$ samples were measured by changing the angle of the sample relative to the incident light in two separate planes. Representative spectra are shown in figure 4.19. Generally, the further the antennas were from being perpendicular to the direction of propagation of the incoming light and being parallel to the polarization of the light, the lower intensity the signal. Changing the angle did not decrease the plasmonic background significantly compared to the decrease in signal due to the decrease in enhancement.

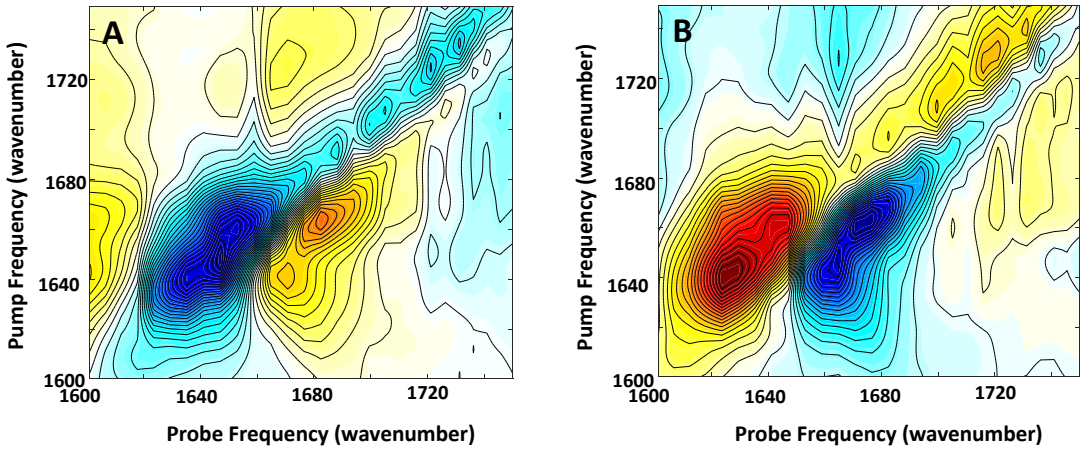

Figure 4.8 2D IR spectra of $NaK2K_{WT}$ with A) No phase correction B) appropriate phase correction

Spectra taken on the antennas require phase corrections due to Fano line shape distortions. This method was previously developed by Hamm and colleagues.[72] The Fano

lineshapes occur when you are slightly off resonance with the plasmon absorbance. In the thin, rough gold the IR light is so far off of the resonance that it does not lead to distortions. The impact of the correction is demonstrated in figure 4.8. The additional peak to the left of the overtone is a result of the Fano line shape. It is eliminated when the phase correction is properly applied. A marker of a correctly applied phase correction are diagonal and overtone peaks that are close to equal in A consequence of the correction is the occasional flip in magnitude between the diagonal and overtone peaks, depending on which phase correction is applied. This, however, does not change the interpretation of these spectra.

Three different versions of the 'narrow' array were created to slightly tweak the best center frequency of the plasmon for ion channel ester samples. 'Window 1' was the original array. 'Window 2' has slightly narrower spacing in the dimension of the long axis of the antennas and was slightly shifted to lower frequencies. 'Window 3' has slightly wider spacing in the long axis of the antenna and absorbs at higher frequencies. Window 1 is centered at 1752 cm^{-2}, window 2 is centered at 1730 cm^{-1}, and window 3 is centered at 1795 cm^{-1}. FTIR

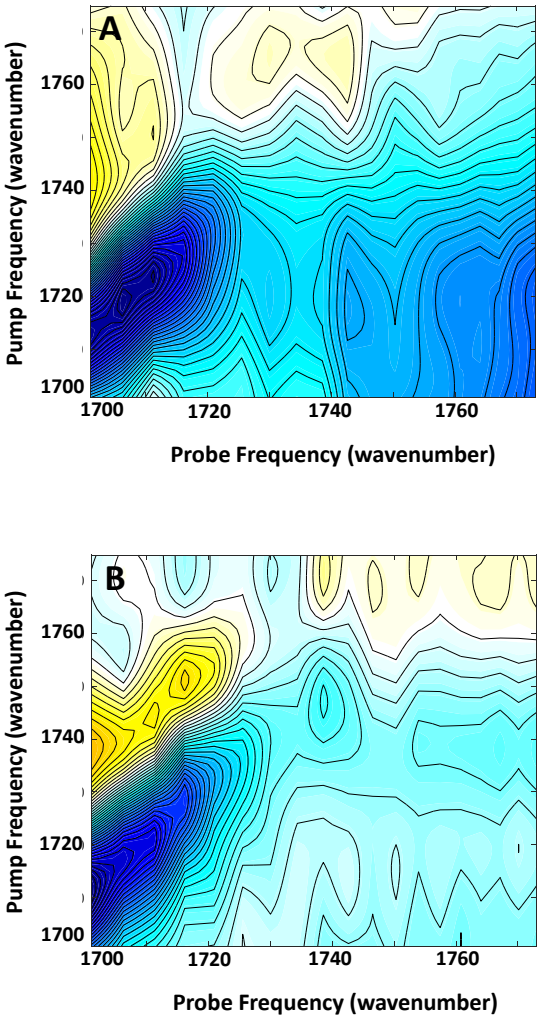

Figure 4.9 Representative of comparing A) $NaK2K_{WT}$ and B) $NaK2K_{ester}$ on gold nanoantennas.

spectra of the absorbance of the three antennas are seen in figure 4.20. 2D IR spectra were acquired of NaK2K$_{WT}$ and NaK2K$_{ester}$ on all three arrays. Two arrays were on a window, and one contained a NaK2K$_{WT}$ sample and one contained a NaK2K$_{ester}$ sample. The samples do not touch each other, but being on the same window allows for the arrays to be created under identical conditions. On each window, there was no strong, discernable ester peak that differed between the NaK2K$_{WT}$ and NaK2K$_{ester}$ spectra. Generally, there was little difference between the windows, so the original array was selected as 'best'. A representative comparison for 'window 2' is shown in figure 4.9. Every window with antennas displayed a peak at 1720 cm^{-1}, even when taking 2D IR spectra of just the antenna array. This peak is consistent with the absorbance of the PMMA polymer used in the lithography of the antennas. The PMMA peak persisted even with plasma etching to eradicate PMMA.

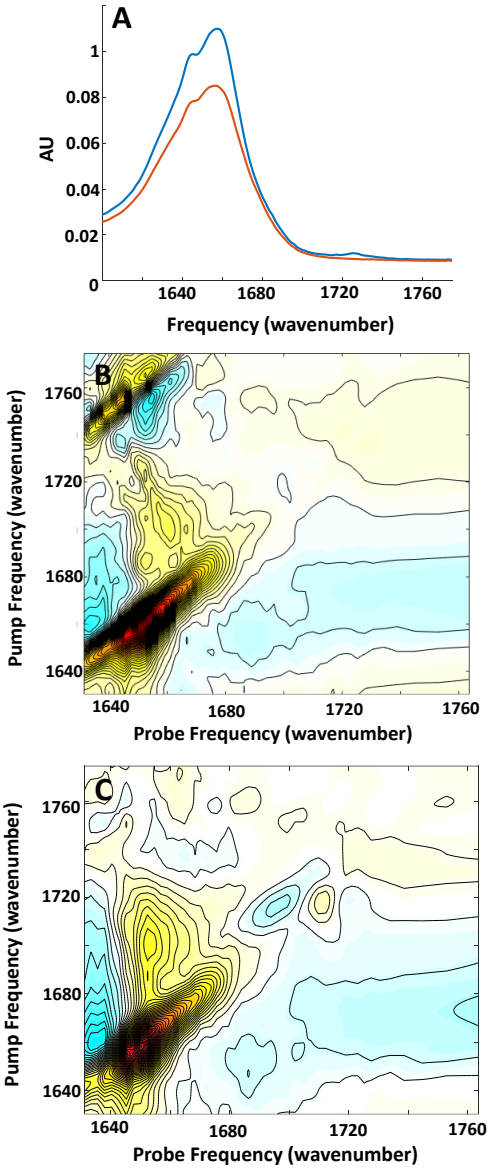

Figure 4.10 A) FTIR overlay of NaK2K$_{ester}$ (blue) and NaK2K$_{WT}$ (red) B) 2D IR spectrum of NaK2K$_{WT}$ C) 2D IR spectrum of NaK2K$_{ester}$

4.3.3 Highly concentrated samples of ester-labelled ion channels

New samples of NaK2K$_{WT}$, NaK2K$_{ester}$, KcsA$_{WT}$, and KcsA$_{ester}$ were prepared with

a protein concentration of about 10 mg/mL. Samples were created with 10 layers of the more concentrated sample of $NaK2K_{WT}$ and $NaK2K_{ester}$ on bare CaF_2 windows. FTIR spectra of the two samples are shown in figure 4.10A. 2D IR spectra were then acquired for each and are shown in figure 4.10B-C. In the ester spectra, there is clearly a peak at 1725 cm^{-1} that is not present in the $NaK2K_{WT}$ sample. 2D IR spectra are shown with a 400-fs delay between the pump and probe pulses for clarity.

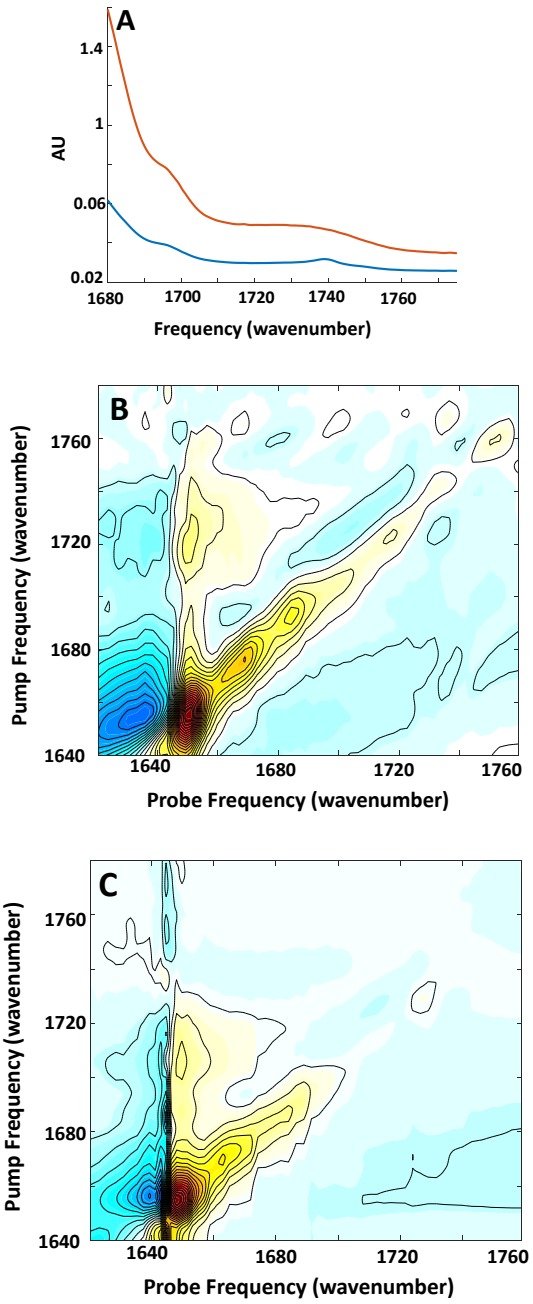

Figure 4.11 A) FTIR of $KcsA_{ester}$ (blue) and $KcsA_{WT}$ (red) zoomed it to see the features in the ester carbonyl region B) 2D IR spectrum of $KcsA_{WT}$ C) 2D IR spectrum of $KcsA_{ester}$

Samples of 10 layers of the highly concentrated samples of $KcsA_{WT}$ and $KcsA_{ester}$ were created on bare CaF_2 windows. FTIR spectra of both were taken and are shown in figure 4.11A. Subsequently, 2D IR spectra were also acquired of the samples show in figure 4.11B-C. There are more peaks in the ester region of these samples. There is a shoulder at about 1695 cm^{-1} in all spectra. In the FTIR of $KcsA_{WT}$, there is a broad peak centered at 1735 cm^{-1}. This is also seen in the 2D IR spectrum of $KcsA_{WT}$ where there

is a broad signal around 1730-1735 cm^{-1}. In the FTIR of the $KcsA_{ester}$ there is a sharper peak at 1739 cm^{-1}. There is also a peak at 1737 cm^{-1} in the 2D IR spectrum of $KcsA_{ester}$. However, when the $KcsA_{WT}$ and $KcsA_{ester}$ 2D IR spectra are compared, they are difficult to distinguish from each other, though they are more distinguishable in the FTIR spectrum.

4.3.4 Spectral diffusion measurements of ester labels

For the highly concentrated samples of the ester labelled ion channels, spectra were taken at various delay times between the pump and probe pulses to measure spectral diffusion times. Spectra were measured from time 0 as defined by when the second pump pulse and probe pulse are overlapped in time, and therefore signal is strongest. Spectra were taken at two negative delay times to ensure that time 0 is being captured. Spectra were collected at 0, 100, 200, 300, 500, 1000, 2000 fs for NaK2K. Representative spectra of the ester peak from select waiting times are shown in figure 4.12. Spectra were collected at 0, 100, 200, 300, 400, 500, 650, 800, 1000, 1250, 1500, 2000, 2500, and 3000 fs for $KcsA_{ester}$. Representative spectra of the ester peak from select waiting times are shown in figure 4.13. More delay times were used for KcsA as it became the focus of the project for the immediate future. Using more waiting times for NaK2K is necessary to complete the data set.

4.4 Discussion

4.4.1 Surface-enhanced spectra of ester-labelled ion channels

There were initially very promising results with the surface enhanced methods. Previously, surface-enhanced 2D IR spectroscopy has been used to measure a single layer of proteins both embedded in a membrane, or directly tethered to the surface.[121–123] In both cases, a thin, rough gold layer was used to generate localized surface plasmons. Furthermore,

nanoantennas have been used to measure membrane bound proteins and also ester stretches in lipids.[75,124] Indeed, in the spectra that were taken, there was very strong signal in the amide I region of the mid-IR. However, in the case of the 3-nm thick rough gold, no ester signal was detected.

Focus then moved to using the nanoantennas, which, since they are resonant with the frequency of interest, provide greater enhancement. A larger intensity of the amide I vibration was observed, of about twice the intensity of the rough gold. Despite promising signal intensities from the amide I mode which matched the intensity observed when there was an observable ester label in the 60-layer sample, there was an unexpected signal in the ester carbonyl region. The signal appeared at 1720 cm^{-1} even when the nanoantennas were measured alone. It was determined that the signal was likely coming from residual PMMA that was not completely removed by the electron beam or by acetone lift off. Further attempts were made to remove residual PMMA by extended boiling in acetone in the liftoff process. After PMMA continued signal persisting after increased cleaning, plasma etching was used after electron beam lithography and after liftoff in order to remove a small layer of the entire sample. Even after these extensive efforts, the PMMA signal remained. The vibration signal of the ester carbonyl in PMMA overlaps well with the expected frequency of the backbone ester carbonyl. Therefore, any amount of signal will significantly complicate spectral analysis. However, work with ion channels without ester labels, for example, isotope labelling experiments, may benefit from the signal enhancement from the nanoantennas.

4.4.2 2D IR spectroscopy of $NaK2K_{WT}$ and $NaK2K_{ester}$

Using 10 layers of 10 mg/mL $NaK2K_{WT}$ and $NaK2K_{ester}$ samples yielded FTIR and 2D IR spectra with evident peaks in the ester carbonyl region for just the $NaK2K_{ester}$ sample as seen

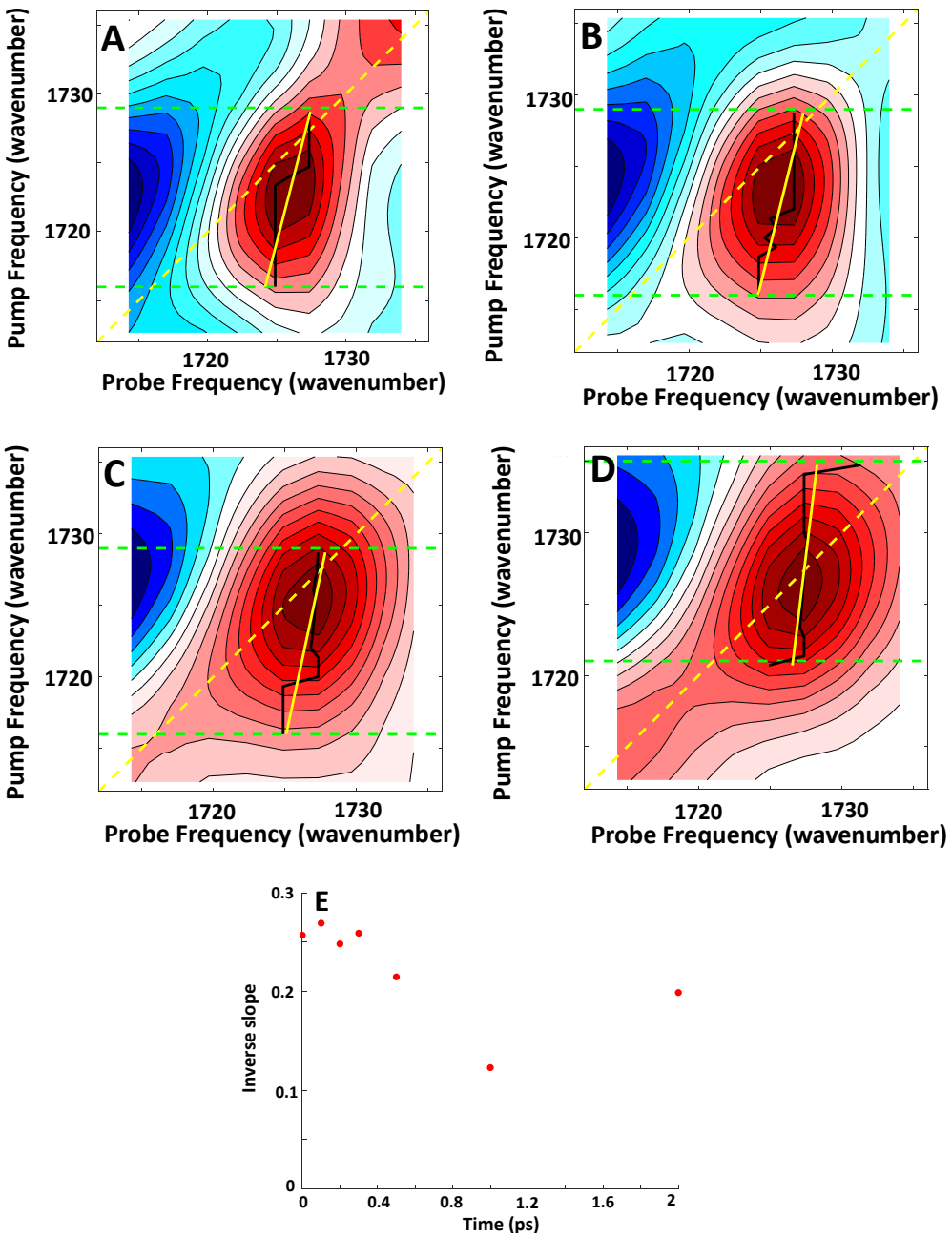

Figure 4.12 Center-line slope analysis example of NaK2K$_{ester}$. The solid black line shows the maximum value between the green dotted boundaries. The solid yellow line is a fitted slope of the maximum values. The dotted yellow line is the diagonal as a guide to the eye. A) NaK2K$_{ester}$ at 0 fs, B) NaK2K$_{ester}$ at 200 fs C) NaK2K$_{ester}$ at 500 fs, D) NaK2K$_{ester}$ at 1000 fs E) Ester center-line slope as a function of delay time.

as in figure 4.10. The peak was observed at 1725 cm^{-1}. Previous trends determined for hydrogen binding environments for the ester carbonyl suggest that this frequency is consistent with the carbonyl participating in one hydrogen bond.[91] This may suggest the presence of water in the channel. However, more study is needed as the impact of ions is not as well known. Tokmakoff

and colleagues have demonstrated that the presence of potassium will shift the ester carbonyl (as well the amide I) to lower frequencies in ester-containing ionophores.[12] The frequency observed in the $NaK2K_{ester}$ spectrum is lower than that observed by Tokmakoff and colleagues in 2D IR however, so it is possible that the observed frequency is influenced by both hydrogen bonding as well as a nearby potassium ion. More work is necessary, likely in conjunction with MD simulation and subsequent 2D IR spectra calculation to better understand the meaning of the ester carbonyl frequency.

2D IR spectra were obtained of the ester carbonyl peak at different delay times between the pump and probe. The ester carbonyl peak was then analyzed with center-line slope analysis to begin to extract spectral diffusion times as another way to probe the dynamics of the system. Spectra of the ester carbonyl along with the center-line slope fit are shown in figure 4.12. The data suggest a vibrational lifetime of the ester carbonyl of greater than 1 ps, though more data points will be necessary to properly fit the line. The 2 ps point appears to be an outlier due to an underlying scatter which, therefore, complicates the fit. However, there is a clear change in the lineshape of the ester carbonyl peak over time. The fit of this line can also inform the number of configurations due to the number of exponentials in the fit. For example, this data could support the hypothesis of the ester mutation introducing a third potassium binding configuration.

Another interesting observation was made from looking at the full spectra of the samples at different waiting times. There are cross peaks visible between certain amide I frequencies and the ester carbonyl stretch which also decay as seen in figure 4.13. Further analysis with MD simulations or a combination of ester and isotope labels could reveal the source of the cross peak. It is likely neighboring residues, but there are also interactions with residues behind the collapsed water pocket that could contribute to the coupling and be a source of the cross peaks.

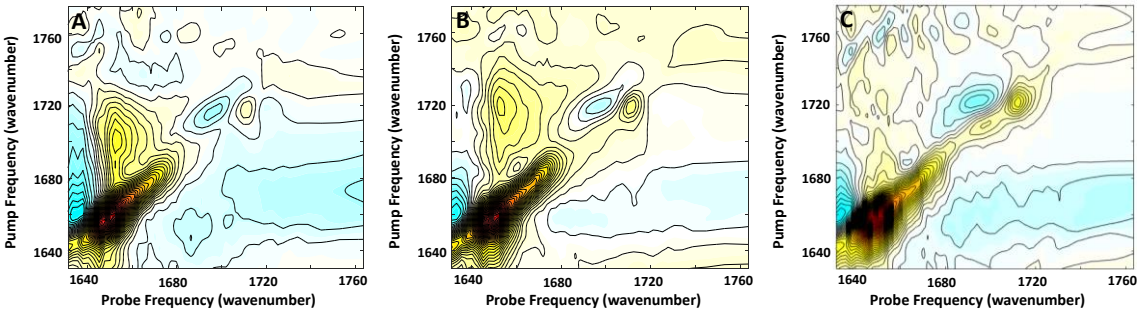

Figure 4.13 NaK2K$_{ester}$ at A) 100 fs, B) 300 fs C) 1000 fs delay time. Cross peaks are evident on the left of the diagonal.

4.4.3 2D IR spectroscopy of KcsA$_{WT}$ and KcsA$_{ester}$

FTIR and 2D IR spectra of KcsA$_{WT}$ and KcsA$_{ester}$ were taken, and there was a peak seen in the expected ester carbonyl region. However, this sample was more complicated to interpret than that of NaK2K. The beginning of this difficulty is evident in the FTIR spectrum. First, there is a shoulder in the FTIR at 1695 cm^{-1}. In the 2D IR spectra this appears as a more independent peak rather than a shoulder due to the inherent peak narrowing of 2D IR. This peak may be due to a side chain with an ester, namely Asp or Glu which absorb in the same region as other ester carbonyls and are also highly sensitive to hydrogen bonding.[115] It is likely that the peak is resulting from the bulk of the protein since it is present in all samples and all spectra. As a note, there are many similarities in sequence between the KcsA and NaK2K sequences, and they both contain Asp and Glu.

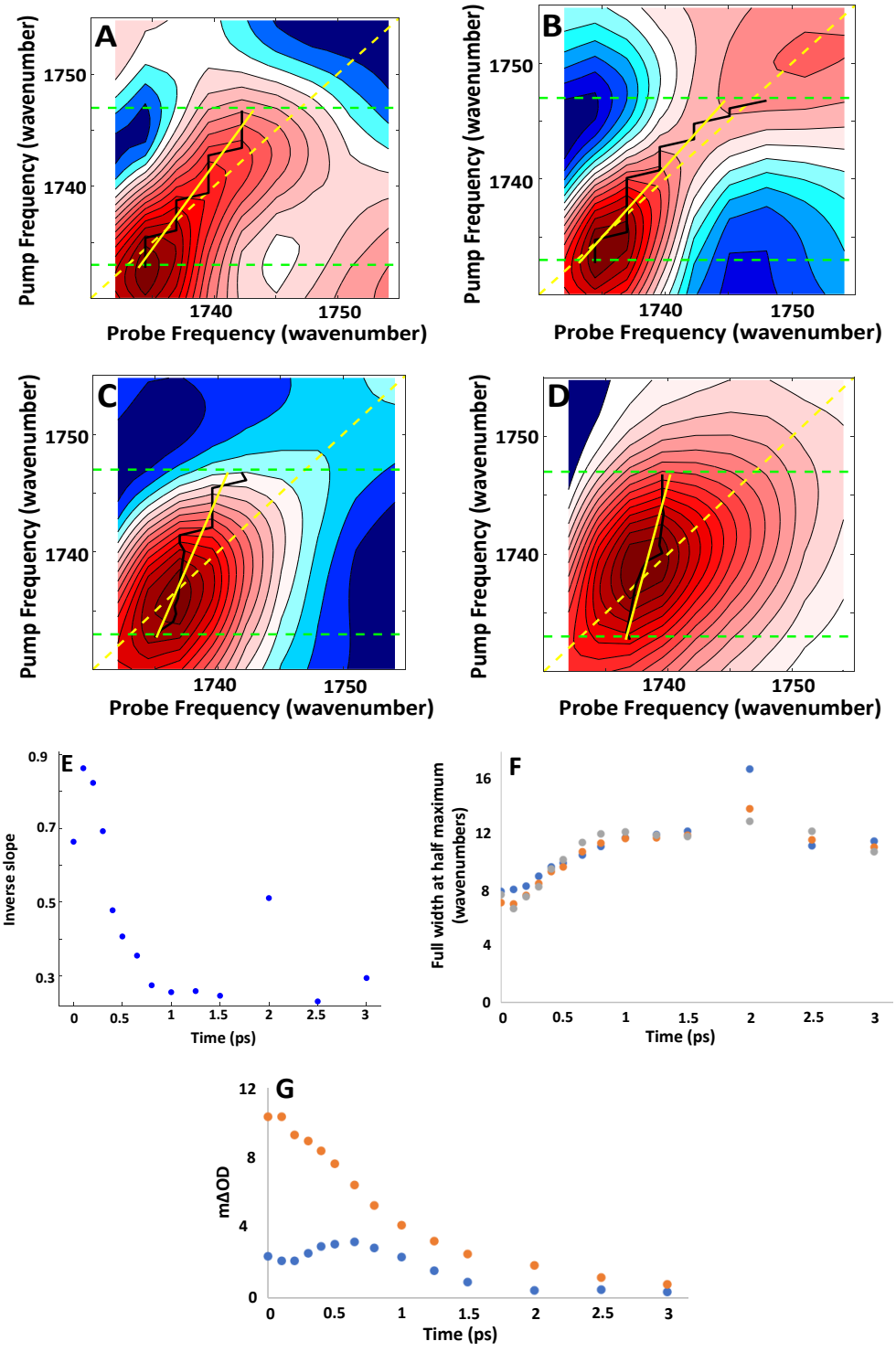

Figure 4.14 Center-line slope analysis example of $KcsA_{ester}$. The solid black line shows the maximum value between the green dotted boundaries. The solid yellow line is a fitted slope of the maximum values. The dotted yellow line is the diagonal as a guide to the eye. A) $KcsA_{ester}$ at 0 fs, B) $KcsA_{ester}$ at 200 fs C) $KcsA_{ester}$ at 500 fs, D) $KcsA_{ester}$ at 1000 fs E) Ester center-line slope as a function of delay time. F) Full-width at half maximum of peaks at 1736 cm^{-1} (blue), 1739 cm^{-1} (orange), 1741 cm^{-1} (gray) as a function of time. G) Peak intensity of ester 1736 cm^{-1} (blue) and amide 1694 cm^{-1} (orange) peaks as a function of time.

1730 cm^{-1} in the $KcsA_{WT}$ spectrum. The underlying signal is also present in the $KcsA_{ester}$ sample, though the FTIR spectrum of $KcsA_{ester}$ also has a narrow peak with similar shape to the ester-label peak in $NaK2K_{ester}$. In the FTIR the difference between the ester-label peak and other underlying signals is fairly clear. However, in the 2D IR spectra, there is variability in the ability to confidently ascribe the ester label to a peak in the spectrum, rather than a peak arising from the underlying signal. The underlying signal is likely from residual lipids from protein expression. Even a single lipid molecule can give signal in this region that competes with the ester-label signal, since lipid molecules often have two ester carbonyls linking the headgroup to the tails. The reason for not seeing the lipids in the NaK2K samples is unclear, and there appeared to be sample to sample variability in KcsA samples, suggesting that the presence of lipids may be variable depending on the specific purification process. Work continues in determining if subtraction can be used to isolate the ester-label signal, or if there are other ways to disentangle these competing signals.

2D IR spectra of the $KcsA_{ester}$ sample were taken at a series of delay times. Spectra of the ester carbonyl region as well as a tentative CLS analysis are shown in figure 4.14A-E. The CLS analysis is tentative because it assumes a single transition being measured.[8,78] Having multiple peaks causes more elongation along the diagonal not caused by spectral diffusion or a lack thereof. Furthermore, the center frequency of the ester carbonyl peak appears to shift as a function of time. It is extremely unlikely that the peaks centers are changing over time, but rather there are transitions with different lifetimes, so as one decays faster than the other, the center frequency of the sum of the peaks shifts, rather than the vibrational frequencies themselves changing. Therefore, other methods of analysis to measure the decay of signal over time were also employed including looking at peak width along the pump axis and the intensity of a peak

over time. These analyses are shown in figure 4.14F-G. All seem to indicate a lifetime of between 1500 and 2000 fs. However, a precise value is difficult to designate until the correct peak assignment for the ester-label is clear.

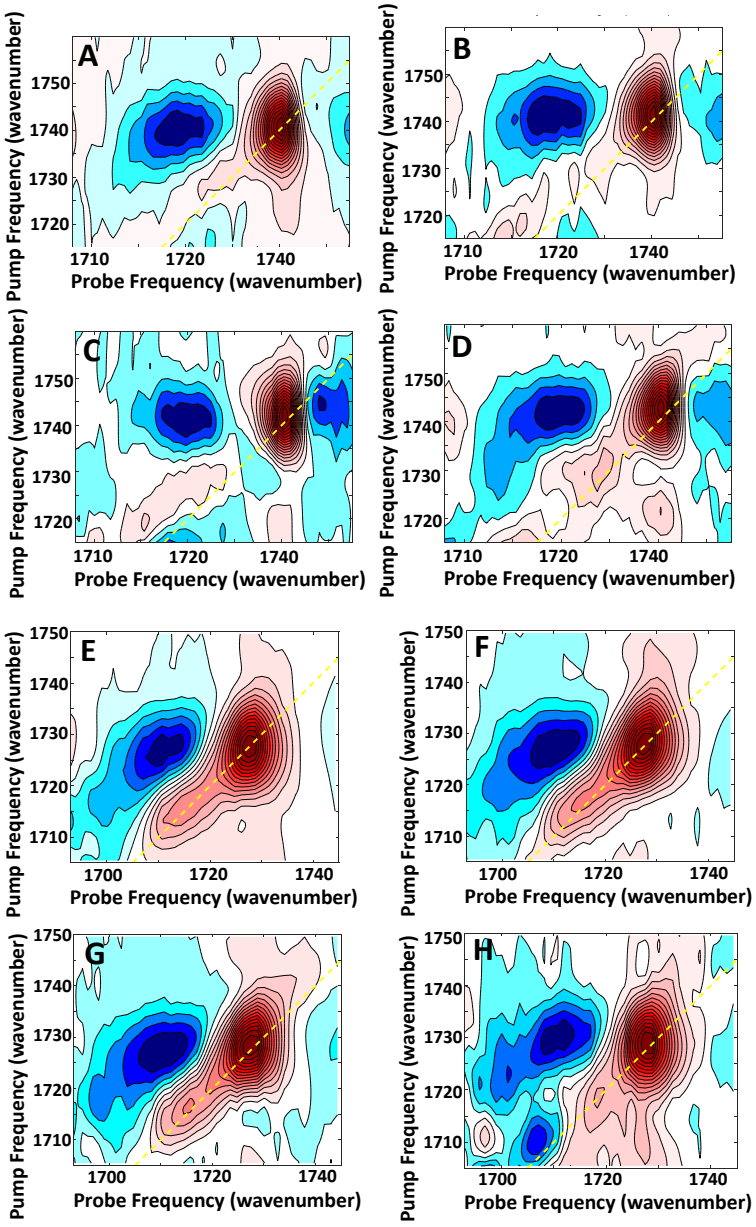

Figure 4.15 Subtracted 2D IR spectra of ester labels in ion channels. Spectra of wild type channels were subtracted from ester-labeled samples to isolate the ester label. A) $KcsA_{ester}$ at 0 fs delay, B) $KcsA_{ester}$ at 200 fs delay, C) $KcsA_{ester}$ at 500 fs delay, D) $KcsA_{ester}$ at 1000 fs delay, E) $NaK2K_{ester}$ at 0 fs delay, A) $NaK2K_{ester}$ at 200 fs delay, A) $NaK2K_{ester}$ at 500 fs delay, A) $NaK2K_{ester}$ at 1000 fs delay.

The data presented in figure 4.14G is very interesting in that it shows that the amide (orange) and ester (blue) are reaching their maxima at different delay times between the pump and probe. This suggests that there is some temporal chirp in the laser pulse. Temporal chirp is where the frequencies in the laser pulse are distributed in time. In 4.14G it is evident that the light at 1750 cm^{-1} appears to be hitting the sample over 500 fs after the light at 1660 cm^{-1}, based on where the peak intensity is the highest. Temporal chirp can be compensated for by applying corrections in the acoustic

optical modulator. The group velocity dispersion was changed until the time 0 of the amide I and time 0 of the ester carbonyl were the same.

Spectra were retaken of both KcsA and NaK2K at different delay times as shown in figure 4.15 after addressing the issues with the temporal chirp. The shown spectra generated from the WT constructs were then subtracted from the spectra generated from the ester constructs. Interestingly, there appears to not be a change in lineshape as a function of time. Lack of spectral diffusion in this new data suggests that earlier experiments showing spectral diffusion were in fact measuring the relaxation of residual lipids rather that of the ester label itself.

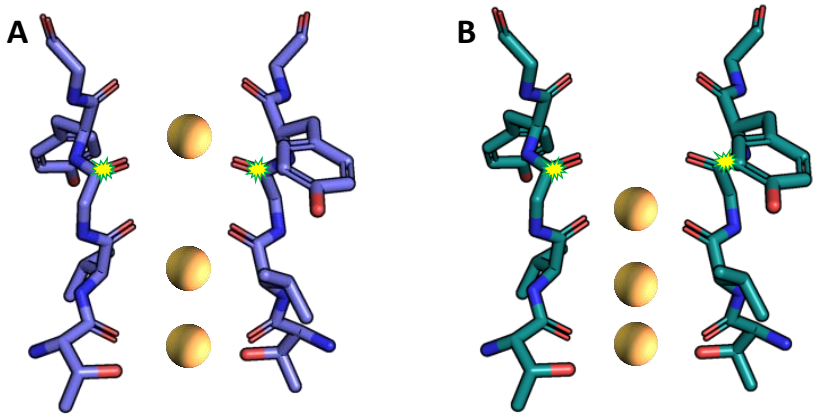

Figure 4.16 Representative cartoons of the selectivity filter of A) $KcsA_{ester}$ and B) $NaK2K_{ester}$. Yellow stars indicate the labelled carbonyl. Yellow spheres represent potassium ions.

Furthermore, the relatively 'round'—or at least not elongated nature of the peaks suggests perhaps a very static structure. Finally, these data further validate the observation that the ester label peaks are at different frequencies in $KcsA_{ester}$ and $NaK2K_{ester}$, despite having their labels at equivalent positions in the selectivity filter. In $KcsA_{ester}$, the ester label is found at 1745 cm^{-1} and in $NaK2K_{ester}$ the ester carbonyl is found at 1725 cm^{-1}. Interestingly, this corresponds to crystallography data that indicates that the ion occupancy of the two ester constructs is different. Soon-to-be-published data from the Valiyaveetil group indicates that in the crystal structure of $KcsA_{ester}$, the S2 site is collapsed and contains no ion. In $NaK2K_{ester}$, preliminary data indicates a

lack of ion occupancy at S1. These possible ion configurations are shown in figure 4.16. The label is between the S1 and S2 sites in the selectivity filter and is therefore also sensitive to these changes. As discussed earlier, previous work looking at ester carbonyl vibrations has shown that increases in hydrogen bonding as well as increase in ion concentration both result in the ester carbonyl vibration to shift to lower frequency. MD simulations may provide further information as to how the equivalent ester labels cause different effects in $KcsA_{ester}$ and $NaK2K_{ester}$.

4.5 Conclusions and Future Work

In this chapter I have presented significant process in observing an ester-labelled ion channel and making interesting measurements to probe the dynamics of the selectivity filter. Sample preparation has been optimized and various enhancement methods were also explored. Though the enhancement methods did not work for this particular application, they may be useful for future isotope label experiments. Ester carbonyl peaks were observed in both KcsA and NaK2K constructs. Preliminary waiting times experiments outline further questions to probe with these systems. What factors are influencing the ester carbonyl frequencies such as presence of an ion, water, or empty binding site? MD simulations may be able to shed light on this question, especially if the simulations are used to generate model 2D IR spectra. Furthermore, with a fuller set of waiting time data of $NaK2K_{ester}$ the vibrational lifetime as well as the number of exponentials in the fit may inform the number of ion binding configurations in the ester constructs. Beyond the immediate set of experiments, 2D IR spectra can generated for each of the ester sites in order to directly probe the ion configurations responsible for decreasing C-type inactivation, or the experiments can be expanded beyond the ion channels studied here.

Furthermore, the experiments set a precedent for the possibility of using a single isotope label to study the dynamics and ion occupancy of wild type ion channels.

4.6 References

(1) Hille, B. Ionic Channels of Excitable Membranes 2nd Edition. *Journal of The Electrochemical Society*. 1987, p 343.

(2) LeMasurier, M.; Heginbotham, L.; Miller, C. KcsA: It's a Potassium Channel. *J. Gen. Physiol.* **2001**, *118* (3), 303–314.

(3) MacKinnon, R. Potassium Channels and the Atomic Basis of Selective Ion Conduction (Nobel Lecture). *Angewandte Chemie - International Edition*. 2004, pp 4265–4277.

(4) Åqvist, J.; Luzhkov, V. Ion Permeation Mechanism of the Potassium Channel. *Nature* **2000**, *404* (6780), 881–884.

(5) Loussouarn, G.; BarÃ^3, I.; Escande, D. KCNQ1 K+ Channel Mediated Cardiac Channelopathies. In *Ion Channels*; Humana Press: Totowa, NJ, 2006; pp 167–183.

(6) Abdelsayed, M.; Sokolov, S. Voltage-Gated Sodium Channels: Pharmaceutical Targets via Anticonvulsants to Treat Epileptic Syndromes. *Channels (Austin).* **2013**, *7* (3), 146–152.

(7) Spampanato, J.; Escayg, A.; Meisler, M. H.; Goldin, A. L.; Anido, A.; Helmers, S. L.; Goldin, A. L.; Escayg, A. Functional Effects of Two Voltage-Gated Sodium Channel Mutations That Cause Generalized Epilepsy with Febrile Seizures plus Type 2. *J. Neurosci.* **2001**, *21* (19), 7481–7490.

(8) Berneche, S.; Roux, B. A Microscopic View of Ion Conduction through the K+ Channel. *Proc. Natl. Acad. Sci.* **2003**, *100* (15), 8644–8648.

(9) Kratochvil, H. T.; Maj, M.; Matulef, K.; Annen, A. W.; Ostmeyer, J.; Perozo, E.; Roux, B.; Valiyaveetil, F. I.; Zanni, M. T. Probing the Effects of Gating on the Ion Occupancy of the K+ Channel Selectivity Filter Using Two-Dimensional Infrared Spectroscopy. *J. Am. Chem. Soc.* **2017**, *139* (26), 8837–8845.

(10) Bernèche, S.; Roux, B. Energetics of Ion Conduction through the K+channel. *Nature* **2001**, *414* (6859), 73–77.

(11) Tilegenova, C.; Marien Cortes, D.; Jahovic, N.; Hardy, E.; Hariharan, P.; Guan, L.; Cuello, L. G. Structure, Function, and Ion-Binding Properties of a K+ Channel Stabilized in the 2,4-Ion–Bound Configuration. *Proc. Natl. Acad. Sci. U. S. A.* **2019**, *116* (34), 16829–16834.

(12) Lam, Y. L.; Zeng, W.; Sauer, D. B.; Jiang, Y. The Conserved Potassium Channel Filter

Can Have Distinct Ion Binding Profiles: Structural Analysis of Rubidium, Cesium, and Barium Binding in NaK2K. *J. Gen. Physiol.* **2014**, *144* (2), 181–192.

(13) Sauer, D. B.; Zeng, W.; Raghunathan, S.; Jiang, Y. Protein Interactions Central to Stabilizing the K + Channel Selectivity Filter in a Four-Sited Configuration for Selective K + Permeation. *Proc. Natl. Acad. Sci.* **2011**, *108* (40), 16634–16639.

(14) Doyle, D. A.; Cabral, J. M.; Pfuetzner, R. A.; Kuo, A.; Gulbis, J. M.; Cohen, S. L.; Chait, B. T.; MacKinnon, R. The Structure of the Potassium Channel: Molecular Basis of K + Conduction and Selectivity. *Science (80-.).* **1998**, *280* (5360), 69–77.

(15) Derebe, M. G.; Sauer, D. B.; Zeng, W.; Alam, A.; Shi, N.; Jiang, Y. Tuning the Ion Selectivity of Tetrameric Cation Channels by Changing the Number of Ion Binding Sites. *Proc. Natl. Acad. Sci.* **2011**, *108* (2), 598–602.

(16) Zhou, Y.; Morais-Cabral, J. H.; Kaufman, A.; Mackinnon, R. Chemistry of Ion Coordination and Hydration Revealed by a K+channel-Fab Complex at 2.0 Å Resolution. *Nature* **2001**, *414* (6859), 43–48.

(17) Noskov, S. Y.; Bernéche, S.; Roux, B. Control of Ion Selectivity in Potassium Channels by Electrostatic and Dynamic Properties of Carbonyl Ligands. *Nature* **2004**, *431* (7010), 830–834.

(18) Valiyaveetil, F. I.; Sekedat, M.; MacKinnon, R.; Muir, T. W. Structural and Functional Consequences of an Amide-to-Ester Substitution in the Selectivity Filter of a Potassium Channel. *J. Am. Chem. Soc.* **2006**, *128* (35), 11591–11599.

(19) Zhou, Y.; MacKinnon, R. The Occupancy of Ions in the K+selectivity Filter: Charge Balance and Coupling of Ion Binding to a Protein Conformational Change Underlie High Conduction Rates. *J. Mol. Biol.* **2003**, *333* (5), 965–975.

(20) Kratochvil, H. T.; Carr, J. K.; Matulef, K.; Annen, A. W.; Li, H.; Maj, M.; Ostmeyer, J.; Serrano, A. L.; Raghuraman, H.; Moran, S. D.; et al. Instantaneous Ion Configurations in the K+ Ion Channel Selectivity Filter Revealed by 2D IR Spectroscopy. *Science* **2016**, *353* (6303), 1040–1044.

(21) Kopfer, D. A.; Song, C.; Gruene, T.; Sheldrick, G. M.; Zachariae, U.; de Groot, B. L.; Quigley, A.; Grieben, M.; Goubin, S.; Mukhopadhyay, S.; et al. Ion Permeation in K+ Channels Occurs by Direct Coulomb Knock-On. *Science (80-.).* **2014**, *346* (6207), 352–355.

(22) Kopec, W.; Köpfer, D. A.; Vickery, O. N.; Bondarenko, A. S.; Jansen, T. L. C.; de Groot, B. L.; Zachariae, U. Direct Knock-on of Desolvated Ions Governs Strict Ion Selectivity in K+ Channels. *Nat. Chem.* **2018**, *10* (8), 813–820.

(23) Lu, T.; Ting, A. Y.; Mainland, J.; Jan, L. Y.; Schultz, P. G.; Yang, J. Probing Ion Permeation and Gating in a K+ Channel with Backbone Mutations in the Selectivity Filter. *Nat. Neurosci.* **2001**, *4* (3), 239–246.

(24) Bernèche, S.; Roux, B. A Gate in the Selectivity Filter of Potassium Channels. *Structure* **2005**, *13* (4), 591–600.

(25) Matulef, K.; Komarov, A. G.; Costantino, C. A.; Valiyaveetil, F. I. Using Protein Backbone Mutagenesis to Dissect the Link between Ion Occupancy and C-Type Inactivation in K + Channels. *Proc. Natl. Acad. Sci.* **2013**, *110* (44), 17886–17891.

(26) Matulef, K.; Annen, A. W.; Nix, J. C.; Valiyaveetil, F. I. Individual Ion Binding Sites in the K+ Channel Play Distinct Roles in C-Type Inactivation and in Recovery from Inactivation. *Structure* **2016**, *24* (5), 750–761.

(27) Cuello, L. G.; Jogini, V.; Cortes, D. M.; Perozo, E. Structural Mechanism of C-Type Inactivation in K+ Channels. *Nature* **2010**, *466* (7303), 203–208.

(28) Cordero-Morales, J. F.; Cuello, L. G.; Zhao, Y.; Jogini, V.; Cortes, D. M.; Roux, B.; Perozo, E. Molecular Determinants of Gating at the Potassium-Channel Selectivity Filter. *Nat. Struct. Mol. Biol.* **2006**, *13* (4), 311–318.

(29) Cuello, L. G.; Jogini, V.; Cortes, D. M.; Pan, A. C.; Gagnon, D. G.; Dalmas, O.; Cordero-Morales, J. F.; Chakrapani, S.; Roux, B.; Perozo, E. Structural Basis for the Coupling between Activation and Inactivation Gates in K+ Channels. *Nature* **2010**, *466* (7303), 272–275.

(30) Cordero-Morales, J. F.; Jogini, V.; Lewis, A.; Vásquez, V.; Cortes, D. M.; Roux, B.; Perozo, E. Molecular Driving Forces Determining Potassium Channel Slow Inactivation. *Nat. Struct. Mol. Biol.* **2007**, *14* (11), 1062–1069.

(31) Hoshi, T.; Zagotta, W. N.; Aldrich, R. W. Two Types of Inactivation in Shaker K+ Channels: Effects of Alterations in the Carboxy-Terminal Region. *Neuron* **1991**, *7* (4), 547–556.

(32) Hoshi, T.; Armstrong, C. M. C-Type Inactivation of Voltage-Gated K+ Channels: Pore Constriction or Dilation? *J. Gen. Physiol.* **2013**, *141* (2), 151–160.

(33) Zimmer, J.; Doyle, D. A.; Günter Grossmann, J. Structural Characterization and PH-Induced Conformational Transition of Full-Length KcsA. *Biophys. J.* **2006**, *90* (5), 1752–1766.

(34) Moran, S. D.; Zanni, M. T. How to Get Insight into Amyloid Structure and Formation from Infrared Spectroscopy. *J. Phys. Chem. Lett.* **2014**, *5* (11), 1984–1993.

(35) Mukherjee, P.; Kass, I.; Arkin, I.; Zanni, M. T. Picosecond Dynamics of a Membrane Protein Revealed by 2D IR. *PNAS March* **2006**, *7* (10), 3528–3533.

(36) Rodrigo, D.; Tittl, A.; Ait-Bouziad, N.; John-Herpin, A.; Limaj, O.; Kelly, C.; Yoo, D.; Wittenberg, N. J.; Oh, S.-H.; Lashuel, H. A.; et al. Resolving Molecule-Specific Information in Dynamic Lipid Membrane Processes with Multi-Resonant Infrared Metasurfaces. *Nat. Commun.* **2018**, *9* (1), 2160.

(37) Barth, A. The Infrared Absorption of Amino Acid Side Chains. *Progress in Biophysics and Molecular Biology*. 2000, pp 141–173.

(38) Ahmed, I. A.; Gai, F. Simple Method to Introduce an Ester Infrared Probe into Proteins. *Protein Sci.* **2017**, *26* (2), 375–381.

(39) Pazos, I. M.; Ghosh, A.; Tucker, M. J.; Gai, F. Ester Carbonyl Vibration as a Sensitive Probe of Protein Local Electric Field. *Angew. Chemie Int. Ed.* **2014**, *53* (24), 6080–6084.

(40) Hamm, P.; Zanni, M. *Concepts and Methods of 2D Infrared Spectroscopy*; 2011; Vol. 9781107000.

(41) Wals, K.; Ovaa, H. Unnatural Amino Acid Incorporation in E. Coli: Current and Future Applications in the Design of Therapeutic Proteins. *Front. Chem.* **2014**, *2*.

(42) Sarid, D.; Challener, W. Localized Surface Plasmons. In *Modern Introduction to Surface Plasmons*; 2013; pp 201–255.

(43) Giannini, V.; Fernández-Domínguez, A. I.; Heck, S. C.; Maier, S. A. Plasmonic Nanoantennas: Fundamentals and Their Use in Controlling the Radiative Properties of Nanoemitters. *Chem. Rev.* **2011**, *111* (6), 3888–3912.

(44) Adato, R.; Altug, H. In-Situ Ultra-Sensitive Infrared Absorption Spectroscopy of Biomolecule Interactions in Real Time with Plasmonic Nanoantennas. *Nat. Commun.* **2013**, *4* (1), 2154.

(45) Singh, P. SPR Biosensors: Historical Perspectives and Current Challenges. *Sensors Actuators B Chem.* **2016**, *229*, 110–130.

(46) Aouani, H.; Rahmani, M.; Šípová, H.; Torres, V.; Hegnerová, K.; Beruete, M.; Homola, J.; Hong, M.; Navarro-Cía, M.; Maier, S. A. Plasmonic Nanoantennas for Multispectral Surface-Enhanced Spectroscopies. *J. Phys. Chem. C* **2013**, *117* (36), 18620–18626.

(47) Shim, S.-H.; Zanni, M. T. How to Turn Your Pump–Probe Instrument into a Multidimensional Spectrometer: 2D IR and Vis Spectroscopiesvia Pulse Shaping. *Phys. Chem. Chem. Phys.* **2009**, *11* (5), 748–761.

(48) Fenn, E. E.; Fayer, M. D. Extracting 2D IR Frequency-Frequency Correlation Functions from Two Component Systems. *J. Chem. Phys.* **2011**, *135* (7), 074502.

(49) Tek, G.; Hamm, P. A Correction Scheme for Fano Line Shapes in Two-Dimensional Infrared Spectroscopy. *J. Phys. Chem. Lett.* **2020**, *11* (15), 6185–6190.

(50) Birdsall, E. R.; Petti, M. K.; Saraswat, V.; Ostrander, J. S.; Arnold, M. S.; Zanni, M. T. Structure Changes of a Membrane Polypeptide under an Applied Voltage Observed with Surface-Enhanced 2D IR Spectroscopy. *J. Phys. Chem. Lett.* **2021**, *12* (7), 1786–1792.

(51) Petti, M. K.; Ostrander, J. S.; Saraswat, V.; Birdsall, E. R.; Rich, K. L.; Lomont, J. P.;

Arnold, M. S.; Zanni, M. T. Enhancing the Signal Strength of Surface Sensitive 2D IR Spectroscopy. *J. Chem. Phys.* **2019**, *150* (2).

(52) Ostrander, J. S.; Lomont, J. P.; Rich, K. L.; Saraswat, V.; Feingold, B. R.; Petti, M. K.; Birdsall, E. R.; Arnold, M. S.; Zanni, M. T. Monolayer Sensitivity Enables a 2D IR Spectroscopic Immuno-Biosensor for Studying Protein Structures: Application to Amyloid Polymorphs. *J. Phys. Chem. Lett.* **2019**, *10* (14).

(53) Adato, R.; Yanik, A. A.; Amsden, J. J.; Kaplan, D. L.; Omenetto, F. G.; Hong, M. K.; Erramilli, S.; Altug, H. *Ultra-Sensitive Vibrational Spectroscopy of Protein Monolayers with Plasmonic Nanoantenna Arrays*.

(54) Ganim, Z.; Tokmakoff, A.; Vaziri, A. Vibrational Excitons in Ionophores: Experimental Probes for Quantum Coherence-Assisted Ion Transport and Selectivity in Ion Channels. *New J. Phys.* **2011**, *13*.

4.7 Supplemental Information

4.7.1 Supplemental Figures

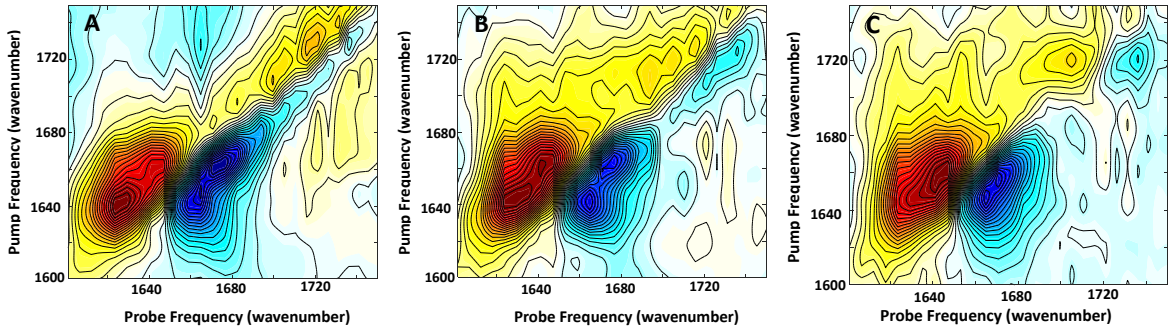

Figure 4.17 Impact of delay time on experimental background. NaK2KWT on nanoantennas with A) 0 fs of delay B) 200 fs of delay and C) 500 fs of delay

Spectra of NaK2K$_{WT}$ on nanoantennas were taken at various delay times and are shown in figure 4.15. Plasmonic background is seen in the background along the diagonal, but decreases as delay time between the second pump pulse and the probe pulse decreases. Spectra were phase corrected to even the magnitudes of the diagonal and overtone peaks. Due to the background, test

spectra of ion channel samples on the nanoantennas were generally obtained with a 400-500 fs delay time for quick verification.

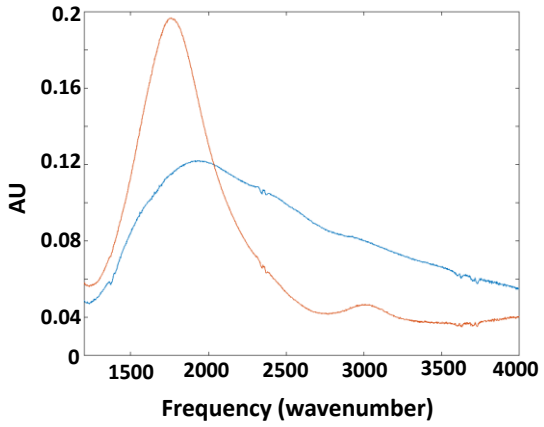

Figure 4.19 FTIR spectra of the narrow (orange) and broad (blue) nanoantenna arrays.

FTIR spectra were obtained of the 'narrow' and 'broad' nanoantenna arrays and are shown in figure 4.18. The 'narrow' array was centered at 1752 cm^{-1}. The 'broad' array was centered at about 1800 cm^{-1}. The difference in the width of the absorbance is due to the spacing of the array elements. In the 'narrow' array, the antennas are close together in the long axis of the antenna and well-spaced in the short axis of the antenna. The electric fields are concentrated at the ends of the antennas, and when they are close, they create a hot spot.[117] In the 'broad' array, the antennas are close together in the short axis of the antenna and well-spaced in the long axis of the antenna. Since the ends are no longer close, there is less intensity, but a broader absorbance.

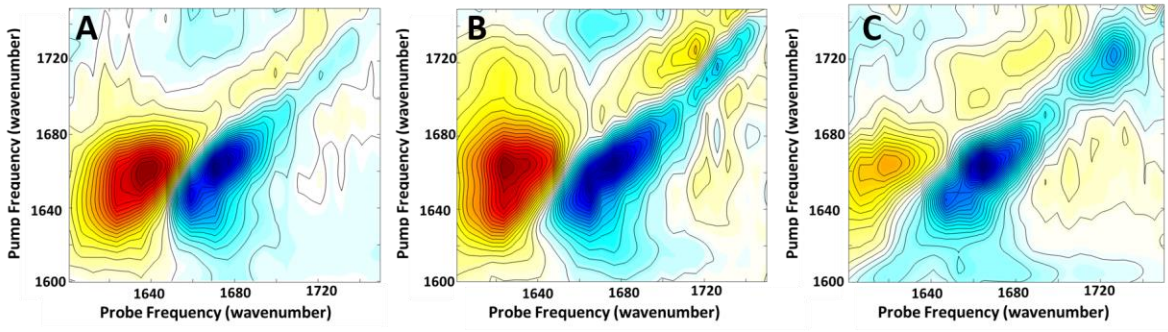

Figure 4.18 Angular dependent 2D IR spectra of $NaK2K_{WT}$ on nanoantenna. A) At 0 degrees. B) At 30 degrees rotating perpendicular to the direction of light propagation. C) At 30 degrees rotating in the plane of the direction of light propagation.

2D IR spectra of NaK2K$_{WT}$ on the narrow antenna were collected at different angles. Representative spectra are shown in figure 4.19. The spectra are phase corrected. The sample cell was rotated perpendicular to the direction of light propagation and in the plane of the direction of light propagation. As the antennas moved further from the optimum geometry in figure 4.19A, signal enhancement decreased and spectra became noisier.

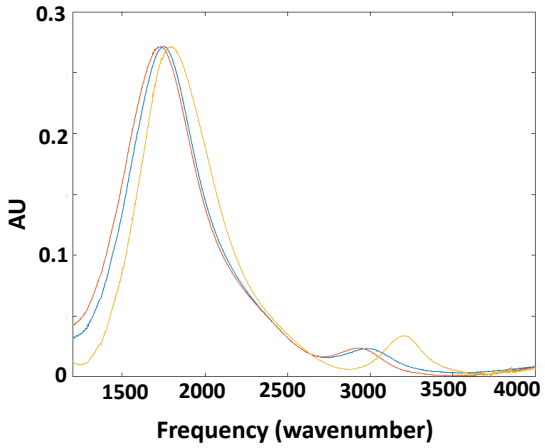

Figure 4.20 FTIR absorption spectra of three slightly different nanoantenna arrays. Window 1 (blue) has a length of 2243 nm, Window 2 (orange) has a length of 2334 nm, and Window 3 (yellow) has a length of 2152 nm.

FTIR absorbance spectra of the three 'narrow' nanoantenna arrays are shown in figure 4.17. Here the change in dimension of the arrays and the resulting change in center frequency is demonstrated. The original 'narrow' array is the same as 'window 1' with a center frequency of 1752 cm^{-1}. 'Window 2' is centered at 1731 cm^{-1}. Spacing in the short axis of the antenna is the same between all antennas. In the long axis, the sum of the antenna and gap are the same between 'window 1' and 'window 2', but in 'window 2' the antenna is longer and the gap is smaller. The lower frequency is logical since the length of an antenna is positively correlated with the center of the absorbance spectrum in *wavelength*.[117] 'Window 3'is centered at 1795 cm^{-1}. In the long axis, the sum of the antenna and gap are the same between 'window 1' and 'window 3' as well. In 'window 3' the antenna is shorter and the gap is larger. Again, this results in a higher frequency due to the correlation between antenna length and center *wavelength*.

5 Enhancement of Signal through Polarization[2]

Surfaces and interfaces are ubiquitous in nature. From cell membranes, to photovoltaic thin films, surfaces have important function in both biological and materials systems. Spectroscopic techniques have been developed to probe systems like these, such as sum frequency generation (SFG) spectroscopies. The advantage of SFG, a second-order spectroscopy, is that it can distinguish between signals produced from molecules in the bulk versus on the surface. We propose a polarization scheme for third-order spectroscopy experiments, like pump-probe and 2D spectroscopy, to select for surface signals and not bulk signals. This proposed polarization condition uses one pulse perpendicular compared to the other three to isolate cross-peaks arising from molecules with polar and uniaxial (i.e., biaxial) order at a surface while removing the signal from bulk isotropic molecules. In this work, we focus on two of these cases: XXXY and YYYX, which differ by the sign of the cross-peak they create. We compare this technique to SFG and VCD to provide insight as to the behavior of the cross-peak signal. We propose that these singularly cross-polarized schemes provide odd-ordered spectroscopies the *surface-specificity* typically associated with even-ordered techniques.

5.1 Introduction

Molecules on a surface or at interfaces are known to align in some amount of order, which is important for many branches of chemistry. Ordering can occur in one-direction

[2] Reprinted with permission from Megan K. Petti, Joshua S. Ostrander, **Erin R. Birdsall**, Miriam Bohlmann Kunz, Zachary Armstrong, Ariel M. Alperstein, and Martin T. Zanni. *A Proposed Method to Obtain Surface Specificity with Pump-probe and 2D Spectroscopies* J. Phys. Chem A. 2020, 124, 17, 3471–3483

I contributed to this work by verifying the mathematical basis of the technique as well as helping to write the paper.

(uniaxial) or two-directions (biaxial). Examples of these types of ordered systems are depicted in Figure 5.1B. At the top of the figure are two examples of biaxial systems, an α-helical peptide in a lipid bilayer[125,126] and a small molecule, α-pinene, on a silica surface[127]. Both of these systems have a specified tilt (θ) and twist angle (ψ) relative to the surface, making then biaxial systems. A system that might be expected to be largely uniaxial is water at an air interface (Figure 5.1B, bottom)[128,129]. Here, there is a defined tilt angle (θ), but the molecules might sample all twist angles (ψ). In this work, we focus on surface systems with biaxial order or non-uniform uniaxial order. Other systems that contain biaxial order include membrane proteins within lipid bilayers[130,131], self-assembled monolayers[77,132,133], polymer films[134–137], catalytic molecules tethered to a surface[60,138], and some liquid crystals[139,140]. These systems have reduced symmetry at a macroscopic level due to the molecular alignment that can alter chemical and material properties of the system.

In general, molecules at surfaces and interfaces are difficult to study because they are few in number and are usually overwhelmed by signal from the bulk. However, there are linear and nonlinear spectroscopies well suited to the task.[73,141] These nonlinear techniques can be divided into two categories: *surface-sensitive* and *surface-specific*. In general, any technique can be *surface-sensitive*, as it only requires the technique to have adequate sensitivity to measure the small number of molecules present in a surface system, such as a monolayer of chemisorbed molecules.[60,88,142,143] Some examples of *surface-sensitive* 2D spectroscopic techniques in the infrared is the work of Fayer and Hamm. Fayer has shown that 2D IR spectroscopy has the sensitivity to measure a single monolayer when the local oscillator intensity is reduced at an interface.[66,132,144] Hamm has taken a different approach and used an attenuated total reflection geometry (ATR) in combination with localized surface plasmons of metallic nanoparticle coated

surfaces to provide enhancement of the signal of molecules near the surface.[64,65,88,142] *Surface-specific* techniques, on the other hand, are only able to detect signals that are produced by molecules at a surface or interface and not the signals from molecules present in the bulk, such as at an interface of two bulk materials.[4,30–34] Normally, the technical distinction between *surface-sensitive* and *surface-specific* non-linear techniques is the order of the susceptibility measured. For example, sum frequency generation (SFG) spectroscopy is an even-ordered spectroscopy that measures the second order susceptibility and is inherently sensitive to surfaces.[35,36] In general, even-ordered susceptibilities of a centrosymmetric media, like a bulk solution, average to zero in the dipole approximation.[37] However, if the symmetry of the system is broken, like at an

interface, then the even-ordered susceptibilities become significant. Due to this dependence on the symmetry of the system, even-ordered spectroscopies only measure signals from interfacial molecules, without any interference of bulk signals, making these techniques *surface-specific*.[38] Typically, odd-ordered spectroscopies cannot make this same type of distinction as the susceptibilities from both the bulk system and the surface system will be relevant regardless of the centrosymmetry of the system.

At the microscopic level, a reduction of symmetry can occur when an individual component of a system has a specified direction, such as when a molecule has a chiral center. Being able to distinguish between enantiomers requires measuring signatures that are intrinsic to

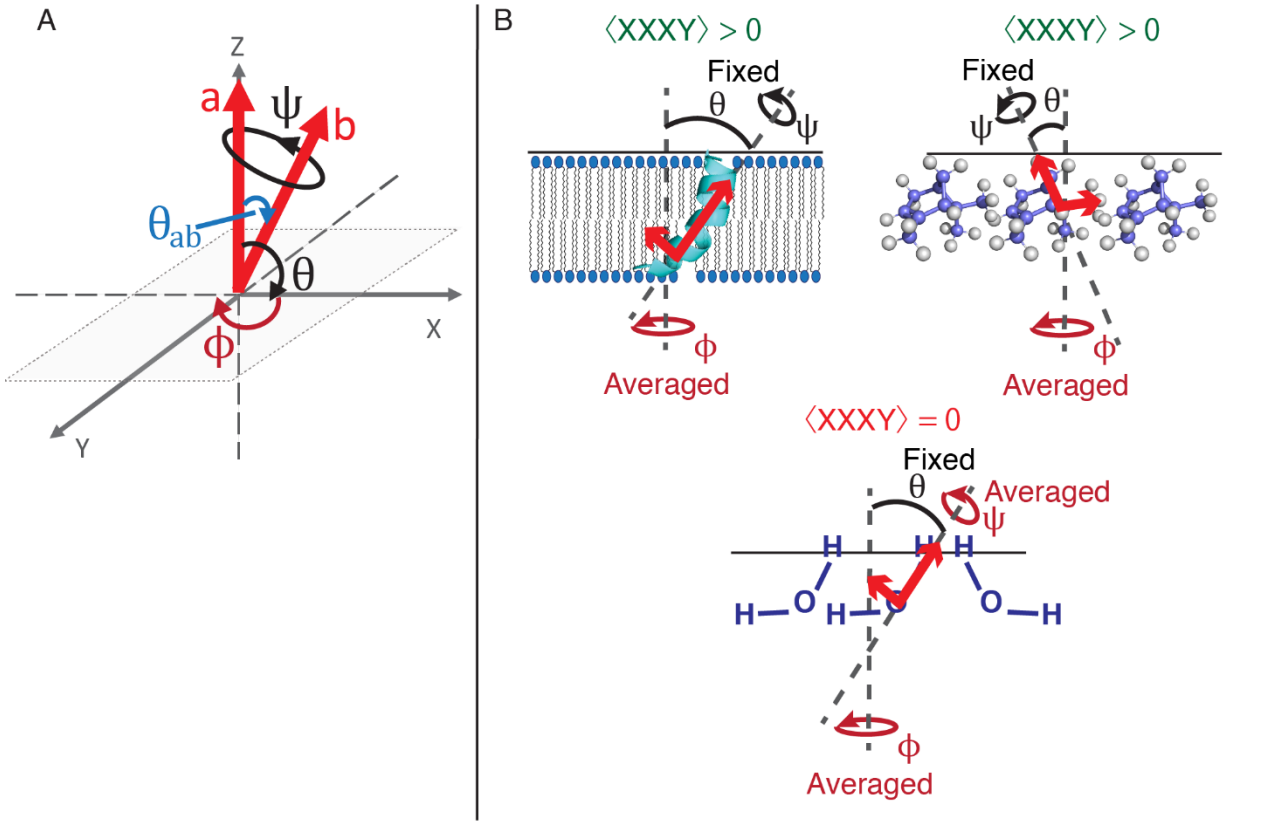

Figure 5.5.1 (a) Schematic of the orientation of two coupled oscillators, a and b, depicted as red arrows in XYZ space. ϕ is the XY plane, θ is in the ZX plane, and ψ is twist angle of the oscillators. Z is the direction light is propagating. (b) Examples of surface systems that have biaxial symmetry (top) and an example that does not have biaxial symmetry (bottom).

a specific chirality. Circular dichroism is able to accomplish this distinction. Vibrational circular dichroism (VCD) measures the optical activity related to how chiral molecules interact with left versus right circularly polarized infrared light to produce a differential absorption spectra (left-circularly polarized minus right-circularly polarized light).[39–41] Thus, one enantiomer (R-) will produce absorption features with opposite sign of that of the complementary enantiomer (S-). A racemic mixture of molecules will not produce a VCD signal, as the absorption of the two enantiomers will cancel out. Due to this dependence on the molecular structure, VCD has been used to obtain structural information on chemical and biological systems.

In the work presented here, we propose that *surface-specific* information can be obtained from an odd-order (in this case, third-order) experiment for a biaxial surface, meaning that the system has both uniaxial order over the twist (ψ) angle and polar order over the tilt angle (θ). The key is to set one of the pulses perpendicular to the other three in the four-wave mixing process. The same trick can be applied to other third-order techniques, like pump-probe spectroscopy. These select for third-order cross-peaks pathways from molecules at the surface, while the third-order pathways from molecules in the bulk are zero, effectively extending odd-ordered spectroscopies into a *surface-specific* domain. This work is similar to the chirality-induced 2D, a two-dimensional analogue of VCD, spectroscopy proposed by Mukamel and colleagues employing the same polarization scheme.[42,43] The difference is that our work is completely dipole allowed and does not require the molecule to be inherently chiral. The only requirements are 1) that there is macroscopic uniaxial and polar order at the surface and 2) that the molecule or molecules of interest have coupled and non-parallel transition dipoles. A similar approach has been proposed to measure surface-specific signals in nonlinear Raman and linear fluorescence spectroscopic measurments.[44,45] In this manuscript, we provide the mathematical

background and simulated 2D spectra to describe this singularly cross-polarized technique. We also compare our work with SFG and VCD to elaborate on the similarities and differences with our proposed technique.

5.2 Computational Background and Methods

Two-dimensional third-order spectroscopies can be thought of as frequency resolved pump-probe techniques that disperse the frequencies of the pump along one axis and the probe along the other.[46–49] This creates a two-dimensional energy correlation map that provides information about the orientation and energy transfer of these states. For example, consider a simple small molecule that has two coupled states that absorb at different frequencies. This system results in three major characteristics of the spectrum: diagonal peaks, cross-peaks, and the lineshape of these peaks. In this work, we focus on the first two characteristics. The diagonal peaks arise from one state, while the cross-peaks are observed when two states are coupled together. This coupling can be either electronic or mechanical in nature.[49–52]

We are interested in the third-order signals that create these 2D spectrum of both bulk and surface systems. The main difference between these two cases is the macroscopic orientation of the systems i.e., the orientation of an ensemble of molecules. For the bulk system, we consider two coupled oscillators that are dispersed in an isotropic ensemble. For the surface system, we consider two coupled oscillators that are aligned normal to the surface at a specific angle (θ) and have a specified twist angle (ψ) (Figure 5.1A).

The orientation of each of these systems are mapped into the third-order signal and can be described generally by a four-point correlation function as follows:[46–48,53]

$$S \propto \langle(\vec{\mu}_\delta \cdot \vec{E}_d)(\vec{\mu}_\gamma \cdot \vec{E}_c)(\vec{\mu}_\beta \cdot \vec{E}_b)(\vec{\mu}_\alpha \cdot \vec{E}_a)\rangle$$

(5.1)

In equation 5.1, S is the third-order signal that is proportional to the expectation value (represented by the brackets $\langle \ldots \rangle$) of the dipole operator for one particular Feynman pathway. The light-matter interactions for one such pathway is described by the dot product between four arbitrary transition dipole vectors ($\vec{\mu}_\delta$, $\vec{\mu}_\gamma$, $\vec{\mu}_\beta$, $\vec{\mu}_\alpha$) and electric field vectors ($\vec{E}_d$, $\vec{E}_c$, $\vec{E}_b$, $\vec{E}_a$). This function holds under the semi-impulsive limit and the dipole approximation. This equation can further be separated into the magnitude and the direction of these vectors. By ignoring the magnitude of these vectors, the orientational four-point correlation function is described by equation 5.2 where we now represent these unit vectors with a hat ($\widehat{\ }$).

$$S \propto \langle(\hat{\mu}_\delta \cdot \hat{E}_d)(\hat{\mu}_\gamma \cdot \hat{E}_c)(\hat{\mu}_\beta \cdot \hat{E}_b)(\hat{\mu}_\alpha \cdot \hat{E}_a)\rangle$$

(5.2)

Equation 5.2 describes four arbitrary transition dipole directions interacting with four arbitrarily polarized pulses. With this equation, we can calculate the third-order signal in the X, Y, and Z directions by evaluating equation 5.2. We can do this for the many Feynman pathways that describe the possible light-matter interactions for both bulk and surface systems. We choose to only evaluate the four-point correlation function for eight Feynman pathways (*iiii, jjjj, iijj, ijij, ijji, jjii, jiji, jiij*) that describe 2D spectra. In general, Feynman pathways describe the time ordering of interactions between an oscillator (*i* or *j* in this case) with an electric field. A double-sided Feynman diagram, as in Figure 5.2, allows for visualization of how the dipole operator operates. Arrows pointing to the left operate on the bra side, while arrows pointing to the right

operate on the ket side. Figure 5.2 depicts the rephasing and non-rephasing pathways that contribute to the diagonal peaks and cross-peaks in 2D spectra.

To evaluate equation 5.2, four steps are required. First, the defined dipoles (a and b in Figure 5.1A), are rotated into the lab frame. Then, the third-order susceptibility ($\chi^{(3)}$) is calculated by considering the projection of the lab frame dipoles in three-dimensional space. Next, the third-order polarization ($P^{(3)}$) is calculated by convoluting the calculated susceptibility with polarized electric fields. Lastly, the projection of the third-order polarization in the direction of detection is calculated.[44,48,54]

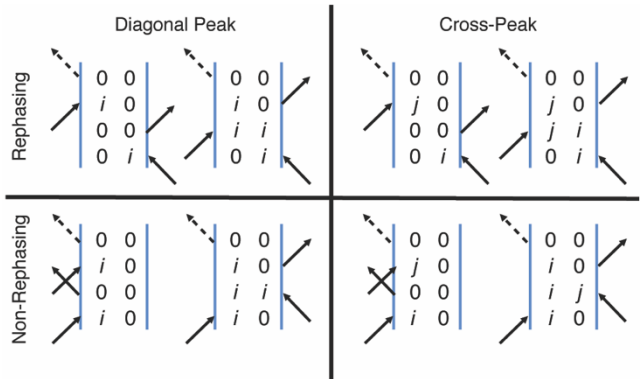

Figure 5.5.2 Double sided Feynman diagrams for arbitrary oscillators i and j for both rephasing and non-rephasing pathways that describe the diagonal and cross-peaks in third-order spectroscopy. The diagonal peaks are shown as interactions only with i and can be represented as *iiii*. The cross-peaks have interactions with both *i* and *j* and can be represented as *iijj*, *ijij*, and *ijji*. Note, *ijji* is a non-rephasing pathway, *ijij* is a rephasing pathways, and *iijj* is both.

For the first step in this calculation, we begin by rotating the defined dipoles into the lab frame. To do so, one may use spherical harmonics[55] or a tensor method.[53] We have chosen to use Euler angles to calculate the dependence of the signal on orientation.[54] With this method we first take our two oscillators defined in the molecular frame and rotate them into the lab frame via a Euler rotation matrix. The projection of these lab frame dipoles is then calculated in the X, Y, and Z directions.

Next, the third-order susceptibility is calculated by considering the macroscopic orientation of the system of interest. For the bulk system, the molecules are isotropic; therefore; to obtain a macroscopic orientation of the sample, all possible configurations in three-dimensional space must be considered. Thus, the third-order susceptibility is integrated over all

space that is defined in spherical coordinates by the three angles: ϕ, θ, and ψ. These angles are evaluated from 0 to 2π, 0 to π, and 0 to 2π, respectively. For the surface system, the surface limits the possible orientations of the molecule, introducing anisotropy and reducing the symmetry of the system. Figure 5.1A defines the surface system where there are two coupled oscillators, a and b, in the XZ plane (the surface is shown in the XY plane). The angle θ_{ab} separates the two dipoles. In the cases discussed, θ_{ab} is set to 30°. Other values for θ_{ab} have also been evaluated (results shown in Figures 5.7 – 5.10). In the case where molecules at the surface are highly ordered, the tilt angle (θ), and the twist angle (ψ) are set, creating a system with polar and uniaxial order. In other words, the system is biaxial, leading to ensemble differences only in the ϕ dimension. Thus, for the surface system, the evaluation of the third-order susceptibility need only be evaluated over ϕ. In general, systems that satisfy this type of symmetry are self-assembled monolayers, thin-films, lipid bilayers, and surface-oriented membrane proteins monolayers.[15,56,57]

We then calculate the third-order macroscopic polarization by taking the evaluated susceptibilities and accounting for the polarization of each pulse. The resulting macroscopic polarization is summed over all possible combinations in the X, Y, and Z directions. We then determine detected signal by calculating the projection of the signal in all possible directions of detection. We consider two cases for detecting the signal. In the first case, the detected signal is parallel to the incident light, while in the second case the detected signal is perpendicular to the incident light. We distinguish between these polarization conditions by referring to them as either XXXX (parallel detection) or XXXY (perpendicular detection). We note that by convention, for four-wave mixing experiments, the polarization notation above refers to the polarization of light used where the fourth interaction is from a local oscillator. In our

calculations, we refer to the fourth interaction as the direction of the detected signal, although the use of an external local oscillator would result in the same conclusions. Figure 5.1A depicts the X and Y directions with the Z direction normal to the surface. The final projections of the third-order macroscopic polarization correspond to the orientational four-point correlation function described by equation 5.2.

Overall, we evaluate the detected signal for the Feynman pathways associated with third-order spectroscopies for both bulk and surface systems under two polarization conditions; XXXX and XXXY. We then use those results to map how these pathway responses influence the diagonal and cross-peak signals in a 2D spectrum. Additional details of the procedure and simulations are given in the supplemental material.

5.3 Results and Discussion

In the following, we divide our Results and Discussion into four sections (orientational four-point correlation functions, diagonal and cross-peak intensities, simulated 2D spectra, and comparison to SFG and VCD) to investigate the polarization scheme XXXY from the bottom up. In other words, we begin by evaluation of the four-point correlation functions for XXXY and use that information to simulate 2D spectra. This method provides insight into how the XXXY polarization scheme can be used to detect signals from surface systems and not the bulk.

5.3.1 Orientational Four-Point Correlation Functions

The orientational four-point correlation function solutions for isotropic systems have previously been published and are rewritten here in equations 5.3 and 5.4.[48,53] There is no variation in the detected signal as a function of twist (ψ) and tilt (θ) angles (Figure 5.12).

$$\langle(\hat{\mu}_i \cdot \hat{E}_X)(\hat{\mu}_i \cdot \hat{E}_X)(\hat{\mu}_i \cdot \hat{E}_X)(\hat{\mu}_i \cdot \hat{E}_X)\rangle = \frac{1}{8\pi^2}\int_0^{2\pi} d\psi \int_0^{\pi} d\theta \int_0^{2\pi} d\phi \sin\theta(\sin\phi \sin\theta)^4 = \frac{1}{5}$$

(5.3)

$$\langle(\hat{\mu}_i \cdot \hat{E}_X)(\hat{\mu}_i \cdot \hat{E}_X)(\hat{\mu}_j \cdot \hat{E}_X)(\hat{\mu}_j \cdot \hat{E}_X)\rangle$$

$$= \frac{1}{8\pi^2}\int_0^{2\pi} d\psi \int_0^{\pi} d\theta \int_0^{2\pi} d\phi \sin\theta(\sin\phi \sin\theta)^2(\sin\theta_{ab}\,(-\sin\psi\cos\theta\sin\phi$$

$$+ \cos\phi\cos\psi) + \sin\theta\sin\phi\cos\theta_{ab})^2 = \frac{1}{15}(2(\cos\theta_{ab})^2 + 1)$$

(5.4)

For the XXXX polarization conditions for the bulk isotropic system, the constant value is 1/5 for pathways that only interact with one oscillator (*iiii* and *jjjj*). For the other six pathways that

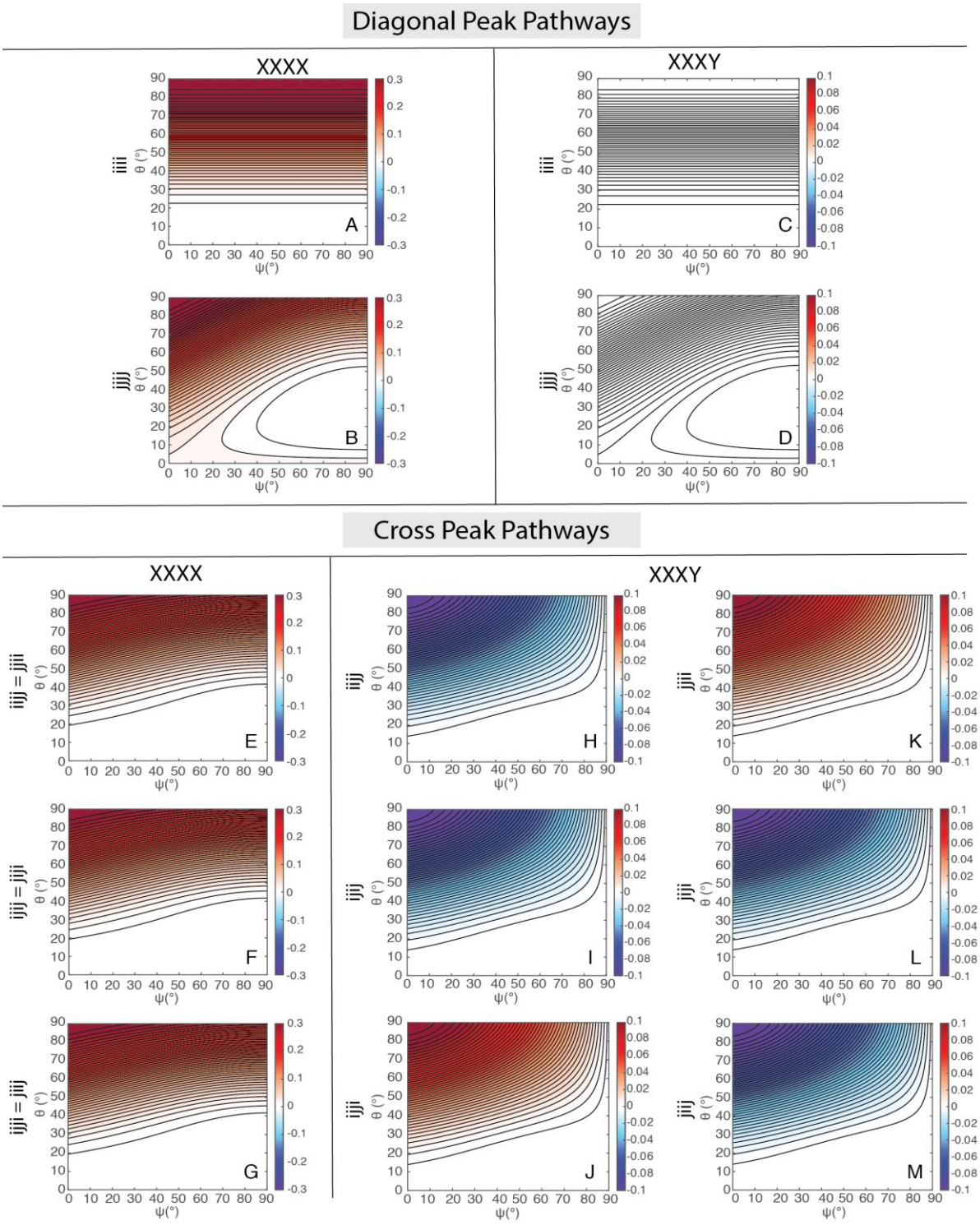

Figure 5.5.3 Orientational four-point correlation function values for the pathways *iiii*, *jjjj*, *iijj*, *ijij*, *ijji*, *jjii*, *jiji*, and *jiij* as a function of θ and ψ for the surface system using two different polarization conditions: XXXX and XXXY.

involve interactions with both oscillators, the constant value is equivalent for all pathways (*iijj* = *jjii* = *ijij* =*jiji* = *ijji* = *jiij*) and depends on the angle between the two oscillators (θ_{ab}). For the

XXXY case, the signal of the bulk system for all pathways goes to zero (Figure 5.12), because the functions are odd (equations 5.29-5.31).

Evaluation of the orientational four-point correlation function for the surface system leads to different functions. Due to the order imposed by the surface, the system is azimuthally isotropic, and the resulting third-order susceptibility is integrated over ϕ. This leads to an orientational dependence on the detected signal for the surface system as a function of θ and ψ for all the pathways considered for both XXXX and XXXY (Figure 5.3). We plot the signal of eight Feynman pathways for the XXXX and XXXY polarization schemes for the surface system as a function of $\theta = 0° - 90°$ and $\psi = 0° - 90°$. All possible values of θ and ψ have been investigated and can be found in figure 5.11. The difference between the two polarization conditions for the surface system is readily apparent. For XXXX, all eight pathways have positive values that depend on the θ and ψ values and the six cross-peak pathways are equivalent (Figure 5.3E-G). In XXXY, the *iiii* and *jjjj* pathways are zero, while the remaining six cross-peak pathways provide a response as a function of θ and ψ. In other words, the XXXY four-point correlation functions are even-order functions over ϕ for the cross-peak pathways. Thus, these functions are not zero when integrating between 0 and 2π. Moreover, the cross-peak pathways are not equivalent in the XXXY case. For the XXXY polarization configuration, $iijj = -jjii$, $ijij = jiji$, and $ijji = -jiij$. Also, for the *iijj*, *ijij*, *jiji*, and *jiij* pathways, the response has flipped sign (is now negative) when compared to the XXXX polarization condition. These differences in the pathway response have implications for the sign of the signals observed in an XXXY configuration.

We note that setting any one of the pulses in the four-wave mixing process perpendicular to the other three pulses should produce the same results as XXXY. For the surface system, this

means that the diagonal peak pathways are zero, while the cross-peak pathways are not, while for the bulk system, all pathways are zero. There are eight possible polarization schemes (XXXY, XXYX, XYXX, YXXX, YYYX, YYXY, YXYY, and XYYY) that are all able to detect surface signals. However, while the schemes are equivalent for the *iiii* and *jjjj* pathways, the schemes are not completely equivalent for the off-diagonal cross-peak total functions. For the surface system, we outline these differences by calculating the total four-point correlation function for an off-diagonal cross-peak (the *i-j* cross-peak) for two of these eight possible schemes: XXXY and XXYX.

The pathways that make up the *i-j* off-diagonal cross-peak are the rephasing *ijij*, rephasing *iijj*, and non-rephasing *iijj* pathways. In the argument that follows we assume that all pathways contribute equally. If the pathways contributions were unequal, the intensity of the peaks in the spectra would be modulated. In the XXXY polarization configuration, the *ijij* and *iijj* pathways are equivalent. For these pathways, as there are two interactions with oscillator *i* in the X direction, one interaction with *j* in the X direction, and one interaction with *j* in the Y direction. Equation 5.5 evaluates the orientational four-point correlation function for the surface with a XXXY polarization scheme for both the *ijij* and *iijj* pathways.

$$\begin{aligned}\langle(\hat{\mu}_i\cdot\hat{E}_X)(\hat{\mu}_j\cdot\hat{E}_X)(\hat{\mu}_i\cdot\hat{E}_X)(\hat{\mu}_j\cdot\hat{E}_Y)\rangle &= \langle(\hat{\mu}_i\cdot\hat{E}_X)(\hat{\mu}_i\cdot\hat{E}_X)(\hat{\mu}_j\cdot\hat{E}_X)(\hat{\mu}_j\cdot\hat{E}_Y)\rangle \\ &= \frac{1}{2\pi}\int_0^{2\pi} d\phi\,(\sin\phi\sin\theta)^2(\sin\theta_{ab}(-\sin\psi\cos\theta\sin\phi + \cos\phi\cos\psi) \\ &+ \sin\theta\sin\phi\cos\theta_{ab})(\sin\theta_{ab}(-\sin\psi\cos\theta\cos\phi - \sin\phi\cos\psi) \\ &+ \sin\theta\sin\phi\cos\theta_{ab}) \\ &= -\frac{\cos\psi\sin\theta_{ab}\,(\sin\theta)^2}{4}(\cos\theta_{ab}\sin\theta - \cos\theta\sin\psi\sin\theta_{ab})\end{aligned}$$

(5.5)

On the other hand, when we consider the *ijij* and *iijj* pathways in XXYX, the pathways are not equivalent. In the case of *iijj*, there are two interactions with oscillator *i* in the X direction, one interaction with oscillator *j* in the X direction, and one interaction with oscillator *j* in the Y direction. For *ijij*, there are instead two interactions with oscillator *j* in the X direction, one interaction with oscillator *i* in the X direction, and one interaction with oscillator *i* in the Y direction. These leads to two different four-point correlation functions for the *ijij* and *iijj* pathways in the XXYX polarization scheme. These are evaluated in equations 5.6 and 5.7.

$$\langle(\hat{\mu}_i \cdot \hat{E}_X)(\hat{\mu}_j \cdot \hat{E}_X)(\hat{\mu}_i \cdot \hat{E}_Y)(\hat{\mu}_j \cdot \hat{E}_X)\rangle$$

$$= \frac{1}{2\pi}\int_0^{2\pi} d\phi \sin\phi \sin\theta \,(\sin\theta_{ab}(-\sin\psi\cos\theta\cos\phi - \sin\phi\cos\psi)$$

$$+ \sin\theta\sin\phi\cos\theta_{ab})^2 \cos\phi\sin\theta = \frac{\cos\psi\sin\theta_{ab}\,(\sin\theta)^2}{4}(\cos\theta_{ab}\sin\theta$$

$$- \cos\theta\sin\psi\sin\theta_{ab})$$

(5.6)

$$\langle(\hat{\mu}_i \cdot \hat{E}_X)(\hat{\mu}_i \cdot \hat{E}_X)(\hat{\mu}_j \cdot \hat{E}_Y)(\hat{\mu}_j \cdot \hat{E}_X)\rangle$$

$$= \frac{1}{2\pi}\int_0^{2\pi} d\phi \,(\sin\phi\sin\theta)^2(\sin\theta_{ab}(-\sin\psi\cos\theta\sin\phi + \cos\phi\cos\psi)$$

$$+ \sin\theta\sin\phi\cos\theta_{ab})(\sin\theta_{ab}(-\sin\psi\cos\theta\cos\phi - \sin\phi\cos\psi)$$

$$+ \sin\theta\sin\phi\cos\theta_{ab})$$

$$= -\frac{\cos\psi\sin\theta_{ab}\,(\sin\theta)^2}{4}(\cos\theta_{ab}\sin\theta - \cos\theta\sin\psi\sin\theta_{ab})$$

(5.7)

These differences in the orientational four-point correlation functions of the *iijj* and *ijij* pathways leads to a different value for the total function that defines the off-diagonal cross-peak that depends on the polarization used. In the case of XXXY, where the rephasing *ijij*, rephasing *iijj*, *and* non-rephasing *iijj* are equivalent, then the total contribution to the off-diagonal cross-peak will just be three times that of equation 5.5. This total function is expressed in equation 5.8. For XXYX, ijij and *iijj* have four-point correlation functions that differ in the sign of the function; *iijj* is the negative of *ijij*. To obtain the total, we add the function for *ijij* (Eq. 5.6) to twice that of the function for *iijj* (Eq. 5.7) (to account for the rephasing and non-rephasing pathways contributions), leading to the result in equation 5.9 for the total off-diagonal cross-peaks in XXYX:

$$XXXY_{off-diagonal\ cross-peak} = -\frac{3\cos\psi\sin\theta_{ab}\,(\sin\theta)^2}{4}(\cos\theta_{ab}\sin\theta - \cos\theta\sin\psi\sin\theta_{ab})$$

(5.8)

$$XXYX_{off-diagonal\ cross-peak} = -\frac{\cos\psi\sin\theta_{ab}\,(\sin\theta)^2}{4}(\cos\theta_{ab}\sin\theta - \cos\theta\sin\psi\sin\theta_{ab})$$

(5.9)

Equation 5.8 and equation 5.9 provide the following relationship between the polarization conditions XXXY and XXYX for the surface system:

$$XXXY_{off-diagonal\ cross-peak} = 3\ XXYX_{off-diagonal\ cross-peak}$$

(5.10)

Equation 5.10 shows that the off-diagonal cross-peak intensity of XXXY will be three times that of the off-diagonal cross-peak intensity in XXYX. We can do this same analysis of the orientational four-point correlations functions for the other six polarization schemes to determine the relationships between them. Table 5.1 depicts these relationships. The evaluated orientational four-point correlation functions for the remaining six polarization schemes can be found in the supplemental material (Eq. 5.15-5.28). It should be noted that while this argument only considers the *i-j* cross-peak, the same conclusions can be made when considering the *j-i* cross-peak.

Table 5.1 Relationships between all possible singularly cross-polarized cross-peak four-point correlation functions.

Mostly X interactions	Mostly Y interactions
XXXY = 3XXYX	YYYX = 3YYXY
YXXX = 3 XYXX	XYYY = 3 YXYY
Overall Relationships	
XXXY = −YXXX = −YYYX = XYYY	
XXYX = −XYXX = −YYXY = YXYY	

5.3.2 Diagonal and Cross-Peak Intensities

The differences between the bulk and surface systems pathways shown in Figure 5.12 and Figure 5.3 ultimately influence the 2D spectra collected. By considering what pathways contribute to which peaks, we can elucidate how the diagonal and cross-peaks differ between the bulk and surface systems. The *iiii* and *jjjj* pathways correspond to diagonal peaks. The *iijj* and *ijij* pathways correspond to the lower *i-j* cross-peak (as oscillator *i* is set to absorb at a lower energy), and the *jjii* and *jiji* pathways correspond to the upper *j-i* cross-peak. The non-rephasing *ijji* and the non-rephasing *jiij* pathway contains cross-peaks that appear on the diagonal. We plot the normalized (to the maximum value) diagonal and cross-peak intensity dependence on θ and ψ for both bulk and surface systems in Figure 5.4. It is assumed that each pathway contributes equally. As before, we consider the XXXX and XXXY polarization conditions. For the bulk, we obtain the expected result. For the XXXX polarization, there is no dependence on θ and ψ angles as the macroscopic orientation is isotropic, leading to a constant value (Figure 5.4A and Figure 5.4F). In this case, the constant value is negative and corresponds to the ground state bleach. For the XXXY case, the bulk response goes to zero for both the diagonal and cross-peaks (Figure 5.4B and Figure 5.4G), consistent with the values obtained for the bulk pathways (Figure 5.12). For the surface system, the diagonal and cross-peak responses are different between the two polarization cases. For the XXXX case, the diagonal and cross-peak responses of the surface have a negative response that depends on the θ and ψ values of the system, corresponding to ground state bleach (Figure 5.4C and Figure 5.4H). However, this is not true for the XXXY case. Here, the diagonal and cross-peak responses are different signs (Figure 5.4D-E and Figure 5.4I-J, boxed in grey). The *i* diagonal peak intensity is solely from the non-rephasing *ijji* pathway that has an on-diagonal cross-peak and the *j* diagonal peak is from the non-rephasing *jiij* pathway. These have opposite signs relative to each other, just like the pathway responses in Figure 5.3J

and 5.3M. The other pathways that contribute to the diagonal peaks (*iiii* and *jjjj*) are zero as seen in Figure 5.3C and 5.3D. Thus, the only signals observed from a surface detected in XXXY result from cross-peak pathways. The sign of the upper (*j*-*i*) and lower (*i*-*j*) off-diagonal cross-peaks are also opposite (Figure 5.4I-J) from each other. Moreover, the fact that the lower off-diagonal cross-peak has the opposite sign between the XXXY and XXXX configurations is a signature of the surface response. This sign change is a direct consequence of the sign of the *iijj*, *ijij*, *jjii*, and *jiji* pathways. The sign changes provide a clear indication for detecting the signal only from molecules at the surface.

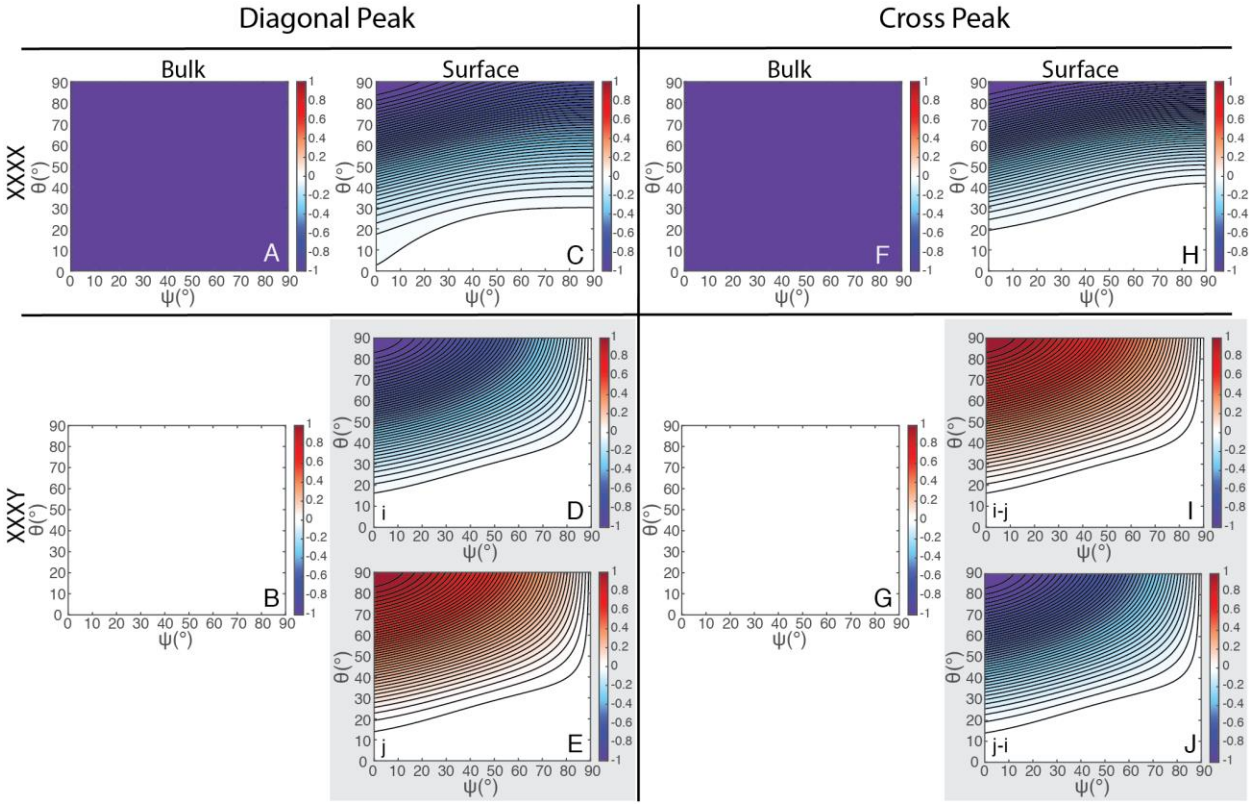

Figure 5.5.4 Normalized diagonal and cross peak dependences on θ and ψ angles for both bulk and surface systems for two different polarization conditions: XXXX and XXXY.

5.3.3 Simulated Two-Dimensional Spectra

We further investigate the surface response by simulating representative 2D spectra of two coupled oscillators based on our calculations above. In these simulations, two well-separated arbitrary wavelengths are defined for oscillator *i* and oscillator *j*. *i* and *j* corresponds to the lower energy and higher energy transition, respectively. This diagonalized Hamiltonian uses fixed diagonal and off-diagonal anharmonicities by assuming that the oscillators are close to harmonic and thus scale as $\mu_{12}^2 = 2\mu_{01}^2$. The angle between the two dipoles (θ_{ab}) is set to 30° as in the calculations above. Using the original dipoles defined in Figure 5.1, the coupling term (β) is found between the two oscillators (Eq. 5.38). This coupling constant is then used to determine the mixing angle (α) between the two dipoles (Eq. 5.41). Based on this mixing angle, the two dipoles are redefined (Eq. 5.42-5.43). The magnitude of these new vectors defines the transition dipole strength. This transformation effectively maps the relative orientation and the coupling of the dipoles to the intensity of the transitions. The 2D spectra are simulated by using the orientational response of each pathway calculated in Figure 5.3 and weighting them by the transition dipole strength. These values are then plugged into the third-order rephasing and non-rephasing response functions. Equations 5.11 and 5.12 are representative rephasing ($R_1^{(3)}$) and non-rephasing ($R_4^{(3)}$) response functions for the diagonal peaks of one oscillator, *i*.

$$R_1^{(3)}(t_3, t_2, t_1) \propto -\langle(\hat{\mu}_i \cdot \hat{E}_d)(\hat{\mu}_i \cdot \hat{E}_c)(\hat{\mu}_i \cdot \hat{E}_b)(\hat{\mu}_i \cdot \hat{E}_a)\rangle |\mu_i|^4 e^{i\omega_i(t_1 - t_3) - (t_1 + t_3)/T_2} \quad (5.11)$$

$$R_4^{(3)}(t_3, t_2, t_1) \propto -\langle(\hat{\mu}_i \cdot \hat{E}_d)(\hat{\mu}_i \cdot \hat{E}_c)(\hat{\mu}_i \cdot \hat{E}_b)(\hat{\mu}_i \cdot \hat{E}_a)\rangle |\mu_i|^4 e^{-i\omega_i(t_1 + t_3) - (t_1 + t_3)/T_2} \quad (5.12)$$

In equations 5.11 and 5.12, the term in the brackets ($\langle\langle(\hat{\mu}_i \cdot \hat{E}_d)(\hat{\mu}_i \cdot \hat{E}_c)(\hat{\mu}_i \cdot \hat{E}_b)(\hat{\mu}_i \cdot \hat{E}_a)\rangle\rangle$), is the value of the orientational four-point correlation function that was evaluated in Figure 5.3. $|\mu_i|^4$ is the magnitude of the dipole to the fourth power. t_3 and t_1 are the coherence times in the probe and pump dimensions respectively. T_2 is the dephasing time (set to 2 ps for these simulations). To create the total rephasing spectra and total non-rephasing spectra, the third-order response function for each Feynman pathway that contribute to the diagonal peaks, the cross-peaks, and the excited state absorptions are summed together. Each of these third-order response functions are provided in the supplementary material (Eq. 5.32-5.37). A Fourier transform along both the pump and probe dimension are performed, taking the spectra to the frequency domain. The non-rephasing and rephasing spectra in the frequency domain are then added together to obtain purely absorptive spectrum. The spectrum produced represent changes that are purely due to the orientation of the system under investigation. Table 5.3 and Table 5.4 contains the specific parameters for each simulated 2D spectra.

For the surface response, we chose to investigate the signal produced when $\theta = 30°$ and $\psi = 30°$ (other conditions have also been calculated, see Figure 4.10). The bulk two dimensional spectra are also simulated. We also choose to investigate the complimentary polarization

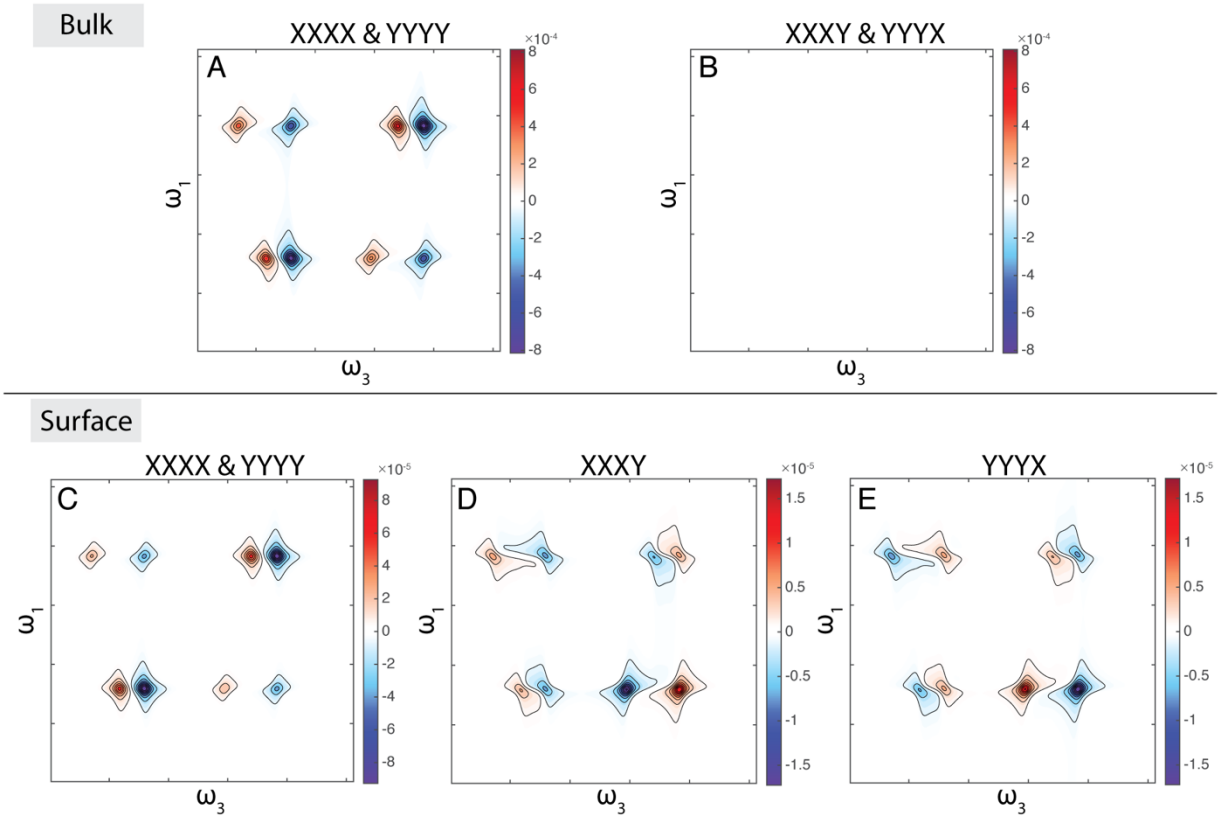

Figure 5.5.5 Simulated two dimensional spectra for two coupled oscillators in both bulk and surface systems under four polarization conditions: XXXX, YYYY, XXXY, and YYYX. The angle between the two oscillators is θ_{ab}=30°. For the surface system, oscillator a is along the *z* axis, while b is in the XZ plane, as shown in Figure 4.1. For the surface two dimensional spectra, $\theta = 30°$ and $\psi = 30°$.

conditions, YYYY and YYYX, as well. While these polarization conditions are the same for the bulk case (as you are effectively just rotating the plane by 90°), for the surface system, the order in which the interactions between X and Y occur matter, similar to the difference to left vs. right-handed polarized light in VCD. This leads to different responses in the 2D spectra as discussed below. The plotting convention we choose to use is a negative ground state bleach for the bulk

isotropic system under a parallel polarization scheme. Thus, any differences from this convention are of consequence.

In Figure 5.5, A and B are for bulk systems. For the XXXX and YYYY cases, each pathway has the same response (Figure 5.12), resulting in the same 2D spectrum. The probe frequency is plotted on the horizontal axis, while the pump frequency is plotted on the vertical axis. The spectrum is unnormalized, and the resulting intensity is purely due to the orientation of the dipoles and the transition dipole strength. We see two diagonal peaks, one for each oscillator, with both a negative ground state bleach (blue) and a positive excited state absorption (red). Both an upper (*j*-*i*) and lower (*i*-*j*) cross-peak are seen. For the bulk system investigated with the XXXY and YYYX, once again the pathway responses are the same (Figure 5.12), leading to the same 2D spectrum. However, the value of the pathways in a XXXY or YYYX polarization configuration are zero, leading to zero signal in the 2D spectrum, as seen by the colormap of the spectra in Figure 5.5B.

The 2D spectra of the surface are different in intensity and sign from that of the bulk and are shown in the Figure 5.5C-E. Again, the XXXX and YYYY responses are the same for the surface system (Figure 5.13), and thus produce the same spectrum (Figure 5.5C). Two diagonal peaks with a ground state bleach and excited state absorption are observed, as well as upper and lower cross-peaks. In the XXXY polarization configuration of the surface (Figure 5.5D), the 2D spectrum is quite different than the all-parallel-polarization case. Our conventional diagonal peaks associated with the *iiii* and *jjjj* pathways are completely gone, consistent with the values of the pathways seen in Figure 5.3. Instead, all we observe are cross-peaks. The non-rephasing on-diagonal cross-peak from the *ijji* and *jiij* pathway appear in place of the purely absorptive diagonal peaks. The two on-diagonal cross-peaks are opposite in sign as predicted in Figure 5.4D

and 5.4E. The non-rephasing *ijji* pathway leads to a negative ground state bleach for the lower on-diagonal cross-peak, while the non-rephasing *jiij* pathways leads to a positive ground state bleach for the upper on-diagonal cross-peak. Two off-diagonal cross-peaks are present in the XXXY spectrum in both the upper and lower quadrant, just like in the XXXX/YYYY polarization. However, in the XXXY case, the upper and lower cross-peak are opposite in sign and different in magnitude. The lower cross-peak has flipped sign as compared to the off-diagonal cross-peak in the XXXX/YYYY case. Here, the ground state bleach of the lower off-diagonal cross-peak is now positive (red) while the excited state absorption is negative (blue) (Figure 5.5D). The upper cross-peak, however, maintains the conventional sign of the ground state bleach and excited state absorption. Although, the magnitude is less than that of the lower off-diagonal cross-peak. This can be explained by considering the contributions of the *jjii* and *jiji* pathways to that cross-peak. The pathways that contribute to the *j-i* off-diagonal cross-peak are the rephasing *jiji*, rephasing *jjii*, and non-rephasing *jjii* pathways. As seen in Figure 5.3, the *jjii* pathway is positive while the *jiji* pathway is negative. Thus, the *jiji* pathways cancels with one of the *jjii* pathways, leaving only one contribution from the *jjii* pathway. This causes the upper diagonal cross-peak to be 1/3 the signal strength of the lower diagonal cross-peak.

Furthermore, the surface spectrum is also different in the YYYX case (Figure 5.5E). Here, the spectrum is just the negative of the XXXY case, as predicted by Table 5.1. This makes intuitive sense when the order of the pulses is considered. In the XXXY configuration, the first three interaction are in the X direction and the last is in the Y direction. This rotation of light is in the clockwise direction (relative to the axes defined in Figure 5.1A). When the YYYX polarization configuration is used, this is equivalent to rotating light in a counter-clockwise direction. Moreover, if −Y−Y−YX polarization condition is used, the sign of the signals follows that of the XXXY configuration as the interactions are still performed in a clockwise matter. The −X−X−XY polarization, follows that of the YYYX configuration by the same argument. The pathway responses for the YYYX polarization are plotted in Figure 5.13.

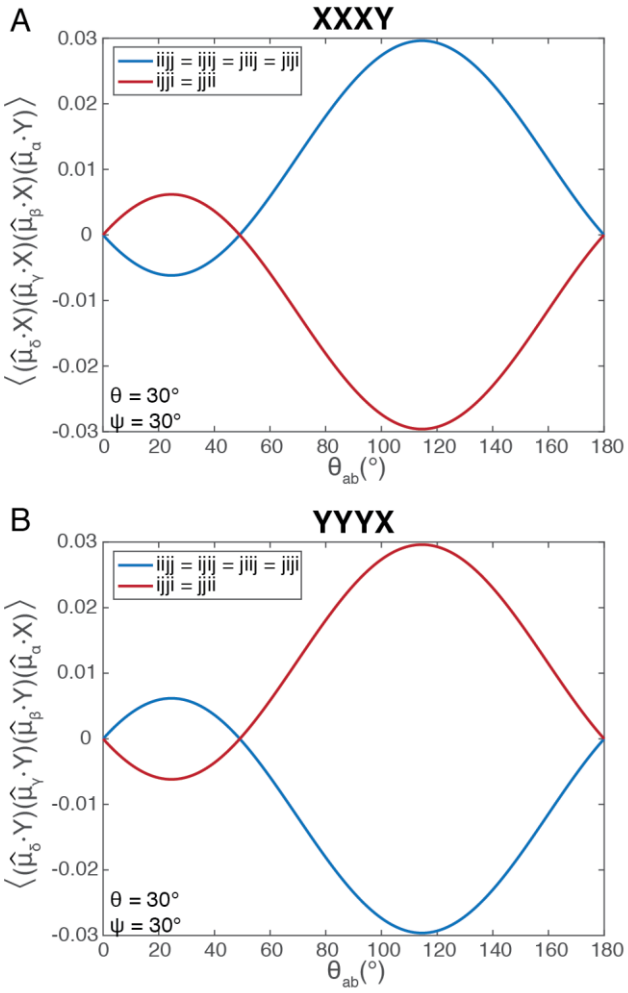

Figure 5.5.6 Cross-peak pathway dependence on θ_{ab} for θ=30° and for ψ=30° for XXXY and YYYX polarization conditions. *iijj*, *ijij*, *jiij*, and *jiji* pathways are equivalent for the XXXY and YYYX functions and are plotted in blue. The *ijji* and *jjii* pathways is plotted is plotted in red.

To further understand the origin of the flipped sign of the off-diagonal cross-peaks, we consider how the lower cross-peak depend on θ_{ab}. Figure 5.9 shows the 2D spectra in the XXXX and XXXY configurations for the same two oscillators depicted in Figure 5.1, but with

different values of θ_{ab}. The lower off-diagonal cross-peak does not always flip sign for the XXXY configuration when compared to the XXXX case. The origin of this difference comes in the sign of the response for the *iijj* and *ijij* pathways. Figure 5.6 plots these pathway responses for a value of $\theta = 30°$ and $\psi = 30°$ as a function of θ_{ab}. In both the XXXY and YYYX polarization configuration, *iijj* and *ijij* are equivalent and shown in blue, whereas *ijji* is plotted in red. In the XXXY case, the *iijj* and *ijij* path is negative for θ_{ab} less than 49.11°, and positive θ_{ab} greater than 49.11° (Figure 5.6A). Conversely, in the YYYX case, when θ_{ab} is less than 49.11°, the *iijj* and *ijij* responses are positive and become negative when θ_{ab} is greater than 49.11° (Figure 5.6B). The *ijji* pathway follows the opposite trend of the *iijj* and *ijij* pathways in both the XXXY and YYYX cases. From the simulated 2D spectra in Figure 5.5 and Figure 5.9, it is clear that the off-diagonal cross-peak have the opposite sign, relative to the all parallel detection case, when these *iijj* and *ijij* pathways have a negative value. This flipping dependence of the cross-peaks as a function of θ_{ab} provides insight into the orientation of the molecule at the surface. By measuring both XXXY and YYYX, we can obtain insight into the value of θ_{ab} depending on in which spectrum the cross-peak has flipped sign relative to the parallel case. If the cross-peak sign has flipped in the XXXY case, then θ_{ab} is less than 49.11°, while if it is flipped in the YYYX case then θ_{ab} is greater than 49.11°. However, it should be noted that the θ_{ab} at which the flipped sign of the cross-peak occurs also depends on the θ and ψ values of the surface system (Figure 5.14), as well as on the dipole's original orientation relative to the surface (Figure 5.15). The same analysis can also be done with the upper cross-peak.

In the proposed singularly cross-polarized scheme, enhancement techniques can be used as long as the polarization is retained. All types of experimental geometry may be used as well (i.e., BOXCARS, pump-probe, or ATR). While the calculations presented in the main text

assume an incident angle of all three pulses to be normal to the surface (i.e., collinear), this is unrealistic in experimental practice. Figure 5.16 shows how the pathway responses (*iiii, jjjj, ijij, iijj, ijji, jiji, jjii, jiji*) and the diagonal and cross-peak signals change as a function of incident angle between the pump and probe for different surface orientations. Overall, the trends discussed above are independent of the incident angle on the sample. The diagonal peak pathways are zero when using a singularly cross-polarized scheme and the sign of the cross-peak changes. However, the intensity of the signal does decrease as the incident angle between the pump and probe increases. When considering the intensity of the signal to quantify the orientation and structure of a system, the polarization relative to the surface must also be considered.

5.3.4 Comparison to SFG and VCD

The singularly cross-polarized technique above builds off of previous work by Simpson and Mukamel and demonstrates that *surface-specific* information can be obtained with a third-order spectroscopy.[42–45] In this section, we compare the proposed technique to VCD, SFG, chirality-induced 2D IR, and conventional 2D spectroscopy to provide insight into the similarities and differences between these spectroscopies. Table 5.2 provides a summary of these comparisons.

Table 5.2 Comparison of different spectroscopies to singularly cross-polarized 2D spectroscopy.

Category	VCD	SFG	Chiral Induced 2D IR	Conventional 2D Optical Spectroscopy	Singularly Cross-polarized 2D Spectroscopy

Susceptibility order	χ^1	χ^2	χ^3	χ^3	χ^3	χ^3
Signal Intensity	$\propto \mu m$	$\propto \alpha\mu$	$\propto r\mu^4$	$\propto \mu^4$	$\propto \mu_i^2\mu_j^2$	$\propto \mu_i^2\mu_j^2$
Systems Studied	Bulk	Interfaces Surfaces	Bulk	Bulk	Interfaces Surfaces	Bulk
Molecule Requirements	Chiral	Chiral or achiral	Chiral	Chiral or achiral	Chiral or achiral	Chiral

The first comparison made in Table 5.2 across the five spectroscopies of interest is the order of the susceptibility measured. VCD is a linear spectroscopy, while the three 2D spectroscopies (chiral induced, conventional, singularly cross-polarized) are non-linear third-order experiments. SFG is a non-linear even-order technique that measures the second-order susceptibility. These differences influence what determines the intensity of the signal and the type of systems that can be studied.

SFG is the only even-ordered spectroscopy considered in the table (although further comparisons could be made to 2D SFG). The signal intensity of SFG relies on both the transition dipole (μ) and the Raman tensor (or transition polarizability) (α) of the vibration of interest. SFG also measures interfaces and surfaces with *surface-specificity*, as the SFG signal of bulk centrosymmetric systems go to zero. This is similar to singularly cross-polarized 2D spectroscopy that also measures signals from interfaces and surfaces. However, the important distinction is that for the third-order case the signal relies on the transition dipole squared of two

coupled states ($\mu_i^2\mu_j^2$). Thus, for the singularly cross-polarized 2D spectroscopy, the molecules at the surface must be coupled in a non-parallel way to produce cross-peaks in the 2D spectra of the surface. In conventional 2D spectroscopy, the signal strength of a single state is dependent on the transition dipole to the fourth. These types of signals are not observed in the singularly cross-polarized technique. But the cross-peak signal intensity observed in conventional 2D spectra is equivalent to what is observed in the singularly cross-polarized scheme, meaning that they depend on the transition dipole squared of two coupled states. Conventional 2D spectroscopy has been used to study bulk systems extensively,[58,59] although, there are examples of 2D spectroscopy studying monolayers and surfaces in a *surface-sensitive* way.[73] The singularly cross-polarized technique would complement existing even-ordered spectroscopies, like SFG, by providing structural sensitivity due to coupling, dynamics through lineshape analysis, and other observables typical of 2D IR/Vis spectroscopies, but for surfaces specifically.

VCD and chirality induced 2D IR both rely on measuring bulk chiral molecules. The signal strength of VCD is determined by the rotational strength (r), or the dot product of the transition dipole and the magnetic dipole (μm), which can be rewritten as the cross-product of two transition dipoles.[60] Chirality induced 2D IR is the two-dimensional equivalent of VCD whose signal strength depends on the rotational strength and the transition dipole to the fourth power ($r\mu^4$).[42,43] The chiral induced signals are detected by using the same pulse sequence as proposed for the singularly cross-polarized 2D spectroscopy: XXXY. The difference between chirality induced 2D IR and singularly cross-polarized 2D spectroscopy is the type of systems and molecules measured. In the chirality induced 2D spectroscopy, bulk chiral molecules are measured, resulting in both diagonal peak and cross-peaks associated with 2D spectroscopy in general. For the singularly cross-polarized technique proposed here, the XXXY pulse sequence is

applied to a surface system, removing the requirement that the molecule be chiral. Moreover, the singularly cross-polarized technique is completely dipole allowed. However, only cross-peaks are observed in this spectrum as described above. VCD, chirality induced 2D IR, and singularly cross-polarized 2D spectroscopy all measure reduced symmetry systems, but how the symmetry is reduced is in different ways. For VCD and chirality induced 2D IR, the molecules themselves are chiral, and thus have reduced symmetry, while for the technique proposed here, the surface induces a reduced symmetry system. Thus, all three of the spectroscopies can be considered "chiral" methods. Chiral methods work for chiral molecules in the bulk as well as chiral and achiral molecules on a surface. Thus, the singularly cross-polarized technique is applicable to bulk chiral molecules, as well as chiral and achiral molecules on a surface. In the case where an interface of where the molecules probed are chiral, the technique proposed here is no longer *surface-specific* if there is bulk solution present the sample. Here, the signals from both the chiral bulk molecules and the chiral surface molecules will be detected in the singularly cross-polarized method (Table 5.2). This also true when SFG is applied to chiral bulk molecules and the visible beam is resonant with the electronic state of chiral molecule.[145–147] However, these bulk chiral SFG signals are different from the surface chiral SFG signals in probed with a chiral SFG method that are indeed *surface-specific.*[148–152]

5.4 Conclusions

We have computed how to extend third-order spectroscopies, like 2D infrared and 2D electronic spectroscopies, into the *surface-specific* regime. We do this by taking advantage of how the macroscopic orientation of molecules at the surface is mapped onto the third-order signal under specific polarizations. By using a singularly cross-polarized detection scheme, all

peaks in the bulk system, as well as diagonal peaks in the surface system, are zero. This leaves only cross-peaks from the ordered surface in the detected spectrum. Previously, only even-ordered spectroscopies, such as SFG, have been able to discern between signals from the bulk and the surface, by only measuring the response from the molecules at the surface or interface. Our proposed polarization scheme provides third-order spectroscopies that same capability typically only associated with even-ordered spectroscopies. Moreover, the dependence of the sign of the cross-peaks with the polarization used provides evidence of signals only from the surface and not from the bulk. The proposed method is a completely dipole allowed chiral method, as the sign of the signal depends of the macroscopic polarization of light. This same pulse sequence has been demonstrated to work for bulk chiral molecules.[42,43] We propose to use the XXXY polarization condition on a surface, which induces chirality to the system independent of whether the molecules on the surface are chiral or not.

Previously, different polarization conditions have been used to specifically interrogate cross-peaks in bulk systems.[51,69–71] Here, we provide an approach to probe cross-peaks from surface system without influence from the bulk. These surface systems must be biaxial, meaning that there is long range order over two axes. In our simulations, the surface system we studied had in the tilt (θ) and twist (ψ) angles. In practice, this technique might be used to study any ordered biaxial system, such as a monolayer, crystal, or exposed and buried interfaces. These systems would include both chemisorbed and physiosorbed self-assembled monolayers, ordered two-dimensional thin films, and membrane proteins in lipid bilayers. Despite a low number of molecules in these systems (1 nmol/cm^2 or less)[153], 2D spectroscopies are capable of such measurements.[16,19,22,24,28,73,74]

The singularly cross-polarized 2D spectroscopy proposed here does not hold for every system. The molecule or molecules of interest must have transition dipoles that are coupled in a non-parallel way to create cross-peaks. For vibrational spectroscopy, this is common for small molecules with multiple functional groups. For electronic spectroscopy, coupled chromophores or different electronic states in the same molecule are applicable. However, cross-peaks from vibrational progressions in the ground or excited state would not work as the transition dipoles of those transitions are usually parallel. The system can have variation in the twist and title angle of the transitions with respect to the surface, however the size of the variation will impact the size of the observed signals in the singularly cross-polarized scheme. The size of the observed signal will also be modulated by how well the polarization of light is maintained, with imperfect polarization leading to decreased signal.

In this work, the singularly cross-polarized scheme proposed broadens the capabilities of an already impressive technique. From observing coherences in light harvesting proteins,[75–77] to probing the singlet fission process of TIPS-pentacene,[78] to monitoring the chemical exchange of hydrogen bond formation,[79,80] and detecting changes in protein structure and aggregation,[58,81,82] 2D spectral measurements of bulk systems provide insight on both the structure and dynamics of such systems.[83] These same types of measurements can now be done at a surface, where the structure and dynamics of may be altered do to surface packing, surface diffusion, and differences in solvation.

5.5 References

(1) Page, R. C.; Kim, S.; Cross, T. A. Transmembrane Helix Uniformity Examined by Spectral Mapping of Torsion Angles. *Structure* **2008**, *16*, 787–797.

(2) Özdirekcan, S.; Rijkers, D. T. S.; Liskamp, R. M. J.; Killian, J. A. Influence of

Flanking Residues on Tilt and Rotation Angles of Transmembrane Peptides in Lipid Bilayers. A Solid-State 2H NMR Study. *Biochemistry* **2005**, *44*, 1004–1012.

(3) Ho, J.; Psciuk, B. T.; Chase, H. M.; Rudshteyn, B.; Upshur, M. A.; Fu, L.; Thomson, R. J.; Wang, H. F.; Geiger, F. M.; Batista, V. S. Sum Frequency Generation Spectroscopy and Molecular Dynamics Simulations Reveal a Rotationally Fluid Adsorption State of α-Pinene on Silica. *J. Phys. Chem. C* **2016**, *120*, 12578–12589.

(4) Nihonyanagi, S.; Yamaguchi, S.; Tahara, T. Ultrafast Dynamics at Water Interfaces Studied by Vibrational Sum Frequency Generation Spectroscopy. *Chem. Rev.* **2017**, *117*, 10665–10693.

(5) Zhang, Z.; Piatkowski, L.; Bakker, H. J.; Bonn, M. Ultrafast Vibrational Energy Transfer at the Water/Air Interface Revealed by Two-Dimensional Surface Vibrational Spectroscopy. *Nat. Chem.* **2011**, *3*, 888–893.

(6) Yang, P.; Glukhova, A.; Tesmer, J. J. G.; Chen, Z. Membrane Orientation and Binding Determinants of G Protein-Coupled Receptor Kinase 5 as Assessed by Combined Vibrational Spectroscopic Studies. *PLoS One* **2013**, *8*, 1–11.

(7) Xiao, D.; Fu, L.; Liu, J.; Batista, V. S.; Yan, E. C. Y. Amphiphilic Adsorption of Human Islet Amyloid Polypeptide Aggregates to Lipid/Aqueous Interfaces. *J. Mol. Biol.* **2012**, *421*, 537–547.

(8) Yan, C.; Yuan, R.; Nishida, J.; Fayer, M. D. Structural Influences on the Fast Dynamics of Alkylsiloxane Monolayers on SiO2 Surfaces Measured with 2D IR Spectroscopy. *J. Phys. Chem. C* **2015**, *119*, 16811–16823.

(9) Yan, C.; Yuan, R.; Pfalzgraff, W. C.; Nishida, J.; Wang, L.; Markland, T. E.; Fayer, M. D. Unraveling the Dynamics and Structure of Functionalized Self-Assembled Monolayers on Gold Using 2D IR Spectroscopy and MD Simulations. *Proc. Natl. Acad. Sci. U. S. A.* **2016**, *113*, 4929–4934.

(10) Ding, B.; Laaser, J. E.; Liu, Y.; Wang, P.; Zanni, M. T.; Chen, Z. Site-Specific Orientation of an a-Helical Peptide Ovispirin-1 from Isotope-Labeled SFG Spectroscopy. *J. Phys. Chem. B* **2013**, *117*, 14625–14634.

(11) Stein, R. S. The X-Ray Diffraction, Birefringence, and Infrared Dichroism of Stretched Polyethylene. III. Biaxial Orientation. *J. Polym. Sci.* **1958**, *31*, 335–343.

(12) Uejo, H.; Hoshino, S. Structure of Biaxially Oriented Polypropylene Film. *J. Appl. Polym. Sci.* **1970**, *14*, 317–328.

(13) Rhee, S.; White, J. L. Crystal Structure and Morphology of Biaxially Oriented Polyamide 12 Films. *J. Polym. Sci. Part B Polym. Phys.* **2002**, *40*, 1189–1200.

(14) Krishnaswamy, R. K. A Method to Characterize the Biaxial Orientation of The. **2000**, *38*, 182–193.

(15) Rosenfeld, D. E.; Nishida, J.; Yan, C.; Gengeliczki, Z.; Smith, B. J.; Fayer, M. D. Dynamics of Functionalized Surface Molecular Monolayers Studied with Ultrafast Infrared Vibrational Spectroscopy. *J. Phys. Chem. C* **2012**, *116*, 23428–23440.

(16) Rosenfeld, D. E.; Gengeliczki, Z.; Smith, B. J.; Stack, T. D. P.; Fayer, M. D. Structural Dynamics of a Catalytic Monolayer Probed by Ultrafast 2D IR Vibrational Echoes. *Science.* **2011**, *334*, 634–639.

(17) Leube, H. F.; Finkelmann, H. Optical Investigations on a Liquid-crystalline Side-chain Polymer with Biaxial Nematic and Biaxial Smectic A Phase. *Die Makromol. Chemie* **1991**, *192*, 1317–1328.

(18) Yuan, W. Z.; Yu, Z. Q.; Lu, P.; Deng, C.; Lam, J. W. Y.; Wang, Z.; Chen, E. Q.; Ma, Y.; Tang, B. Z. High Efficiency Luminescent Liquid Crystal: Aggregation-Induced Emission Strategy and Biaxially Oriented Mesomorphic Structure. *J. Mater. Chem.* **2012**, *22*, 3323–3326.

(19) Kraack, J. P.; Hamm, P. Surface-Sensitive and Surface-Specific Ultrafast Two-Dimensional Vibrational Spectroscopy. *Chem. Rev.* **2017**, *117*, 10623–10664.

(20) Ghosh, A.; Ho, J.-J.; Serrano, A. L.; Skoff, D. R.; Zhang, T.; Zanni, M. T. Two-Dimensional Sum-Frequency Generation (2D SFG) Spectroscopy: Summary of Principles and Its Application to Amyloid Fiber Monolayers. *Faraday Discuss.* **2015**, *177*, 493–505.

(21) Kraack, J. P.; Kaech, A.; Hamm, P. Surface Enhancement in Ultrafast 2D ATR IR Spectroscopy at the Metal-Liquid Interface. *J. Phys. Chem. C* **2016**, *120*, 3350–3359.

(22) Lotti, D.; Hamm, P.; Kraack, J. P. Surface-Sensitive Spectro-Electrochemistry Using Ultrafast 2D ATR IR Spectroscopy. *J. Phys. Chem. C* **2016**, *120*, 2883–2892.

(23) Kraack, J. P.; Frei, A.; Alberto, R.; Hamm, P. Ultrafast Vibrational Energy Transfer in Catalytic Monolayers at Solid-Liquid Interfaces. *J. Phys. Chem. Lett.* **2017**, *8*, 2489–2495.

(24) Nishida, J.; Yan, C.; Fayer, M. D. Enhanced Nonlinear Spectroscopy for Monolayers and Thin Films in Near-Brewster's Angle Reflection Pump-Probe Geometry. *J. Chem. Phys.* **2017**, *146*, 094201.

(25) Xiong, W.; Zanni, M. T. Signal Enhancement and Background Cancellation in Collinear Two-Dimensional Spectroscopies. *Opt. Lett.* **2008**, *33*, 1371.

(26) Lotti, D.; Hamm, P.; Kraack, J. P. Surface-Sensitive Spectro-Electrochemistry Using Ultrafast 2D ATR IR Spectroscopy. *J. Phys. Chem. C* **2016**, *120*, 2883–2892.

(27) Kraack, J. P.; Lotti, D.; Hamm, P. 2D Attenuated Total Reflectance Infrared Spectroscopy Reveals Ultrafast Vibrational Dynamics of Organic Monolayers at Metal-Liquid Interfaces. *J. Chem. Phys.* **2015**, *142*.

(28) Kraack, J. P.; Kaech, A.; Hamm, P. Surface Enhancement in Ultrafast 2D ATR IR Spectroscopy at the Metal-Liquid Interface. *J. Phys. Chem. C* **2016**, *120*, 3350–3359.

(29) Kraack, J. P.; Hamm, P. Vibrational Ladder-Climbing in Surface-Enhanced, Ultrafast Infrared Spectroscopy. *Phys. Chem. Chem. Phys.* **2016**, *18*, 16088–16093.

(30) Rey, N. G.; Dlott, D. D. Studies of Electrochemical Interfaces by Broadband Sum Frequency Generation. *J. Electroanal. Chem.* **2017**, *800*, 114–125.

(31) Wang, Z.; Carter, J. A.; Lagutchev, A.; Yee, K. K.; Seong, N. H.; Cahilll, D. G.; Dlott, D. D. Ultrafast Flash Thermal Conductance of Molecular Chains. *Science.* **2007**, *317*, 787–790.

(32) Bredenbeck, J.; Ghosh, A.; Smits, M.; Bonn, M. Ultrafast Two Dimensional-Infrared Spectroscopy of a Molecular Monolayer. *J. Am. Chem. Soc.* **2008**, *130*, 2152–2153.

(33) Ghosh, A.; Smits, M.; Bredenbeck, J.; Dijkhuizen, N.; Bonn, M. Femtosecond Time-Resolved and Two-Dimensional Vibrational Sum Frequency Spectroscopic Instrumentation to Study Structural Dynamics at Interfaces. *Rev. Sci. Instrum.* **2008**, *79*.

(34) Bredenbeck, J.; Ghosh, A.; Nienhuys, H.-K.; Bonn, M. Interface-Specific Ultrafast Two-Dimensional Vibrational Spectroscopy. *Acc. Chem. Res.* **2009**, *42*, 1332–1342.

(35) Zhu, X. D.; Suhr, H.; Shen, Y. R. Surface Vibrational Spectroscopy by Infrared-Visible Sum Frequency Generation. *Phys. Rev. B* **1987**, *35*, 3047–3050.

(36) Shen, Y. R. Surface Properties Probed by Second-Harmonic and Sum-Frequency Generation. *Nature* **1989**, *337*, 519–525.

(37) Lambert, A. G.; Davies, P. B.; Neivandt, D. J. Implementing the Theory of Sum Frequency Generation Vibrational Spectroscopy: A Tutorial Review. *Appl. Spectrosc. Rev.* **2005**, *40*, 103–145.

(38) Geiger, F. M. Second Harmonic Generation, Sum Frequency Generation, and $\chi^{(3)}$: Dissecting Environmental Interfaces with a Nonlinear Optical Swiss Army Knife. *Annu. Rev. Phys. Chem.* **2009**, *60*, 61–83.

(39) Rhee, H.; Kim, S. S.; Jeon, S. J.; Cho, M. Femtosecond Measurements of Vibrational Circular Dichroism and Optical Rotatory Dispersion Spectra. *ChemPhysChem*

2009, *10*, 2209–2211.

(40) Rhee, H.; June, Y. G.; Lee, J. S.; Lee, K. K.; Ha, J. H.; Kim, Z. H.; Jeon, S. J.; Cho, M. Femtosecond Characterization of Vibrational Optical Activity of Chiral Molecules. *Nature* **2009**, *458*, 310–313.

(41) Kwac, K.; Lee, K. K.; Han, J. B.; Oh, K. I.; Cho, M. Classical and Quantum Mechanical/Molecular Mechanical Molecular Dynamics Simulations of Alanine Dipeptide in Water: Comparisons with IR and Vibrational Circular Dichroism Spectra. *J. Chem. Phys.* **2008**, *128*.

(42) Zhuang, W.; Sgourakis, N. G.; Li, Z.; Garcia, A. E.; Mukamel, S. Discriminating Early Stage A 42 Monomer Structures Using Chirality-Induced 2DIR Spectroscopy in a Simulation Study. *Proc. Natl. Acad. Sci.* **2010**, *107*, 15687–15692.

(43) Abramavicius, D.; Zhuang, W.; Mukamel, S. Probing Molecular Chirality via Excitonic Nonlinear Response. *J. Phys. B At. Mol. Opt. Phys.* **2006**, *39*, 5051–5066.

(44) Davis, R. P.; Moad, A. J.; Goeken, G. S.; Wampler, R. D.; Simpson, G. J. Selection Rules and Symmetry Relations for Four-Wave Mixing Measurements of Uniaxial Assemblies. *J. Phys. Chem. B* **2008**, *112*, 5834–5848.

(45) Deng, F.; Ulcickas, J. R. W.; Simpson, G. J. Theoretical Foundation for Electric-Dipole-Allowed Chiral-Specific Fluorescence Optical Rotary Dispersion (F-ORD) from Interfacial Assemblies. *J. Phys. Chem. Lett.* **2016**, *7*, 4248–4252.

(46) Mukamel, S. *Principles of Nonlinear Optical Spectroscopy*; Oxford University Press: New York, 1995.

(47) Cho, M. *Two-Dimensional Optical Spectroscopy*; Taylor & Francis Group: Boca Raton, 2009.

(48) Hamm, P.; Zanni, M. T. *Concepts and Methods of 2D Infrared Spectroscopy*; Cambridge University Press: New York, 2011.

(49) Khalil, M.; Demirdöven, N.; Tokmakoff, A. Coherent 2D IR Spectroscopy: Molecular Structure and Dynamics in Solution. *J. Phys. Chem. A* **2003**, *107*, 5258–5279.

(50) Hochstrasser, R. M. Two-Dimensional Spectroscopy at Infrared and Optical Frequencies. *Proc. Natl. Acad. Sci.* **2007**, *104*, 14190–14196.

(51) Read, E. L.; Engel, G. S.; Calhoun, T. R.; Mančal, T.; Tae, K. A.; Blankenship, R. E.; Fleming, G. R. Cross-Peak-Specific Two-Dimensional Electronic Spectroscopy. *Proc. Natl. Acad. Sci. U. S. A.* **2007**, *104*, 14203–14208.

(52) Pisliakov, A. V.; Mančal, T.; Fleming, G. R. Two-Dimensional Optical Three-

Pulse Photon Echo Spectroscopy. II. Signatures of Coherent Electronic Motion and Exciton Population Transfer in Dimer Two-Dimensional Spectra. *J. Chem. Phys.* **2006**, *124*.

(53) Hochstrasser, R. M. Two-Dimensional IR-Spectroscopy: Polarization Anisotropy Effects. *Chem. Phys.* **2001**, *266*, 273–284.

(54) Laaser, J. E.; Zanni, M. T. Extracting Structural Information from the Polarization Dependence of One- and Two-Dimensional Sum Frequency Generation Spectra. *J. Phys. Chem. A* **2013**, *117*, 5875–5890.

(55) Nishida, J.; Fayer, M. D. Theory of Third-Order Spectroscopic Methods to Extract Detailed Molecular Orientational Dynamics for Planar Surfaces and Other Uniaxial Systems. *J. Chem. Phys.* **2014**, *140*.

(56) Ataka, K.; Giess, F.; Knoll, W.; Naumann, R.; Haber-Pohlmeier, S.; Richter, B.; Heberle, J. Oriented Attachment and Membrane Reconstitution of His-Tagged Cytochrome c Oxidase to a Gold Electrode: In Situ Monitoring by Surface-Enhanced Infrared Absorption Spectroscopy. *J. Am. Chem. Soc.* **2004**, *126*, 16199–16206.

(57) Ataka, K.; Stripp, S. T.; Heberle, J. Surface-Enhanced Infrared Absorption Spectroscopy (SEIRAS) to Probe Monolayers of Membrane Proteins. *Biochim. Biophys. Acta - Biomembr.* **2013**, *1828*, 2283–2293.

(58) Ghosh, A.; Ostrander, J. S.; Zanni, M. T. Watching Proteins Wiggle: Mapping Structures with Two-Dimensional Infrared Spectroscopy. *Chem. Rev.* **2017**, *117*, 10726–10759.

(59) Ganim, Z.; Chung, H. S.; Smith, A. W.; DeFlores, L. P.; Jones, K. C.; Tokmakoff, A. Amide I Two-Dimensional Infrared Spectroscopy of Proteins. *Acc. Chem. Res.* **2008**, *41*, 432–441.

(60) Krummel, A. T.; Zanni, M. T. Interpreting DNA Vibrational Circular Dichroism Spectra Using a Coupling Model from Two-Dimensional Infrared Spectroscopy. *J. Phys. Chem. B* **2006**, *110*, 24720–24727.

(61) Ji, N.; Shen, Y. R. Optically Active Sum Frequency Generation from Molecules with a Chiral Center: Amino Acids as Model Systems. *J. Am. Chem. Soc.* **2004**, *126*, 15008–15009.

(62) Belkin, M. A.; Shen, Y. R. Non-Linear Optical Spectroscopy as a Novel Probe for Molecular Chirality. *Int. Rev. Phys. Chem.* **2005**, *24*, 257–299.

(63) Zheng, R. H.; Chen, D. M.; Wei, W. M.; He, T. J.; Liu, F. C. Theoretical Investigation of Doubly Resonant IR-UV Sum-Frequency Vibrational Spectroscopy of Binaphthol Chiral Solution. *J. Phys. Chem. B* **2006**, *110*, 4480–4486.

(64) Haupert, L. M.; Simpson, G. J. Chirality in Nonlinear Optics. *Annu. Rev. Phys. Chem.* **2009**, *60*, 345–365.

(65) Moad, A. J.; Simpson, G. J. A Unified Treatment of Selection Rules and Symmetry Relations for Sum-Frequency and Second Harmonic Spectroscopies. *J. Phys. Chem. B* **2004**, *108*, 3548–3562.

(66) Perry, J. M.; Moad, A. J.; Begue, N. J.; Wampler, R. D.; Simpson, G. J. Electronic and Vibrational Second-Order Nonlinear Optical Properties of Protein Secondary Structural Motifs. *J. Phys. Chem. B* **2005**, *109*, 20009–20026.

(67) Simpson, G. J. Molecular Origins of the Remarkable Chiral Sensitivity of Second-Order Nonlinear Optic. *ChemPhysChem* **2004**, *5*, 1301–1310.

(68) Fu, L.; Liu, J.; Yan, E. C. Y. Chiral Sum Frequency Generation Spectroscopy for Characterizing Protein Secondary Structures at Interfaces. *J. Am. Chem. Soc.* **2011**, *133*, 8094–8097.

(69) Mehlenbacher, R. D.; McDonough, T. J.; Kearns, N. M.; Shea, M. J.; Joo, Y.; Gopalan, P.; Arnold, M. S.; Zanni, M. T. Polarization-Controlled Two-Dimensional White-Light Spectroscopy of Semiconducting Carbon Nanotube Thin Films. *J. Phys. Chem. C* **2016**, *120*, 17069–17080.

(70) Zanni, M. T.; Ge, N. H.; Yung Sam Kim; Hochstrasser, R. M. Two-Dimensional IR Spectroscopy Can Be Designed to Eliminate the Diagonal Peaks and Expose Only the Crosspeaks Needed for Structure Determination. *Proc. Natl. Acad. Sci. U. S. A.* **2001**, *98*, 11265–11270.

(71) Réhault, J.; Helbing, J. Angle Determination and Scattering Suppression in Polarization-Enhanced Two-Dimensional Infrared Spectroscopy in the Pump-Probe Geometry. *Opt. Express* **2012**, *20*, 21665.

(72) Love, J. C.; Estroff, L. A.; Kriebel, J. K.; Nuzzo, R. G.; Whitesides, G. M. *Self-Assembled Monolayers of Thiolates on Metals as a Form of Nanotechnology*; 2005; Vol. 105.

(73) Petti, M. K.; Ostrander, J. S.; Saraswat, V.; Birdsall, E. R.; Rich, K. L.; Lomont, J. P.; Arnold, M. S.; Zanni, M. T. Enhancing the Signal Strength of Surface Sensitive 2D IR Spectroscopy. *J. Chem. Phys.* **2019**, *150*, 024707.

(74) Yan, C.; Thomaz, J. E.; Wang, Y.-L.; Nishida, J.; Yuan, R.; Breen, J. P.; Fayer, M. D. Ultrafast to Ultraslow Dynamics of a Langmuir Monolayer at the Air/Water Interface Observed with Reflection Enhanced 2D IR Spectroscopy. *J. Am. Chem. Soc.* **2017**, *139*, 16518–16527.

(75) Scholes, G. D.; Fleming, G. R.; Olaya-Castro, A.; van Grondelle, R. Lessons from

Nature about Solar Light Harvesting. *Nat. Chem.* **2011**, *3*, 763–774.

(76) Scholes, G. D.; Fleming, G. R. On the Mechanism of Light Harvesting in Photosynthetic Purple Bacteria: B800 to B850 Energy Transfer. *J. Phys. Chem. B* **2000**, *104*, 1854–1868.

(77) Wang, C.; Flanagan, M. L.; McGillicuddy, R. D.; Zheng, H.; Ginzburg, A. R.; Yang, X.; Moffat, K.; Engel, G. S. Bacteriophytochrome Photoisomerization Proceeds Homogeneously Despite Heterogeneity in Ground State. *Biophys. J.* **2016**, *111*, 2125–2134.

(78) Jones, A. C.; Kearns, N. M.; Ho, J.-J.; Flach, J. T.; Zanni, M. T. Impact of Non-Equilibrium Molecular Packings on Singlet Fission in Microcrystals Observed Using 2D White-Light Microscopy. *Nat. Chem.* **2020**, *12*, 40-47.

(79) Kim, Y. S.; Hochstrasser, R. M. Chemical Exchange 2D IR of Hydrogen-Bond Making and Breaking. *Proc. Natl. Acad. Sci. U. S. A.* **2005**, *102*, 11185–11190.

(80) Fayer, M. D. Dynamics of Liquids, Molecules, and Proteins Measured with Ultrafast 2D IR Vibrational Echo Chemical Exchange Spectroscopy. *Annu. Rev. Phys. Chem.* **2009**, *60*, 21–38.

(81) Buchanan, L. E.; Dunkelberger, E. B.; Tran, H. Q.; Cheng, P.-N. N.; Chiu, C.-C. C.; Cao, P.; Raleigh, D. P.; de Pablo, J. J.; Nowick, J. S.; Zanni, M. T. Mechanism of IAPP Amyloid Fibril Formation Involves an Intermediate with a Transient Beta-Sheet. *Proc. Natl. Acad. Sci. U. S. A.* **2013**, *110*, 19285–19290.

(82) Alperstein, A. M.; Ostrander, J. S.; Zhang, T. O.; Zanni, M. T. Amyloid Found in Human Cataracts with Two-Dimensional Infrared Spectroscopy. *Proc. Natl. Acad. Sci. U. S. A.* **2019**, *116*, 6602–6607.

(83) Petti, M. K.; Lomont, J. P.; Maj, M.; Zanni, M. T. Two-Dimensional Spectroscopy Is Being Used to Address Core Scientific Questions in Biology and Materials Science. *J. Phys. Chem. B* **2018**, *122*, 1771–1780.

5.6 Supplemental Information

In the main text of this manuscript, the system investigated was composed of two dipoles separated by an angle (θ_{ab}) of 30°. For the bulk system simulations, these dipoles were dispersed in an isotropic manner. For the surface system simulations, these dipoles were aligned in the XZ plane (Figure 1B) and then averaged over the azimuthal angle (ϕ). In this supplemental, we explore the angle dependences (θ_{ab}, θ, and ψ) on the pathway values and two-dimensional (2D)

spectra for this surface system. We also report the pathway values for both bulk and surface systems in the YYYY and YYYX configurations that were used to simulate 2D spectra in the main text. The sign dependence of the cross-peak pathways as a function of θ_{ab} is also evaluated. Next, we explore the influence of the orientations for the surface sample on the sign of the signal detected in both the XXXY and YYYX configurations. We also describe how the incident angle between the pump and probe pulses effects the signals detected in a XXXY polarization. Lastly, we report the orientational four-point correlation functions for the remaining six singularly cross-polarized schemes mentioned in the main text, as well as the third-order response functions and parameters used to simulate 2D spectra.

5.6.1 Angular Dependence

The orientation of a system is mapped onto the third-order signal by the orientational four-point correlation function. To evaluate the orientational dependence more closely, we begin by changing only one parameter: θ_{ab}. The signal of eight pathways (*iiii, jjjj, iijj, ijij, ijji, jjii, jiji,* and *jiij*) are calculated for four different θ_{ab} values (0°, 45°, 60°, and 90°) for the same surface system as depicted in figure 5.1B. Figure 5.7 and figure 5.8 report the pathway response as a function of θ and ψ when using a XXXX and XXXY polarization configuration.

For XXXX, all the pathways provide positive responses for each θ_{ab} investigated. The differences between the four θ_{ab} values are in the second oscillator (*jjjj*) and the cross-peak pathways (*iijj, ijij, ijji, jjii, jiji, jiij*). The pathway associated with the first oscillator, *i*, (*iiii*) is independent of θ_{ab} as can be seen in the top row of figure 5.7. The response for this pathway increases as θ increases, corresponding to the dipole moving from the z-direction towards the x-

direction in which the light is polarized. The *iiii* response is constant across the ψ dimension for all θ_{ab} values investigated. The second oscillator pathways, *jjjj*, have different responses as a function of θ_{ab}. These pathways become less intense along the θ and ψ dimension as θ_{ab} increases, relating how the components of this dipole in the x-direction change strength as a

function of θ_{ab}. For $\theta_{ab} = 0°$, the *jjjj* pathway is identical to the *iiii* pathway. In fact, all the pathways for $\theta_{ab} = 0°$ are the same, as the two dipoles are perfectly parallel and there are no orientational differences between interactions with either oscillator. The cross-peak pathways (*iijj, ijij, ijji, jjii, jiji,* and *jiij*) are identical for each θ_{ab}(0°, 45°, 60°, and 90°) in the XXXX

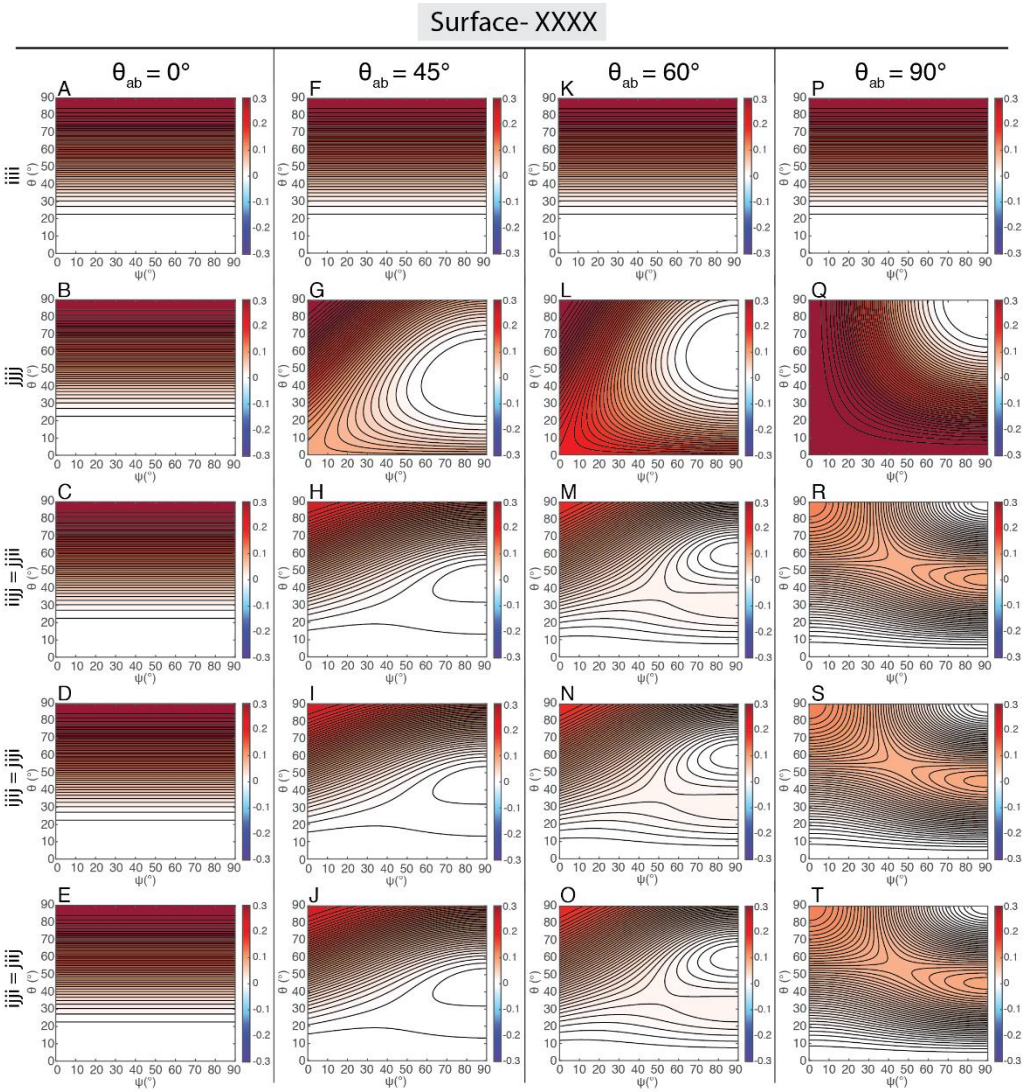

Figure 5.5.7 Detected signal in a XXXX polarization configuration for the pathways *iiii, jjjj, iijj, ijij, ijji, jjii, jiji,* and *jiij* as a function of θ and ψ for the surface system discussed in the main text, but with the θ_{ab} values of 0°, 45°, 60°, and 90°.

scheme. All of the responses are positive and again reflex the components of the dipoles in the x-direction that are interrogated by using x-polarized light.

We continue by examining the pathway responses with different θ_{ab} for the XXXY

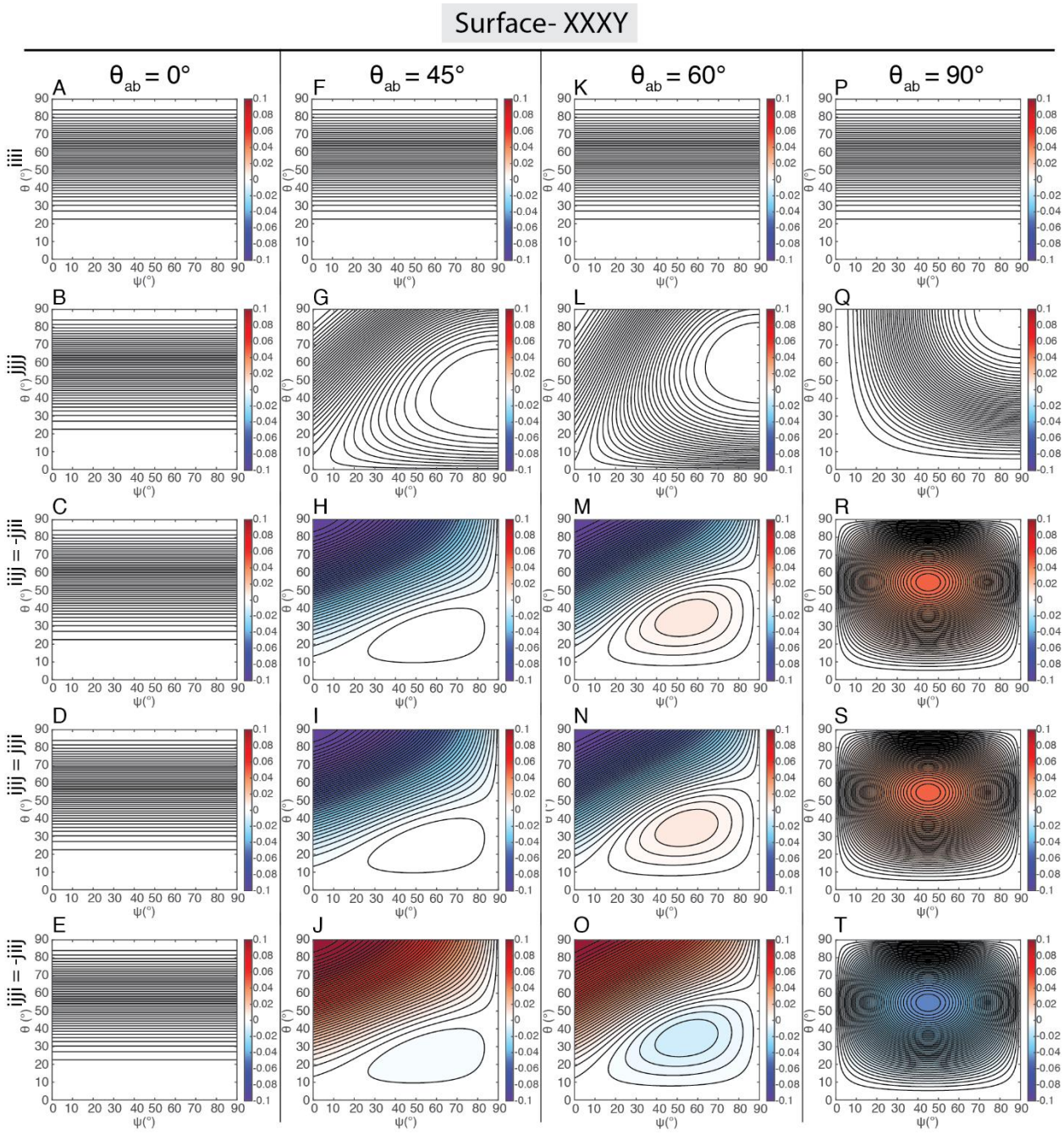

Figure 5.5.8 Detected signal in a XXXY polarization configuration for the pathways *iiii, jjjj, iijj, ijij, ijji, jjii, jiji,* and *jiij* as a function of θ and ψ for the surface system discussed in the main text, but with the θ_{ab} values of 0°, 45°, 60°, and 90°.

polarization configuration. These results are shown in figure 5.8. The pathways that consist of only one oscillator interactions (*iiii*, *jjjj*, first two rows in Figure 5.8), corresponding to diagonal peaks in 2D spectra are zero. The cross-peak pathway responses for the XXXY configuration show differences as a function of θ_{ab}. For $\theta_{ab} = 0°$, all the cross-peak pathways are zero. In this case, where the two oscillators are completely parallel, there is no difference between the cross-peak pathways and the diagonal pathways that depend on orientation. For the other θ_{ab} values, the sign of the cross-peak responses depends on θ_{ab}. For the $\theta_{ab} = 30°$ and 45° (see main text for θ_{ab}= 30°), the pathways *iijj*, *ijij*, *jiji*, and *jiij* are negative, while the *ijji* and *jjii* response are positive. As θ_{ab} increases, this trend begins to flip sign. This is seen in the response of cross-peak responses of θ_{ab}= 60°, where positive components in the response of *iijj*= $-$*jjii* and *ijij*= *jiji* begin to appear at $\theta = 30°$ and $\psi = 40° - 70°$. The same is seen in the *ijji*= $-$*jiij* response of $\theta_{ab} = 60°$, but negative components growing in. By the time $\theta_{ab} = 90°$, the sign of the responses has completely flipped. In this case, the *iijj*, *ijij*, *jiij* and *jiji* pathways are positive, while *ijji* and *jjii* are negative.

We now simulate the 2D spectra for $\theta_{ab} = 0°$, 45°, 60°, and 90° for the XXXX and XXXY polarization configurations. These results are shown in figure 5.9. For these simulations, θ and ψ were both set to 30°. The simulated 2D spectra show two diagonal peaks and two off-diagonal cross-peaks for the XXXX polarization when $\theta_{ab} > 0°$. When $\theta_{ab} = 0°$, the coupling between the two dipoles is very large, leading to higher energy transition corresponding to the *j* oscillator. The intensity and anharmonicity of the cross-peaks are a function of θ_{ab} and provides

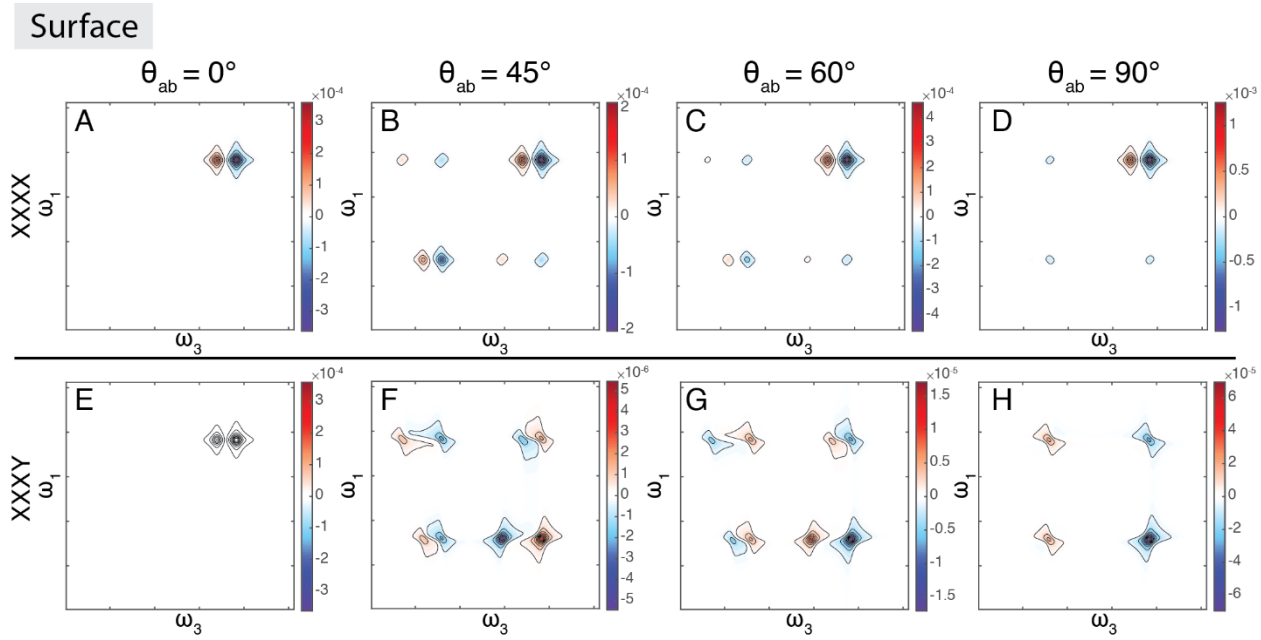

Figure 5.5.9 Simulated two-dimensional spectra in XXXX and XXXY polarization configurations for the surface system discussed in the main text, but with the θ_{ab} values of 0°, 45°, 60°, and 90°.

information on the coupling between the two oscillators. As θ_{ab} increases, the intensity of the cross-peaks decreases and the anharmonicity of the cross-peaks increases. This is exaggerated in the case where $\theta_{ab} = 90°$, where the cross-peak anharmonicity is so great that the cross-peak overtone is not observed over the frequency range plotted.

The 2D spectra for the XXXY polarization are similar to that reported in the main text for $\theta_{ab} = 30°$, except for the case where $\theta_{ab} = 0°$. In the latter case, the simulated 2D spectra for XXXY is zero. This is expected as the pathways in figure 4.8 are all zero when $\theta_{ab} = 0°$. The

simulated XXXY spectra for $\theta_{ab} = 45°$, contains only cross-peaks, both on and off the diagonal. In this case, the lower off-diagonal cross-peak has flipped sign (positive ground state bleach) when compared to the same cross-peak in the XXXX case, while the upper off-diagonal cross-peak does not flip sign (negative ground state bleach). This directly correlates to the pathway values for the *iijj, ijij, jjii* and *jiji* pathways shown in figure 5.8. The upper off-diagonal cross-peak is also 1/3 the intensity of the lower off-diagonal cross-peak as discussed in the main text. The on-diagonal cross-peaks are due to the non-rephasing *ijji* and *jiij* pathways. Here, the upper on-diagonal cross-peak has a positive ground state bleach and corresponds to the negative *jiji* pathway, while the lower on-diagonal cross-peak has a negative ground state bleach due to the positive *ijji* pathway. These results are consistent with those for the $\theta_{ab} = 30°$ as discussed in the main text. The 2D spectra for $\theta_{ab} = 60°$ has the same on-diagonal and off-diagonal cross-peaks as expected for the XXXY polarization. However, the sign of these peaks follows the opposite sign trend when compared to the $\theta_{ab} = 45°$ spectra. This is due to the value of the pathways that make up these peaks. For the off-diagonal cross-peaks, the *iijj, ijij,* and *jiji* pathways are positive, while the *jjii* is negative. For the on-diagonal cross-peak, the *ijji* pathway is negative and the *jiij* pathway is positive. The results for a $\theta_{ab} = 60°$ degrees are also true for the $\theta_{ab} = 90°$ spectra.

We next explore the influence of θ and ψ on 2D spectra for a specific θ_{ab}. Figure 5.10 shows simulated 2D spectra for the surface system with θ_{ab} = 30°, but with different θ and ψ values. Two polarization conditions are considered: XXXX and XXXY. θ, ψ values of 0° and

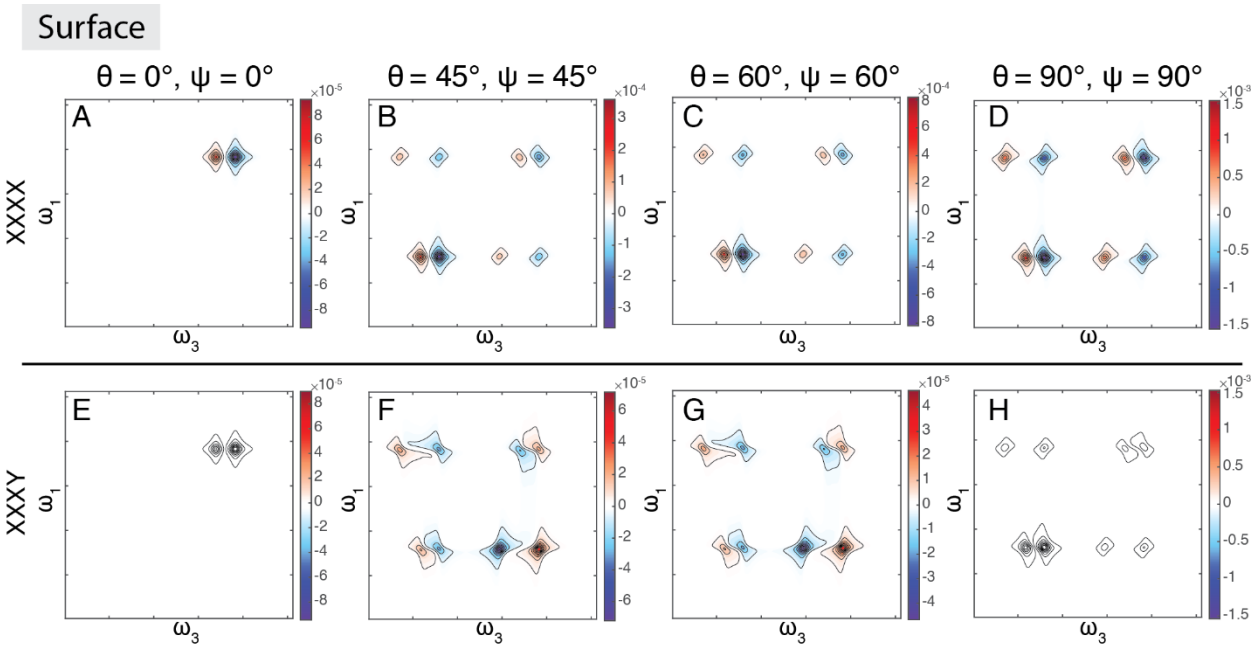

Figure 5.5.10 Simulated two-dimensional spectra in XXXX and XXXY polarization configurations for the surface system discussed in the main text, but with the θ,ψ values of 0°, 45°, 60°, and 90°.

90° show the two extreme cases. When θ and ψ= 0°, only one diagonal peak is seen in XXXX that corresponds to the second oscillator, *j*. In the XXXY polarization, the same spectrum is seen except that the diagonal peak is zero. When θ and ψ = 90°, two diagonal peaks associated with each oscillator are observed in XXXX, as well as an upper and lower off-diagonal cross-peak. For XXXY, these same peaks are present but have all gone to zero. For the values in-between these extremes (θ,ψ = 45°, 60°), the XXXX and XXXY spectra are similar to that shown in figure 5.4. The only difference is the intensity of the spectrum. For both cases, the XXXX spectra contain two diagonal peaks and two off-diagonal cross-peaks, while the XXXY spectra only shows cross-peaks. At both these θ and ψ values, the lower off-diagonal cross-peaks (associated with the *iijj* and *ijij*) pathways have flipped sign compared to the XXXX spectra

lower cross-peak. This result is consistent with these pathways having a positive value (Fig. 5.3). The upper off-diagonal cross-peak retains a negative ground state bleach and is 1/3 of the intensity of the lower cross-peak. The on-diagonal cross-peaks have opposite signs when compared to each other due to the negative equivalence ($ijji = -jiij$) between the *ijji* and *jiij* pathways. These trends are all consistent with what was observed in the main text.

Overall, when a singularly cross-polarized scheme is used (like XXXY or YYYX), the signals produced in the 2D spectra are rooted in the orientation at the surface. The signature of the off-diagonal cross-peaks having the opposite sign in XXXY when compared to the same signal in XXXX is dependent on the θ_{ab} of the system, as described in the main text, but also depends on the θ and ψ values as well (Fig. 5.10).

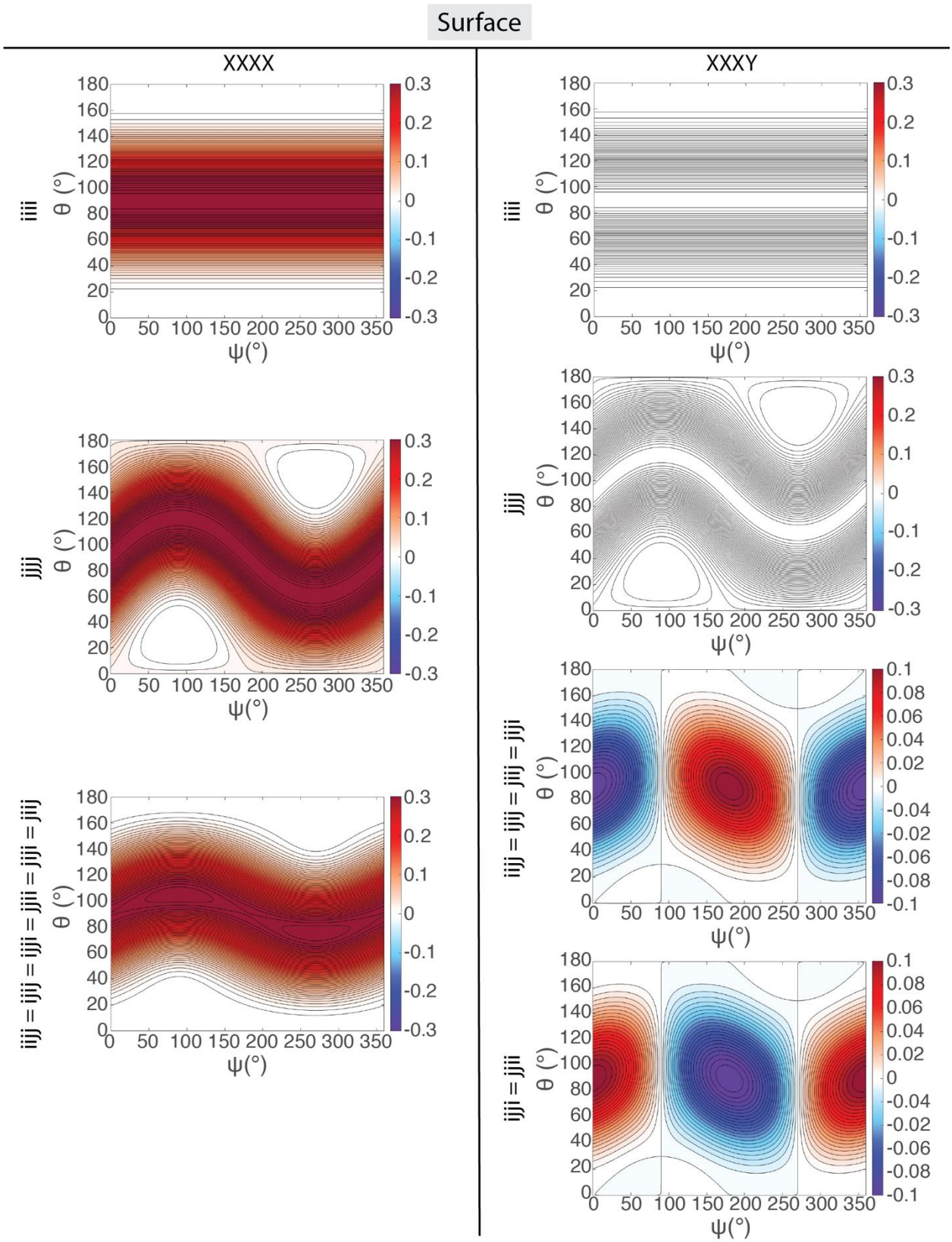

Figure 5.5.11 Detected signal for the pathways *iiii*, *jjjj*, *iijj*, *ijij*, *ijji*, *jjii*, *jiji*, and *jiij*, as a function of all values of θ and ψ for the surface system discussed in the main text using two different polarization conditions: XXXX and XXXY.

In the main text and the previous discussion, the pathway responses were plotted from $\theta = 0° - 90°$ and $\psi = 0° - 90°$. However, θ can range from 0° to 180° and ψ can be from 0° to 360°. In figure 5.11, we plot all eight Feynman pathways values from the surface system described in figure 4.1A for the XXXX and XXXY polarization configurations. In all cases, the plots have inversion symmetry around θ = 90° and ψ = 180°. In the XXXX polarization case, all the pathway values are positive and the cross-peak pathways are equivalent. In the XXXY polarization, the diagonal peak pathways are 0 for all values of θ and ψ. For the cross-peak pathway, *iijj* = *ijij* = *jiij* = *jiji* and *ijji* = *jjii*. These two sets of cross-peak values are opposite from each other but can have either positive or negative values depending on the θ and ψ values. All cross-peak values are 0 through ψ = 90° and 270°. These pathways dependencies on θ and ψ demonstrate how the orientation of the system is mapped onto the third-order response.

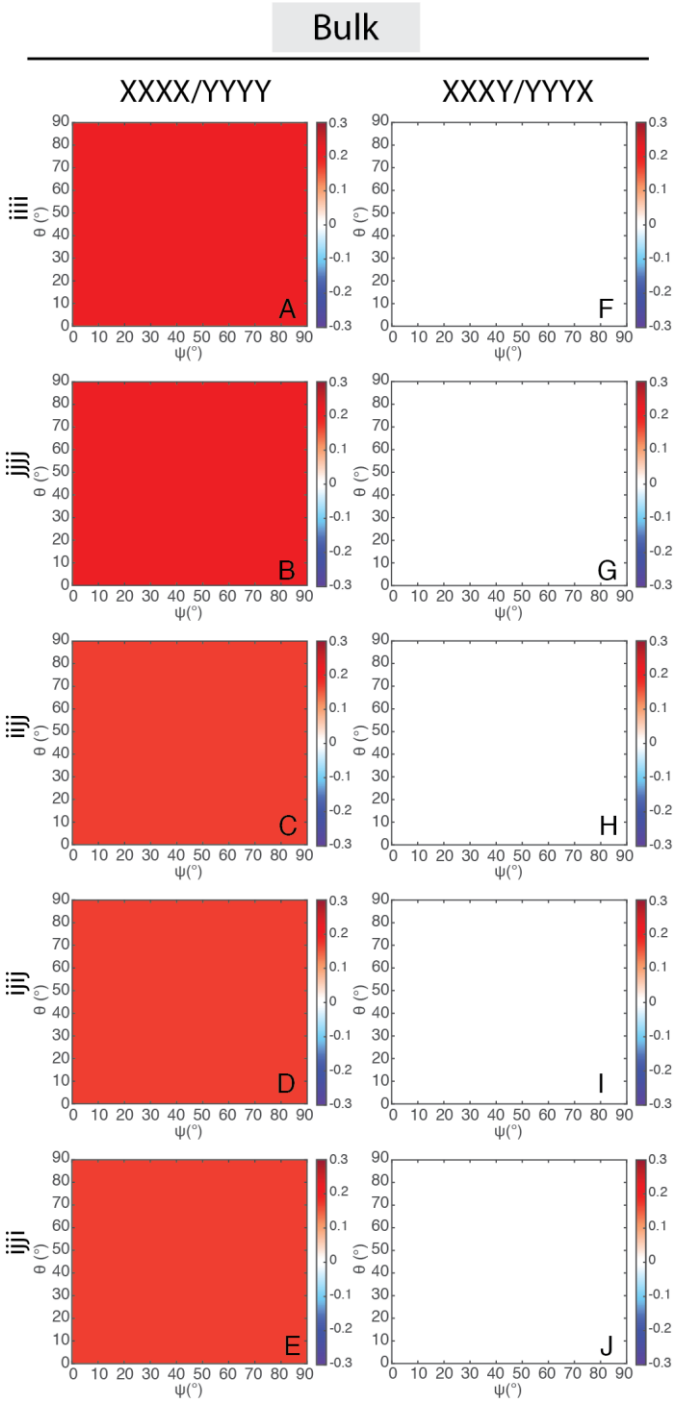

Figure 5.5.12 Detected signal for the pathways *iiii*, *jjjj*, *iijj*, *ijij*, and *ijji* as a function of θ and ψ for the bulk system discussed in the main text for four polarization conditions: XXXX, YYYY, XXXY, and YYYX. In this case, XXXX = YYYY and XXXY = YYYX. *jjii*, *jiji*, and *jiij* pathways are not plotted as they are equivalent to *iijj*, *ijij*, and *ijji* for the bulk system.

5.6.2 YYYY and YYYX Polarization Configurations

The main text reports the XXXX, YYYY, XXXY and YYYX 2D spectra for the bulk system and YYYY and YYYX spectra of the surface system described in figure 5.1A. Here we report the pathways that contribute to these spectra. Figure 5.12 shows the *iiii*, *jjjj*, *iijj*, *ijij*, and *ijji* pathways for the bulk system for the XXXX, YYYY, XXXY and YYYX polarizations. For the bulk system, the XXXX and XXXY polarizations are equivalent to the YYYY and YYYX polarizations, respectively. For XXXX/YYYY, the pathways are a constant value over θ and ψ, corresponding to the four-point correlation functions described by equations 5.3 and 5.4 in the main text. For the XXXY/YYYX cases, all the pathways are zero.

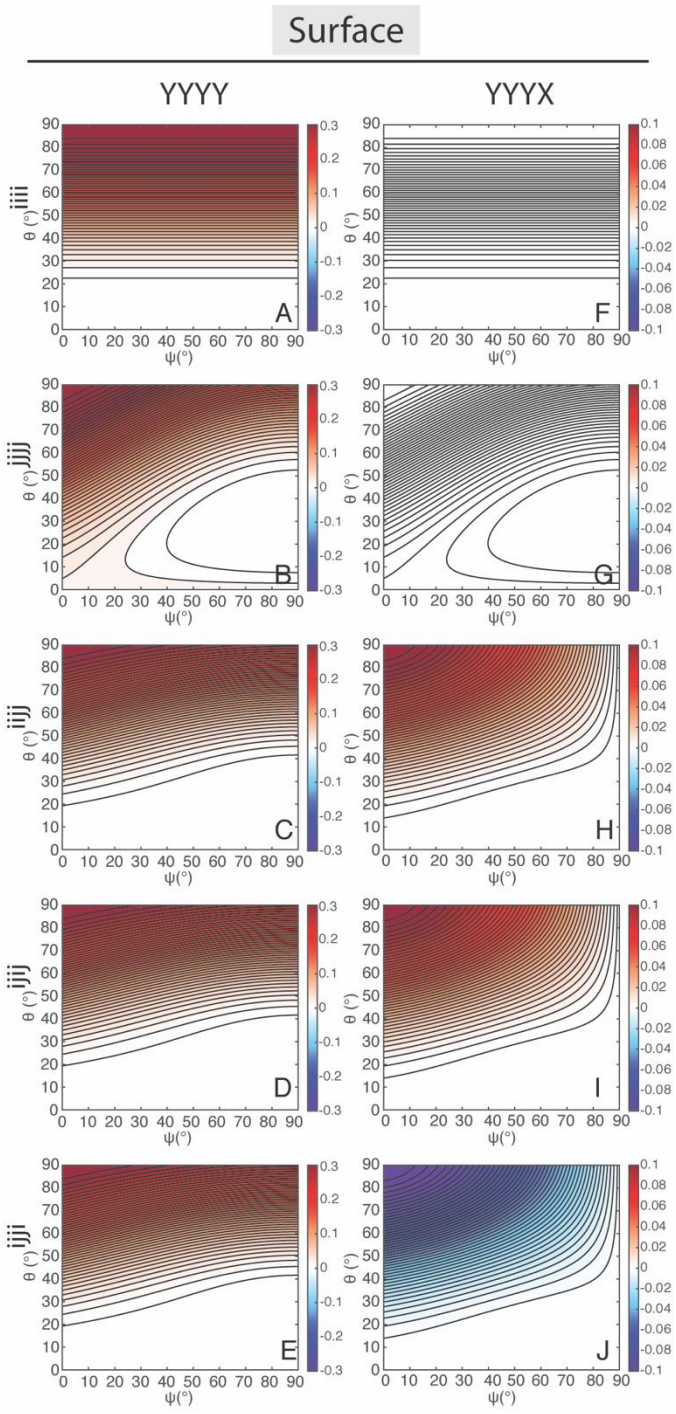

Figure 5.5.13 Detected signal for the pathways *iiii*, *jjjj*, *iijj*, *ijij*, and *ijji* as a function of θ and ψ for the surface system discussed in the main text using two different polarization conditions: YYYY and YYYX. *jjii*, *jiji*, and *jiij* are equivalent to *iijj*, *ijij*, and *ijji* in the YYYY polarization, but are not plotted. In the YYYX polarization, *iijj* = *ijij* = *jiji* = *jiij* and *iiii* = *jiii*.

Figure 5.13 reports the pathway responses for the surface system described in figure 5.1A for the YYYY and YYYX polarization schemes. The YYYY responses are the same as the XXXX responses in figure 5.3. In both YYYX and XXXY polarization configurations, the diagonal peak pathways are zero (*iiii* and *jjjj*). However, the cross-peak pathways of YYYX are opposite of XXXY. In the YYYX case, the *iijj* and *ijij* pathways are positive, while the *ijji* pathway is negative. In the XXXY polarization, the opposite is true (Fig. 5.3). This corresponds to differences in four-point correlation function. We write each of these explicitly for the *iijj* =*ijij* pathway and the *ijji* pathway for both the XXXY (Eq. 5.15-5.16) and YYYX (Eq. 5.22-5.23) polarization combinations in the orientational four-point correlation function section of the supplemental

material. We do not explicitly plot the *jjii*, *jiji*, and *jiij* pathways in figure 5.13, but those values can be determined by the relationships that $iijj = -jjii$, $ijij = jiji$, and $ijji = -jiij$.

5.6.3 Change in sign of cross-peak as a function of θ_{ab} for different θ and ψ values

As discussed in the main text, the sign of the lower off-diagonal cross-peak depends on the value of θ_{ab} and the polarization employed. When using a singularly cross-polarized scheme (like XXXY or YYYX), the θ_{ab} at which the cross-peak pathways switches sign depends on the θ and ψ values as well. For different θ and ψ values, the six cross-peak pathway responses are plotted as a function of θ_{ab} in figure 5.14. Figure 5.14A plots the cross-peak response for XXXY, while figure 5.14B plots the response for YYYX. The red lines correspond to $\theta = 30°, \psi = 30°$ (same values reported in main

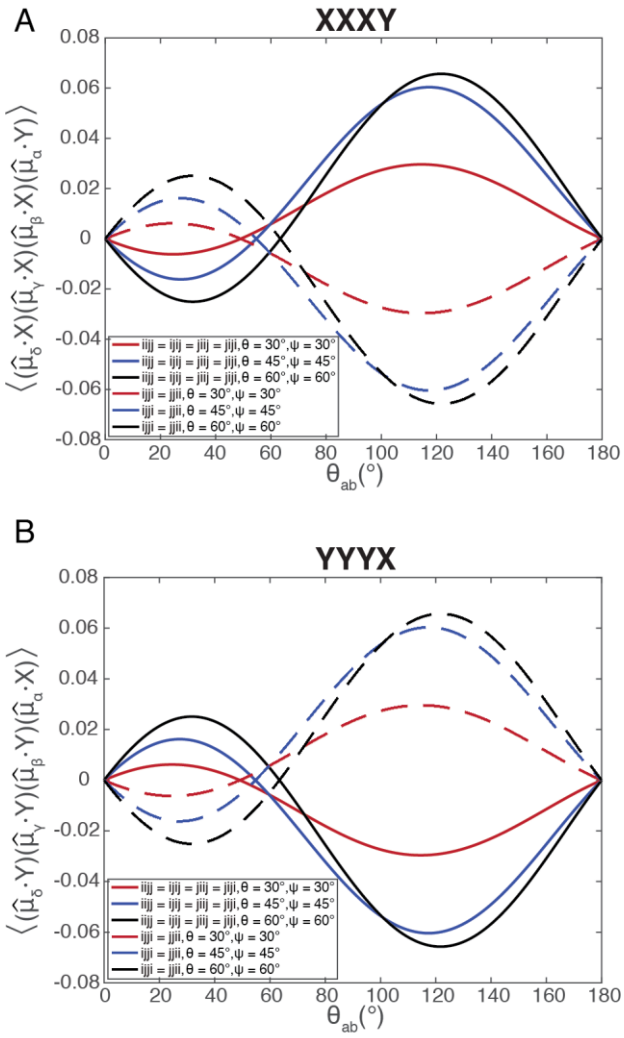

Figure 5.5.14 Cross-peak pathway dependence on θ_ab for θ=30°,45°,60° and ψ=30°,45°,60° for the XXXY and YYYX polarization conditions. *iijj*, *ijij*, *jiij* and *jiji* are equivalent for the XXXY and YYYX functions and are plotted in solid lines. The *ijji* is equivalent to the *jjii* pathway and are plotted as dashed lines.

text Fig. 5.6), the blue lines correspond to $\theta = 45°, \psi = 45°$, and the black lines correspond to $\theta = 60°, \psi = 60°$. A solid line represents the *iijj = ijij = jiij = jiji* pathways, while a dotted line represents the *ijji = jjii* pathways.

The sign difference between the cross-peak pathways for the XXXY and YYYX polarizations are retained for all angles of θ and ψ evaluated. These differences are discussed in the main text. What is shown in figure 5.14 is that the angle at which the lower *i-j* cross-peak pathways switch sign is dependent on the θ and ψ angles of the system. This switching angle increases as θ and ψ increase. For $\theta = 30°, \psi = 30°$, the pathways switch sign at $\theta_{ab} = 49.1°$. For $\theta = 45°, \psi = 45°$, this angle is $\theta_{ab} = 54.7°$, and for $\theta = 60°, \psi = 60°$ is $\theta_{ab} = 63.4°$.

5.6.4 Orientation Dependence

So far, all of the cases explored in both the main text and the supplementary information have focused on one orientation of the surface dipoles with variation in the three angles that define these dipoles (θ_{ab}, θ, and ψ). This surface was defined as having one dipole in the Z direction, while the other was in the XZ plane. We next investigate the differences in orientation at a macroscopic level by changing what planes we define the original dipoles to lie in. We explore three different cases: XY plane (1), XY plane (2), and YZ plane. These surface systems are drawn in the top row of figure 5.15. We set the angle between the two dipoles to be 30° and θ and ψ to also be 30° so that we can directly compare the results to that discussed in the main text.

We simulate the 2D spectra for these three surface systems for two polarization conditions: XXXY and YYYX. In all cases we see only cross-peaks, both on and off of the

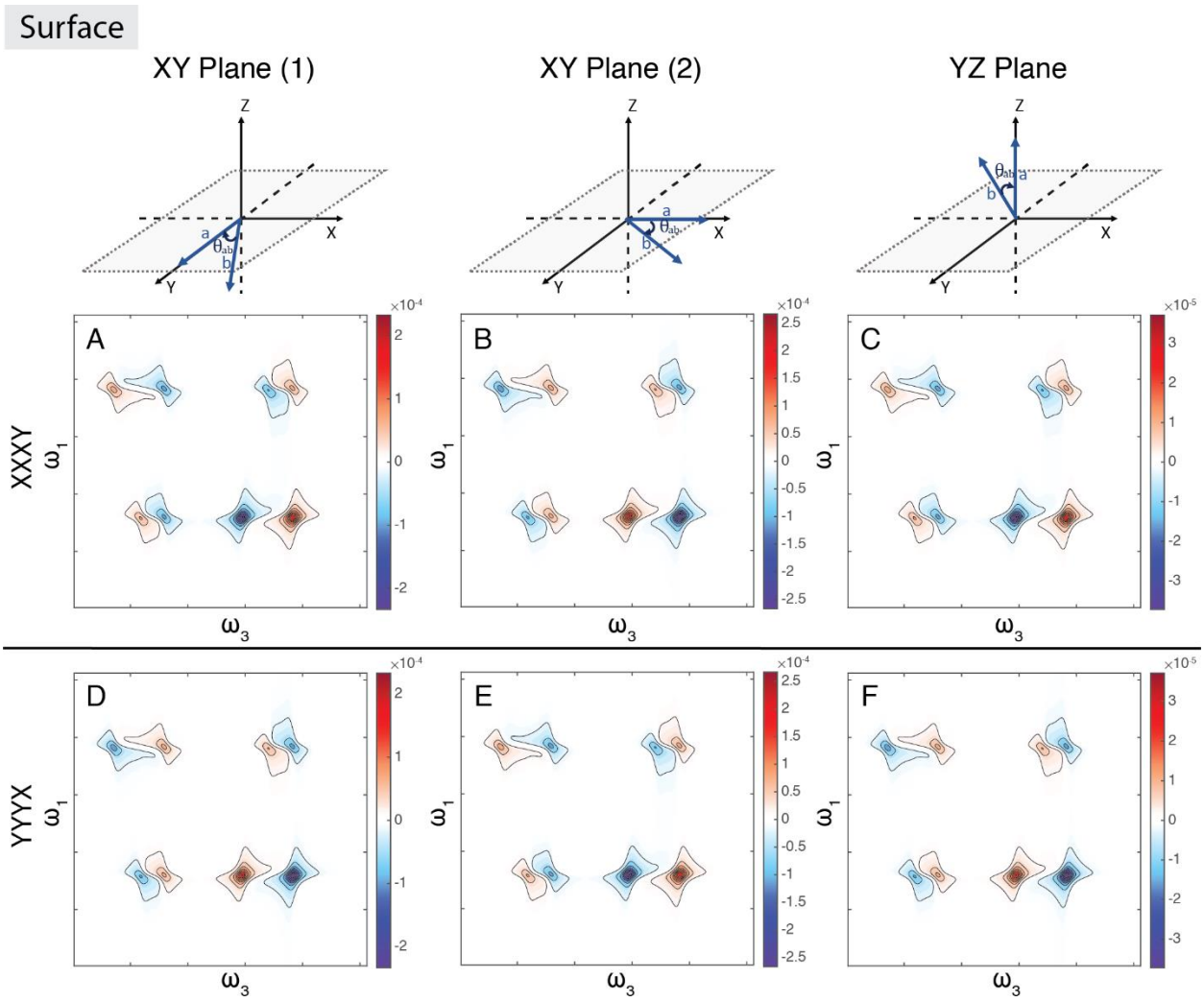

Figure 5.5.15 Schematic of three different surface systems (XY plane (1), XY plane (2), YZ plane) and simulated two-dimensional spectra in XXXY and YYYX polarization configurations for the three different surface systems. For each spectrum θ_{ab}=30°,θ=30°,ψ=30°.

diagonal. A positive ground state bleach for the lower off-diagonal cross-peak has flipped sign when compared to the all-parallel polarization cases. This is true for two of the surfaces systems in the XXXY polarization scheme: XY plane (1) and YZ plane. In these cases, the major components of the dipoles lie in the YZ plane. For XY plane (1) (Figure 5.15A) and the YZ plane (Figure 5.15C), the dipole **a** is in the YZ plane with the major components of **b** also remaining in that plane. For the XY plane (2), dipole **a** lies in the X direction. The major components of dipole **b** are also in this direction. For this system, the lower off-diagonal cross-

peak flips sign (i.e., is positive) when using an YYYX polarization scheme as seen in figure 5.15E. Thus, the lower *i-j* cross-peak will flip phase if the *i* oscillators lies within the singularly cross-polarized direction, or if either *i* or *j*'s major components lie in that plane.

We note that the system defined originally in the YZ plane surresponses to a 90° rotation of the original system (Figure 5.1A) over ϕ. The resulting XXXY and YYYX spectra are the same as the XZ plane system, indicating that the integration over ϕ is being performed correctly. On the other hand, the difference between the two XY plan systems is a rotation in ψ, or the twist angle. This rotation around the molecular twist angle leads to the difference in sign between figure 5.15A and 5.9B for the same polarization condition. The dependence of the sign of the cross-peak on ψ influences what types of systems can be measured using a singularly cross-polarized scheme. Such systems are biaxial, meaning that there is order in two directions.

5.6.5 Incident Angle Dependence

The above discussion, as well as that in the main text, have assumed that the incident angle of all pulses were normal to the surface. We acknowledge that in actual experimental set ups, this is not true. In the following we explore the incident angle dependence of the signal if we consider a pump-probe geometry where the probe is offset from the pump and the pump is perfectly normal to the surface.

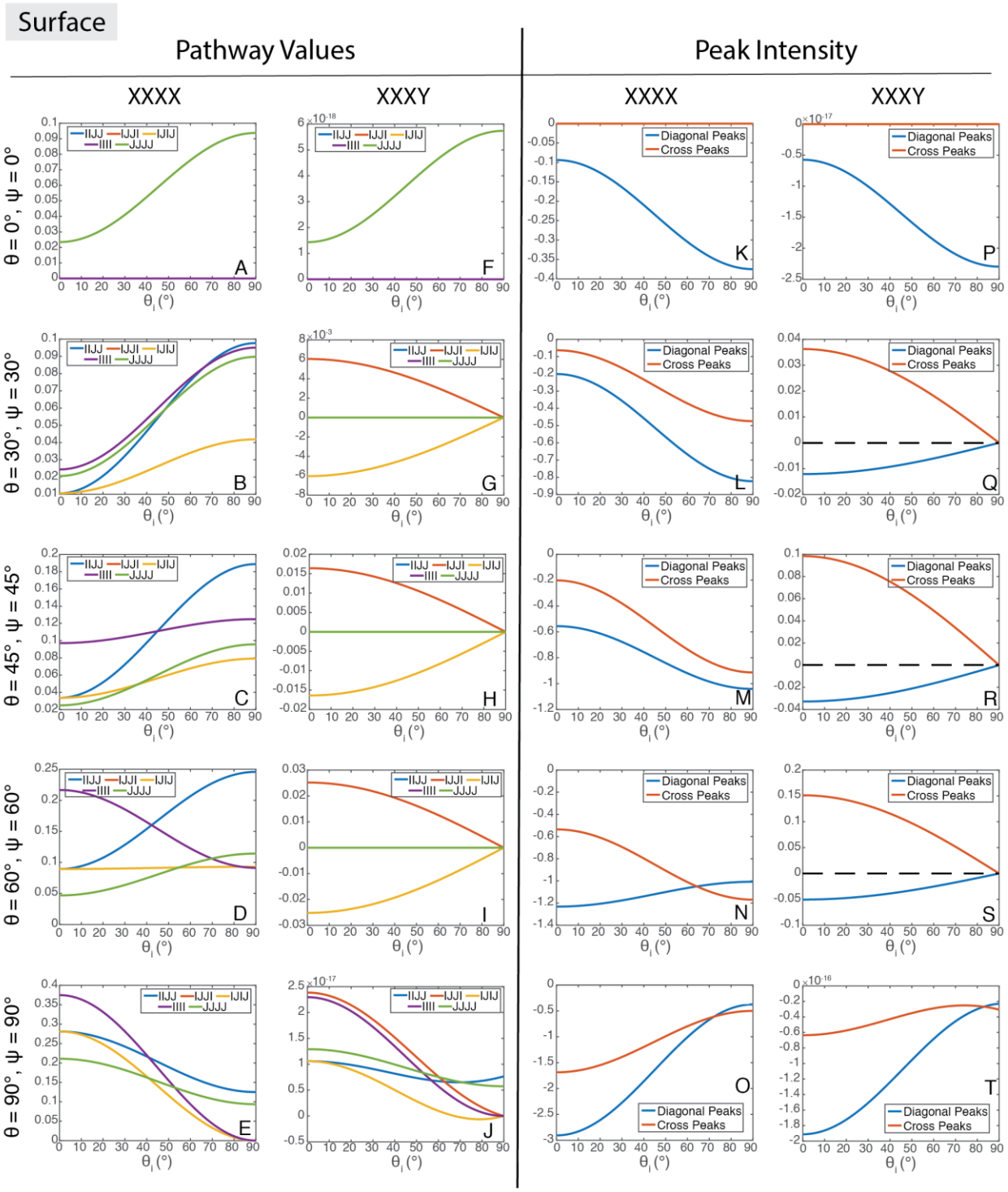

Figure 5.5.16 Diagonal and lower cross-peak pathway values and peak intensities as a function of incident angle between the pump and probe for the surface system described in the main text, but with θ,ψ values of 0°, 45°, 60°, and 90°. θ_{ab} is 30° for all spectra.

Figure 5.16 describes the pathway and peak intensity dependence on the incident angle of the probe (0° to 90°) for two polarization conditions: XXXX and XXXY. The same surface system described by figure 5.1A is used for the calculations. We evaluated five cases for $\theta = \psi$ (0°, 30°, 45°, 60°, and 90°). For five Feynman pathways (*iiii, jjjj, iijj, ijij, ijji*). For the pathway values, the cases where $\theta,\psi = 0°$ and 90° are the extremes. When θ ,$\psi = 0°$, only the *jjjj* pathway contributes. As a function of incident angle (θ_i), the *jjjj* pathway is always positive in the XXXX polarization (Figure 5.16A). For the XXXY polarization, all the pathways are zero (10^{-18}), as expected (Figure 5.16J). When $\theta,\psi = 90°$, all pathways have a positive value that decreases as a function of incident angle in the XXXX polarization (Figure 5.16E) and are zero (10^{-17}) in the XXXY configuration (Figure 5.16J). For the remaining three cases, in the XXXX polarization configuration, all the pathways continue to be a positive value, independent of the incident angle and are shown in figures 5.16B-D. In the XXXY configuration, this is not the case. When $\theta,\psi = 30°$, 45°, and 60°, the *iijj* and *ijij* cases are equivalent and negative (as predicted for this system in Fig. 5.3) over all incident angles, while *ijji* is positive (Figure 5.16G-I). The two diagonal pathways are zero for all incident angle in XXXY (Figure 5.16G-I).

The right half of figure 5.16 looks at how the pathways plotted on the left lead to the signal for the diagonal and lower *i-j* cross-peaks in a 2D spectrum for XXXX and XXXY polarizations. For the XXXX case, all diagonal and cross-peak values are negative as a function of incident angle, corresponding to a negative ground state bleach (Figure 5.16K-O). This result is independent of the θ,ψ values. For the XXXY case, the diagonal and lower cross-peak signals are both zero when $\theta,\psi = 0°$ and $= 90°$, consistent with the pathway values shown on the left side of figure 5.16. However, when θ and ψ are 30°, 45°, and 60°, the diagonal and cross-peak values have different signs as a function of incident angle (Figure 5.16Q-S). In these cases, the

diagonal peak intensity is due to the on-diagonal cross-peak from the non-rephasing *ijji* pathway, while the cross-peak intensity is due to the *iijj* and *ijij* pathways. The positive value for the cross-peak intensity when a XXXY polarization is used is what is expected based on the pathways shown on the left in figure 5.16 and figure 5.3 of the main text. The cross-peak maintains this positive value as a function of incident angle before converging to zero at an incident angle of 90°. This result indicates that the surface signal will maintain a flipped sign in the off-diagonal cross-peak independent of the incident angle of the probe.

5.6.6 Orientational Four-Point Correlation Functions

In the main text, the orientational four-point correlation functions are evaluated for the lower off-diagonal cross-peak pathways (*iijj* and *ijij*) for two of the possible eight singularly cross-polarized schemes. Here we report the four-point correlation functions for the remaining six polarization schemes shown in Table 1 in the main text for three pathways pathways (*iijj*, *ijij*, and *ijji)*. While the following equations only provide the solution for the lower off-diagonal cross-peaks (*iijj* and *ijij*) and the lower on-diagonal cross-peaks (*ijji*), the upper off-diagonal cross-peaks and upper on-diagonal cross-peaks can be described by the following relationships: $iijj = -jjii$, $ijji = -jiij$, and $ijij = jiji$. We also report the diagonal peak and cross-peak pathways for the bulk system in XXXY.

To evaluate the orientational four-point correlation function the dipoles (**a** and **b**, in Fig. 5.1A) are first rotated into the lab frame with an Euler rotation matrix. The new dipoles are defined as:

$$a' = \begin{pmatrix} \sin\phi \sin\theta \\ \cos\phi \sin\theta \\ \cos\theta \end{pmatrix}$$

(5.13)

$$b' = \begin{pmatrix} \sin\theta_{ab}\,(-\sin\psi\cos\theta\sin\phi + \cos\phi\cos\psi) + \sin\theta\sin\phi\cos\theta_{ab} \\ \sin\theta_{ab}\,(-\sin\psi\cos\theta\cos\phi - \sin\phi\cos\psi) + \sin\theta\sin\phi\cos\theta_{ab} \\ \sin\psi\sin\theta_{ab}\sin\theta + \cos\theta\cos\theta_{ab} \end{pmatrix}$$

(5.14)

In the following, $\hat{\mu_i}$ corresponds to a' and $\hat{\mu_j}$ corresponds to b'. The brackets ($\langle \quad \rangle$) indicate to evaluate the expectation value of argument. $\hat{E}_X$ is equal to a vector defined in the X direction ([1,0,0]) and $\hat{E}_Y$ is equal to a vector defined in the Y direction ([0,1,0]).

<u>XXXY:</u> $iijj = ijij \neq ijji$

$$\begin{aligned} \langle(\hat{\mu}_i \cdot \hat{E}_X)(\hat{\mu}_j \cdot \hat{E}_X)(\hat{\mu}_i \cdot \hat{E}_X)(\hat{\mu}_j \cdot \hat{E}_Y)\rangle &= \langle(\hat{\mu}_i \cdot \hat{E}_X)(\hat{\mu}_i \cdot \hat{E}_X)(\hat{\mu}_j \cdot \hat{E}_X)(\hat{\mu}_j \cdot \hat{E}_Y)\rangle \\ &= \frac{1}{2\pi}\int_0^{2\pi} d\phi\,(\sin\phi\sin\theta)^2(\sin\theta_{ab}(-\sin\psi\cos\theta\sin\phi + \cos\phi\cos\psi) \\ &+ \sin\theta\sin\phi\cos\theta_{ab})(\sin\theta_{ab}(-\sin\psi\cos\theta\cos\phi - \sin\phi\cos\psi) \\ &+ \sin\theta\sin\phi\cos\theta_{ab}) \\ &= -\frac{\cos\psi\sin\theta_{ab}\,(\sin\theta)^2}{4}(\cos\theta_{ab}\sin\theta - \cos\theta\sin\psi\sin\theta_{ab}) \end{aligned}$$

(5.15)

$$\langle(\hat{\mu}_i \cdot \hat{E}_X)(\hat{\mu}_j \cdot \hat{E}_X)(\hat{\mu}_j \cdot \hat{E}_X)(\hat{\mu}_i \cdot \hat{E}_Y)\rangle$$

$$= \frac{1}{2\pi}\int_0^{2\pi} d\phi \sin\phi \sin\theta \,(\sin\theta_{ab}(-\sin\psi\cos\theta\sin\phi + \cos\phi\cos\psi)$$

$$+ \sin\theta\sin\phi\cos\theta_{ab})^2 \cos\phi\sin\theta$$

$$= \frac{\cos\psi\sin\theta_{ab}\,(\sin\theta)^2}{4}(\cos\theta_{ab}\sin\theta - \cos\theta\sin\psi\sin\theta_{ab})$$

(5.16)

<u>XXYX:</u> $iijj = ijji \neq ijij$

$$\langle(\hat{\mu}_i \cdot \hat{E}_X)(\hat{\mu}_j \cdot \hat{E}_X)(\hat{\mu}_i \cdot \hat{E}_Y)(\hat{\mu}_j \cdot \hat{E}_X)\rangle$$

$$= \frac{1}{2\pi}\int_0^{2\pi} d\phi \sin\phi \sin\theta \,(\sin\theta_{ab}(-\sin\psi\cos\theta\cos\phi - \sin\phi\cos\psi)$$

$$+ \sin\theta\sin\phi\cos\theta_{ab})^2 \cos\phi\sin\theta = \frac{\cos\psi\sin\theta_{ab}\,(\sin\theta)^2}{4}(\cos\theta_{ab}\sin\theta$$

$$- \cos\theta\sin\psi\sin\theta_{ab})$$

(5.17)

$$\langle(\hat{\mu}_i \cdot \hat{E}_X)(\hat{\mu}_i \cdot \hat{E}_X)(\hat{\mu}_j \cdot \hat{E}_Y)(\hat{\mu}_j \cdot \hat{E}_X)\rangle = \langle(\hat{\mu}_i \cdot \hat{E}_X)(\hat{\mu}_j \cdot \hat{E}_X)(\hat{\mu}_j \cdot \hat{E}_Y)(\hat{\mu}_i \cdot \hat{E}_X)\rangle$$

$$= \frac{1}{2\pi}\int_0^{2\pi} d\phi\,(\sin\phi\sin\theta)^2(\sin\theta_{ab}(-\sin\psi\cos\theta\sin\phi + \cos\phi\cos\psi)$$

$$+ \sin\theta\sin\phi\cos\theta_{ab})(\sin\theta_{ab}(-\sin\psi\cos\theta\cos\phi - \sin\phi\cos\psi)$$

$$+ \sin\theta\sin\phi\cos\theta_{ab})$$

$$= -\frac{\cos\psi\sin\theta_{ab}\,(\sin\theta)^2}{4}(\cos\theta_{ab}\sin\theta - \cos\theta\sin\psi\sin\theta_{ab})$$

(5.18)

<u>XYXX:</u> $iijj \neq ijij = ijji$

$$\langle(\hat{\mu}_i \cdot \hat{E}_X)(\hat{\mu}_i \cdot \hat{E}_Y)(\hat{\mu}_j \cdot \hat{E}_X)(\hat{\mu}_j \cdot \hat{E}_X)\rangle$$

$$= \frac{1}{2\pi}\int_0^{2\pi} d\phi\sin\phi\sin\theta\,(\sin\theta_{ab}(-\sin\psi\cos\theta\sin\phi + \cos\phi\cos\psi)$$

$$+ \sin\theta\sin\phi\cos\theta_{ab})(\sin\theta_{ab}(-\sin\psi\cos\theta\cos\phi - \sin\phi\cos\psi)$$

$$+ \sin\theta\sin\phi\cos\theta_{ab})\cos\phi\sin\theta$$

$$= \frac{\cos\psi\sin\theta_{ab}\,(\sin\theta)^2}{4}(\cos\theta_{ab}\sin\theta - \cos\theta\sin\psi\sin\theta_{ab})$$

(5.19)

$$\langle(\hat{\mu}_i \cdot \hat{E}_X)(\hat{\mu}_j \cdot \hat{E}_Y)(\hat{\mu}_i \cdot \hat{E}_X)(\hat{\mu}_j \cdot \hat{E}_X)\rangle = \langle(\hat{\mu}_i \cdot \hat{E}_X)(\hat{\mu}_j \cdot \hat{E}_Y)(\hat{\mu}_j \cdot \hat{E}_X)(\hat{\mu}_i \cdot \hat{E}_X)\rangle$$

$$= \frac{1}{2\pi}\int_0^{2\pi} d\phi\,(\sin\phi\sin\theta)^2(\sin\theta_{ab}(-\sin\psi\cos\theta\sin\phi + \cos\phi\cos\psi)$$

$$+ \sin\theta\sin\phi\cos\theta_{ab})(\sin\theta_{ab}(-\sin\psi\cos\theta\cos\phi - \sin\phi\cos\psi)$$

$$+ \sin\theta\sin\phi\cos\theta_{ab})$$

$$= -\frac{\cos\psi\sin\theta_{ab}\,(\sin\theta)^2}{4}(\cos\theta_{ab}\sin\theta - \cos\theta\sin\psi\sin\theta_{ab})$$

(5.20)

<u>YXXX:</u> $ijj = ijij = ijji$

$$\langle(\hat{\mu}_i \cdot \hat{E}_Y)(\hat{\mu}_i \cdot \hat{E}_X)(\hat{\mu}_j \cdot \hat{E}_X)(\hat{\mu}_j \cdot \hat{E}_X)\rangle = \langle(\hat{\mu}_i \cdot \hat{E}_Y)(\hat{\mu}_j \cdot \hat{E}_X)(\hat{\mu}_i \cdot \hat{E}_X)(\hat{\mu}_j \cdot \hat{E}_X)\rangle$$

$$= \langle(\hat{\mu}_i \cdot \hat{E}_Y)(\hat{\mu}_j \cdot \hat{E}_X)(\hat{\mu}_j \cdot \hat{E}_X)(\hat{\mu}_i \cdot \hat{E}_X)\rangle$$

$$= \frac{1}{2\pi}\int_0^{2\pi} d\phi\sin\phi\sin\theta\,(\sin\theta_{ab}(-\sin\psi\cos\theta\sin\phi + \cos\phi\cos\psi)$$

$$+ \sin\theta\sin\phi\cos\theta_{ab})^2\cos\phi\sin\theta$$

$$= \frac{\cos\psi\sin\theta_{ab}\,(\sin\theta)^2}{4}(\cos\theta_{ab}\sin\theta - \cos\theta\sin\psi\sin\theta_{ab})$$

(5.21)

<u>YYYX:</u> $iijj = ijij \neq ijji$

$$\langle(\hat{\mu}_i \cdot \hat{E}_Y)(\hat{\mu}_i \cdot \hat{E}_Y)(\hat{\mu}_j \cdot \hat{E}_Y)(\hat{\mu}_j \cdot \hat{E}_X)\rangle = \langle(\hat{\mu}_i \cdot \hat{E}_Y)(\hat{\mu}_j \cdot \hat{E}_Y)(\hat{\mu}_i \cdot \hat{E}_Y)(\hat{\mu}_j \cdot \hat{E}_X)\rangle$$

$$= \frac{1}{2\pi}\int_0^{2\pi} d\phi\,(\cos\phi\sin\theta)^2(\sin\theta_{ab}(-\sin\psi\cos\theta\sin\phi + \cos\phi\cos\psi)$$

$$+ \sin\theta\sin\phi\cos\theta_{ab})(\sin\theta_{ab}(-\sin\psi\cos\theta\cos\phi - \sin\phi\cos\psi)$$

$$+ \sin\theta\sin\phi\cos\theta_{ab})$$

$$= \frac{\cos\psi\sin\theta_{ab}\,(\sin\theta)^2}{4}(\cos\theta_{ab}\sin\theta - \cos\theta\sin\psi\sin\theta_{ab})$$

(5.22)

$$\langle(\hat{\mu}_i \cdot \hat{E}_Y)(\hat{\mu}_j \cdot \hat{E}_Y)(\hat{\mu}_j \cdot \hat{E}_Y)(\hat{\mu}_i \cdot \hat{E}_X)\rangle$$

$$= \frac{1}{2\pi}\int_0^{2\pi} d\phi\sin\phi\sin\theta\,(\sin\theta_{ab}(-\sin\psi\cos\theta\cos\phi - \sin\phi\cos\psi)$$

$$+ \sin\theta\sin\phi\cos\theta_{ab})^2\cos\phi\sin\theta$$

$$= -\frac{\cos\psi\sin\theta_{ab}\,(\sin\theta)^2}{4}(\cos\theta_{ab}\sin\theta - \cos\theta\sin\psi\sin\theta_{ab})$$

(5.23)

<u>YYXY:</u> $iijj = ijji \neq ijij$

$$\langle(\hat{\mu}_i \cdot \hat{E}_Y)(\hat{\mu}_i \cdot \hat{E}_Y)(\hat{\mu}_j \cdot \hat{E}_X)(\hat{\mu}_j \cdot \hat{E}_Y)\rangle = \langle(\hat{\mu}_i \cdot \hat{E}_Y)(\hat{\mu}_j \cdot \hat{E}_Y)(\hat{\mu}_j \cdot \hat{E}_X)(\hat{\mu}_i \cdot \hat{E}_Y)\rangle$$

$$= \frac{1}{2\pi}\int_0^{2\pi} d\phi\,(\cos\phi\sin\theta)^2(\sin\theta_{ab}(-\sin\psi\cos\theta\sin\phi + \cos\phi\cos\psi)$$

$$+ \sin\theta\sin\phi\cos\theta_{ab})(\sin\theta_{ab}(-\sin\psi\cos\theta\cos\phi - \sin\phi\cos\psi)$$

$$+ \sin\theta\sin\phi\cos\theta_{ab})$$

$$= \frac{\cos\psi\sin\theta_{ab}\,(\sin\theta)^2}{4}(\cos\theta_{ab}\sin\theta - \cos\theta\sin\psi\sin\theta_{ab})$$

(5.24)

$$\langle(\hat{\mu}_i \cdot \hat{E}_Y)(\hat{\mu}_j \cdot \hat{E}_Y)(\hat{\mu}_i \cdot \hat{E}_X)(\hat{\mu}_j \cdot \hat{E}_Y)\rangle$$

$$= \frac{1}{2\pi}\int_0^{2\pi} d\phi\sin\phi\sin\theta\,(\sin\theta_{ab}(-\sin\psi\cos\theta\cos\phi - \sin\phi\cos\psi)$$

$$+ \sin\theta\sin\phi\cos\theta_{ab})^2\cos\phi\sin\theta$$

$$= -\frac{\cos\psi\sin\theta_{ab}\,(\sin\theta)^2}{4}(\cos\theta_{ab}\sin\theta - \cos\theta\sin\psi\sin\theta_{ab})$$

(5.25)

<u>YXYY:</u> $iijj \neq ijij = ijji$

$$\langle(\hat{\mu}_i \cdot \hat{E}_Y)(\hat{\mu}_i \cdot \hat{E}_X)(\hat{\mu}_j \cdot \hat{E}_Y)(\hat{\mu}_j \cdot \hat{E}_Y)\rangle$$

$$= \frac{1}{2\pi}\int_0^{2\pi} d\phi\sin\phi\sin\theta\,(\sin\theta_{ab}(-\sin\psi\cos\theta\cos\phi - \sin\phi\cos\psi)$$

$$+ \sin\theta\sin\phi\cos\theta_{ab})^2\cos\phi\sin\theta$$

$$= -\frac{\cos\psi\sin\theta_{ab}\,(\sin\theta)^2}{4}(\cos\theta_{ab}\sin\theta - \cos\theta\sin\psi\sin\theta_{ab})$$

(5.26)

$$\langle(\hat{\mu}_i \cdot \hat{E}_Y)(\hat{\mu}_j \cdot \hat{E}_X)(\hat{\mu}_i \cdot \hat{E}_Y)(\hat{\mu}_j \cdot \hat{E}_Y)\rangle = \langle(\hat{\mu}_i \cdot \hat{E}_Y)(\hat{\mu}_j \cdot \hat{E}_X)(\hat{\mu}_j \cdot \hat{E}_Y)(\hat{\mu}_i \cdot \hat{E}_Y)\rangle$$

$$= \frac{1}{2\pi}\int_0^{2\pi} d\phi\,(\cos\phi\sin\theta)^2(\sin\theta_{ab}(-\sin\psi\cos\theta\sin\phi + \cos\phi\cos\psi)$$

$$+ \sin\theta\sin\phi\cos\theta_{ab})(\sin\theta_{ab}(-\sin\psi\cos\theta\cos\phi - \sin\phi\cos\psi)$$

$$+ \sin\theta\sin\phi\cos\theta_{ab})$$

$$= \frac{\cos\psi\sin\theta_{ab}\,(\sin\theta)^2}{4}(\cos\theta_{ab}\sin\theta - \cos\theta\sin\psi\sin\theta_{ab})$$

(5.27)

<u>XYYY:</u> $iijj = ijij = ijji$

$$\langle(\hat{\mu}_i \cdot \hat{E}_X)(\hat{\mu}_i \cdot \hat{E}_Y)(\hat{\mu}_j \cdot \hat{E}_Y)(\hat{\mu}_j \cdot \hat{E}_Y)\rangle = \langle(\hat{\mu}_i \cdot \hat{E}_X)(\hat{\mu}_j \cdot \hat{E}_Y)(\hat{\mu}_i \cdot \hat{E}_Y)(\hat{\mu}_j \cdot \hat{E}_Y)\rangle$$

$$= \langle(\hat{\mu}_i \cdot \hat{E}_X)(\hat{\mu}_j \cdot \hat{E}_Y)(\hat{\mu}_j \cdot \hat{E}_Y)(\hat{\mu}_i \cdot \hat{E}_Y)\rangle$$

$$= \frac{1}{2\pi}\int_0^{2\pi} d\phi\sin\phi\sin\theta\,(\sin\theta_{ab}(-\sin\psi\cos\theta\cos\phi - \sin\phi\cos\psi)$$

$$+ \sin\theta\sin\phi\cos\theta_{ab})^2\cos\phi\sin\theta$$

$$= -\frac{\cos\psi\sin\theta_{ab}\,(\sin\theta)^2}{4}(\cos\theta_{ab}\sin\theta - \cos\theta\sin\psi\sin\theta_{ab})$$

(5.28)

From these equations, the relationships in Table 5.1 can be found for the pathways that contribute to the off-diagonal cross-peaks. In the following three equations (Eq. 5.29-5.31), we report the orientational four-point correlation function for the *iiii*, *iijj*, *ijij*, and *ijji* pathways in an

XXXY scheme for the bulk system. As in the surface case, the *iijj* and *ijij* pathways are equivalent and can be described by the same four-point correlation function. However, there is no distinction between the *i-j* and *j-i* cross-peak in the bulk case. Overall, all of these functions for the bulk system are zero in an XXXY scheme.

Bulk XXXY:

$$\langle(\hat{\mu}_i \cdot \hat{E}_X)(\hat{\mu}_i \cdot \hat{E}_X)(\hat{\mu}_i \cdot \hat{E}_X)(\hat{\mu}_i \cdot \hat{E}_Y)\rangle$$
$$= \frac{1}{8\pi^2}\int_0^{2\pi} d\psi \int_0^{\pi} d\theta \int_0^{2\pi} d\phi \sin\theta(\sin\phi \sin\theta)^3(\cos\phi \sin\theta) = 0$$

(5.29)

$$\langle(\hat{\mu}_i \cdot \hat{E}_X)(\hat{\mu}_i \cdot \hat{E}_X)(\hat{\mu}_j \cdot \hat{E}_X)(\hat{\mu}_j \cdot \hat{E}_Y)\rangle = \langle(\hat{\mu}_i \cdot \hat{E}_X)(\hat{\mu}_j \cdot \hat{E}_X)(\hat{\mu}_i \cdot \hat{E}_X)(\hat{\mu}_j \cdot \hat{E}_Y)\rangle$$
$$= \frac{1}{8\pi^2}\int_0^{2\pi} d\psi \int_0^{\pi} d\theta \int_0^{2\pi} d\phi \sin\theta(\sin\phi \sin\theta)^2(\sin\theta_{ab}(-\sin\psi\cos\theta\sin\phi$$
$$+ \cos\phi\cos\psi)$$
$$+ \sin\theta\sin\phi\cos\theta_{ab})(\sin\theta_{ab}(-\sin\psi\cos\theta\cos\phi - \sin\phi\cos\psi)$$
$$+ \sin\theta\sin\phi\cos\theta_{ab}) = 0$$

(5.30)

$$\langle(\hat{\mu}_i \cdot \hat{E}_X)(\hat{\mu}_j \cdot \hat{E}_X)(\hat{\mu}_j \cdot \hat{E}_X)(\hat{\mu}_i \cdot \hat{E}_Y)\rangle$$

$$= \frac{1}{8\pi^2}\int_0^{2\pi} d\psi \int_0^{\pi} d\theta \int_0^{2\pi} d\phi \sin\theta(\sin\phi \sin\theta)(\sin\theta_{ab}\,(-\sin\psi\cos\theta\sin\phi$$

$$+ \cos\phi\cos\psi) + \sin\theta\sin\phi\cos\theta_{ab})^2\,(\cos\phi\sin\theta) = 0$$

(5.31)

5.6.7 Third-Order Response Functions and Parameters for 2D Spectra Simulations

The following section reports the third-order response functions used to generate the 2D spectra in the main text as well as in the supplemental. The simulated spectra are calculated in the time domain by calculating the rephasing spectra ($\sum_{i=1,2,3} R_i^{(3)}$, Eq. 5.32-5.34) and non-rephasing spectra ($\sum_{i=4,5,6} R_i^{(3)}$, Eq. 5.35-5.47) separately. A double Fourier transform over both the pump and probe dimensions is done to show the rephasing and non-rephasing spectra in the frequency domain. The two frequency domain spectra are then added together to obtain a purely absorptive spectrum. Below are the third-order responses associated with rephasing and non-rephasing spectra.

$$R_1^{(3)}(t_3, t_2, t_1) = -(\langle(\hat{\mu}_i \cdot \hat{E}_d)(\hat{\mu}_i \cdot \hat{E}_c)(\hat{\mu}_i \cdot \hat{E}_b)(\hat{\mu}_i \cdot \hat{E}_a)\rangle|\mu_i|^4 e^{i\omega_i(t_1-t_3)-(t_1+t_3)/T_2}$$

$$+ \langle(\hat{\mu}_j \cdot \hat{E}_d)(\hat{\mu}_j \cdot \hat{E}_c)(\hat{\mu}_j \cdot \hat{E}_b)(\hat{\mu}_j \cdot \hat{E}_a)\rangle|\mu_j|^4 e^{i\omega_j(t_1-t_3)-(t_1+t_3)/T_2}$$

$$+ \langle(\hat{\mu}_i \cdot \hat{E}_d)(\hat{\mu}_j \cdot \hat{E}_c)(\hat{\mu}_i \cdot \hat{E}_b)(\hat{\mu}_j \cdot \hat{E}_a)\rangle|\mu_i|^2|\mu_j|^2 e^{i(\omega_i t_1-\omega_j t_3)-(t_1+t_3)/T_2}$$

$$+ \langle(\hat{\mu}_j \cdot \hat{E}_d)(\hat{\mu}_i \cdot \hat{E}_c)(\hat{\mu}_j \cdot \hat{E}_b)(\hat{\mu}_i \cdot \hat{E}_a)\rangle|\mu_i|^2|\mu_j|^2 e^{i(\omega_j t_1-\omega_i t_3)-(t_1+t_3)/T_2})$$

(5.32)

$$R_2^{(3)}(t_3,t_2,t_1) = -(\langle(\hat{\mu}_i\cdot\hat{E}_d)(\hat{\mu}_i\cdot\hat{E}_c)(\hat{\mu}_i\cdot\hat{E}_b)(\hat{\mu}_i\cdot\hat{E}_a)\rangle|\mu_i|^4 e^{i\omega_i(t_1-t_3)-(t_1+t_3)/T_2}$$
$$+\langle(\hat{\mu}_j\cdot\hat{E}_d)(\hat{\mu}_j\cdot\hat{E}_c)(\hat{\mu}_j\cdot\hat{E}_b)(\hat{\mu}_j\cdot\hat{E}_a)\rangle|\mu_j|^4 e^{i\omega_j(t_1-t_3)-(t_1+t_3)/T_2}$$
$$+\langle(\hat{\mu}_i\cdot\hat{E}_d)(\hat{\mu}_i\cdot\hat{E}_c)(\hat{\mu}_j\cdot\hat{E}_b)(\hat{\mu}_j\cdot\hat{E}_a)\rangle|\mu_i|^2|\mu_j|^2 e^{i(\omega_i t_1-\omega_j t_3)-(t_1+t_3)/T_2}$$
$$+\langle(\hat{\mu}_j\cdot\hat{E}_d)(\hat{\mu}_j\cdot\hat{E}_c)(\hat{\mu}_i\cdot\hat{E}_b)(\hat{\mu}_i\cdot\hat{E}_a)\rangle|\mu_i|^2|\mu_j|^2 e^{i(\omega_j t_1-\omega_i t_3)-(t_1+t_3)/T_2})$$

(5.33)

$$R_3^{(3)}(t_3,t_2,t_1) = -(\langle(\hat{\mu}_i\cdot\hat{E}_d)(\hat{\mu}_i\cdot\hat{E}_c)(\hat{\mu}_i\cdot\hat{E}_b)(\hat{\mu}_i\cdot\hat{E}_a)\rangle|\mu_i|^3|\mu_{2i}| e^{i(\omega_i t_1-\omega_{2i} t_3)-(t_1+t_3)/T_2}$$
$$+\langle(\hat{\mu}_j\cdot\hat{E}_d)(\hat{\mu}_j\cdot\hat{E}_c)(\hat{\mu}_j\cdot\hat{E}_b)(\hat{\mu}_j\cdot\hat{E}_a)\rangle|\mu_j|^3|\mu_{2j}| e^{i(\omega_j t_1-\omega_{2j} t_3)-(t_1+t_3)/T_2}$$
$$+\langle(\hat{\mu}_i\cdot\hat{E}_d)(\hat{\mu}_i\cdot\hat{E}_c)(\hat{\mu}_j\cdot\hat{E}_b)(\hat{\mu}_j\cdot\hat{E}_a)\rangle|\mu_i|^3|\mu_{i+j}| e^{i(\omega_i t_1-\omega_{i+j} t_3)-(t_1+t_3)/T_2}$$
$$+\langle(\hat{\mu}_j\cdot\hat{E}_d)(\hat{\mu}_j\cdot\hat{E}_c)(\hat{\mu}_i\cdot\hat{E}_b)(\hat{\mu}_i\cdot\hat{E}_a)\rangle|\mu_j|^3|\mu_{i+j}| e^{i(\omega_j t_1-\omega_{i+j} t_3)-(t_1+t_3)/T_2}$$
$$+\langle(\hat{\mu}_i\cdot\hat{E}_d)(\hat{\mu}_j\cdot\hat{E}_c)(\hat{\mu}_i\cdot\hat{E}_b)(\hat{\mu}_j\cdot\hat{E}_a)\rangle|\mu_i||\mu_{i+j}||\mu_j|^2 e^{i(\omega_i t_1-\omega_{i+j} t_3)-(t_1+t_3)/T_2}$$
$$+\langle(\hat{\mu}_j\cdot\hat{E}_d)(\hat{\mu}_i\cdot\hat{E}_c)(\hat{\mu}_j\cdot\hat{E}_b)(\hat{\mu}_i\cdot\hat{E}_a)\rangle|\mu_j||\mu_{i+j}||\mu_i|^2 e^{i(\omega_j t_1-\omega_{i+j} t_3)-(t_1+t_3)/T_2})$$

(5.34)

$$R_4^{(3)}(t_3,t_2,t_1) = -(\langle(\hat{\mu}_i\cdot\hat{E}_d)(\hat{\mu}_i\cdot\hat{E}_c)(\hat{\mu}_i\cdot\hat{E}_b)(\hat{\mu}_i\cdot\hat{E}_a)\rangle|\mu_i|^4 e^{-i\omega_i(t_1+t_3)-(t_1+t_3)/T_2}$$
$$+\langle(\hat{\mu}_j\cdot\hat{E}_d)(\hat{\mu}_j\cdot\hat{E}_c)(\hat{\mu}_j\cdot\hat{E}_b)(\hat{\mu}_j\cdot\hat{E}_a)\rangle|\mu_j|^4 e^{-i\omega_j(t_1+t_3)-(t_1+t_3)/T_2}$$
$$+\langle(\hat{\mu}_i\cdot\hat{E}_d)(\hat{\mu}_j\cdot\hat{E}_c)(\hat{\mu}_j\cdot\hat{E}_b)(\hat{\mu}_i\cdot\hat{E}_a)\rangle|\mu_i|^2|\mu_j|^2 e^{-i(\omega_i t_1+\omega_j t_3)-(t_1+t_3)/T_2}$$
$$+\langle(\hat{\mu}_j\cdot\hat{E}_d)(\hat{\mu}_i\cdot\hat{E}_c)(\hat{\mu}_i\cdot\hat{E}_b)(\hat{\mu}_j\cdot\hat{E}_a)\rangle|\mu_i|^2|\mu_j|^2 e^{-i(\omega_j t_1+\omega_i t_3)-(t_1+t_3)/T_2})$$

(5.35)

$$R_5^{(3)}(t_3,t_2,t_1) = -(\langle(\hat{\mu}_i\cdot\hat{E}_d)(\hat{\mu}_i\cdot\hat{E}_c)(\hat{\mu}_i\cdot\hat{E}_b)(\hat{\mu}_i\cdot\hat{E}_a)\rangle|\mu_i|^4 e^{-i\omega_i(t_1+t_3)-(t_1+t_3)/T_2}$$
$$+\langle(\hat{\mu}_j\cdot\hat{E}_d)(\hat{\mu}_j\cdot\hat{E}_c)(\hat{\mu}_j\cdot\hat{E}_b)(\hat{\mu}_j\cdot\hat{E}_a)\rangle|\mu_j|^4 e^{-i\omega_j(t_1+t_3)-(t_1+t_3)/T_2}$$
$$+\langle(\hat{\mu}_i\cdot\hat{E}_d)(\hat{\mu}_i\cdot\hat{E}_c)(\hat{\mu}_j\cdot\hat{E}_b)(\hat{\mu}_j\cdot\hat{E}_a)\rangle|\mu_i|^2|\mu_j|^2 e^{-i(\omega_i t_1+\omega_j t_3)-(t_1+t_3)/T_2}$$
$$+\langle(\hat{\mu}_j\cdot\hat{E}_d)(\hat{\mu}_j\cdot\hat{E}_c)(\hat{\mu}_i\cdot\hat{E}_b)(\hat{\mu}_i\cdot\hat{E}_a)\rangle|\mu_i|^2|\mu_j|^2 e^{-i(\omega_j t_1+\omega_i t_3)-(t_1+t_3)/T_2})$$

(5.36)

$$R_6^{(3)}(t_3,t_2,t_1) = -(\langle(\hat{\mu}_i\cdot\hat{E}_d)(\hat{\mu}_i\cdot\hat{E}_c)(\hat{\mu}_i\cdot\hat{E}_b)(\hat{\mu}_i\cdot\hat{E}_a)\rangle|\mu_i|^3|\mu_{2i}| e^{-i(\omega_i t_1+\omega_{2i} t_3)-(t_1+t_3)/T_2}$$
$$+\langle(\hat{\mu}_j\cdot\hat{E}_d)(\hat{\mu}_j\cdot\hat{E}_c)(\hat{\mu}_j\cdot\hat{E}_b)(\hat{\mu}_j\cdot\hat{E}_a)\rangle|\mu_j|^3|\mu_{2j}| e^{-i(\omega_j t_1+\omega_{2j} t_3)-(t_1+t_3)/T_2}$$
$$+\langle(\hat{\mu}_i\cdot\hat{E}_d)(\hat{\mu}_i\cdot\hat{E}_c)(\hat{\mu}_j\cdot\hat{E}_b)(\hat{\mu}_j\cdot\hat{E}_a)\rangle|\mu_i|^3|\mu_{i+j}| e^{-i(\omega_i t_1+\omega_{i+j} t_3)-(t_1+t_3)/T_2}$$
$$+\langle(\hat{\mu}_j\cdot\hat{E}_d)(\hat{\mu}_j\cdot\hat{E}_c)(\hat{\mu}_i\cdot\hat{E}_b)(\hat{\mu}_i\cdot\hat{E}_a)\rangle|\mu_j|^3|\mu_{i+j}| e^{-i(\omega_j t_1+\omega_{i+j} t_3)-(t_1+t_3)/T_2}$$
$$+\langle(\hat{\mu}_i\cdot\hat{E}_d)(\hat{\mu}_j\cdot\hat{E}_c)(\hat{\mu}_j\cdot\hat{E}_b)(\hat{\mu}_i\cdot\hat{E}_a)\rangle|\mu_i||\mu_{i+j}||\mu_j|^2 e^{-i(\omega_i t_1+\omega_{i+j} t_3)-(t_1+t_3)/T_2}$$
$$+\langle(\hat{\mu}_j\cdot\hat{E}_d)(\hat{\mu}_i\cdot\hat{E}_c)(\hat{\mu}_i\cdot\hat{E}_b)(\hat{\mu}_j\cdot\hat{E}_a)\rangle|\mu_j||\mu_{i+j}||\mu_i|^2 e^{-i(\omega_j t_1+\omega_{i+j} t_3)-(t_1+t_3)/T_2})$$

(5.37)

In equations 5.32-5.37, the argument in the brackets ($\langle(\hat{\mu}_\delta\cdot\hat{E}_d)(\hat{\mu}_\gamma\cdot\hat{E}_c)(\hat{\mu}_\beta\cdot\hat{E}_b)(\hat{\mu}_\alpha\cdot\hat{E}_a)\rangle$) is the value of the orientational four-point correlation function. $|\mu_\delta|^x$ is the magnitude of the dipole to the x power. t_3 and t_1 are the coherence times in the probe and pump dimensions respectively. T_2 is the dephasing time and is set to 2 ps for these simulations. To find $|\mu_\delta|^x$, the coupling constant (β) between the two dipoles, $\hat{\mu}_i$ and $\hat{\mu}_j$ must be taken into account.. β is

based on the direction of the two dipoles and the distance between them ($\overrightarrow{r_{iJ}}$). Equations 5.38-5.40 describe β, $\overrightarrow{r_{iJ}}$, and the magnitude of $\overrightarrow{r_{iJ}}$ (r).

$$\beta_{ij} = \frac{1}{4\pi\epsilon_o}\left(\frac{\overrightarrow{\mu_i}\cdot\overrightarrow{\mu_J}}{r_{ij}^3} - 3\frac{(\overrightarrow{r_{iJ}}\cdot\overrightarrow{\mu_i})(\overrightarrow{r_{iJ}}\cdot\overrightarrow{\mu_J})}{r_{ij}^5}\right)$$

(5.38)

$$\overrightarrow{r_{iJ}} = \begin{pmatrix} {}^1\!/_2 \sin\theta_{ab} \\ 0 \\ {}^1\!/_2 - {}^1\!/_2 \cos\theta_{ab} \end{pmatrix}$$

(5.39)

$$r = \sqrt{\frac{1}{2} - \frac{1}{2}\cos\theta_{ab}}$$

(5.40)

Note, that $\overrightarrow{r_{iJ}}$ only describes the distance between two dipoles in the XZ plane and is different when other orientations of the dipoles are used, such as in the spectra produces in figure 5.15. The coupling constant is then used to calculate the mixing angle (α) of the two dipoles. The two dipoles are then redefined by taking into account this mixing. Equations 5.41-5.43 describe these values, where ω_i and ω_j are two well-separated arbitrary wavelengths at which each dipole absorbs.

$$\tan 2\alpha = 2\frac{\beta_{ij}}{\hbar\omega_j - \hbar\omega_i}$$

(5.41)

$$\overrightarrow{\mu_i'} = \cos\alpha \cdot \overrightarrow{\mu_i} - \sin\alpha \cdot \overrightarrow{\mu_j}$$

(5.42)

$$\overrightarrow{\mu_j'} = \sin\alpha \cdot \overrightarrow{\mu_i} + \cos\alpha \cdot \overrightarrow{\mu_j}$$

(5.43)

To describe the transition dipoles of the overtones, it is assumed that the dipoles are close to a harmonic oscillator and so scale as $\mu_{12}^2 = 2\mu_{01}^2$.

Table 5.3 describes the r, β, and α values used for each spectrum calculated with a different θ_{ab}. For the 2D spectra calculated in different planes relative to the surface in figure 5.15, the same values hold for when $\theta_{ab} = 30°$. The only difference in the spectra in figure 5.15 is the directions in which $\overrightarrow{r_{ij}}$, $\overrightarrow{\mu_i'}$, and $\overrightarrow{\mu_j'}$ are defined. Table 5.4 provides the values of the orientational four-point correlation function for the eight Feynman pathways evaluated (*iiii*, *jjjj*, *iijj*, *ijij*, *ijji*, *jjii*, *jiji*, and *jiij*) for the 2D spectra shown in both the main text and the supplemental.

Table 5.3 Parameters of 2D Spectra Simulations

$\boldsymbol{\theta_{ab}}$	$\boldsymbol{r}$	$\boldsymbol{\beta_{ij}}$	$\boldsymbol{\alpha}$

0.000001*	7.451×10^{-9}	1.924×10^{23}	0.7854
30	0.2588	1.455	0.02488
45	0.3827	−0.5020	−0.008590
60	0.5000	−0.6366	−0.01089
90	0.7071	−0.3376	−0.005777

*In order to still evaluate the spectra, a value close to 0 was used

Table 5.4 Values of Orientational Four-Point Correlation Function used to simulate 2D Spectra

Figure 5.5				
Bulk: $\theta_{ab} = 30°$				
	XXXX	XXXY	YYYY	YYYX
iiii	0.2	1.225×10^{-17}	0.2	1.225×10^{-17}
jjjj	0.2	1.225×10^{-17}	0.2	1.225×10^{-17}
ijij	0.1667	1.021×10^{-17}	0.1667	1.021×10^{-17}
iijj	0.1667	1.021×10^{-17}	0.1667	1.021×10^{-17}
ijji	0.1667	1.021×10^{-17}	0.1667	1.021×10^{-17}
jiji	0.1667	1.021×10^{-17}	0.1667	1.021×10^{-17}
jjii	0.1667	1.021×10^{-17}	0.1667	1.021×10^{-17}
jiij	0.1667	1.021×10^{-17}	0.1667	1.021×10^{-17}
Surface ZX: $\theta_{ab} = 30°, \theta = 30°, \psi = 30°$				
	XXXX	XXXY	YYYY	YYYX
iiii	0.02441	1.494×10^{-18}	0.02441	1.494×10^{-18}

jjjj	0.0206	1.261×10^{-18}	0.0206	1.261×10^{-18}
ijij	0.01055	−0.00604	0.01055	0.00604
iijj	0.01055	−0.00604	0.01055	0.00604
ijji	0.01055	0.00604	0.01055	−0.00604
jiji	0.01055	−0.00604	0.01055	0.00604
jjii	0.01055	0.00604	0.01055	−0.00604
jiij	0.01055	−0.00604	0.01055	0.00604

Figure 5.9

Surface ZX: $\theta_{ab} = 0°, \theta = 30°, \psi = 30°$

	XXXX	XXXY		
iiii	0.02441	1.494×10^{-18}		
jjjj	0.02441	1.494×10^{-18}		
ijij	0.02441	1.494×10^{-18}		
iijj	0.02441	1.494×10^{-18}		
ijji	0.02441	1.494×10^{-18}		
jiji	0.02441	1.494×10^{-18}		
jjii	0.02441	1.494×10^{-18}		
jiij	0.02441	1.494×10^{-18}		

Surface ZX: $\theta_{ab} = 45°, \theta = 30°, \psi = 30°$

	XXXX	XXXY		
iiii	0.02441	1.494×10^{-18}		
jjjj	0.05269	3.226×10^{-18}		

ijij	0.01211	-0.001904		
iijj	0.01211	-0.001904		
ijji	0.01211	0.001904		
jiji	0.01211	-0.001904		
jjii	0.01211	0.001904		
jiij	0.01211	-0.001904		
Surface ZX: $\theta_{ab} = 60°, \theta = 30°, \psi = 30°$				
	XXXX	XXXY		
iiii	0.02441	1.494 x 10^{-18}		
jjjj	0.1237	7.573 x 10^{-18}		
ijij	0.01931	0.005958		
iijj	0.01931	0.005958		
ijji	0.01931	-0.005958		
jiji	0.01931	0.005958		
jjii	0.01931	-0.005958		
jiij	0.01931	0.005958		
Surface ZX: $\theta_{ab} = 90°, \theta = 30°, \psi = 30°$				
	XXXX	XXXY		
iiii	0.02441	1.494 x 10^{-18}		
jjjj	0.3278	2.007 x 10^{-17}		
ijij	0.04193	0.024		
iijj	0.04193	0.024		

ijji	0.04193	-0.024		
jiji	0.04193	0.024		
jjii	0.04193	-0.024		
jiij	0.04193	0.024		
Figure 5.10				
Surface ZX: $\theta_{ab} = 30°, \theta = 0°, \psi = 0°$				
	XXXX	XXXY		
iiii	0	0		
jjjj	0.02344	1.435 x 10^{-18}		
ijij	0	0		
iijj	0	0		
ijji	0	0		
jiji	0	0		
jjii	0	0		
jiij	0	0		
Surface ZX: $\theta_{ab} = 30°, \theta = 45°, \psi = 45°$				
	XXXX	XXXY		
iiii	0.09709	5.945 x 10^{-18}		
jjjj	0.02497	1.529 x 10^{-18}		
ijij	0.03362	-0.01639		
iijj	0.03362	-0.01639		
ijji	0.03362	0.01639		

jiji	0.03362	-0.01639		
jjii	0.03362	0.01639		
jiij	0.03362	-0.01639		
Surface ZX: $\theta_{ab} = 30°, \theta = 60°, \psi = 60°$				
	XXXX	XXXY		
iiii	0.2167	1.327 x 10^{-17}		
jjjj	0.04679	2.865 x 10^{-18}		
ijij	0.08929	-0.0252		
iijj	0.08929	-0.0252		
ijji	0.08929	0.0252		
jiji	0.08929	-0.0252		
jjii	0.08929	0.0252		
jiij	0.08929	-0.0252		
Surface ZX: $\theta_{ab} = 30°, \theta = 90°, \psi = 90°$				
	XXXX	XXXY		
iiii	0.375	2.296 x 10^{-17}		
jjjj	0.2109	1.292 x 10^{-17}		
ijij	0.2812	1.059 x 10^{-17}		
iijj	0.2812	1.059 x 10^{-17}		
ijji	0.2812	2.385 x 10^{-17}		
jiji	0.2812	1.059 x 10^{-17}		
jjii	0.2812	2.385 x 10^{-17}		

jiij	0.2812	1.059×10^{-17}		
Figure 5.14				
Surface XY (1): $\theta_{ab} = 30°, \theta = 30°, \psi = 30°$				
		XXXY		YYYX
iiii		1.506×10^{-17}		1.506×10^{-17}
jjjj		2.018×10^{-17}		2.018×10^{-17}
ijij		-0.08167		0.08167
iijj		-0.08167		0.08167
ijji		0.08167		-0.08167
jiji		-0.08167		0.08167
jjii		0.08167		-0.08167
jiij		-0.08167		0.08167
Surface XY (2): $\theta_{ab} = 30°, \theta = 30°, \psi = 30°$				
		XXXY		YYYX
iiii		2.007×10^{-17}		2.007×10^{-17}
jjjj		2.296×10^{-17}		2.018×10^{-17}
ijij		0.09335		-0.09335
iijj		0.09335		-0.09335
ijji		-0.09335		0.09335
jiji		0.09335		-0.09335
jjii		-0.09335		0.09335
jiij		0.09335		-0.09335

Surface YZ: $\theta_{ab} = 30°, \theta = 30°, \psi = 30°$				
		XXXY		YYYX
iiii		1.494 x 10^{-18}		1.494 x 10^{-18}
jjjj		1.189 x 10^{-17}		1.189 x 10^{-17}
ijij		−0.01304		0.01304
iijj		−0.01304		0.01304
ijji		0.01304		−0.01304
jiji		−0.01304		0.01304
jjii		0.01304		−0.01304
jiij		−0.01304		0.01304

6 List of Publications

6.1 Published

- **Erin R. Birdsall**, Megan K. Petti, Vivek Saraswat, Joshua S. Ostrander, Michael S. Arnold, and Martin T. Zanni. Structure Changes of a Membrane Polypeptide under an Applied Voltage Observed with Surface-Enhanced 2D IR Spectroscopy J. Phys. Chem. Lett. 2021, 12, 7, 1786–1792
- Megan K. Petti, Joshua S. Ostrander, **Erin R. Birdsall**, Miriam Bohlmann Kunz, Zachary Armstrong, Ariel M. Alperstein, and Martin T. Zanni. A Proposed Method to Obtain Surface Specificity with Pump-probe and 2D Spectroscopies J. Phys. Chem A. 2020, 124, 17, 3471–3483
- Joshua S. Ostrander, Justin P. Lomont, Kacie L. Rich, Vivek Saraswat, Benjamin R. Feingold, Megan K. Petti, **Erin R. Birdsall**, Michael S. Arnold, and Martin T. Zanni. Monolayer Sensitivity Enables 2D IR Spectroscopic Immuno-biosensor for Studying Protein Structures: Application to Amyloid Polymorphs. J. Phys. Chem. Lett. 2019, 10, 14, 3836-3962.
- Megan K. Petti, Joshua S. Ostrander, Vivek A. Saraswat, **Erin R. Birdsall,** Kacie Rich, Justin P. Lomont, Michael S. Arnold, and Martin T. Zanni, Enhancing the signal strength of surface sensitive 2D IR spectroscopy The Journal of Chemical Physics 2019 150:2

6.2 In Preparation

- **Erin Birdsall***, Matt Ryan*, […] Xuhui Huang, Francis Valiyaveetil, Martin Zanni. Backbone ester mutant in selectivity filter of different potassium channels reveal differences in ion occupancy via 2D IR spectroscopy.

- Rich, Kacie. L., Fields, Caitlyn. R., Lomont, Justin. P., Maj, Michał, Simonett, Shane P., Stapleton, Donald S., **Birdsall, Erin. R**., Petti, Megan. K., Alperstein, Ariel M., Evens, K. K., Das, Tarasankar, Keller, Mark P., Attie, Alan D., Zanni, Martin T. A Strategy for Trapping Cytotoxic Oligomers of Amyloids with Application to Human Islet Amyloid Polypeptide

  *Authors contributed equally

7 Chapter for the General Public

I have included this chapter in order to communicate my research to the general public. The work we do in the Zanni group is meant to better understand the world and it is vital to communicate these ideas to the public who, through tax dollars, fund the work that we do and therefore have a stake in our results. Many thanks to the Wisconsin Initiative for Science Literacy at UW-Madison for the opportunity to communicate my work to the public.

7.1 1. Introduction

Consider a biological cell. They are little bubbles of life with machinery contained within a lipid membrane. The lipids are fatty acids that are flexible yet separate what is inside and outside the cell. These lipid membranes are considered to be bilayers because they are formed of two layers of lipids. The ‘heads’ of the lipids face outwards and the ‘tails’ face inwards. Membranes help to also maintain concentrations of ions, charged atoms and molecules, within the cell. Often, there is a charge difference between the inside and the outside of the cell, due to different concentrations of these ions on either side called the resting potential or voltage. However, cells need to be able to communicate with each other and import and export nutrients and waste. To do this, many proteins are embedded in the membrane. Typically, each membrane

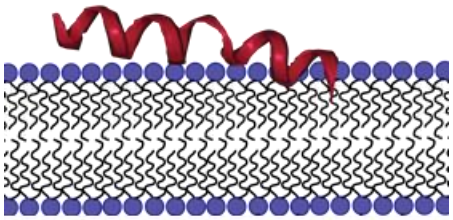

Figure 1. A section of lipid bilayer. The heads are in purple and the tails are in black lines. The red helix shows a membrane-associated protein sitting on top in a neutral position.

protein has one job to do: sense hormones, actively transport small molecules, or allow for the passive transport of ions across the membrane, causing a change in the membrane voltage. Proteins are made up of components called amino acids. Amino acids are bonded together through a peptide bond which create the 'backbone' of the protein like a string of beads. Each amino acid (there are 20 common ones) also has a section called the 'side chain' which dangles from the backbone and is unique to each amino acid. My Ph.D. work has been centered on figuring out how these membrane-bound proteins are moving in the membrane in order to do their jobs. Understanding typical protein function is important as a baseline to compare to proteins that cause disease, which ultimately can lead to rational drug design that specifically targets the disease-causing attribute of the protein. For example, in diseases where there are issues with ion channels not working properly due to mutations, like some forms of myotonia, leading to muscular contraction and seizures, channel blockers are used as a pharmacological tool to alleviate symptoms. The ability to block channels comes from knowing how healthy channels look and function.

7.2 2. An aside on the technique

The main technique that I have used to answer these questions is called two-dimensional

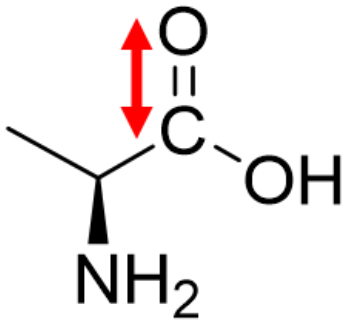

Figure 2. The chemical structure of an amino acid, alanine. We are mostly interested in the stretch between the C and the O as indicated by the red arrow. The amide I vibration that we study actually also includes the nitrogen atom and its hydrogens.

infrared spectroscopy (2D IR spectroscopy). This technique involves using an ultrafast laser to look at the vibrational energy of molecules. Molecules are constantly in motion. They vibrate and rotate in space, even in materials that are solid. All of these movements correspond to a certain amount of energy. We are concerned with vibrational energies. These can be easily imagined by thinking about two balls on a spring. Each ball represents an atom: in our case one is a little heavier than the other. The heavier ball is oxygen and the lighter ball is carbon. The bond between the two atoms is the spring. Depending on the two atoms, the spring might be a little tighter or looser. Each bond, or spring, has a characteristic vibrational energy, which we think about in frequency. The characteristic frequency can be changed depending on the environment around the atoms we are looking at. For example, the hydrogens in water can push and pull on the oxygen. Or a positively charged ion, like a potassium ion, can interact strongly with the partial negative charge on the oxygen. These interactions will increase the 'heaviness' of the oxygen and will change the frequency.

The energy of these frequencies is the same as infrared (IR) light. We shine our IR light on the molecules and we can measure how much of the energy is absorbed. By seeing the precise wavelength of light that is absorbed by our molecule, we can identify the atoms present, and also learn something about the orientation and environment of those molecules. Lastly, we use ultrafast laser systems (there are 1000 laser pulses per second, and each pulse is faster than one *trillionth* of a second long) so that we can see what is happening to these molecules over time. Molecules vibrate on the scale of picoseconds (one trillionth of a second) and proteins move on the scale of microseconds to milliseconds (one millionth to one thousandth of a second).

What makes this technique two-dimensional, is that we are actually using multiple pulses of light that interact with our sample. They are called the pump and probe pulses and that is how

we label the axes. The pump pulse interacts with our sample first and puts energy into the vibration of interest. Then, after a designated amount of time the probe pulse interacts with the sample to see what happened to the pump energy. Then we can calculate the change in the optical density which we call ΔOD which provides us with a spectrum. The Δ (delta) is used in many instances to mean 'change'. The 2D IR spectroscopy can be thought of as one friend calling another about their engagement. The friend is obviously excited from this interaction. Then, the new fiancée of the first friend also calls the friend right after, and sees how excited they are, compared to their normal state. The interactions between the pulse of light (new fiancés) and the sample (their mutual friend) tell us about the energy levels of the sample or friend.

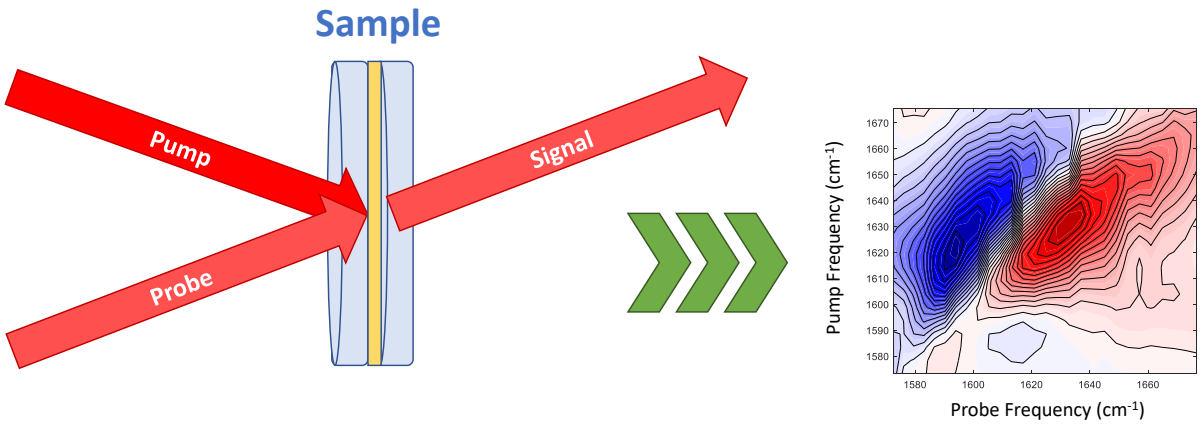

Figure 3. Graphic showing sample set up of 2DIR spectroscopy and a model spectrum representing the kind of data collected. The red arrows represent infrared light. The pump and probe overlap in time and space at the sample. Then we collect the signal beam and process the data. We then get a spectrum as shown here. This spectrum is of a voltage sensing domain discussed below.

7.3 3. The problem and our proposed solution

We started this project by thinking about how much is still not known about ion channels in membranes. Ion channels are a class of membrane-bound proteins that open and close after a physiological trigger and passively transport ions like potassium, sodium, and calcium across the

membrane. In humans, they play a vital role in nerve cells. The electric signals down nerve cell axons are perpetuated by voltage-gated (voltage controlled) ion channels which open when the voltage across the membrane changes. The continued opening of the channels successively down the axon of the nerve cell keeps triggering the voltage for the next ion channel, eventually signaling the release of neurotransmitters to the next neuron. The signal moves just like a series of dominos down the nerve cell. What is very interesting about ion channels is that they typically only allow one ion to flow through, but the ions flow through at a rate that is almost equivalent to just an open hole in the cell membrane. We want to know: what is it about the structure of these proteins that allow this to be possible? How are these proteins moving after a stimulus? How are the ions flowing through the channel? And finally, can we use our ultrafast laser systems to be able to 'watch' the movements in these channels in real time? Many of these experiments have not been done yet, but we are currently working on techniques to make them possible.

2D IR is an excellent technique to make these measurements. We are able to measure the amide I vibration, which is largely composed of the stretching vibration of the carbon and oxygen in the backbone of a protein. This vibrational frequency is very well studied and characterized. Proteins can take on different secondary structures like helices which look like hair ringlets and sheets which look like stacked lasagna noodles. Since these structures create different environments for the atoms we are interested in, the frequencies of these vibrations are also different. 2D IR also allows us to look more in depth at the way that vibrations interact with each other. This is a phenomenon called coupling, and it can be thought of as walking a dog on a leash. The speed of the dog when it stops to sniff causes a change in the speed of its human due to tension through the leash which couples them. We see cross peaks in the spectra when this occurs and we are able to see what parts of the sample are interacting with each other. Cross

peaks are shown as the peaks not on the diagonal in figure 4. The shapes of the peaks in the 2D IR spectra also give us information about the environment of the vibration. Elongated ovals along the diagonal mean that there is less structure or slower molecular motions, and more circular peaks on the diagonal indicate more structure or faster molecular motions. There are experiments that we do that help parse the difference between the motions and the structure. The last piece of data that 2D IR offers is the ability to extract information about orientation in space, when we have a sample that is on a surface. For example, when we have a single lipid bilayer with membrane proteins in it, we can calculate the angle of insertion of the protein by using our spectra! This means that our technique yields a lot of information when we are asking questions about environment, movement, and orientation of our proteins.

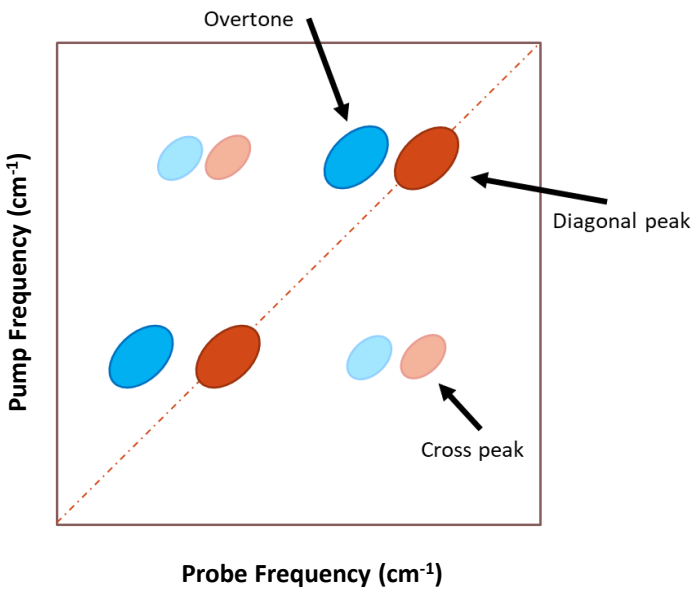

Figure 4. A cartoon 2DIR spectrum of two, coupled vibrations. Shades of red represent positive peaks and shades of blue represent negative peaks. The diagonal peaks fall on the diagonal line and represent the main vibration. The overtones next to them are the next higher in energy vibration. Cross peaks between the two peaks show the coupling between the two vibrations.

7.4 4. Developing a proof-of-concept to measure voltage-gated proteins

The first step in starting to study ion channels was to develop a method to work with a single bilayer and our protein of interest. We needed to use a single bilayer for two main reasons: we wanted to have a membrane that was oriented in space in order to see how the sample protein

moved relative to the membrane, and we also wanted to put a voltage across our sample to mimic the biological context of our proteins. Even if we had an oriented, but stacked, bilayer, it would be dangerous to apply a voltage since with each successive layer added, more of a voltage would have to be applied for the proteins to 'sense' the appropriate voltage due to the inherent electrical characteristics of a lipid membrane. However, if we just have a single bilayer of lipid and protein, there are not enough molecules to generate a nice signal. To counteract this, we used gold nanoparticles to enhance the signal. The gold nanoparticles are tiny drops of gold—only about 3-10 nm in size. This is incredibly small; a red blood cell is 6000 nm across. The gold nanoparticles are sometimes called nanoislands because under a microscope they look like little islands on an ocean. When IR light shines on the nanoislands, they create 'hot spots'. The hot spots are formed due to the IR light causing the electrons in the gold to bounce back and forth across each island inducing areas of highly concentrated energy. By placing our sample on these nanoislands, we are able to 1) enhance our signal, 2) tether our membrane to the gold by using lipids with sulfur attached to their heads, which readily bond to gold, allowing us to orient our sample and 3) use the gold as an electrode to create our voltage!

To test the viability of these methods, we used a smaller membrane protein. Alamethicin is a small membrane-associating protein that is produced by a fungus *Trichoderma viride*. The fungus creates alamethicin because it is an antibiotic. Alamethicin is drawn to a lipid membrane and will aggregate into groups of 6-8 individual proteins and form pores in the membrane. These pores are devastating to cells as they interfere with cell homeostasis, or stable conditions: hence its antibiotic effect. Alamethicin was a good candidate for our experiments because it is known to be triggered to aggregate and insert into the membrane based on either a change in pH or in

voltage. We could then verify our ability to measure a change of voltage by comparing the results to the pH experiments.

I took 2DIR spectra of alamethicin at a neutral pH and at a basic pH. I also took 2DIR spectra at no applied voltage and an applied voltage. What we saw was surprising! We expected that there would be a change in the frequency of the vibrations that would correspond to a change in the structure of alamethicin, which had previously been hypothesized. However, we saw instead that there was just a change in intensity of the three main peaks in our spectra. This was the case in both the voltage and the pH data. By using a piece of software developed by a previous graduate student in my group, we were able to model different secondary structures and orientations to determine what was happening to alamethicin when we either increased the pH or applied a voltage across the bilayer. We found that alamethicin structurally is composed of two helical elements connected by a kink in the protein. When alamethicin inserts into the membrane the kink angle changes along with the angle of insertion! We were excited that we were able to not only prove that we could take quality data using this

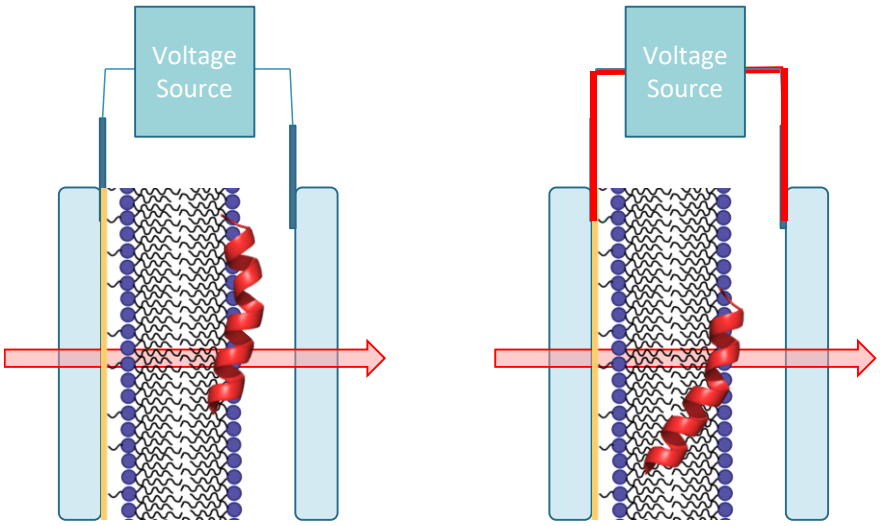

Figure 5. Schematic showing the sample cell with alamethicin on a bilayer tethered to gold (yellow line). Before the voltage is turned on (blue wires), the alamethicin is laying on top of the membrane. Spectra are taken represented by red arrow. Then voltage is turned on (red wires). Then alamethicin will insert into the membrane and more spectra are taken in order to compare.

platform, but also that we were able to contribute to the understanding of alamethicin.

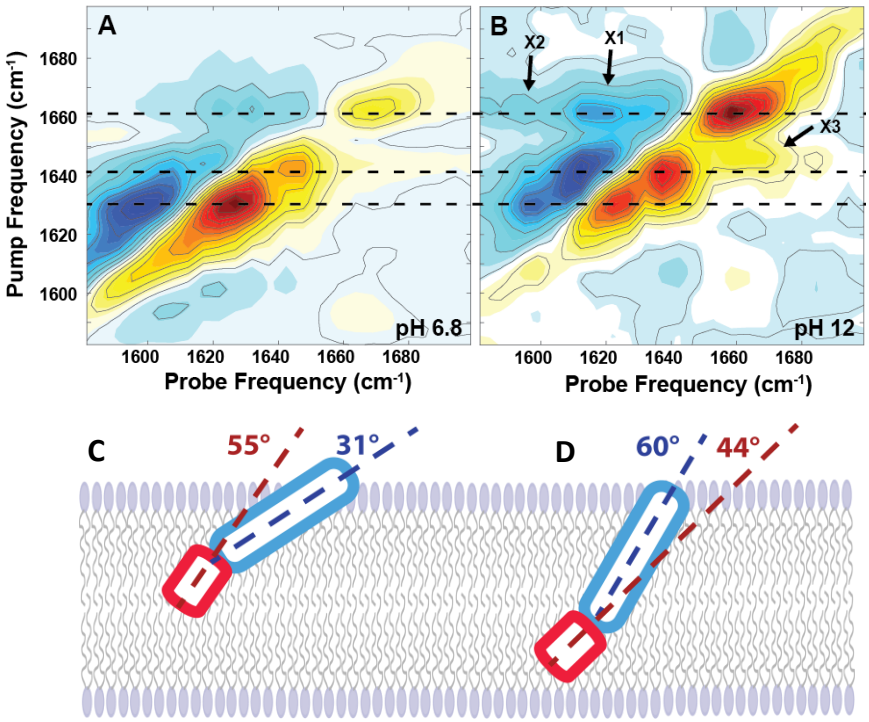

Figure 6. Representative data from my alamethicin project. A) shows the neutral pH spectrum, which is similar to the neutral voltage experiment. B) show the basic pH spectrum which is similar to the applied voltage spectrum. We saw these three peaks shown on the dotted lines are consistent across the spectra. Using modeling to recreate these spectra, we could back calculate the insertion angles of the two sections of alamethicin shown in C) (neutral) and D) (basic/applied voltage).

7.5 5. Looking at ion channel structure

We now had solved half of the problem of figuring out how we were going to study voltage-gated ion channels. However, we were working with a small protein, where we could look at every section of backbone at once and learn about the structure and orientation. The ion channels we want to study have 12 times the number of amino acids compared to alamethicin. This means that instead of seeing individual peaks for different protein structures, all of the peaks bleed together into one broad peak. We want to be able to learn about what is happening at

an individual amino acid, or at least at a small collection of amino acids so that we can best interpret our data.

We are interested in two parts of an ion channel. One is called the voltage sensing domain which, as the name suggests, is the part of the protein that senses a change in voltage. The voltage sensing domain only exists in voltage-gated ion channels and contains many positively-charged amino acids that react to changes in charge, whether it be being attracted to negative charges (opposites attract!) or being pushed, or repelled, by other positive charges. This work on the voltage sensing domain is very exciting though not the main thrust of the work I will present here. Though some preliminary work done on the voltage sensing domain shows us that something is in fact moving when we apply a voltage.

The other part of the ion channel that we are interested in looking at is called the selectivity filter. This is the part of the channel that only allows the particular ion of the channel to move through. The ion channels we study are potassium channels which are especially interesting. When you picture a filter, you probably think of something like a sieve. For example, when I am baking, when I sift my dry mixture of flour, baking powder, and salt, sometimes the salt does not pass through the filter because it is too large in size. The selectivity filter in these proteins actually does the opposite. In the particular ion channel we study, called KcsA, the filter lets potassium through, but prevents sodium, which is smaller, from entering the channel!

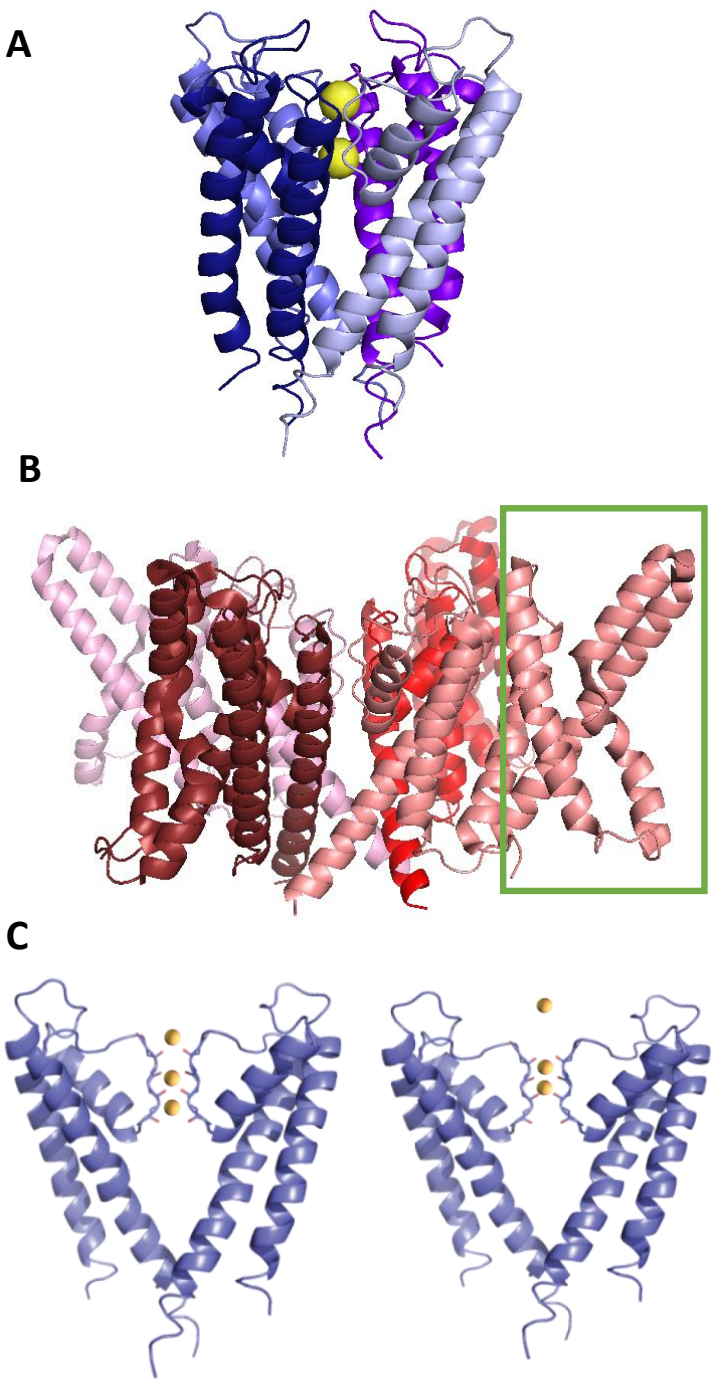

Figure 7. Cartoon images of ion channels. A) Shows KcsA with the four segments shown in different shades of blue and potassium ions in yellow moving through the channel. PDB 1Bl8. B) Shows KvAP, a voltage-gated ion channel with the four segments in different shades of red. The green box indicates the voltage sensing domain of one of the segments. PDB 6UWM. C) Shows different possible potassium configurations in KcsA. Only two of the four sections are shown to see how the selectivity filter interacts with the ions. The inward facing sticks are the carbon and oxygens bonds that we are measuring.

As I mentioned above, the 2DIR spectroscopy we do on proteins looks at how a carbon and oxygen bond vibrates. We are sensitive to changes in this vibration that can occur when an ion or water is next to the oxygen atom. In order to be able to see how these sites in the selectivity filter are impacted by the environment it is in, we need a way to be able to see one site away from the rest of the protein. We do this by creating labels. Labels can be used to change the frequency of the site of interest

in order to see it on its own in the spectrum. One way to make a label is to replace the carbon and the oxygen with heavier isotopes. We are still measuring the same amide I vibration, but the carbon weighs 13 atomic mass units instead of 12 atomic mass units, and the oxygen weighs 18 atomic mass units instead of 16 atomic mass units. Increasing the mass of the carbon and oxygen makes the amide I vibrate more slowly and allows us to look at just the amino acids where we replaced those atoms. A benefit of the isotope labelling technique is that there is no change in the protein structure when this label is added. Another method for labelling is just changing the amino acid to something else. The difference between an amide and an ester is that a nitrogen is being swapped for an oxygen. The ester stretch is higher in energy and also allows us to look directly at the site, but there is a small structural change. We can look at it because it moves the peak out of the bulk, like wearing a neon shirt at the state fair, so your family can find you more easily.

In the work that I am presenting here, we use the ester label. Not only would this be the first time that an ester in a protein backbone is studied using 2D IR spectroscopy, but we also are

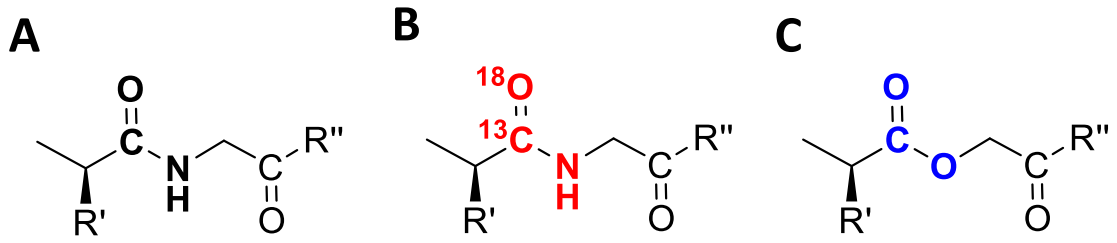

Figure 8. Showing a bonded pair of amino acids with different labelling schemes. R' and R'' are stand-ins for the side chains. A) is the unlabeled sample. B) Is the isotope label sample. Shown in red are the atoms contributing to the vibration. The weight is increased by the isotope labels of the carbon and the oxygen. C) shows the mutations from an amide in A) and B) to an ester (in blue). This will also cause a shift in the vibration.

able to glean information about the structural change. Previous information using different biochemical techniques show that the ester insertion in the selectivity filter has caused the ion

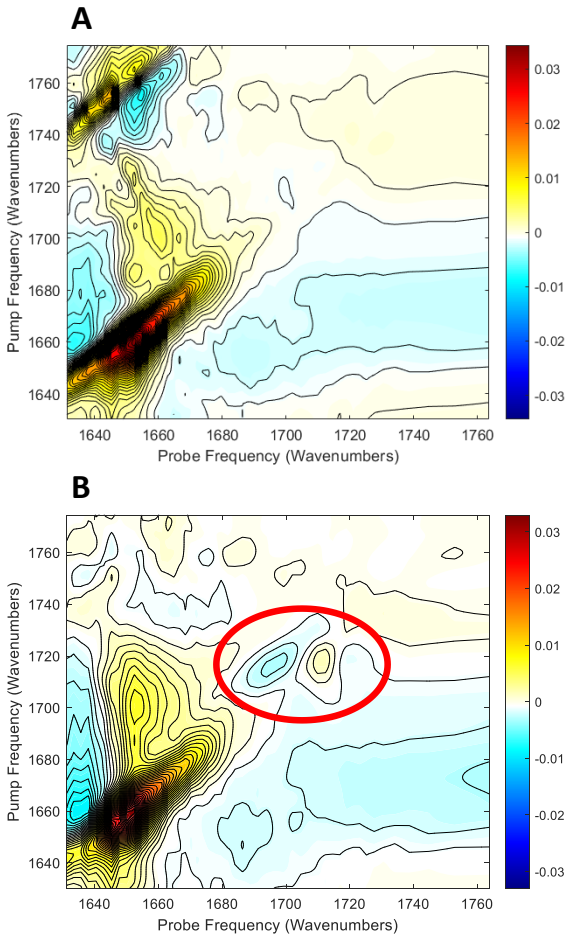

Figure 9. 2DIR spectra demonstrating the use of an ester label. A) NaK2K (a relative channel to Kcsa) without a label. The amide I vibration is the large peak in the lower left corner of the spectrum. B) NaK2K with an ester label. The peak corresponding to the ester vibration is circled in red. Now this specific site in the protein can be analyzed separately from the rest of the protein.

distribution to rearrange and that ions stop flowing through the channel. By systematically changing which amino acid in the channel was switched to an ester, those scientists were able to determine which amino acids are responsible for stopping ion flow. We are currently taking 2D IR spectra of KcsA, our potassium channel, with the ester label and are taking spectra at different time points to learn about how ions are influencing the carbon and oxygen bond. Then we hope to interpret our data with the help of calculations that will allow us to see how the ion channel could be moving.

7.6 6. Conclusions

Most of the work done in my Ph.D. focused on finding ways to make new and exciting measurements on membrane-bound proteins. Many of the problems I have needed to solve have come from figuring out how to make measurements of difficult to work with samples and then being able to take data that allows us to learn something. Furthermore, this work is a leap in progress in method development. Much of the work presented here is ‘basic science’ which

means that we are trying to figure out how the world around us works. Although it is harder to see the impact of this work on things like human health, for example, I think it is similar to the fact that before you can understand how to fix a broken car engine, you also need to know what a working one looks like and understand how it runs. I like to think that the impact of this work, maybe decades down the road, will help us better understand and treat the root of nervous system diseases, based on my creating a useful tool to study ion channels and membrane-bound proteins over the last five years. Next, I will be working at the Smithsonian Institution as a post-doctoral fellow using vibrational spectroscopy, along with other techniques, to study how display cases and other gallery and storage environments interact with the objects on display so that the objects can stay healthy for generations to come.